

Nanoscale Characterization of Amyloid Fibrils and Biomacromolecules by Atomic Force Microscopy Approaches

Présentée le 24 septembre 2020

à la Faculté des sciences de base
Laboratoire de physique de la matière vivante
Programme doctoral en physique

pour l'obtention du grade de Docteur ès Sciences

par

Jiangtao ZHOU

Acceptée sur proposition du jury

Prof. R. Houdré, président du jury
Prof. G. Dietler, Dr S. Sekatski, directeurs de thèse
Prof. T. Knowles, rapporteur
Prof. P. Arosio, rapporteur
Prof. F. Stellacci, rapporteur

Acknowledgements

“The pursuit of PhD is an enduring daring adventure” - Lailah Gifty Akita. Indeed, the journey of pursuing the PhD for me is an explorative trip with challenging tasks and valuable experience at the same time. Prior to this journey, I had absolutely no experience on the atomic force microscope, nor protein aggregation. I was completely unacquainted with this interdisciplinary area which became such a challenge for me, but soon it became so attractive after I had appreciated the beauty of the nanoworld in the nature and the significance of the research. I realized that such a compact device in my hand contained the power to open the window of the nanoworld, that allows me to discover the underlying rules in this nanoworld to conquer the global problems, as well as to indulge my curiosity.

Moreover, I believe that devoting myself to the PhD study is not only for earning a degree, but also for the experience of independently performing a comprehensive research: how to seek an interesting scientific question, to refer to hundreds of publications, to construct the research idea, to design the research plan, to collaborate with colleagues, to perform the experiment, to analyze data, and to sum up a valuable conclusion to the broad readers. This experience is the most valuable treasure I obtained in the last four years of my study.

Hereby, it is my great honor to present you the work that I have accomplished during my PhD study in the following sections. Importantly, these achievements in this thesis could never have been made without the kind advice and generous help from my colleagues and collaborators, and thus I would like to address my sincere acknowledgement.

First of all, I would like to express my highest respect and deepest thank to Prof. Giovanni Dietler and Dr. Sergey Sekatskii, as the two advisors of mine. Giovanni, a supporting mentor and true friend, has been always sharing his scientific vision and giving many insightful ideas in our discussion. I was also very impressed that he always generously offered the unconditional supports when I encountered difficulties or wanted to seek collaboration on my research. And, I appreciate Giovanni for creating the fantastic atmosphere in the group where people are friendly and helpful and I spent four wonderful years. Sergey, I deeply value your kind advice and patient guidance during my studying. I feel so fortunate to stay in the same office with you during my stay, so that I had the opportunity to closely discuss with you, to be advised on every details of the research and to learn from your commitment toward work and research. Besides, I would like to acknowledge Sergey for sharing his wisdom on

more than scientific research, but also personal life. Overall, I cannot express enough gratitude to both Giovanni and Sergey for their dedication on guiding me in the last four years.

Then, I sincerely thank all my colleagues in the group LPMV at EPFL. The atmosphere in the group was so nice and all the members were so friendly and helpful during the wonderful four years. A sincere thank goes to Sandor Kasas for the fruitful discussion and great advice that allows me to work more efficiently. I thank Leonardo for his kind help on solving the problems that we found in the experiments. Thanks to our former member Anton Smirnov for sharing his intelligence in performing the experiment. A great thank to all the current members: Kamila Guerin, Anne-Céline Kohler, Anton Malovichko, Zeno Messi, and Alexander Verkhovsky; and our former members Ekaterina Rostova, Petar Stupar and Wojciech Chomicki. A special thanks goes to Mireille Fasmeyer and Florent Wenger for their administrative and technical supports, and I appreciate Caroline Maillard and Raphael Foschia for their assistance on the experimental instrumentation.

Successively, I would like to address the acknowledgement to Dr. Francesco Ruggeri, Prof. Tuomas Knowles, Manuela Zimmermann and Dr. Georg Meisl for the nice collaborations on the interesting research topic, as well as their kind supports on research material and data analysis. It was a wonderful experience to work with you. Thanks to Prof. Wieslaw Gruszecki, Dr. Renata Welc, Dr. Ludovic Keiserd, Prof. François Gallaired, Dr. Salvatore Assenza, Dr. Ioana M. Ilie and Prof. Amedeo Caflisch for their kind help and professional assistance on the performing experiment and analyzing the research data. A special thank goes to Prof. Raffaele Mezzenga for the kind discussion.

In addition, I want to thank the personnel and research groups at EPFL who kindly shared their facilities to our research, including Prof. Hilal Lashuel (LMNN), Xudong Kong and Prof. Heinis (LPPT), Zaiwei Wang and Prof. Anders Hagfeldt (LPS), and Prof. Aleksandra Radenovic (LBEN).

Lastly, the deepest gratitude goes to my family for their unconditional support and consistent love that is beyond the expression in a short paragraph. Besides, I would like to appreciate my friends in Switzerland, China and other countries, for their inspiration and company in my life.

Lausanne, 5th March 2020

Jiangtao

Abstract

The content of studies in this thesis focuses on the interdisciplinary biophysical research field, in which physical approaches are applied to study the biological phenomena. Specifically, the main object of the research in this thesis is to target biological species, especially the amyloid fibrils by using Atomic Force Microscope (AFM) and several relevant technologies.

First of all, two sections of introduction are given to characterize the methodology and main research targets in this interdisciplinary area. The first chapter aims at the AFM, which is the main technique used throughout this thesis, and we present the history of AFM development, the basic AFM working principle and the cutting-edge AFM technologies. The second introduction targets at protein aggregation and amyloid fibrils, which is the main research topic throughout my PhD study, and we emphasise its biological association with neurodegenerative diseases, the aggregation pathways, molecular structures and the common approaches of protein aggregation characterization.

In the main section, we firstly present the high-resolution AFM and AFM-IR measurement on the LHCII on the chloroplast lipid membrane, and investigation on the regulation of the xanthophyll pigments, including violaxanthin and zeaxanthin, on the supramolecular organization and structural conformation of LHCII on the chloroplast lipid. Then, the novel vis-PTIR technique shows its capability for ultra-sensitive nanoscale imaging and chemical analysis. This AFM-based approach is enhanced by both the gap plasmon and the instrumentation resonance that shows a high-spatial resolution and single-molecule layer sensitivity.

Then, my following researches are focused on the protein aggregation and amyloid fibrils that are associated with various neurodegenerative diseases. The first research target is to investigate the environmental factors on protein aggregation kinetics and amyloid formation. We designed the experimental setup to highlight the influence of sedimentation, microgravity, hydrodynamic flow, air-water interface on the protein aggregation kinetics and distinct microscopic steps of aggregation. The results show that the interface promotes the primary nucleation and hydrodynamics enhances the secondary nucleation, whereas the sedimentation and microgravity contribute no significant impact on the aggregation kinetics.

Similarly, to understand the polymorphism phenomenon encountered in the preceding research, we performed an additional experiment with well-controlled environmental kinetics. This environmental

kinetics originated from the different combinations of hydrodynamics and interface. This experiment proves that the amyloid polymorphism is under the control of environmental kinetics, as well as the order-order transition among the polymorphs. This conclusion is expected to expand our understanding on fibrillization mechanism and also to show its significance in the biomaterial applications.

Last, but not the least, we propose another possible mechanism of amyloid aggregation, hierarchically assembly model (HAM), that enables the protofilament intertwining to form higher-ordered mature fibrils. In this experiment, this novel intertwining model based on statistical result of AFM images, is verified with the modelling and multiple experimental evidences, that may enrich our current knowledge of fibrillization mechanism and mature fibril formation.

In the end of this thesis, we briefly summarize the presented scientific works and their potential in the applications. In addition, we developed the perspective of these research in the future with several examples of the interesting topics.

Keywords: Atomic Force Microscope, AFM-infrared spectroscopy, Photothermal-induced resonance, LHCII, Protein aggregation and amyloid fibrils, Neurodegenerative disease, Environmental control, Aggregation kinetics, Amyloid polymorphism, Amyloid fibrillization mechanism.

Résumé

Le contenu des études de cette thèse se concentre sur le domaine de la recherche biophysique interdisciplinaire, dans lequel des approches physiques sont appliquées pour étudier les phénomènes biologiques. Plus précisément, l'objectif principal de la recherche dans cette thèse est de cibler les espèces biologiques, en particulier les fibrilles amyloïdes en utilisant le microscope à force atomique (AFM) et plusieurs technologies pertinentes.

Tout d'abord, deux sections d'introduction sont données pour caractériser la méthodologie et les principales cibles de recherche dans ce domaine interdisciplinaire. Le premier chapitre porte sur l'AFM, qui est la principale technique utilisée tout au long de cette thèse. Nous présentons l'histoire du développement de l'AFM, le principe de fonctionnement de base de l'AFM et les technologies de pointe de l'AFM. La deuxième introduction porte sur l'agrégation des protéines et les fibrilles amyloïdes, qui est le principal sujet de recherche tout au long de ma thèse, et nous mettons l'accent sur son association biologique avec les maladies neurodégénératives, les voies d'agrégation, les structures moléculaires et les approches communes de la caractérisation de l'agrégation des protéines.

Dans la section principale, nous présentons tout d'abord la mesure AFM et AFM-IR haute résolution sur le LHCII sur la membrane lipidique du chloroplaste, et l'étude de la régulation des pigments xanthophylles, y compris la violaxanthine et la zéaxanthine, sur l'organisation supramoléculaire et la conformation structurelle des LHCII sur le lipide chloroplastique. Ensuite, la nouvelle technique vis-PTIR montre sa capacité à produire des images et des analyses chimiques ultra-sensibles à l'échelle nanométrique. Cette approche basée sur l'AFM est renforcée par le plasmon gap et la résonance d'instrumentation qui montrent une résolution spatiale élevée et une sensibilité de la couche monomoléculaire.

Ensuite, mes recherches suivantes se concentrent sur l'agrégation des protéines et les fibrilles amyloïdes qui sont associées à diverses maladies neurodégénératives. Le premier objectif de recherche est d'étudier les facteurs environnementaux sur la cinétique de l'agrégation des protéines et la formation de l'amyloïde. Nous avons conçu le dispositif expérimental pour mettre en évidence l'influence de la sédimentation, de la microgravité, de l'écoulement hydrodynamique, de l'interface air-eau sur la cinétique d'agrégation des protéines et les différentes étapes microscopiques de l'agrégation. Les résultats montrent que l'interface favorise la nucléation primaire et que l'hydrodynamique améliore la

nucléation secondaire, alors que la sédimentation et la microgravité n'ont pas d'impact significatif sur la cinétique d'agrégation.

De même, pour comprendre le phénomène de polymorphisme rencontré dans les recherches précédentes, nous avons réalisé une expérience supplémentaire avec une cinétique environnementale bien contrôlée. Cette cinétique environnementale est issue des différentes combinaisons de l'hydrodynamique et de l'interface. Cette expérience prouve que le polymorphisme amyloïde est sous le contrôle de la cinétique environnementale, ainsi que de la transition ordre-ordre entre les polymorphes. Cette conclusion devrait élargir notre compréhension du mécanisme de fibrillisation et montrer son importance dans les applications des biomatériaux.

Enfin, nous proposons un autre mécanisme possible d'agrégation amyloïde, le modèle d'assemblage hiérarchique (HAM), qui permet aux protofilaments de s'entrelacer pour former des fibrilles matures d'ordre supérieur. Dans cette expérience, ce nouveau modèle d'entrelacement basé sur le résultat statistique des images AFM, est vérifié par la modélisation et de multiples preuves expérimentales, qui peuvent enrichir nos connaissances actuelles sur le mécanisme de fibrillisation et la formation de fibrilles matures.

À la fin de cette thèse, nous résumons brièvement les travaux scientifiques présentés et leur potentiel dans les applications. De plus, nous avons développé la perspective de ces recherches dans le futur avec plusieurs exemples de sujets intéressants.

Mots-clés: Microscope à force atomique, spectroscopie infrarouge AFM, Résonance photothermique induite, LHCII, Agrégation des protéines et fibrilles amyloïdes, Maladie neurodégénérative, Contrôle de l'environnement, Cinétique d'agrégation, Polymorphisme amyloïde, Mécanisme de fibrillisation amyloïde.

Contents


ACKNOWLEDGEMENTS.....	I
ABSTRACT.....	III
RÉSUMÉ.....	V
LIST OF FIGURES	IX
LIST OF TABLES	XI
LIST OF ABBREVIATIONS.....	XIII
CHAPTER 1 INTRODUCTION OF AFM.....	1
1.1 SPM AND AFM HISTORY	3
1.2 AFM INSTRUMENTATION	4
1.2.1 AFM cantilevers and tips	5
1.2.2 Deflection sensors	6
1.3 AFM FUNDAMENTALS.....	7
1.3.1 Cantilever oscillation and calibration	7
1.3.2 AFM topographic modes	9
1.4 THE OPERATION OF AFM IMAGING	13
1.4.1 AFM scanning parameters.....	13
1.4.2 The quality of scanning AFM probe.....	15
1.4.3 AFM deconvolution effect.....	16
1.5 AFM NANOINDENTATION	16
1.6 AFM FORCE SPECTROSCOPY	17
1.7 AFM-IR NANOSPECTROSCOPY	18
1.8 AFM NANOMOTION SENSOR.....	19
1.9 OTHER CUTTING-EDGE AFM TECHNIQUES	19
CHAPTER 2 PROTEIN AGGREGATION AND RELATED HUMAN DISEASES	21
2.1 PROTEIN MISFOLDING AND NEURODEGENERATIVE DISEASES.....	21
2.1.1 The situation of protein misfolding diseases.....	23
2.1.2 Protein aggregate toxicity	23
2.2 PROTEIN MISFOLDING AND AGGREGATION PATHWAY	24
2.2.1 Aggregation kinetics.....	25
2.2.2 Molecular structure of Amyloid fibril.....	27
2.2.3 Amyloid polymorphism and order-order transitions	28
2.3 FUNCTIONAL MATERIAL AND NANOTECHNOLOGICAL APPLICATIONS OF AMYLOIDS.....	30
2.4 CHARACTERIZATION OF PROTEIN AGGREGATION IN VITRO	32
2.4.1 ThT fluorescence	32
2.4.2 CD spectroscopy.....	34
2.4.3 AFM.....	34
2.4.4 TEM and CryoEM imaging	35
2.4.5 Infrared (IR) spectroscopy.....	36
2.4.6 Solid state NMR and X-ray diffraction	37
CHAPTER 3 REGULATION OF SUPRAMOLECULAR ARCHITECTURES OF LHCI ON LIPID MEMBRANE	39
3.1 INTRODUCTION	41
3.2 EXPERIMENTAL METHODS	43
3.3 RESULTS AND DISCUSSION.....	45
3.4 CONCLUSION	53

CHAPTER 4	GAP-PLASMON ENHANCED PHOTOTHERMAL INDUCED RESONANCE (PTIR)	55
4.1	INTRODUCTION	56
4.2	EXPERIMENTAL METHODS	57
4.3	RESULTS	59
4.3.1	<i>Characterization of Rhodamine 800 dye nanohills</i>	61
4.3.2	<i>Characterization of monolayers of Chlorophyll-a</i>	64
4.3.3	<i>Characterization of amyloid fibrils stained with MB dye</i>	67
4.4	CONCLUSION	70
CHAPTER 5	EFFECT OF SEDIMENTATION, MICROGRAVITY, HYDRODYNAMIC MIXING AND AIR-WATER INTERFACE ON PROTEIN AGGREGATION	71
5.1	INTRODUCTION	73
5.2	EXPERIMENTAL METHODS	74
5.3	RESULTS	76
5.3.1	<i>Nanoscale imaging of α-synuclein amyloid formation</i>	79
5.3.2	<i>Correlation of CD spectroscopy and ThT fluorescence to characterize aggregation</i>	81
5.3.3	<i>Chemical kinetics analysis</i>	85
5.4	CONCLUSION	86
CHAPTER 6	ENVIRONMENTAL CONTROL OF AMYLOID POLYMORPHISM AND ORDER-ORDER TRANSITION AMONG FIBRIL POLYMORPHS	87
6.1	INTRODUCTION	89
6.2	EXPERIMENTAL METHODS	90
6.3	RESULTS	93
6.3.1	<i>Experimental setup and hydrodynamics simulation</i>	93
6.3.2	<i>Conversion of secondary structure of α-Syn aggregates</i>	95
6.3.3	<i>Aggregation kinetics of α-Syn fibrillization</i>	96
6.3.4	<i>The nanoscale characterization of polymorphic amyloid fibrils</i>	97
6.3.5	<i>Order-order transition among fibril polymorphs</i>	102
6.4	CONCLUSION	105
CHAPTER 7	INTERPROTOFILAMENT INTERACTION AND CONFIGURATIONAL IDENTIFICATION OF HIERARCHICALLY TWISTED AMYLOID FIBRILS	107
7.1	INTRODUCTION	109
7.2	EXPERIMENTAL METHODS	110
7.3	RESULTS	116
7.3.1	<i>Morphological evolution of the insulin amyloids</i>	116
7.3.2	<i>Statistical analysis on the morphological features of twisted fibrils</i>	120
7.3.3	<i>Morphological modelling of twisted fibrils</i>	125
7.3.4	<i>Energetics modelling of the twisted fibrils</i>	129
7.4	CONCLUSION	131
CHAPTER 8	CONCLUSION AND FUTURE PERSPECTIVE	133
8.1	THE CONCLUSION ON THE EXPERIMENTAL RESULTS IN THE THESIS	133
8.2	FUTURE DEVELOPMENTS	135
REFERENCES		138

List of Figures

Figure 1.1 The vision of different microscopies.....	2
Figure 1.2 Schematics of a typical atomic force microscope.....	5
Figure 1.3 The design of a number of AFM deflection sensors.....	6
Figure 1.4 The theory of AFM cantilever oscillation.....	7
Figure 1.5 The working principle of typical AFM imaging modes.....	10
Figure 1.6 The AFM driving signal-cantilever amplitude response.....	13
Figure 1.7 Possible scanning artifacts in the AFM imaging.....	14
Figure 1.8 Importance of AFM tip on the image quality.....	15
Figure 1.9 The deconvolution effect of AFM imaging.....	16
Figure 1.10 The force-distance curve and quantitative mapping of multiple properties of sample.....	17
Figure 1.11 Schematics of AFM force spectroscopy applications.....	18
Figure 1.12 The schematics of AFM-IR and AFM nanomotion methods.....	19
Figure 2.1 Schematic representation of the conversion of globular proteins into amyloid fibrils.....	24
Figure 2.2 The analysis on the protein aggregation kinetics.....	26
Figure 2.3 The cryoEM revealed molecular structure of amyloid fibrils.....	27
Figure 2.4 Amyloid polymorphism and order-order transition.....	29
Figure 2.5 Functional applications of amyloid fibrils.....	31
Figure 2.6 The ThT and CD characterization of protein aggregation.....	33
Figure 3.1 Schematic of the xanthophyll cycle under both low and strong light intensity.....	42
Figure 3.2 Schematic of AFM experiment of LHCII on the lipid bilayers.....	44
Figure 3.3 AFM measurement on LHCII protein.....	46
Figure 3.4 AFM measurement on LHCII protein in the presence of the violaxanthin.....	47
Figure 3.5 AFM measurement on LHCII protein in the presence of the zeaxanthin.....	47
Figure 3.6 The morphological comparison of LHCII in the presence/absence of the xanthophylls.....	48
Figure 3.7 AFM-IR characterization of the lipoprotein multibilayers in the presence/absence of the xanthophylls.....	50
Figure 3.8 FLIM analysis of the LHCII-lipid membrane fragments.....	52
Figure 4.1 Schematic representation and characterization of the visible PTIR setup.....	60
Figure 4.2 The simulation of cantilever resonance.....	61
Figure 4.3 The UV-vis absorption spectrum of the 1% Rhodamine 800 dye solution.....	62
Figure 4.4 The visible PTIR measurements of the nanohill-like Rhodamine cluster.....	62
Figure 4.5 The characterization of the nanohill-like Rhodamine cluster.....	63
Figure 4.6 The visible PTIR characterization of chlorophyll-a monolayer.....	65
Figure 4.7 The preparation of MB stained α -Synuclein fibrils.....	67
Figure 4.8 The visible PTIR characterization of methylene blue stained amyloid fibrils.....	68
Figure 4.9 The characterization of α -Synuclein fibrils.....	69
Figure 5.1 Schematic of the experimental approach.....	77
Figure 5.2 High-resolution imaging of amyloid fibrils formation by AFM.....	78

Figure 5.3 Statistical data of the volume of fibrillar aggregates.....	78
Figure 5.4 Comparison of amyloid formation in static conditions in Eppendorf tubes with an air-water interface and syringes without an air-water interface.....	79
Figure 5.5 Morphological characterization of amyloid fibrils after 30 days of incubation.....	80
Figure 5.6 Polymorphism of mature amyloid fibrils produced in each condition.....	81
Figure 5.7 CD and ThT characterization of α -synuclein aggregation at 45 μ M.....	82
Figure 5.8 ThT assay of α -synuclein at different concentrations in each condition	83
Figure 5.9 Global fitting of ThT assay and fitting results	84
Figure 5.10 Effects of environmental stimuli on α -Syn microscopic steps of aggregation	85
Figure 6.1 Experimental setup and CD measurement.....	94
Figure 6.2 Hydrodynamics of the conditions with different sizes of bubble.....	95
Figure 6.3 The α -Syn aggregation kinetics revealed by ThT fluorescence assay.	97
Figure 6.4 AFM images and statistical analysis on the amyloid fibril features	98
Figure 6.5 The fibril height and length distribution	99
Figure 6.6 Nanomechanical properties of amyloid fibrils under each condition.....	100
Figure 6.7 Fibril polymorphism and its correlation with environmental kinetics	101
Figure 6.8 Order-order transition of amyloid fibril by enhancing environmental kinetics.	103
Figure 6.9 The formation multi-stranded ribbon in the experiment.....	104
Figure 7.1 The morphological evolution of full-length insulin aggregates at acidic pH.....	116
Figure 7.2 Aggregation kinetics and secondary-structure transition of insulin self-assembly..	117
Figure 7.3 High-resolution AFM images of insulin aggregates throughout fibrillization.....	118
Figure 7.4 Statistical analysis of the average height of insulin aggregates	119
Figure 7.5 The morphological evolution of insulin aggregates under large ionic-strength conditions	119
Figure 7.6 Snapshots of fibril-fibril interaction and statistical analysis on morphology.....	120
Figure 7.7 Assessment of average and maximal height of hierarchically twisted fibrils	121
Figure 7.8 Evaluation of the periodicity of twisted fibrils.....	123
Figure 7.9 Statistical analysis of amplitude distribution and conformational identification of hierarchically twisted fibrils	124
Figure 7.10 The AFM tip fitting on the modelled fibril geometry	126
Figure 7.11 Intertwining of protofibrils and their configurational interpretation.....	128
Figure 8.1 The represented optical fiber based nanomotion sensor	136



List of Tables

Table 1.1 The comparison of typical properties between AFM with SEM and TEM techniques.....	3
Table 2.1 A collection of diseases and their associated proteins that associated with protein misfolding from more than 50 diseases.....	22
Table 7.1 The protofilament-based modelling on fibril geometry	125

List of abbreviations

AFM	Atomic Force Microscope
AFM-IR spectroscopy	Atomic Force Microscopy infrared spectroscopy
AFM-visible	Atomic Force Microscopy visible-light spectroscopy
APTES	(3-Aminopropyl) triethoxysilane
AWI	Air-water interface
C-AFM	Conductive-Atomic Force Microscope
CD	Circular Dichroism
CFD	Computational fluid dynamics
CryoEM	Cryo-electron Microscopy
DGDG	Digalactosyldiacylglycerol
DM	D-maltoside
DMT	Derjaguin-Müller-Toporov
EFM	Electrostatic force microscope
FD curve	Force-distance curve
FEM	Finite element method
FLIM	Fluorescence lifetime imaging microscopy
FTIR	Fourier-transform infrared spectroscopy
HAM	Hierarchical assembly model
HS-AFM	High-speed AFM
IMH	Integrated maximal height
KPFM	Kelvin Probe Force Microscope
LHCII	Light-harvesting Complexes II
MB	Methylene blue
MEMS	Microelectromechanical systems
MGDG	Monogalactosyldiacylglycerol
NMR	Nuclear magnetic resonance
OBD	Optical beam detection
PTIR	Photothermal-induced resonance
RPM	Random position machine
SEM	Scanning Electron Microscopy
SNR	Single-noise ratio
s-NSOM	Scattering near-field scanning optical microscopy
SPM	Scanning Probe Microscope
STM	Scanning Tunneling Microscope
TEM	Transmission Electron Microscopy
TERS	Tip-enhanced Raman scattering
ThT	Thiothivin T
UHV	Ultra-high vacuum
UV	Ultraviolet

Chapter 1 Introduction of AFM

Nanoscale imaging and characterization is of fundamental significance for various areas of science and technology because it provides an outstanding view of the investigated specimen at nanoscale or even the atomic level that reveals more underlying details. Atomic Force Microscope (AFM) is a high-precision and high-resolution scanning probe microscope (SPM), that provides 3-dimensional (3D) image, with a lateral resolution in the order of nanometers and a high vertical resolution in the order of Angstrom (\AA). This resolution is 1000 times higher than that of the conventional optical microscope, that gifts AFM the ability for precisely imaging various specimen, ranging from single molecule to supramolecular particle. Nowadays AFM and AFM-based technologies are widely used in a diversity of research fields, ranging from physics, chemistry and biology, to material science and nanotechnology.

The basic principle of AFM is quite simple: a very sharp probe on the top of a soft cantilever is employed to scan on the sample surface line-by-line to feel the force of tip-sample interaction. This tip-sample distance-dependent force is very tiny, in the order of Piconewton (pN), but enough to bend the sensitive spring-like cantilever. By screening the deflection of the cantilever with a reflected laser beam on the photodetector, we obtained the 3D topographic information of investigated sample.

Compared with the electron microscope, such as Scanning Electron Microscope (SEM), and Transmission Electron Microscope (TEM), AFM technique also shows the following outstanding advantages that maintains its popularity in many applications until today:

- 1) Resolution: The AFM and TEM could reach sub-nanometer resolution, which is of one order of magnitude higher than that of SEM. By contrast, the spatial resolution optical microscopy and super-resolution microscopy is much lower, in the regime of tens to hundreds of nanometers, as shown in Figure 1.1.
- 2) Scanning environment: Compared with the vacuum working condition of SEM and TEM, AFM imaging can be performed in the ambient condition, both in air and in liquid. This is more convenient for many applications, and scanning in the liquid environment is critical for the biological applications (Table 1.1).

- 3) Sample preparation: SEM imaging requires an electrically conductive sample or a conductive metal-coated insulated sample, and the sample in TEM imaging is limited by the thickness of sample. These requirements largely limit their applications. However, AFM imaging is achieved by physically touching the sample surface with a sharp probe, regardless of sample conductivity and thickness. This simplified requirement opens the window to various applications, such as material surface characterization and biological specimen.
- 4) Flexibility of nanomanipulation: The AFM scheme allows its further development and combination with other techniques. For instance, the electromagnetic enhancement for localized light-matter interaction and single-cellular manipulation and measurement. This flexibility enables AFM to be used as more than a microscopy, but also a universal tool for nanoscale manipulation.

However, the disadvantage of AFM regarding to the imaging time is also evident. Conventional AFM need at least 2-10 minutes for a single image, but both SEM and TEM takes only tens seconds. Nowadays, the appearance of high-speed AFM (HS-AFM) is shifting the situation, with an imaging rate of up to 100-200 ms so that it is widely used to study protein dynamics.

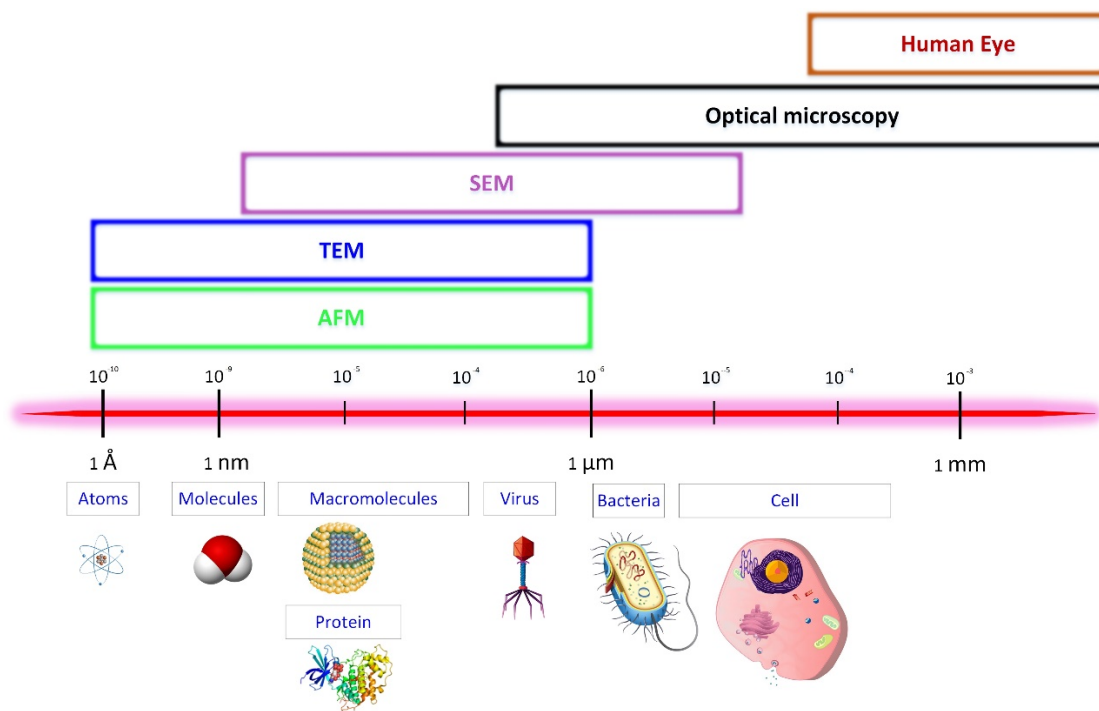


Figure 1.1 The vision of different microscopies. Logarithmic size scale from Angstrom to mm with typical biological species, and the imaging ranges for different microscopy techniques in comparison¹⁻³.

	AFM	TEM	SEM
Sample type	Conductive or Insulate	Conductive	Conductive
Scanning environment	Any	Vacuum	Gas* or vacuum
Spatial resolution	0.1 nm	0.1 nm	5 nm
Imaging time	2-10 min or ms [†]	~1 min	~1 min
Dimension	3D	2D	2D
Surface analysis	Non	Yes	Yes (EDX)

* Environmental SEM

† High-speed AFM

Table 1.1 The comparison of typical properties between AFM with SEM and TEM techniques. Adapted from Ref.^{1,2}.

Moreover, the capability of AFM is beyond topographic imaging. Another two outstanding abilities ensuring its popularity in the current research are the ultrasensitive force measurement and nanoscale manipulation. The former one is to use cantilever to sense tip-sample interaction and to obtain the force-distance curve. This method is used to measure the chemical and biological force at sub-pN scale⁴, and applied in various applications, including protein folding, cell-ligand or cell-cell interactions and nanoscale chemical identifications. On the other hand, as a nanoscale manipulator, AFM is applied in plenty of applications of single molecule manipulation⁵, such as chemical reaction^{6,7} and targeted delivery of single molecule or nanoparticles⁸. This tool is also widely used in diverse multi-disciplinary applications, including chemistry, biology, physics and material science.

1.1 SPM and AFM History

The investigation of surface topography at atomic scale can be rooted in the discovery of scanning tunneling microscope (STM). Immediately after the novel design of STM by Gerd Binnig, Heinrich Rohrer and et al. in 1981⁹, the first successful attempt of surface study at nanoscale was achieved in the following year¹⁰. As the first generation of this device for surface characterization, it provided an unprecedented breakthrough on the spatial resolution and imaging accuracy^{10,11}, which allows for the depiction of the atomic world for the first time.

As a sequel of STM, the design of atomic force microscope was also proposed by Gerd Binnig and et al¹². It enabled the measurement of the force between tip and sample surface, as small as 10^{-18} N,

and thus achieved the measurement of surface topology. The outstanding feature for this “blind microscope” is to physically touch on sample surface and to generate surface map. Thus, other than optical and electron microscope, the features of different types of sample, including transparency and conductivity, do not limit the reconstruction of its surface. Another great advantage of this AFM was that it obtained a preliminary result of a lateral resolution of 30 Å and a vertical resolution of 1 Å¹². More interestingly, this measurement was performed in the ambient condition, not in the vacuum environment as for the cases of electron microscopy. These abilities allow the broad applications, such as AFM-based nanotechnology and biological imaging, to become reality.

In the following decades, AFM techniques were exploited intensively and many advanced developments were applied that largely increased its popularity in various applications. For instance, by applying the voltage on the electrical tip or the sample, we are able to obtain the morphological image as well as the map of electrical properties, such as the conductivity (current distribution), electric properties (surface potential and charge distribution), and surface potential by using conductive-AFM (C-AFM), electrostatic force microscope (EFM) and Kelvin Probe Force Microscope (KPFM) respectively. Similarly, the magnetic properties can be studied with the same approach, while the chemical and nanomechanical properties could also be investigated by analyzing the force-distance curve, which is also widely applied in the field of cell mechanobiology.

More recently, by combining with other relevant technologies, AFM had greatly enhanced the ability of these technologies with fruitful outcomes. For example, infrared (IR) spectroscopy and Raman spectroscopy are widely employed in the biological and chemical analysis but their spatial resolution was low, in the order of hundreds micrometers. However, recent developments on the hybrid approaches, such as AFM-infrared (AFM-IR) nanospectroscopy¹³, achieved morphological and structural mapping with resolution of tens nanometers. This opened an avenue of studying the structural and conformational investigation on the biological species and material samples. Similarly, the combination of AFM and Raman spectroscopy, termed tip-enhanced Raman spectroscopy (TERS), had also proved its unprecedented ability of visualizing the vibration modes of a single molecule¹⁴.

1.2 AFM Instrumentation

To achieve the sub-nanometer precision in AFM measurement, the precisely characterized detection and measurement is required the AFM instrumentation. Typically, AFM system consists of several components, including a cantilever mounted with a sharp probe, a deflection sensor, a piezoelectric scanner and a feedback controller, as shown in Figure 1.2.

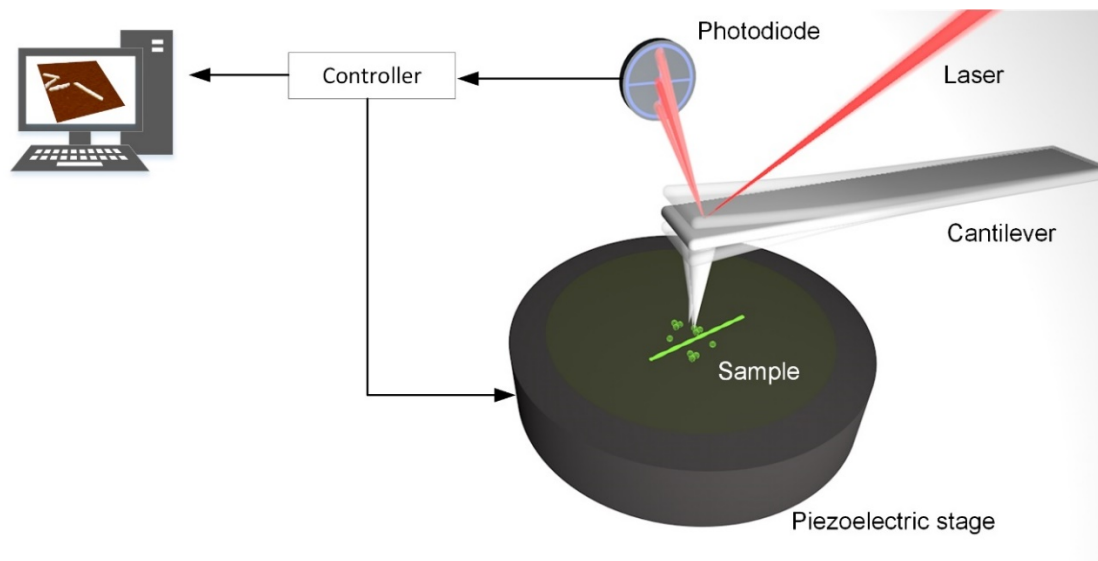


Figure 1.2 Schematics of a typical atomic force microscope. The force-induced deflection of the cantilever during scanning is recorded by the photodiode that generates the topographic data and, on the other hand, provides the reference in the feedback loop to tune the piezoelectric stage.

1.2.1 AFM cantilevers and tips

The cantilever with a sharp probe is of fundamental significance in the AFM measurement. There are two main roles for the tip-mounted AFM cantilever: the first one is using the sharp tip to interplay with the sample and to sense the tip-sample force with a high spatial resolution; the other role is to transit this tiny (\sim pN-nN) force to mechanical deflection of the cantilever, which could be precisely sensed by deflection sensing sensor.

The sharpness of the tip, that is radius of tip apex, is one of the most important factors that determinate the spatial resolution of AFM images. An extreme sharp tip reduces the minimum detectable feature on the AFM image, which better characterize their topography for the high-quality AFM image. Typically, AFM cantilevers are fabricated by using microelectromechanical systems (MEMS) technology, and thus the typical tip apex radius is in the range of 1-20 nm. The tip can be functionalized by chemical molecules, e.g. CO, that could further enlarge the spatial resolution.

The characteristics of the cantilever, such as spring constant and resonance frequency, are critical parameters for AFM scanning. Cantilevers with different mechanical features are normally applied in distinct AFM scanning modes. For example, contact-mode AFM would prefer the soft cantilevers with spring constant in the range of 0.01-10 N/m, while non-contact AFM normally use cantilevers with spring constant of tens N/m and resonant frequency of hundreds kHz. These values are determined by the material and geometry of cantilever, such as thickness and cantilever shape.

1.2.2 Deflection sensors

As the force of tip and sample interaction is extremely small, the deflection of the cantilever is actually tiny and thus the sensor for detecting cantilever motion should be very accurate. The first attempt by Binnig was a tunneling current STM probe¹², however the implementation and operation of this instrument were difficult. Nowadays, there are a number of approaches of deflection sensors were demonstrated, such as interferometer¹⁵, crystal oscillator¹⁶ and piezo-resistive cantilever^{17,18}, as shown in Figure 1.3.

However, the most commonly used and efficient detection approach is the optical beam detection (OBD). The schematic of OBD deflection sensor is presented in Figure 1.3e. The basic principle of OBD deflection sensor is that, a laser beam is focused on the backside of cantilever and then is reflected to a 4-quadrant photodetector. The laser beam reflection records and magnifies the tiny cantilever deflection, showing a larger movement on the photodetector.

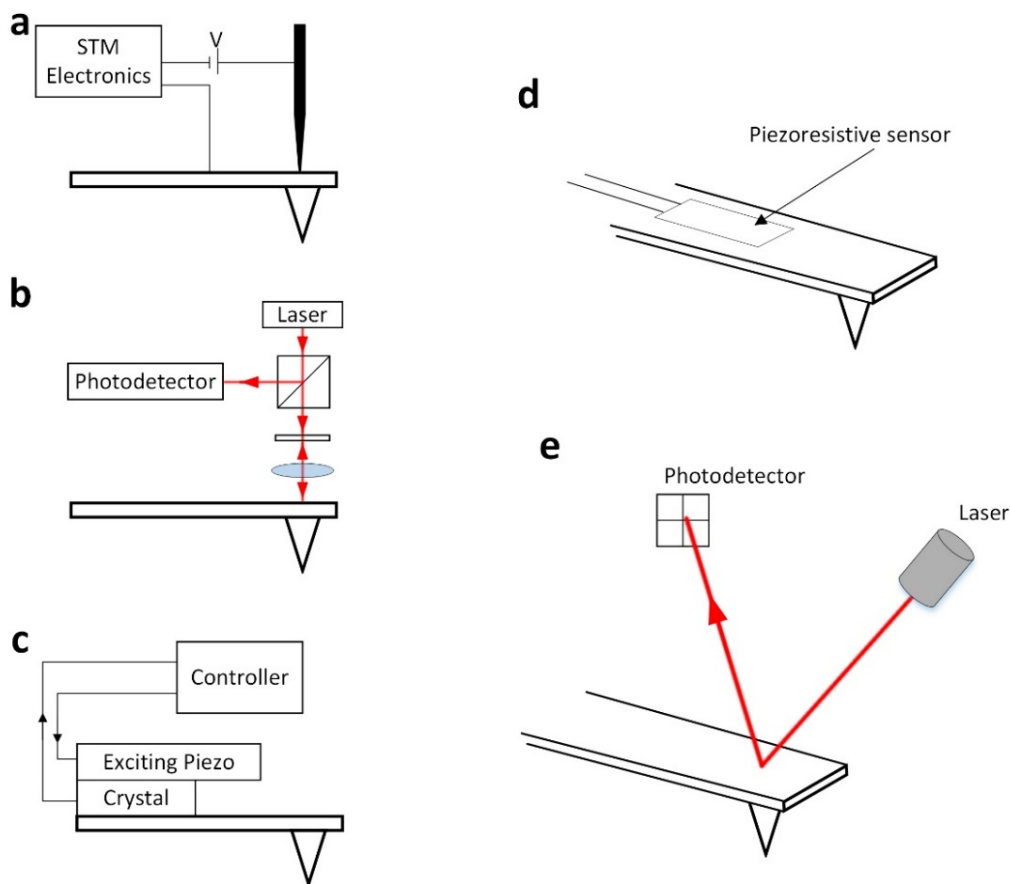


Figure 1.3 The design of a number of AFM deflection sensors. The sensors include the current STM probe (a), interferometer (b), crystal oscillator (c), piezo-resistive cantilever (d) and optical beam detection (e). Adapted from Ref. ¹.

1.3 AFM Fundamentals

In addition to the recent appearance of novel scanning modes, such as point-by-point modes and peck-force mode, there are typically three operating modes for AFM imaging, including contact mode, tapping mode and non-contact mode. Among them, the dynamic AFM imaging, including tapping and non-contact modes that sense the tip-sample force with a vibrating cantilever, is the most commonly used in AFM imaging due to its scanning sensitivity. In the dynamic mode, the cantilever vibrates close to (or at) its resonance frequency. Thus, understanding the theory of cantilever oscillation and its accurate calibration are fundamental in these dynamic modes.

1.3.1 Cantilever oscillation and calibration

1) Cantilever harmonic oscillation

Strictly speaking, the resonance oscillation of cantilever should be studied by performing the 3D modelling. However, the 3D modelling is influenced by various factors, such as the cantilever shape, so that we should consider multiple effects of cantilever oscillation, including the torsional and lateral resonance modes, in the modelling. Thus, the 3D modeling of the cantilever oscillation and its theory could be quite complex.

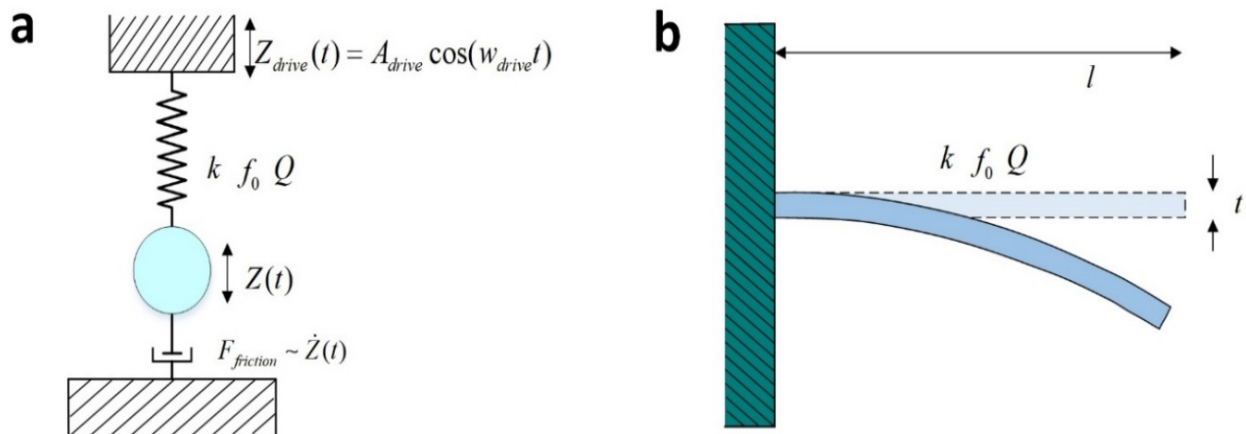


Figure 1.4 The theory of AFM cantilever oscillation. (a) Schematic of a driven damped harmonic oscillator. The mass is driven by a harmonic oscillator through the spring and a damping force is considered between mass and substrate. (b) The scheme of the deflected cantilever beam with a thickness (t) and length (l). The spring constant (k), resonance frequency (f_0) and quality factor (Q) are the important factors that affect the oscillation of the cantilever. Adapted from Ref.³.

In practice, the simplest model of the cantilever, as a harmonic oscillator, is a mass on a spring that could be sufficient (Note, however, that the reduction of 3D model to this simplest 1D one is highly non-trivial). In the dynamic modes, the oscillated cantilever is driven by a piezo

with viscous damping in liquid or gas, which should be considered. Thus, the model of driven harmonic oscillator with damping is more realistic, as shown in Figure 1.4.

Since the frictional force $F_{friction} = -m \frac{w_0}{Q} \dot{Z}(t)$ and the spring force on the oscillating mass $F_{oscillation} = -k(Z(t) - Z_{drive})$, we have the equation of motion:

$$m\ddot{Z}(t) = F_{oscillation} + F_{friction} + F_{t-s} = -k(Z(t) - Z_{drive}) - \frac{w_0}{Q} \dot{Z}(t) + F_{t-s} \quad (1)$$

Here, in this presented 1D model, the equivalent mass m is associated with various parameters, including material and geometry of the cantilever. By replacing $w_0^2 = k/m$, the tip-cantilever in the damped harmonic driven-oscillation system can be described by the equation:

$$\ddot{Z}(t) + \frac{w_0}{Q} \dot{Z}(t) + w_0^2 Z(t) - \frac{w_0^2}{k} F_{tip-sample} = w_0^2 Z_{drive}(t) \quad (2)$$

where $Z(t)$ is the displacement of the mass, w_0 is the angular resonance frequency of the oscillating spring, Q is the quality factor of damping condition, k is the spring constant, F_{t-s} is the force of tip-sample interaction and $Z_{drive}(t) = A_{drive} \cos(w_{drive}t)$ is the displacement of driving oscillator. Thus, we have the oscillation amplitude of mass is:

$$A = \frac{A_{drive}}{\sqrt{[1 - (\frac{w_{drive}}{w_0})^2]^2 + \frac{1}{Q^2} (\frac{w_{drive}}{w_0})^2}} \quad (3)$$

where A_{drive} and w_{drive} are the amplitude and angular frequency of driving oscillation.

2) Cantilever calibration

For precise measurement and analysis based on AFM techniques, the cantilever should be carefully calibrated. An important parameter of the cantilever is the spring constant, which is related to the material and geometry of the cantilever. AFM cantilever is normally made of silicon or silicon nitride material with a typical Young's modulus of around 100 GPa. An approximate estimation of the spring constant of a cantilever is:

$$k = \frac{Et^3w}{4l^3} \quad (4)$$

where E is the Young's modulus, t , w and l are the thickness, width and length of the cantilever respectively. The typically satisfied method to calculate the spring constant of a rectangular cantilever is the Sander method¹⁹:

$$k = 0.1906\rho b^2LQ_rw_f^2\Gamma_i^f(w_f) \quad (5)$$

This equation relates spring constant directly to the plan view dimensions of the cantilever (the width of cantilever b), the density of medium ρ , the quality factor Q_r in liquid, the fundamental mode resonant frequency w_f and $\Gamma_i^f(w_f)$ is the imaginary part of the hydrodynamic function¹⁹. This analytical expression offers a typical satisfied calculation to obtain the spring constant of cantilever in liquid, or in air provided the quality factor $Q_r \gg 1$.

However, in practice, the most common approach for experimental measurement on the normal spring constant is the “thermal calibration” method²⁰. By acquiring the thermal noise spectrum, we could have the spring constant:

$$k = \frac{k_bT}{p} \quad (6)$$

where k_b is Boltzmann's constant, T is the temperature and p is the area under the curve of the thermal noise spectrum. This method is actually most useful in practice, providing considerably accurate value of the spring constant.

1.3.2 AFM topographic modes

As a versatile analytic technique, there are a number of AFM operating modes available for imaging and investigating the different features of the surface at nanoscale. Among them, the most widely-used application is still topographic imaging. Typically, AFM topographic imaging mainly includes three modes: contact mode, tapping (intermittent contact) mode and non-contact mode, where the latter two modes sometimes were termed the dynamic mode.

The main difference between these modes is the oscillation of the cantilever and working distance between probe apex and sample surface (the force of tip-sample interaction). As shown in Figure 1.5a, cantilever probe in the contact mode is the scanning on the surface without cantilever oscillation

while the other two modes oscillate their cantilever at its resonant frequency. Compared to the non-contact mode in which the probe apex vibrates far from the sample surface, the tapping mode enable its probe to tap intermittently on the sample surface. As a result, the tip-sample interacting forces involved are different between these scanning modes.

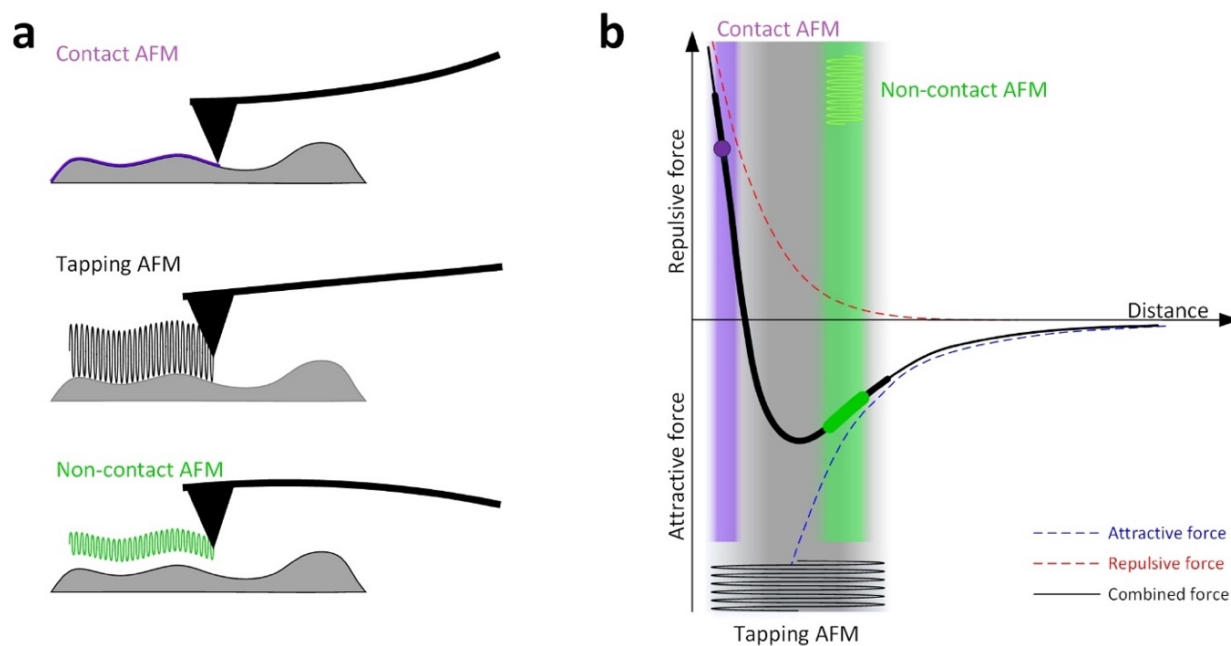


Figure 1.5 The working principle of typical AFM imaging modes. (a) Schematics of the cantilever movement on the sample surface. The violet, black and green curves represent the trajectory of the probe movement. (b) The operation range of different AFM modes on the force-distance curve. The contact mode is performed close to the sample surface in the repulsive force region, the cantilever in the tapping mode largely vibrates in the both repulsive and attractive region, and the cantilever in the non-contact mode vibrates with a small amplitude and senses the sample surface at a distance with a relatively small attractive force.

To understand the tip-sample interaction at the working distance, one should address the question of the force variation between tip and sample as a function of distance. Indeed, in the ultra-small region (within several/tens nm) between very top of the apex on the AFM tip and the scanned sample surface, the interaction force can be approximately appreciated as short-range interaction force, as shown in Figure 1.5b. The force between tip and sample is the combination of attractive force and repulsive force, which both rise as the decrease of tip-sample separation. The attractive force mainly consists of van der Waals interaction that dominate the combined force in long-range ($r > 2\text{\AA}$), where r is the distance between tip and sample. Whereas Pauli repulsion, as a key element of repulsive force, rules the short-range tip-sample interaction ($r < 2\text{\AA}$). Overall, as the tip approaches the sample, the attractive force gradually enlarges to a certain value at distance (around 2\AA), and then repulsive force sharply increases and dominates the tip-sample interaction.

In practice, the situation of tip-sample interaction would be much more complicated. For example, the surface tension would be one of important properties of the scanned sample that could greatly influence the tip-sample interaction. Besides, various further factors in the experimental environment could also significantly impact the tip-sample force, including tip size, viscosity and temperature, but it is not fully discussed here. Figure 1.6b also represents the working distance and the involved force in different scanning modes. As seen, the non-contact mode is operated in the regime of relatively small attractive force, while the contact mode is normally performed with a large tip-sample force involved. The probe in the tapping mode swings between attractive and repulsive force within each oscillation cycle.

1) Contact mode

The contact mode, also named static mode, is the first and simplest mode developed for the AFM scanning and imaging. In contact mode, AFM probe is touching and scanning the sample surface statically without oscillation, where the involved tip-sample interaction is a large repulsive force, as seen in Figure 1.5. The interplay between tip and sample is located in the close region, where the force in this mode is large (tens to hundreds nN) and the slope of force-distance curve is rather steep. This means intensive variation of tip-sample force would be possible while scanning on the rough surface, so that a soft cantilever is typically used in the contact mode with a spring constant of 0.1-10 N/m.

There are several types of contact mode, which are the constant height mode, constant force mode, constant error mode and lateral force mode. In constant force mode, the feedback loop senses the tip-sample interaction by maintaining a constant deflection of cantilever and thus applies a constant force. By contrast, the constant height mode allows a varying force of tip-sample interaction during scanning. The lateral force mode is to measure the friction between tip and sample that laterally bend the cantilever.

There are some advantages of the contact mode. For example, this mode could provide the highest scanning rate as the static cantilever scanning without vibration. Besides, the noise is very low in this mode and thus it is used for the extreme high-resolution AFM images. However, the contact mode is less popular in many current applications of AFM imaging. The main reason is the difficulty in controlling of the force between tip and sample in contact mode. This is because the contact mode is operated in the repulsive force domain, where the large force varies quickly with a slight difference of tip-sample distance. In addition, there is a risk of damaging the probe apex while scanning on the rough sample surface, as well as scratching or destroying the sample.

2) Tapping mode

In tapping mode, the cantilever oscillates during the scanning driven by the piezo at/near its resonant frequency. In amplitude modulation mode, the frequency and amplitude of the oscillation are maintained constant. Normally the amplitude of the oscillation is large (tens to hundreds nm) and tapping on the sample surface, and thus there is still risk of damaging the probe apex. Generally, the tapping mode cantilever is more rigid ($k \sim 40 \text{ N/m}$) with a high quality factor. The tapping mode is a good choice in the applications of large-force surface characterization, such as measuring the nanomechanical properties^{21,22}.

3) Non-contact mode

The cantilever in the non-contact mode oscillates relatively far from the surface, in the regime of several to tens nm, with a smaller amplitude (typically within 30 nm) compared with tapping mode. Thus, the oscillating probe undergoes relatively small attractive force. The rigid cantilever often shows a high resonance frequency of hundreds kHz and a high quality factor.

Non-contact mode is now the most popular mode in the conventional AFM applications. The main advantage of non-contact mode scanning is that, with the large tip-sample distance and small tip-sample force, the high sensitivity of topographic measurement is also maintained. Thus, the cantilever allows a soft and gentle scanning on the sample, which benefits the obtaining a high-quality image and preserving both tip and sample during imaging.

In the feedback loop, a setpoint is required to maintain the desired tip-sample interaction during scanning. In the contact mode, this setpoint is the fixed cantilever deflection and its related tip-sample force. However, in dynamic modes, there are typically two approaches to trace and maintain the scanning: the amplitude modulation and the frequency modulation.

The former modulates the oscillation amplitude at a constant frequency close to its resonant frequency. While the oscillated cantilever during scanning becomes closer to the sample, the peak of amplitude-frequency response shifts to higher frequency, and this peak shifts to lower frequency while the tip moves away from surface, as shown in Figure 1.6. By varying the tip-sample separation to maintain the oscillation amplitude, AFM could trace the morphology of the scanned sample.

The latter regulates the oscillation frequency at a constant oscillation amplitude, with a frequency shift as the feedback for topography. In this mode, we detect the variation of the cantilever resonant frequency to calculate the frequency shift, which caused by the variation of tip-sample distance.

While cantilever is far away from surface, the resonant frequency is $\omega_0 = c\sqrt{k}$, where c is a function of cantilever mass and k is the spring constant. With a force f applied on the surface, the resonant frequency becomes $\omega_0' = c\sqrt{k-f'}$, where f' is the derivative of the applied force. This FM mode is frequently used in ultra-high vacuum (UHV) environment with a phase-locked loop. It is less employed in the conventional AFM imaging due to the high requirement of the instrumentation to trace the resonant frequency, but more recently the bimodal frequency AFM is getting more and more interests due to the high resolution and high contrast material discrimination^{23–25}.

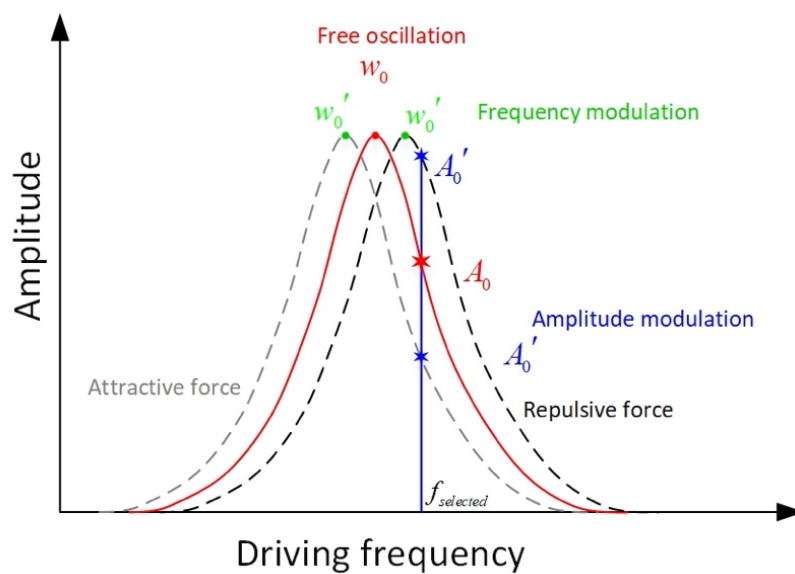


Figure 1.6 The AFM driving signal-cantilever amplitude response. The amplitude of cantilever oscillation against the driving frequency, while approaching and retracting the surface (due to attractive and repulsive force). The red curve indicates amplitude-frequency spectrum of the free oscillation, while the gray and black curves shows the curves under the attractive and repulsive forces respectively. The green and blue signs represent the frequency and amplitude modulation respectively.

1.4 The operation of AFM imaging

In practice, the operation of AFM instrumentation to obtain high-quality AFM images is complicated that requires the attentions on many key features, ranging from sample preparation to optimizing the scanning parameters and image post-processing.

1.4.1 AFM scanning parameters

There are a number of scanning parameters required to be optimized in order to obtain the high-quality AFM images. These parameters should enable a well-controlled tip-sample interaction during scanning that best describes the sample topography. Typically, the following three parameters are the most critical for conventional AFM imaging.

1) Setpoint

The setpoint is typically the desired tip-sample force, to determine a stabilized tip-sample interaction during the scanning on the surface. The resulting error signal, which is the difference between setpoint reference and actual value, is minimized by adjusting the z-piezo according to the signal of feedback loop. The resulting piezo movement provides the height information of the surface topography, while, however, an inappropriate setpoint provides unreal description of the sample morphology, as shown in Figure 1.7. In general, the setpoint in the contact mode is the cantilever deflection (the force applied on tip-sample interaction), while the most common setpoint in the dynamic mode (AM-AFM) is the oscillation amplitude of the cantilever.

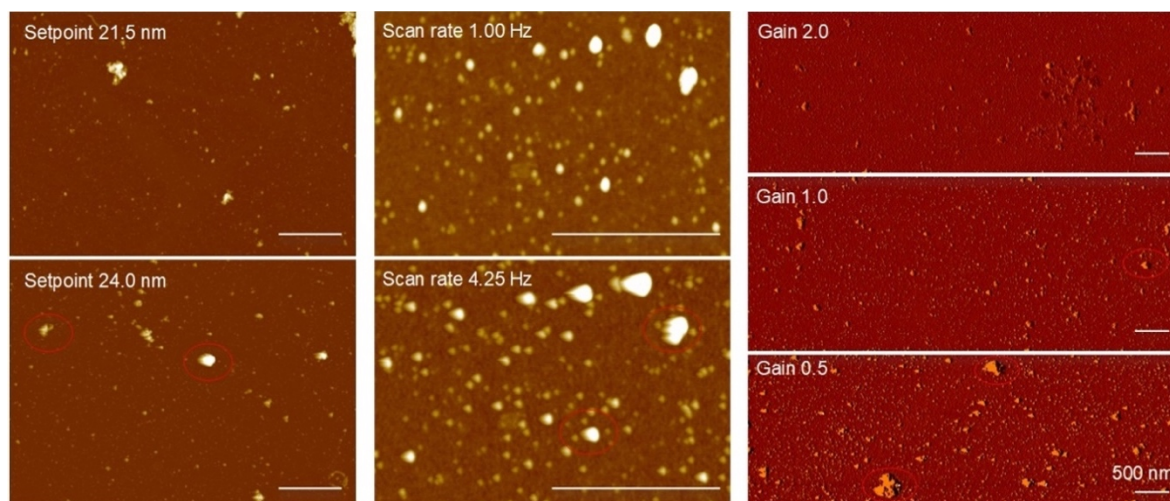


Figure 1.7 Possible scanning artifacts in the AFM imaging. The AFM images in non-contact mode with different scanning parameters, including setpoint (left), scan rate (middle) and gain (right). The AFM images with better scanning parameters are presented on the top. With an inappropriate parameter, the scanned sample shows the unreal profile, sometimes with a “tail” in the direction of scanning. These artifacts are marked with red circles. The scale bar is 500 nm.

2) Scanning rate

The scanning rate is also an important parameter for AFM imaging, especially in the dynamic mode. This is because, the high scan rate might not allow the oscillating probe to trace the real shape of sample within several oscillation cycles. Thus, a relatively slow scanning rate is utilized in the conventional AFM imaging with several to tens minutes. Besides, the selection of scanning rate, in both contact and dynamic modes, should also depend on the sampling speed of AFM electronics, as well as whether or not the electronics is capable of tracing the height information in a high scanning rate (Figure 1.7b). Nevertheless, another solution is to enlarge the resonance frequency of scanning cantilever. Recent advances in the high-speed AFM with short cantilever (resonance frequency of 1-5 MHz) allow the development of AFM with unprecedented scanning rate, up to 100 ms, which is wildly used in many biological applications.

3) Gain

The gain is the feedback response of z-piezo movement to the error signal from feedback loop. In fact, there are multiple gains in the AFM system, including integral gain, proportional gain and differential gain. The adjustment of gain setting could lead to huge difference in the image quality. If the gain is much lower than it should be, the response from the z-piezo will be too slow to trace the sample profile, resulting in the “tails” on the AFM image (Figure 1.7c). More importantly, for the sample with sharp edges, there is a risk of damaging the AFM probe. If the gain is much larger than it should be, high frequency excitations might be generated during scanning, as well as a higher degree of the noise, which may affect the quality of the height information on the AFM images.

1.4.2 The quality of scanning AFM probe

The quality of the scanning probe is another significant factor for acquiring a high-quality AFM image. On one hand, the sharpness of tip apex directly determines the spatial resolution of the AFM image. Furthermore, the high aspect ratio probe can much better describe the specimen with sharp edges by reducing the deconvolution effect, and the diamond coated probe processes a longer life span while scanning stiff samples. On the other hand, the importance of preserving a sharp and clean tip on obtaining a high-quality AFM image is clearly evident. Figure 1.8 shows an example of the problematic probe with a broken apex and the contaminants on the tip, which thus generated artifacts for each object on the AFM image.

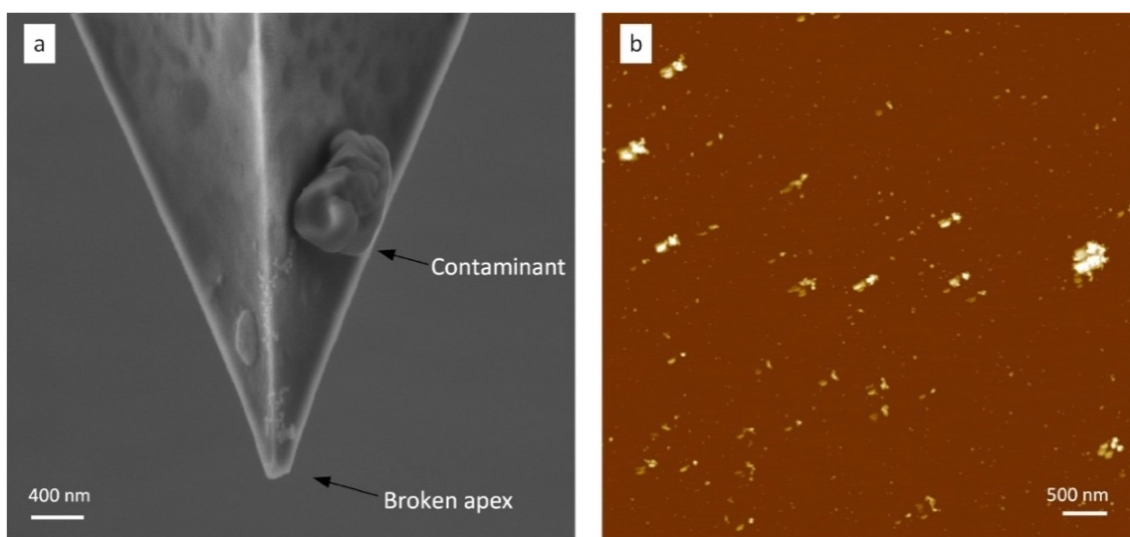


Figure 1.8 Importance of AFM tip on the image quality. (a) The SEM image of a problematic probe, with a broken apex and contaminants attached on the tip. (b) The AFM image generated by a problematic probe with dual scanned structures for each object on the AFM images.

1.4.3 AFM deconvolution effect

The deconvolution effect is a common phenomenon during the AFM scanning that should be considered in analyzing morphological profile. This effect is due to the inverted-pyramid-shaped AFM probe with a typical half cone angle value of ca. 10° , so that AFM tip is not capable of perfectly detecting the precise morphology of the sample with sharp edges, especially for the nanoscale specimen, as shown in Figure 1.9. It is impractical to absolutely eliminate this deconvolution effect, however, plenty of efforts had been made to reduce this effect, such as the carbon nanotube²⁶, nanowire²⁷, or hydrogel assisted²⁸, FIB fabricated²⁹ probes, by increasing the aspect ratio of the AFM probe.

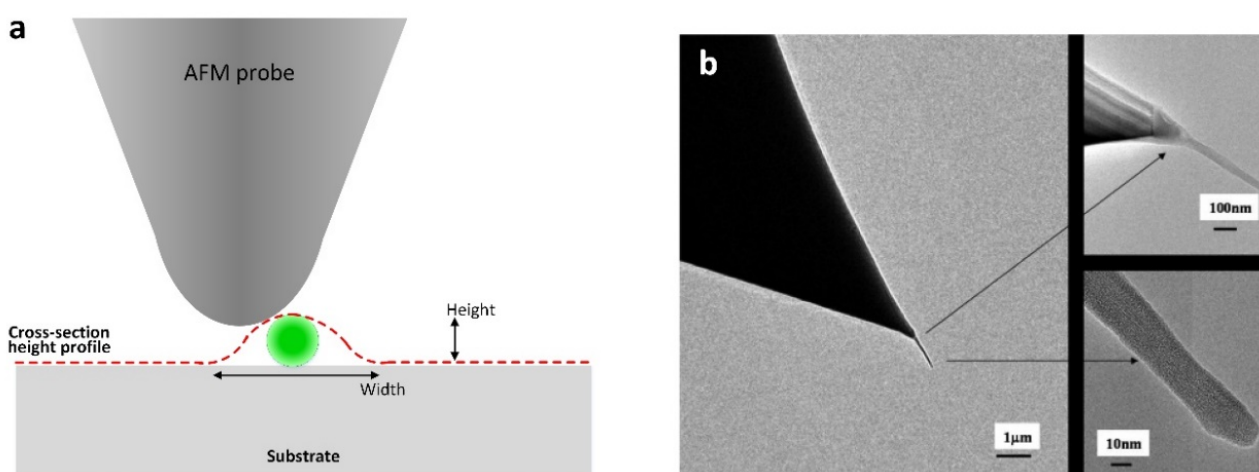


Figure 1.9 The deconvolution effect of AFM imaging. (a) The schematics of deconvolution effect. The AFM probe is scanning on the sample with a smaller size than the tip, while red dashed line is the cross-section height profile of the scanned sample. It is clearly seen that this profile do not match the side edge of the scanned object, while the maximal height of scanned and actual profile match. (b) An example of the high-aspect ratio AFM probe. The single-walled nanotube bundle attached on the silicon AFM probe that provides an apex with a conical geometry and a diameter of 20 nm. Adapted from²⁶.

1.5 AFM nanoindentation

AFM nanoindentation is a non-topographic mode of AFM-based technologies. Instead of acquiring the topographic information, AFM is utilized to apply a certain force at a specific location on the surface, by approaching the tip on and then retracting it from the surface. A typical force-distance curve is shown in Figure 1.10a, and various information could be obtained from this curve, such as Young's modulus, adhesion and deformation. By acquiring the force-distance curve at multiple locations in an array, one could carry out the quantitative AFM nanoindentation. The electronics allows the high precision measurement for the spatial resolution of up to 1 nm and for a force sensitivity in the order of piconewton. Thus, by analyzing each force-distance curve, it is possible for obtaining the topographic image and the map of Young's modulus, deformation and adhesion (Figure 1.10b)³⁰ that reveals more details of the investigated specimen.

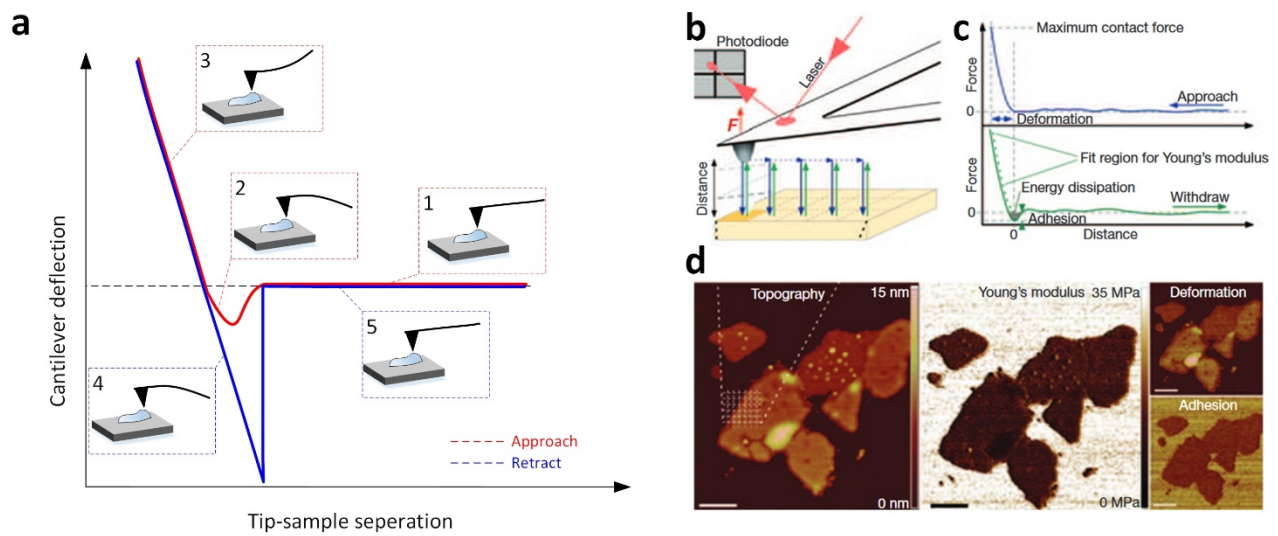


Figure 1.10 The force-distance curve and quantitative mapping of multiple properties of sample. (a) The schematics of the force-distance curve with the approaching (red) and retracting (blue) curves. (b-d) The schematic of the quantitative AFM nanoindentation, with the multiple information from force-distance curve and the corresponding maps of topography, Young's modulus, deformation and adhesion (adapted from Ref.³⁰).

1.6 AFM force spectroscopy

The developments on AFM technologies extended the application toward nanotechnological probing on biological, chemical and physical interactions³¹. Another non-topographic mode is the AFM force spectroscopy that has been widely applied in the cell mechanobiology^{32,33} and protein mechanics^{34,35}. In the former case, the AFM probe is normally used with chemical or biological functionalization, or even replaced by cellular or viral interactions, shown in Figure 1.11a. Thus, by probing specific interactions of cell surfaces, this approach could obtain unique insight into their structural and functional modulation on the surface macromolecules and proteins. The latter application of single-molecule force microscopy is one of the most widespread techniques that are capable of providing the distinctive mechanical fingerprints to study the unfolding and folding dynamics of single protein molecules³⁵ and of identifying their mechanical features³⁴.

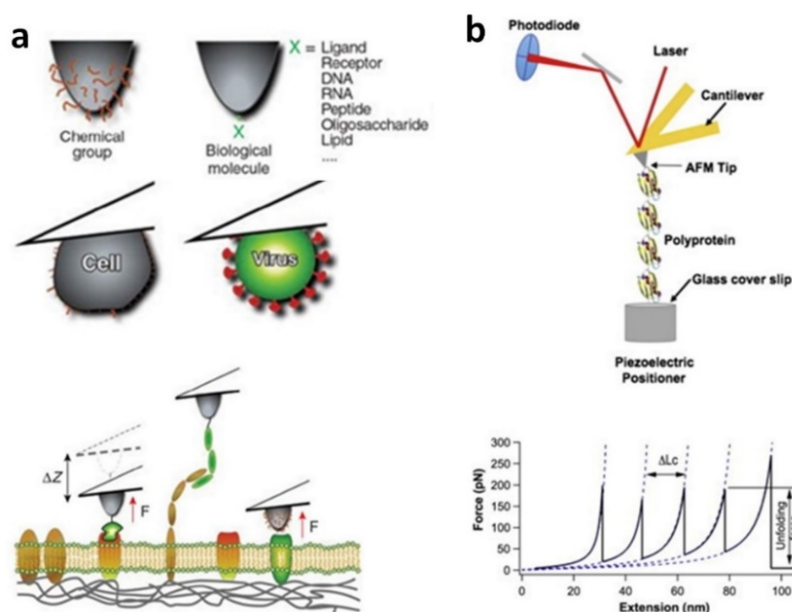


Figure 1.11 Schematics of AFM force spectroscopy applications. (a) The functionalized AFM probe for detecting the chemical, biological, cellular or viral interactions (upper). The schematic representation of the chemical and biological functionalized AFM probes for studying the interaction of cell surface (lower). Adapted from Ref.³³. (b) Schematics of the AFM single-molecule force spectroscopy to study single tandem-repeated polyprotein mechanics (upper) and the force-extension curve from the stretching of such a tandem-repeated polyprotein (lower). Adapted from Ref.³⁵.

1.7 AFM-IR nanospectroscopy

The latest development of AFM technologies drives AFM methodology to combine with other techniques that could enhance greatly advantages in the related field. AFM-infrared (AFM-IR) nanospectroscopy, as one of these combined technologies, is the combination of AFM imaging and infrared spectroscopy. By focusing a pulsed tunable IR laser on the top of AFM probe, the localized temperature will be raised, while the wavenumber of the tunable laser matches the resonant frequency of the molecular vibration of illuminated sample. Then, this rise of localized temperature induces photo-thermal expansion, which could be detected by a soft AFM cantilever, shown in Figure 1.12. With this approach, either the absorption spectrum at a specific location or the absorption map at a certain wavenumber could be obtained. AFM-IR enables surface characterization and chemical analysis with an unprecedented spatial resolution of less than 20 nm¹³. By contrast, the most commercial Fourier-transform infrared spectroscopy (FTIR) could only achieve a spatial resolution of several μm . Thus, this promising approach of nanospectroscopy that can be used to perform unambiguous chemical analysis and compositional characterization at nanoscale, has been widely used applied in material^{36,37} and biological^{38–40} applications.

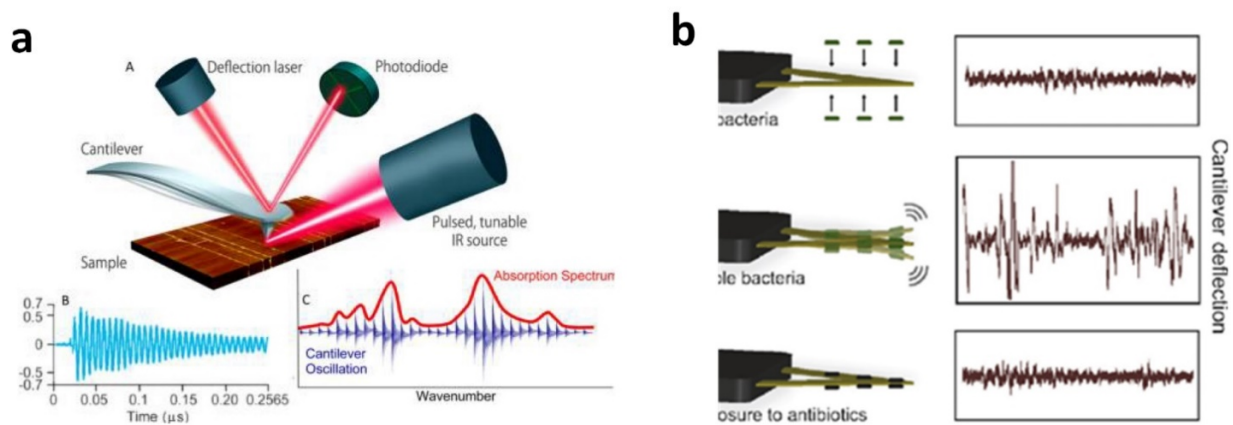


Figure 1.12 The schematics of AFM-IR and AFM nanomotion methods. (a) The schematic diagram of AFM-IR. The pulsed tunable IR laser is focused on the region of probe apex. While light wavelength matches the absorbing bands of sample, it generates the molecular resonance and induces photothermal expansion that can induce the ring-down oscillation of AFM cantilever. The amplitude of oscillation is proportional to IR absorption, and thus the localized IR absorption spectrum can be recorded. Adapted from⁴³. (b) The scheme of typical nanomotion susceptibility test. The intact bare cantilever shows low thermal-noise-driven fluctuations (top) while after the attachment of bacteria, the oscillation signal is large due to possibly their metabolic activity (middle), which becomes again lower after exposure to antibiotics (bottom). Adapted from Ref.⁴¹.

1.8 AFM nanomotion sensor

Compared to the nanoscale characterization in the topographic and non-topographic modes, AFM nanomotion sensor employs a tipless cantilever, providing a rapid and reliable measurement on the vibration of cantilever, as shown in Figure 1.12. The principle of AFM nanomotion sensor is simple achieved by detecting the vibration of cantilever immobilized with the active living organism. Nowadays, the AFM nanomotion sensor is used in the applications of disease diagnose, and drug discovery, such as antibiotic susceptibility/resistance test^{41,42}, as well as the cellular activity⁴³ and life detection⁴⁴. For instance, in the case of antibiotic susceptibility measurement, the living bacteria firstly were immobilized on the tipless cantilever, with very low spring constant (typically less than 0.1 N/m), and the existence of bacteria increases the fluctuation of cantilever. Thus, the response of the bacteria to the antibiotics, including the sensitivity and response time, can be observed by screening the cantilever fluctuation⁴⁵. In this way, we could have a better understanding on the bacteria-antibiotics response, and similarly the technique can be used to study various biological systems.

1.9 Other cutting-edge AFM techniques

In addition to the AFM technologies indicated above, there are plenty of AFM based techniques that widely used in various applications. Hereby, I list several novel approaches based on the principle of AFM that generates considerable impacts in various applications.

- 1) Atomic-resolution AFM imaging: AFM imaging provides sub-nanometer vertical resolution, but the lateral resolution was difficult to be improved. The main difficulty is the size of tip

apex, which is in the order of nanometer, much larger than a single molecule. This problem has not been solved until Leo Gross and his colleagues' work by functionalizing the tip apex with CO molecules as apex termination⁴⁶. They showed an unprecedented lateral resolution for imaging an individual pentacene molecule on Cu(111). After that, more and more researches has been designed on visualizing more molecules and compounds^{47,48}, controlling the single-molecule manipulation⁸, and detecting the chemical synthesis⁴⁹ and single-molecule chemical reaction^{50,51}.

- 2) AFM-Raman spectroscopy: Raman spectroscopy is a popular technique in the applications in the field ranging from the material science to chemistry and biophysics, especially for the identification of molecular composition from complex material, although the problem of spatial resolution is clear. AFM-Raman spectroscopy allows this investigation in a much higher spatial resolution (up to sub-nanometer¹⁴) than the conventional Raman spectroscopy. By employing a metallic tip to excite surface plasmon and thus enhance the sensitivity, tip-enhanced Raman spectroscopy (TERS) attracted great interests and was intensively studied^{52,53}. Besides, recent progresses on AFM-Raman shows that the molecular resonance of a single molecule can be detected¹⁴.
- 3) High-speed AFM (HS-AFM): HS-AFM is a type of recently developed technique that provides fast AFM scanning, with a high spatial resolution and a temporal resolution of up to 100 ms. Nanoscale imaging with such time resolution is perfectly appropriate for visualizing the phenomena in the biological activities, such as protein dynamics and protein-lipid interaction^{54,55}. Typically, HS-AFM is equipped with a short cantilever with a resonant frequency of 1-5 MHz in liquid and a spring constant of 0.1-0.2 N/m to ensure high-performance in the high-speed scanning. More recent advances of HS-AFM, such as height spectroscopy⁵⁶, allow to obtain more detailed information on the biomolecules, at a specific location or at a single line, with an even higher temporal resolution (up to tens μ s).

Chapter 2 Protein aggregation and related human diseases

The origin of protein aggregation and the mechanism of amyloids fibril formation is one of the most important topics that we had been focusing on during my PhD study. This topic will be highlighted and intensively discussed in the several following chapters. Thus, I believe it is worthwhile to give a separate introduction on this topic.

This section includes an introduction on the current situation of neurodegenerative diseases and amyloidosis, their association with protein misfolding and amyloid formation, the current understanding on the mechanism of the aggregation pathway and aggregation kinetics, functional material and nanotechnological application, as well as the techniques for *in vitro* characterization of the protein aggregates and amyloid fibrils.

2.1 Protein misfolding and neurodegenerative diseases

Protein is the architecture from one or more polypeptides, which is a linear long chain of amino acid residues assembled from the DNA decoding process. In the living organisms in nature, protein plays a fundamentally significant role in composing multiple complex organisms and operating their biological activities. To enable these polypeptides to be functional proteins, such polypeptides should be folded into specific structures, including secondary and quaternary structures, which determine their biological activities. One of the surprising characteristics of protein folding is precision and fidelity from polypeptide to the protein with a unique shape⁵⁷. However, there is a risk of failure during this process, termed protein misfolding, which produces protein aggregates especially for certain types of proteins, such as Amyloid- β .

The process of protein misfolding typically starts from the native state or unfolded soluble protein, resulting in the formation and proliferation of insoluble highly-ordered fibrillar (thread-like) aggregates, termed amyloids⁵⁸. The fibrillar aggregates or intermediates yielded during protein misfolding process may show huge pathological significances and the association with various diseases, because of the accumulation of aggregates or their cellular toxicity. So far, more than 50 disorders have been proved to be associated with protein misfolding and protein aggregation, as shown in Table 2.1. These

diseases can be classified as three categories: neurodegenerative diseases, non-neuropathic systemic amyloidosis and non-neuropathic localized amyloidosis. The neurodegenerative diseases, including the Alzheimer's disease and Parkinson's disease, is the neurologic disorders that result from the damage of the central nervous system (CNS). Depending on the amyloid deposition, non-neuropathic amyloidosis can also be sorted as localized and systemic diseases⁵⁹, such as the light chain amyloidosis and Type II diabetes.

	Diseases	Protein or peptide	Number of residues	Structure of protein or peptide
Neurodegenerative diseases				
	<i>Alzheimer's disease</i>	<i>Amyloid-β</i>	<i>37-43</i>	<i>Intrinsically disordered</i>
	<i>Parkinson's disease</i>	<i>α-Synuclein</i>	<i>140</i>	<i>Intrinsically disordered</i>
	<i>Huntington's disease</i>	<i>Huntington fragment</i>	<i>Variable</i>	<i>Mostly intrinsically disordered</i>
	<i>Spongiform encephalopathies</i>	<i>Prion protein</i>	<i>230</i>	<i>Disordered and α-helical</i>
	<i>Familial amyloidotic polyneuropathy</i>	<i>Transthyretin mutants</i>	<i>127</i>	<i>β-sheet</i>
Non-neuropathic systemic amyloidosis				
	<i>Amyloid light chain amyloidosis</i>	<i>Immunoglobulin light chain</i>	<i>90</i>	<i>β-sheet and Ig-like</i>
	<i>Amyloid A amyloidosis</i>	<i>Serum amyloid A1 protein</i>	<i>76-104</i>	<i>α-helical and unknown fold</i>
	<i>Senile systemic amyloidosis</i>	<i>Wild-type transthyretin</i>	<i>127</i>	<i>β-sheet</i>
	<i>Hemodialysis-related amyloidosis</i>	<i>β_2-microglobulin</i>	<i>99</i>	<i>α-helical and Ig-like</i>
	<i>Lysozyme amyloidosis</i>	<i>Lysozyme mutants</i>	<i>130</i>	<i>α-helical and β-sheet</i>
Non-neuropathic localized amyloidosis				
	<i>Type II diabetes</i>	<i>Amylin</i>	<i>37</i>	<i>Intrinsically disordered</i>
	<i>Apolipoprotein A1 amyloidosis</i>	<i>Apo A-1 fragments</i>	<i>80-93</i>	<i>Intrinsically disordered</i>
	<i>Injection-localized amyloidosis</i>	<i>Insulin</i>	<i>21-30</i>	<i>α-helical and insulin-like</i>

Table 2.1 A collection of diseases that associated with protein misfolding from more than 50 diseases, and the features of their associated proteins. Adapted from Ref.^{58,60}.

2.1.1 The situation of protein misfolding diseases

The protein misfolding diseases is causing huge problems and affecting millions of people worldwide. Here, we give a brief introduction to the current situation for several typical protein misfolding diseases, including the Alzheimer's and Parkinson's diseases.

According to the latest report from World Health Organization (WHO), around 50 million people worldwide suffer from dementia. Dementia is a syndrome in which there is deterioration in memory, thinking, behavior and the ability in daily activities, and Alzheimer's disease is the most common form of dementia that contribute to 60-70% of all the cases (<https://www.who.int/news-room/factsheets/detail/dementia>). Moreover, there are nearly 10 million new cases of dementia every year with an increasing trend in the coming years. Although the elderly is commonly affected, it is shown that young victims are more and more common. Thus, Alzheimer's disease is attracting widespread attentions among plenty of government and research institutes worldwide. In United State, the cost for the care of Alzheimer's disease in 2017 was 232 billion, but in comparison, the funding that related to the research on Alzheimer's disease was much less. In the brain of the patient of Alzheimer's disease, plenty of plaques and neurofibrillary tangles, mainly consisting of amyloid- β ($A\beta$) fibrils and tau aggregates respectively, were found, suggesting their association between Alzheimer's disease.

Parkinson's disease is a progressive nervous system disorder that affects movement of body, including regularly tremors, rigid muscles and uncontrolled slow movement. This aged related disease is the second most common neurodegenerative disorder after Alzheimer's disease, with about 10 million victims worldwide. The main pathological feature of Parkinson's disease is the loss of the neuron in the basal ganglia and the presence of the Lewy body, which the accumulation of the α -synuclein (α -Syn) aggregates, in the remaining neurons. More and more strong evidences showed the direct correlation between α -Syn and Parkinson's disease.

2.1.2 Protein aggregate toxicity

The evidences of the association between amyloids and neurodegenerative diseases are proved by the discovery in the patient's brain: amyloid- β aggregates in plaques and tau aggregates in neurofibrillary tangles are related to the Alzheimer's disease, and Lewy bodies with abundant α -synuclein fibrils are the key feature of the patients with Parkinson's disease. Although recent processes on understanding the amyloid fibril and protein aggregates, the mechanism of protein aggregate toxicity in neurodegenerative diseases remains unknown⁶¹.

Current investigations proposed several hypotheses on the possible origin of protein aggregate toxicity: amyloid oligomers, the amyloid fibrils, other oligomers off the pathway to fibrils, the process of fibril growth, or cellular stress⁶¹. These factors can be toxic entities or toxic process that threat the cell by, for example, perturb the integrity of the cellular membrane.

2.2 Protein misfolding and aggregation pathway

In living organisms, there are various amyloidogenic proteins in the native state at a certain level of concentration. Many of these proteins play an important role in the cellular or intercellular activities. For example, α -synuclein appears in the region of presynaptic terminals of the neuron, where α -synuclein interacts with phospholipids and proteins, also contributes to the release of the neurotransmitter and the communication between neurons^{62,63}.

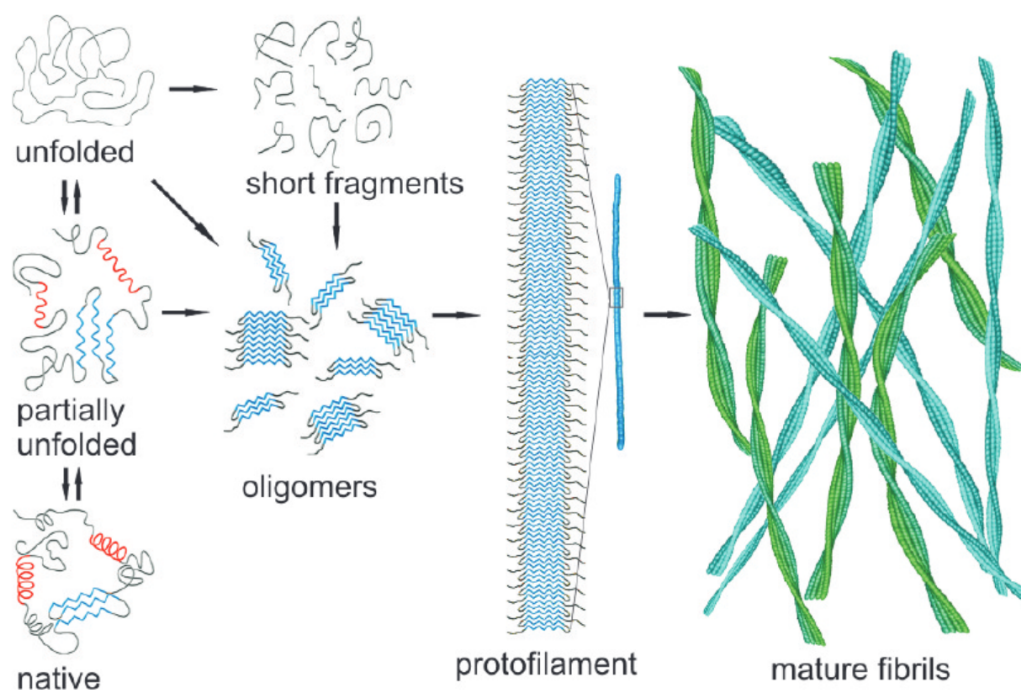


Figure 2.1 Schematic representation of the conversion of globular proteins into amyloid fibrils. The natively folded protein can be generated from the unfolded polypeptide through a partially unfolded conformation, while these states of monomers and short fragments may misfold and form the oligomeric aggregates, and proceed the aggregation to generate the protofilaments and then mature fibrils. Adapted from Ref.⁶⁴

However, the accumulation and aggregation of these natively folded proteins form filamentous fibrils with highly ordered cross- β -sheet structure, as shown in Figure 2.1. The unfolded and partially unfolded proteins may form the cross- β -sheet structure and generates the protein oligomers. Whereas, the natively folded protein may also convert their native structure to form the misfolded oligomers by cascade transition, and this may because there is a lower free-energy level of the aggregated-state

oligomer over the native-state monomer⁶⁵. Then, the oligomer continues the aggregation process and forms the protofilament stabilized with cross- β -sheet structure along the direction of fibril axis. Further, the accumulation of protofilaments interacts with monomeric protein according to different aggregation processes, such as secondary nucleation, and evolves to mature fibrils. In the final solution, there is an equilibrium balance of amyloid fibrils and monomers in the solution.

2.2.1 Aggregation kinetics

A well-known feature of the typical aggregation process is the three characteristic stages: lag phase, growth phase and final plateau regime, as shown in a typical sigmoidal-shaped aggregation kinetics curve in Figure 2.2a. As an initiating phase in the aggregation process, the lag phase is very important and molecular events regulating the lag phase in fibril formation can make a significant importance in determining aggregation kinetics of the whole aggregation process. It is shown that, instead of only primary nucleation as previously described⁶⁶, the lag-phase contains multiple parallel microscopic relations, including the amplification of primary nuclei and the proliferation by secondary nucleation and fragmentation processes^{67,68}. Then, a steep transition zone of the growth phase is followed, where an exponential increase of the aggregate volume indicates the accelerated aggregation progress. After that, the curve reaches a final plateau, suggesting that the amounts of aggregates and monomers in the solution maintain are stable. In this period, the transition from monomer to fibril is saturated, while there is a dynamic equilibrium of the concentration of monomers and aggregates⁶⁷.

This sigmoidal aggregation kinetic curve is associated with the microscopic processes, for example, the exponential reaction in the growth phase is due to the operative pathway⁶⁹. Plenty of studies tried to investigate the link between the aggregation curve and the microscopic processes, but limited results had been achieved. To better understand the aggregation from soluble monomer to mature fibril, a systematic analytical approach of aggregation chemical reaction had been established by Knowles and et al^{60,69,70}. With a quantitative analysis on the experimental kinetic data, this mechanistic framework could clarify the reaction mechanisms by underlying the role of various microscopic aggregation steps, including primary nucleation (from monomers to fibril), elongation (adding monomers to the end of existing aggregates), secondary nucleation (adding monomers on fibril surface) and fragmentation (splitting the existing fibrils), in a specific experiment (Figure 2.2b).

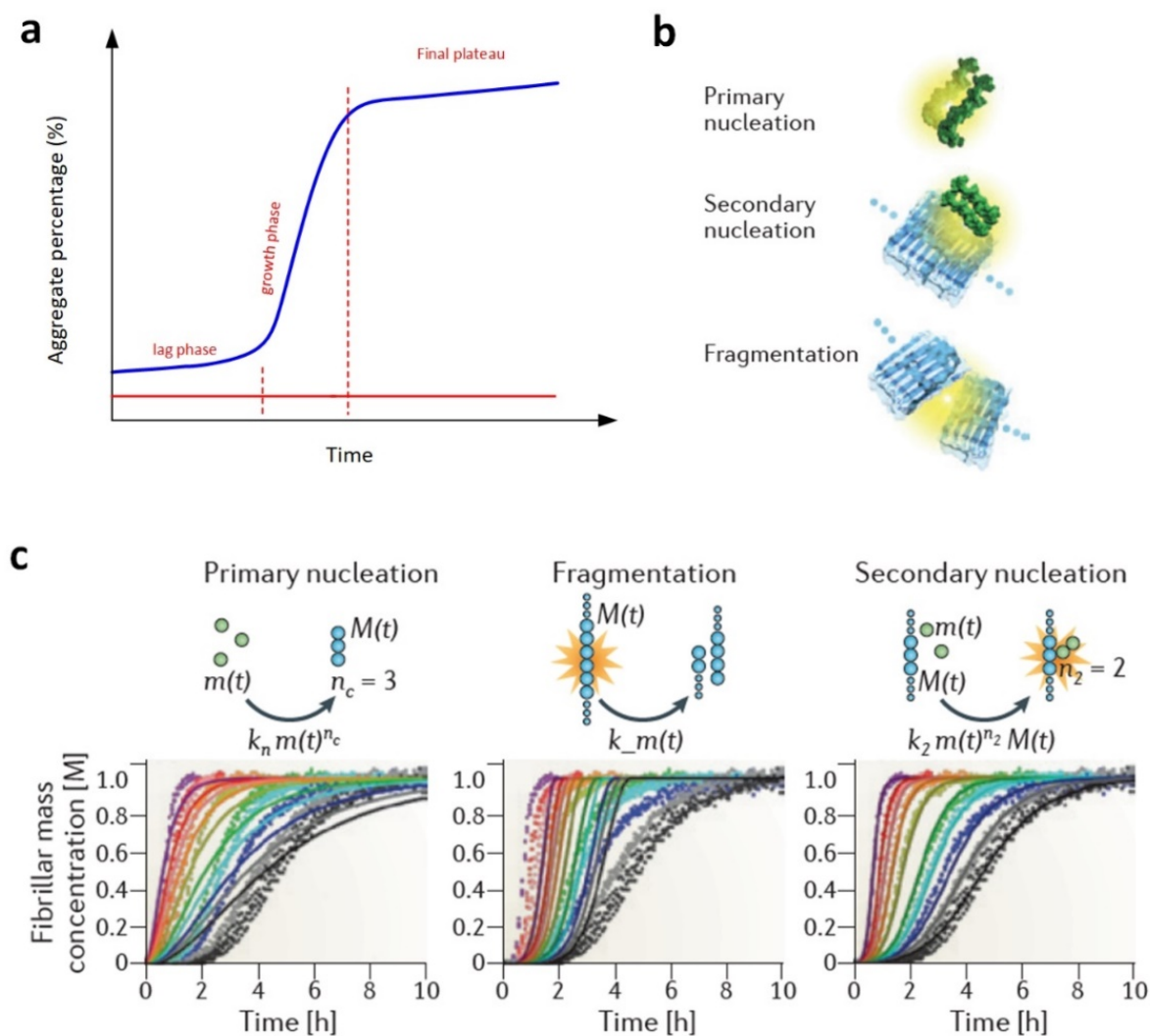


Figure 2.2 The analysis on the protein aggregation kinetics. (a) The typical macroscopic aggregation kinetic curve of amyloid formation, indicating the aggregation concentration (in monomer equivalents, % of total monomer) as a function of time. (b) Microscopic processes underlying amyloid formation: primary nucleation from monomers to fibril; surface catalyzed secondary nucleation from monomers to fibril surface; and fragmentation by splitting the existing fibrils. (c) Comparison of such integrated rate laws with experimental kinetic measurements enables the relative importance of specific microscopic processes to be tested. In this example, the aggregation kinetics for increasing concentrations (colored lines) of the amyloid- β peptide are compared with integrated rate laws that contain primary nucleation (left), fragmentation (center) and monomer-dependent secondary nucleation (right). The data show that secondary nucleation is the dominant process under these conditions. Panels b and c are adapted from Ref.⁶⁰.

These kinetic data of the relative aggregate concentration are typically obtained from macroscopic measurement of Thioflavin T (ThT) fluorescence assay. By comparing the integrated rate laws with experimental kinetic measurements, the relative importance of specific microscopic processes can be tested. In this example (Figure 2.2 c), aggregation kinetics for increasing concentrations of the amyloid- β peptide are compared with integrated rate laws of primary nucleation (left), fragmentation (center) and monomer-dependent secondary nucleation (right), showing that secondary nucleation is the dominant process in this experiment⁶⁰. However, there are several key requirements for analyzing

the data with the nucleation and growth model, including reproducible sigmoidal curves. Also, the complex curve shape with biphasic behavior, which is often due to poor control of initial conditions and insufficient purity, cannot be analyzed⁷¹.

2.2.2 Molecular structure of Amyloid fibril

Mature amyloid fibrils are typically composed of several protofilaments by twisting or stacking each other in the direction of fibril axis. The protofilaments consist of an ordered and repetitive arrangement of hydrogen-bonded intermolecular β -sheets, along the direction of the fibril axis⁶¹. X-ray fibril diffraction studies suggested the dimension and the size of the intermolecular cross- β -sheet structure, with the space between β -strands of 4.8 Å and typical distance between stacked β -sheets of 6-12 Å^{72,73}. Lately, the development of CryoEM^{74,75}, solid-state NMR spectroscopy^{76,77} has facilitated the study on the more detailed molecular structure of amyloid fibrils, as shown in Figure 2.3a. All the experimental results in molecular dimension show that, the hydrogen-bonding network between the β -strands is the critical factor to immobilize and form the thermodynamically stable β -sheet backbone structure along fibril axis^{60,61,74}.

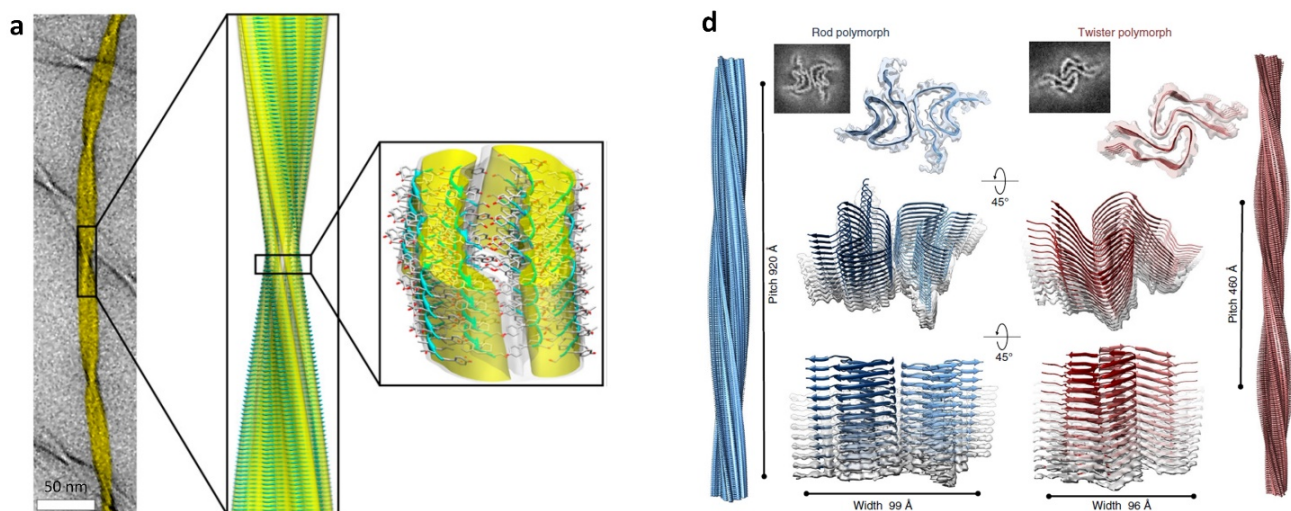


Figure 2.3 The cryoEM revealed molecular structure of amyloid fibrils. (a) Close-up details of the NMR atomic-resolution structure of the triplet 11-residue transthyretin (TTR) fibril fitted into the cryo-EM reconstruction (Center). The background image of the fibril (left) was taken using TEM (scale bar, 50 nm). The fibril surface (right) are shown at 1.0σ (white) and 2.2σ (yellow) above the mean density, respectively, and the constituent β -sheets are shown in a ribbon representation; oxygen, carbon and nitrogen atoms are shown in red, gray and blue, respectively. Adapt from Ref.⁷⁴. (b) The cryo-EM structures of the rod (left) and twister (right) polymorphs of the full-length α -synuclein fibrils shown as density slices (top inset), as semi-transparent surfaces overlaid with their atomic models viewed from two different angles (lower panels). The rod (blue) and twister (red) polymorphs contain two protofilaments composed of stacked β -sheets and packed by an approximate 2_1 screw axis of symmetry. Shown on the left and right sides are the 3D model of the rod and twister fibril polymorphs, respectively, with their distinctively different helical pitches depicted. Adapted from Ref.⁷⁸.

Then, the influence of the intermolecular interactions between β -sheets of the fibril-forming segment on the full-length protein fibril was found. Eisenberg and his colleagues proposed the steric interaction that pairs the β -sheets in the fibril core by studying the amyloid-forming segments^{79–82}. With the protofilament of steric zipper structure, the side chains emanating from the two sheets are tightly interdigitated, like the teeth of zipper⁸³. The steric zippers have dry interfaces between the two sheets, and this hydrophobic effect contributes to the stability of paired-sheet of amyloid fibril. Different types of cross- β -sheet structure can be classified, according to the direction of β -strand (parallel or antiparallel), interacting surface of β -sheet (face-to-face or face-to-back) and orientation of the β -sheet packing (up-up or up-down)⁶¹. The face-to-face packing is the most common sheet-to-sheet steric arrangement, while face-to-back, head-to-tail packing arrangements can be found in many short-peptide fibrils. Besides, the inter-sheet interaction can also generate the side-by-side β -sheet interaction, with the head-to-tail or head-to-head arrangement^{74,84,85}, which is believed to be originated from the hydrogen bonding^{74,86}.

Recent years, the studies of full-length proteins were carried out gradually that shows sub-Angstrom level resolution of the details of amyloid fibrils. The atomic models of mature fibrils of full-length α -Syn^{78,87,88}, A β ⁸⁹, and Tau⁹⁰ proteins show that the steric zippers exist also in a paired β -sheets in the protofilaments. Most populations of these protofilaments show twisted polymorph, while the protofilaments with rod-like polymorph in the case of α -Syn were also observed⁷⁸. Analysis on the established structures of disease-related α -Syn fibrils contributes to the mechanistic understanding to the pathogenesis of synucleinopathies, such as template recruitment and propagation^{78,91}. Besides, drug design targeting these fibrils for the treatment of related protein misfolding diseases can be hinted by considering the molecular structures. For example, the fibril-binding compounds and their derivatives suggest that the increase of binding effect strengths fibril stability and decreases aggregate toxicity, by shifting the equilibrium from toxic oligomers to fibrils⁹².

2.2.3 Amyloid polymorphism and order-order transitions

Amyloid fibril polymorphism, referring to the variation of three-dimensional packing of protofilaments, is a widespread feature of mature fibril formation, irrespective of the types of amyloid fibrils. Remarkably, this phenomena had been observed both *in vitro*⁹³ and *in vivo*⁹⁴, indicating the importance of understanding the association among this polymorphic architectures. High-resolution AFM, cryoEM and TEM are extremely useful tools to reveal the protofilament arrangement of mature fibril at this microscopic scale.

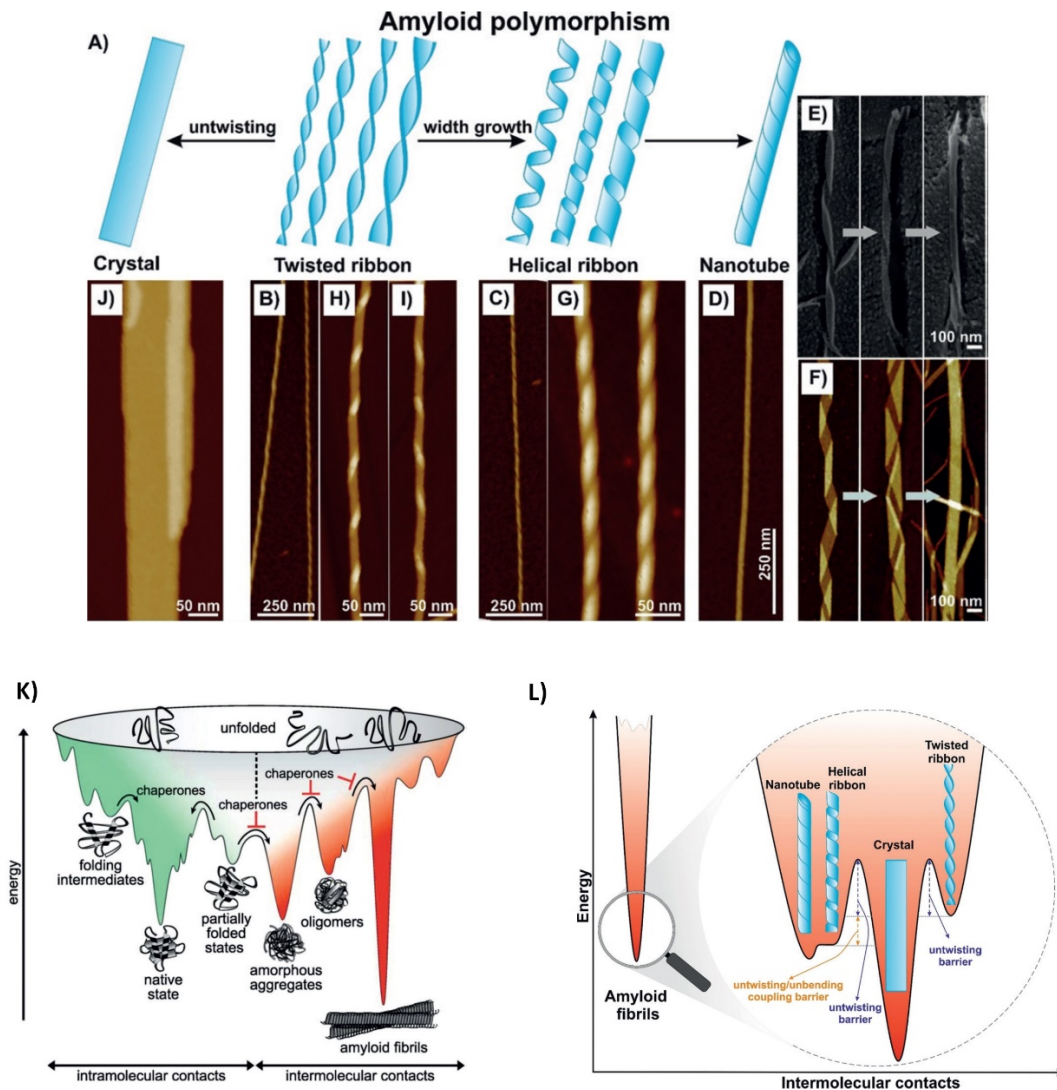


Figure 2.4 Amyloid polymorphism and order-order transition. (a-h) Morphological polymorphism of amyloid fibrils. A) The observed polymorphic sequences in protein and amyloidogenic peptides: twisted ribbons, the most common amyloid polymorph, evolve into either crystal through untwisting and lateral aggregation or helical ribbons upon the increase in lateral width and then nanotube through closure of the edges. AFM image of left-handed twisted ribbon (B), helical ribbon (C) and nanotube (D) amyloid structure assembled from heptapeptide CH3 CONH-bAbAKLVFFCONH2. E) Cryo- SEM and F) AFM height images showing the progressive (see arrows) lateral growth steps and final closing of lysozyme helical ribbons into nanotubes. An AFM image of the right-handed helical ribbon (G), right-handed twisted ribbon (H) and left-handed twisted ribbon (I) amyloid structure assembled from the hexapeptide ILQINS. J) An AFM image of the amyloid crystal structure assembled from the hexapeptide TFQINS. K) The energy landscape of protein folding (green) and aggregation (red). During folding, protein molecules sample various conformations while traveling downhill on a potential free-energy surface (green) toward the thermodynamically favorable native state. Kinetically trapped on- or off-pathway intermediates occupy low-energy wells (folding intermediates and partially folded states). Molecular chaperones assist the folding by lowering free-energy barriers and prevent aberrant intermolecular interactions (red), which can lead to various forms of aggregates (amorphous, oligomeric, fibrillar). Fibrillar (amyloid-like) aggregates may be the most thermodynamically stable. L) Suggested energy landscape for the main amyloid polymorphs: twisted ribbons, helical ribbons, nanotubes, and crystals. Amyloid crystals occupy the ground state in the landscape, whereas all other polymorphs are metastable and occupy relative minima. Panels A-J and L are adapted from ⁹³, and panel K is adapted from ^{100,101}.

The diverse spectrum of the protofilament packing arrangement indicates the existence of twisted-ribbon, helical ribbon, nanotube, rod-like and crystal-like fibrils, as intensively reported in the literature^{85,93,95}. The polymorphic fibrils with different molecular organizations indicate that various intermolecular interactions among the protein aggregates. More interestingly, a clear transition among the

polymorphic fibrils, assembled from the heptapeptide $\text{CH}_3\text{CONH-}\beta\text{A}\beta\text{AKLVFF-CONH}_2$, was observed^{93,96,97}, which greatly expanded our understanding on the interplay among different fibril polymorphs. For this heptapeptide, as shown in Figure 2.4a-f, the most commonly-founded twisted fibril shows two pathways of further transition: 1) the twisted fibrils untwist themselves and further laterally assemble to form crystals, 2) twisted fibrils maintain or further enlarge the twisting while increase lateral width, transiting to helical ribbons and further evolving to nanotube shape. Between these two pathways, there is a competition between the intrinsic chirality of building blocks that favors twisted structures and a mechanical strain that suppresses twisting^{98,99}, that determines the final polymorphs of amyloid fibril.

As shown in Figure 2.4k, the traditional argument from the perspective of energy landscape, is that unfolded protein molecules samples various conformations traveling downhill towards the thermodynamically favorable native state, while the intermolecular contacts may bring these proteins to a more thermodynamically stable state, as a form of amyloid fibril. However, the observation on the fibril polymorphism proved that amyloid polymorphs might occupy different energy levels on the energy landscape (Figure 2.4l). For the case of this heptapeptide⁹³, the amyloid crystals occupy the absolute minimum on the energy landscape among all possible amyloid polymorphs, as the most thermodynamically stable state of the aggregates in this experiment. Then the nanotube fibrils show slightly higher free energy, while twisted fibrils occupy a relatively high level compared to other polymorphs. However, for the protein with a larger number of polypeptide, there is a possibility of variation on the existence of these amyloid polymorphs and their transition, due to the different mechanism in the mechanical strain and intrinsic chirality during fibril formation¹⁰².

2.3 Functional material and nanotechnological applications of amyloids

Pathological amyloid aggregates have been proved to be associated with a series of protein misfolding diseases, including various neurodegenerative disorders. On the other hand, various proteinaceous structures are the fundamental building blocks of the functional materials in nature. Inspired by formation of amyloids and functional materials, a number of remarkable self-assembling material systems have been developed^{103,104}. As functional materials, amyloid shows the outstanding features compared with other functional materials, including the biocompatibility, high stiffness, self-assembling behavior, as well as the excellent mechanical and electronic properties. Lately, the amyloid-based functional materials has been attracting more and more attentions in the various emerging applications, including the biomedical (drug delivery¹⁰⁵⁻¹⁰⁷, artificial tissues^{108,109} and biomimetic bones¹⁰⁸), biosensing¹¹⁰ and optoelectronics¹¹¹⁻¹¹⁴ fields, as showed in Figure 2.5.

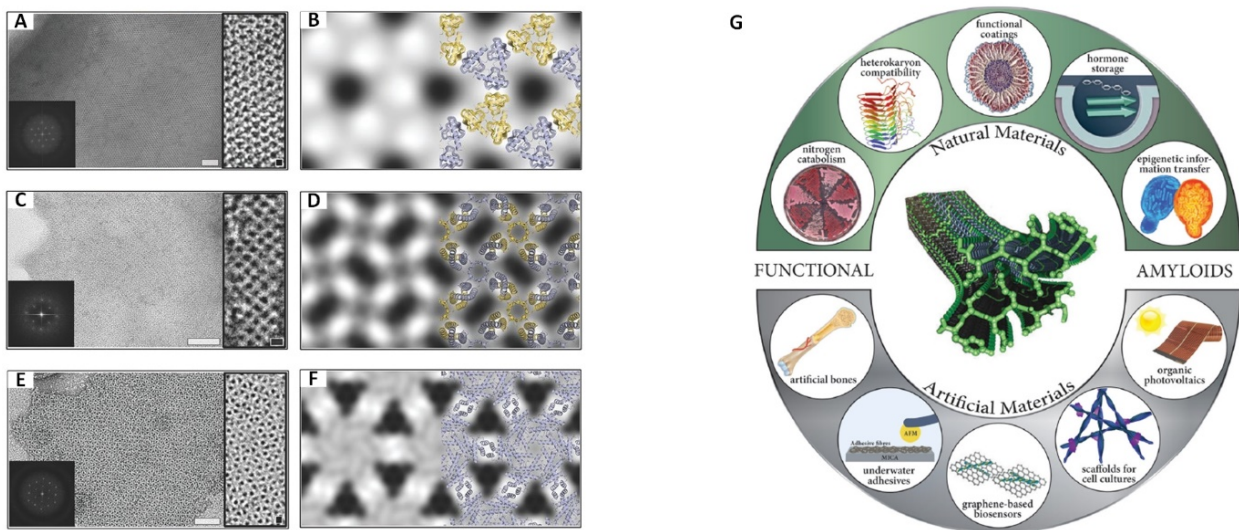


Figure 2.5 Functional applications of amyloid fibrils. (A-F) Negatively stained large *E. coli*-grown array, with inserts of higher magnification view with lattice spacing and Fourier transform of the large array (left), and projection map at 15 Å calculated from a large array with inserted overlay of the p3Z_42 (A, B), p4Z_9 (C, D), and p6_9H (E, F) design model on the projection map. The scale bar is 50 nm. Adapted from Ref. ¹⁰⁴. (G) The schematic road map to the diversity in functions of the amyloids-based materials. Adapted from Ref. ¹¹⁵.

An excellent example of programmed biological self-assembly for potential nanomaterial application is the 2D protein arrays that mediated by noncovalent protein-protein interface¹⁰⁴. Like the DNA origami^{116–118}, 2D protein lattices are designed with highly ordered structure that can be applied in structure determination and nanomaterial engineering.

Another example of amyloid-based functional material is the biomimetic material. Being the protein assembly, amyloid based material is thus biocompatible while used in various biomedical applications, e.g. bone-mimetic material. Compared with other biological materials^{119,120}, amyloid fibrils show remarkably high stiffness, with the value of Young's modulus (E) of the range of GPa, which could be the most rigid proteinaceous material in nature¹²⁰, such as dragline silk as a densely packed hydrogen-bonded β -strands analogous with the E value of up to 10 Gpa^{120–122}. The bone-mimetic material were made from the biomimetic nanocomposites of hydroxyapatite platelets and lysozyme amyloid fibrils, that shows well-organized layered hierarchical structures with close physical properties and inorganic/organic ratio compared to real bone¹⁰⁸.

By adhering to the surface of amyloid fibrils, layered nanocomposites could be used to bridge 2D organic/inorganic stacks and nanotechnological applications¹¹⁵. By combining graphene and β -lactoglobulin fibrils from milk, the graphene-amyloid biodegradable nanocomposites could be prepared. Here amyloids act as the enzyme-sensing substrate and graphene contributed to the electron conductivity and mechanical strength¹¹⁰. Amyloid-carbon hybrid membranes were also developed for

universal water purification with the ability of filtering several types of heavy metal ions simultaneously¹²³. Impressively, the use of insulin amyloid fibrils was applied in the light-emitting devices by mixing with red, yellow and blue emitting dyes to obtain the white-light emitting diodes^{111,114}. Various applications, such as the controlling of photophysical properties, in the electronic and photonic devices based on insulin fibrils can be found¹¹¹⁻¹¹⁴. Moreover, the emerging technique of amyloid scaffolds is rapidly used in promoting and controlling cell growth^{124,125}.

2.4 Characterization of Protein aggregation in vitro

To obtain a full picture of amyloid fibrillization mechanism and aggregation behavior, there are several features of protein aggregates to be characterized, including chemical reactions, secondary structural transition, morphological imaging, mechanical properties and atomic-level structure analysis, which could offer. These characterization approaches contain various biochemical and biophysical techniques, including Thioflavin T (ThT) fluorescence, circular dichroism (CD) spectroscopy, cryo-electron microscopy (cryoEM) imaging, AFM, infrared (IR) spectroscopy, nuclear magnetic resonance (NMR) and X-ray scattering.

Among these techniques, some are the bulk techniques that give an overall description of the protein aggregation in the bulk solution. Macroscopic measurements were performed in the bulk solution, including ThT fluorescence, CD spectroscopy and IR spectroscopy. By contrast, single molecular techniques, such as cryoEM and AFM, shows the morphological and molecular properties of individual aggregates. With the recent processes on these single-molecular techniques, precise and statistical analysis on the protein aggregates reveals much details that benefit related studies.

2.4.1 *ThT fluorescence*

A very common approach to investigate amyloid formation is to use the dye that specifically stained to β -sheet structures and amyloid fibrils. The first dye for amyloid detection was Congo red, which however required a laborious staining process, and the dye's enigmatic "apple green birefringence" is difficult to interpret¹²⁶. *Thioflavin T (ThT)*, is a benzothiazole dye that has been widely used to visualize the presence of misfolded amyloid aggregation since the first demonstration in 1959¹²⁷. So far, the usage of ThT dye can be found in various amyloid investigation, ranging from histological study, to chemical kinetics, imaging and structural analysis^{128,129}.

At molecular level, amyloid fibrils share the cross- β -sheet architecture, showing the laminated β -sheet with strands orderly organized perpendicular to the fibril axis direction. ThT dye could specifically binds to the β -sheet structure both *in vitro* and *in vivo*, due to the presence of the specific ThT-binding sites on the β -sheet architecture. Meanwhile, the two planer segments on ThT structure mutually rotate to change its chirality, resulting in a dramatic shift of the excitation (from 385 nm to 450 nm) and emission maximum (from 445 nm to 482 nm)¹³⁰. Thus, the presence of β -sheet aggregates is validated by detecting ThT fluorescence signal, and the amount of amyloid aggregates could be measured by monitoring the enhancement of the fluorescence signal, as shown in Figure 2.6a.

Although ThT dye is widely used, the structural basis of the binding specificity of amyloid-dye interaction is not fully understood¹²⁸. The increasing studies on the ThT-fibril interaction generally revealed the existence of the ThT-binding sites on the cross- β -sheet binding sites, regardless to distinct amino acid sequences. One of the popular interpretations, according to the X-ray studies, suggests that ThT interacts with β -sheet by docking on surfaces by forming tyrosine cross-strand ladder, rather than in the space between adjacent ladders¹²⁹. Further studies later may show a more comprehensive insight onto amyloid structure and the molecular mechanism of ThT binding to amyloid fibril. This might provide a deeper understanding on the result of ThT experiments and offer guidance for designing the amyloid diagnostics, inhibitors and therapeutics¹³⁰.

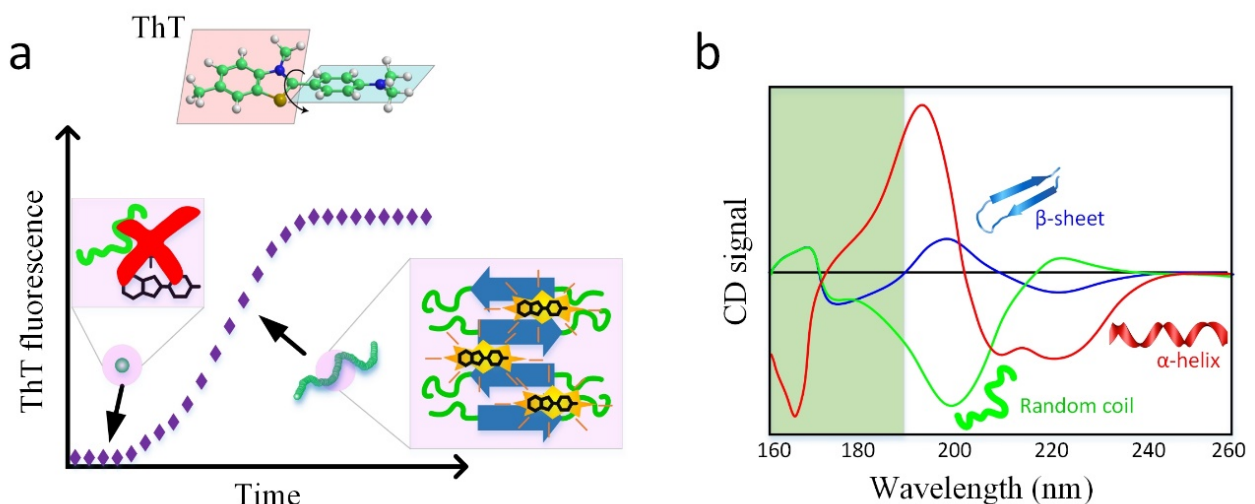


Figure 2.6 The ThT and CD characterization of protein aggregation. (a) Schematic representation of the typical curve of ThT fluorescence assay. The structure of ThT molecule is noted on the top with mutual rotation of two planer ThT segments before and after binding to β -sheet structure. (b) Typical CD spectra of helical (red), β -sheet (blue), and random coil (green) protein. The low wavelength data in the green shaded area to the left of the vertical black line are generally only accessible using the synchrotron radiation circular dichroism (SRCD), whereas the data to the right of the line are accessible by both SRCD and conventional CD instruments. Panel b is adapted from Ref. ¹³¹

2.4.2 CD spectroscopy

Circular dichroism (CD) spectroscopy is a well-established biophysical tool for the structural characterization of molecules containing a chiral center or a 3D structure that provides a chiral environment, such as proteins and nucleic acids¹³². This technique measures the differential absorption of left- and right-handed circularly polarized light in the bulk solution due to the structural asymmetry. It is especially widely used for the evaluation of protein secondary structure, from the CD absorption signals in the far-ultraviolet (UV) wavelength region (180 nm-240 nm). This derives from the amide chromophores of the peptide bonds, with two types of electron transitions: $n \rightarrow \pi^*$ transition at around 222 nm, and $\pi \rightarrow \pi^*$ transitions at ~208 and 190 nm. Thus, the protein structural information can be observed by recording the differential absorption at distinct wavelength.

The dichroic fingerprint on the CD absorption spectrum allows the specific diagnose of the protein secondary structure with a high precision: 1) The random coil structure, also termed irregular or intrinsically disordered structure, shows a large $\pi\pi^*$ absorption dip around 198 nm. 2) α -helix structure demonstrates a typical absorption spectrum with a positive maximum near 190 nm and dual negative maxima at 208 and 222 nm. 3) β -sheet structure generally signatures a positive and negative maximum near 195 and 218 nm respectively^{132,133}, as seen in Figure 2.6b.

Besides, CD spectroscopy in the far UV region can also be used to detect the protein-ligand interactions^{132,134} and to measure the protein folding and unfolding¹³⁵. Additionally, the information of tertiary structure can be obtained from the environmental dependent CD spectra of protein aromatic residues in the near UV region (250 nm-300 nm).

2.4.3 AFM

As described in Chapter one, AFM is a powerful tool to investigate the properties of protein aggregates and amyloid fibrils at the single-aggregate level. AFM technique provides 3-D morphological maps of the aggregates with a sub-nanometer vertical resolution. This ability allows the morphological conformation of the homogeneous or heterogeneous species, such as monomer, oligomer, proto-filament and mature fibril, in the process of amyloid aggregation. Importantly, the statistical analysis on multiple individual protein aggregates could give a full and precise assessment of the characteristics of heterogeneous protein assemblies¹³⁶.

Moreover, as the development of AFM instrumentation, various advanced AFM-based technologies are available in studying protein aggregates. HS-AFM imaging in liquid environment is lately popular

that indicates the dynamics of protein-protein aggregation¹³⁷ and aggregates-lipid membrane interaction¹³⁸. Recent progresses on the HS-AFM revealed the structural dynamics of A β aggregation, with two different growth pathways that produce two distinct polymorphs: straight fibrils and spiral fibrils¹³⁹. Except for the morphological characterization, AFM could be performed to acquire the nanomechanical properties by carrying out the nanoindentation measurement^{140,141}. Such type of nanomechanical measurements by AFM was carried out for different amyloid fibril systems, yielding a Young's modulus range of 0.2-14 GPa^{70,120,136}, which is close to the GPa range obtained from other characterizing approaches, such as X-ray diffraction¹⁴² and cryoEM¹⁴³. Besides, the internal nanomechanical properties of amyloid fibril can also be detected by stretching the fibril and recording with the AFM-based force-distance curve¹⁴⁴.

2.4.4 TEM and CryoEM imaging

Negatively stained electron microscopy (EM) imaging is a common technique to observe the morphology of amyloid fibrils in the literature^{145,146}. TEM investigations showed an unprecedented close view of amyloid fibrils morphology in the early stage of studying neurodegenerative diseases^{147,148}. On the TEM images, various features of amyloid fibrils can be observed and carefully characterized, including the fibril shapes and polymorphism, as well as the morphological features, such as fibril width and periodicity¹⁴⁹.

The emergence of cryogenic electron microscopy (cryoEM) greatly improved the investigation on the morphology and molecular structure of amyloid fibrils. Compared with other approaches offering molecular resolution, such as X-ray crystallography and NMR spectroscopy, the advantage of this approach is the ability of determining the unprecedented details of the structure of proteins and macromolecular complexes in the single-particle specimens, without the need of homogeneous specimen and the crystallization process¹⁵⁰. By applying the samples in the environment of vitreous water at the cryogenic temperature, with the recent advances in the detecting method and software algorithms, the determination of molecular structures of biological structures at near-atomic resolution ($< 4\text{\AA}$) has been becoming reality¹⁵⁰.

Another key element of the popularity of single particle cryo-EM in amyloid structure analysis, is its power in dealing with heterogeneous assemblies. Amyloid fibrils typically show polymorphic morphologies that is variable with the protofilament packing structures, such as twisted, helical and rod-like fibrils. Such phenomena limit the resolution of the approaches averaging the fibril structures. However, single particle cryo-EM can be used to computationally extract short segments of the fibrils and to classify them into structurally homogeneous subsets^{151,152}. Recent years, this approach has

succeeded in yielding a series of molecular structures of short peptides, such as protein transthyretin (TTR 105-115)⁷⁴ and Ig light chains (AL peptide)¹⁵³, as well as the fibrils of physiologically relevant amyloid proteins including prions¹⁵⁴, a-synuclein^{78,87,88}, A β ₄₂⁸⁹ and tau⁹⁰.

More recently, the molecular structures revealed by cryoEM show its own unique amyloid fibril structural signature, with at an atomic resolution^{74,78,90,153}. With these evidences, we could understand the hypothesized links between protein aggregates and clinical phenotype, that possibly benefits the development of the targeted approaches for structure-based drug design and the biomarkers for early diagnose of diseases¹⁵².

2.4.5 Infrared (IR) spectroscopy

Infrared spectroscopy is a spectroscopic method that involves infrared radiation to measure the molecular vibration of the studied samples, for identifying and analyzing the molecular structure of the organic and inorganic compounds. It covers a range of distinct techniques, mostly based on absorption spectroscopy. According to the characteristic peaks on the absorption spectrum, one could obtain the chemical characterization of the species, including gas, liquid or solid. The Fourier-transform Infrared (FTIR) spectrometer is one of the most commonly used laboratory techniques, due to the advantages of the high signal-to-noise ratio, fast measurement and high sensitivity. The region for IR spectrum is consisted of near-, mid- and far-infrared, ranging from 0.7-1000 μm , where majority of the literature were focused on the mid-infrared region, 4000-400 cm^{-1} (2.5-25 μm), due to the fundamental association between the vibration and molecular structure. In FTIR, the IR absorption occurs while a photon in the infrared region transfers to a molecule and excites to a higher energy state, resulting in the vibrations of molecular bonds, such as stretching, bending, twisting, rocking and wagging. The fingerprint of IR absorbance peaks is determined by the intrinsic physicochemical properties of the corresponding molecule bonds and functional groups.

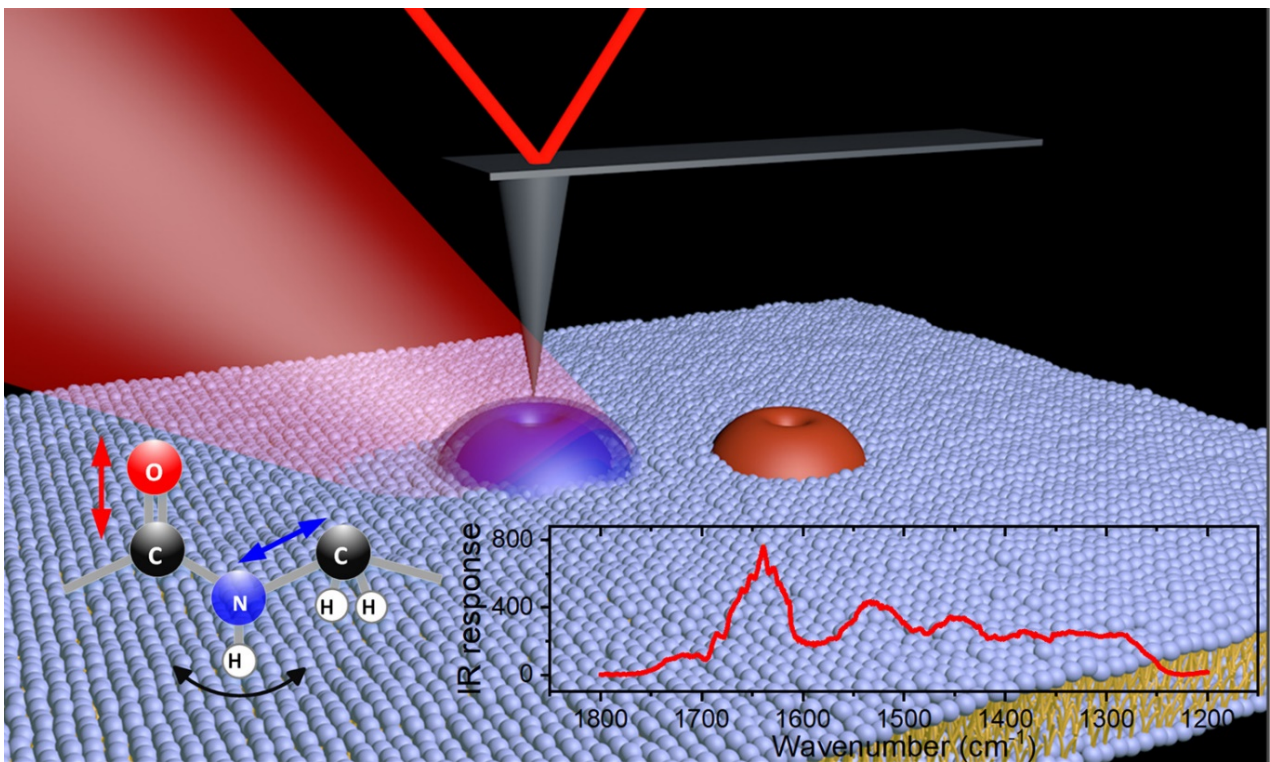
One disadvantage of FTIR technology is the spatial resolution, which shows only several micrometers for the conventional IR measurement. Remarkably, the recent advances in the AFM-IR, which is the combination of AFM and IR spectroscopy, is attracting more and more attention due to the great enhancement of spatial resolution to up to tens nanometers, due to the advantages of AFM cantilever^{37,155}. Currently, AFM-IR had been proved to be capable of revealing remarkable structural details on the surface of heterogeneous components, and thus is widely used in various fields, including polymers¹⁵⁶⁻¹⁵⁸, materials^{36,159,160} and biological science^{40,161-163}.

2.4.6 Solid state NMR and X-ray diffraction

Revealing atomic-level structures for cross- β spines is important for understanding the fibrillar nature of amyloid, which were intensively studied by X-ray diffraction. The X-ray diffraction pattern of cross- β structure consists of an X-ray reflection at ~ 4.8 Å resolution along the fibril direction and another X-ray reflection at ~ 6 - 12 Å resolution perpendicular to the fibril direction^{61,80}. This indicates the spaces between the β -strands and the spaces between the tightly interacted β -sheets, respectively, as the common motif of cross- β structure. Moreover, X-ray diffraction studies also revealed the dual-sheet motif, termed steric zipper, with two adhered β -sheets by the interdigitation of the side chains of the mating strands^{61,79-83}. Such a self-complementary structure is caused by several factors: the polar hydrogen bonds, van der Waals forces that form interacting pairs of β -sheet, and the entropy of the water molecules released from the inner faces of mating β -sheets⁶¹.

As another primary tool for structural biology, the advent of solid-state nuclear magnetic resonance (NMR) enables the revealing of the protein fibril structures at atomic resolution, with the prerequisite of large objects with local order¹⁶⁴. Molecular structure determination with this spectroscopic method is based on combining short-distance information and structures result from triangulation using a large array of distance from the 2D correlation spectra^{77,164,165}. So far, the 3D structures of various amyloid fibrils, including A β , α -synuclein and HET-s prion, had been solved by using solid state NMR⁶¹. These latest advances in the solid state NMR could be capable of contributing to solve the 3D structure of the polymorphic amyloid fibrils^{61,164,166}.

Chapter 3 Regulation of supramolecular architectures of LHCII on lipid membrane



This chapter is based on a published work in the journal *Biochemica et Biophysica Acta (BBA) – Bioenergetics*, with the following information:

Jiangtao Zhou¹, Sergey Sekatskii¹, Renata Welc², Giovanni Dietler¹ and Wieslaw I. Gruszecki^{2*}. **The role of the xanthophyll cycle pigments in the regulation of supramolecular organization of the photosynthetic complex LHCII in lipid membranes studied by high-resolution imaging and nanospectroscopy.** *BBA – Bioenergetics*. 1861 (2), 148117, 2020.

Affiliations:

1. *Laboratory of Physics of Living Matter, Ecole Polytechnique Fédérale de Lausanne (EPFL), CH-1015 Lausanne, Switzerland*
2. *Department of Biophysics, Institute of Physics, Maria Curie-Skłodowska University, 20-031 Lublin, Poland*

Abstract. The xanthophyll cycle is a regulatory mechanism operating in the photosynthetic apparatus of plants. It consists in the conversion of the xanthophyll pigment violaxanthin to zeaxanthin, and vice versa, in response to light intensity. According to the current understanding, one of the modes of regulatory activity of the xanthophyll cycle may be associated with the influence of violaxanthin and zeaxanthin on a molecular organization of pigment-protein antenna complexes in the photosynthetic membranes, and indirectly on photoprotective quenching of excitation energy excess. In the present work, we analyzed the effect of violaxanthin and zeaxanthin on the molecular organization of light-harvesting complex II (LHCII), the largest photosynthetic antenna pigment-protein complex of plants, in the environment of membranes formed with chloroplast lipids. Nanoscale imaging based on atomic force microscopy (AFM) showed that the presence of exogenous xanthophylls promotes the formation of the protein supramolecular structures substantially different from those formed in the absence of xanthophylls. Nanoscale infrared (IR) absorption spectral analysis, performed with the application of AFM-IR nanospectroscopy, on such LHCII architectures suggests that zeaxanthin links LHCII antenna to supramolecular structures and maintains the stability by forming inter-molecular β -structures. Meanwhile, the molecules of violaxanthin act as “molecular spacers” preventing self-aggregation of the protein, potentially leading to uncontrolled dissipation of excitation energy of LHCII-bound chlorophylls. This latter mechanism was demonstrated with the application of fluorescence lifetime imaging microscopy (FLIM). The intensity-averaged chlorophyll *a* fluorescence lifetime determined in the LHCII samples without exogenous xanthophylls at the level of 0.72 ns was

substantially higher in the samples containing exogenous violaxanthin (2.14 ns). On the other hand, in the case of the structures formed under the presence of zeaxanthin the average lifetime was even lower (0.49 ns) thus suggesting a role of this xanthophyll in promotion of the formation of the supramolecular structures characterized by effective chlorophyll excitation quenching. This mechanism can be considered as a representation of the overall photoprotective activity of the xanthophyll cycle.

3.1 Introduction

Life on the Earth is fueled by sunlight and photosynthesis is practically the sole mechanism that enables conversion of the energy of electromagnetic radiation to the forms that can be directly used to drive biochemical reactions in living cells. The fact that photosynthesis should function effectively in an environment characterized by extreme changes in light intensity, e.g. owing to the day-night cycle, has become a source of evolutionary challenge towards the creation of regulatory strategies adjusting the density of excitations in the photosynthetic apparatus to the current possibilities of photochemical reactions¹⁶⁷.

One of the mechanisms operating in higher plants and green alga, which is believed to belong to such a class of regulatory processes, is the xanthophyll cycle¹⁶⁸. The xanthophyll cycle comprises the light-intensity-controlled enzymatic reactions leading to de-epoxidation of violaxanthin to zeaxanthin and the reactions in the opposite direction¹⁶⁸. Importantly, violaxanthin is accumulated in the photosynthetic apparatus exposed to low light intensity while accumulation of zeaxanthin is characteristic to plants which experience high-light-induced overexcitation¹⁶⁸. Such an observation implies that the xanthophyll cycle can be an element of the overall response of the photosynthetic apparatus to variable light intensity, in particular to strong light, as illustrated in Figure 3.1. It has to be stressed that such a regulatory activity is vital to plants as an element of the photoprotective defense strategy against oxidative photo-damage. This is due to the three major reasons: (i) the photosynthesizing organisms are evolutionary-adopted to absorb effectively light quanta, (ii) chlorophyll is an extremely efficient photosensitizer able to generate the singlet oxygen, and finally (iii) due to the fact that molecular oxygen is just generated in the photosynthetic apparatus of plants, via water splitting. The fact that the mutant plants lacking the violaxanthin de-epoxidase enzyme are substantially less resistant to high light provides a strong support for such an argumentation¹⁶⁹.

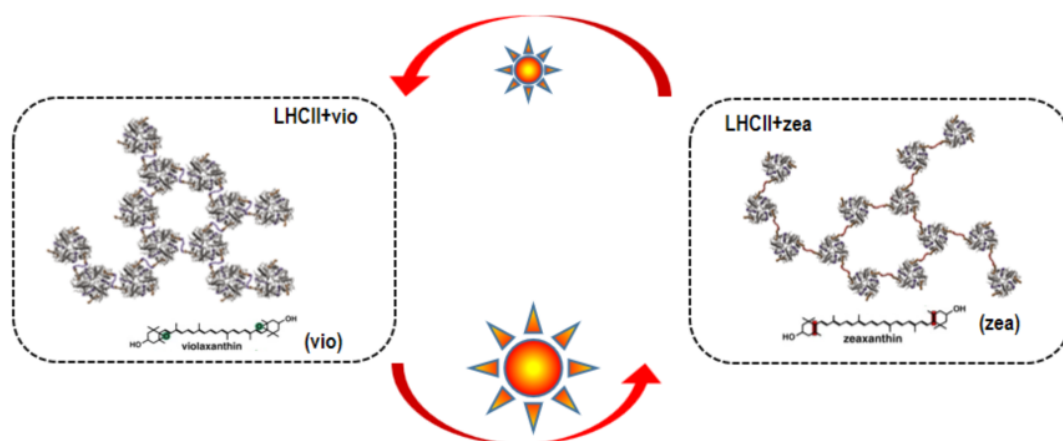


Figure 3.1 Schematic of the xanthophyll cycle under both low and strong light intensity. The xanthophyll cycle comprises the light-intensity-controlled enzymatic reactions leading to de-epoxidation of violaxanthin to zeaxanthin and the reactions in the opposite direction¹⁶⁸. The effect of violaxanthin and zeaxanthin will then modulate the molecular organization of LHCII in the environment of membranes formed with chloroplast lipids.

There are several concepts regarding molecular mechanisms via which the xanthophyll cycle pigments are involved in the photoprotective activity. One of the popular mechanisms implies a direct chlorophyll excitation quenching via zeaxanthin, realized by the singlet-singlet excitation energy transfer between the Q_y and the S_1 ($^1A_1^g$) states¹⁷⁰. Another mechanism involves excessive chlorophyll excitation quenching by the low-energy traps of the zeaxanthin cation radicals¹⁷¹. An alternative concept is based on possible structural modification of the pigment-protein complexes by xanthophylls or xanthophyll-controlled reorganization of the antenna protein network^{172–176}.

In the present work, we explore the latter mechanism via addressing the problem of possible effect of the xanthophyll cycle pigments on molecular organization of the largest photosynthetic antenna complex in plants LHCII, in the environment of the bilayer formed with the chloroplast lipids. In addition to the fluorescence lifetime imaging microscopy, we applied high-resolution AFM phase imaging, as well as a novel hybrid technique combining AFM and infrared (AFM-IR) nanospectroscopy^{13,155}, in order to get insight into molecular mechanisms involved in this regulation. These AFM technologies are nowadays widely used in studying and manipulating the biological species¹⁷⁷, protein-lipid membrane and other intermolecular interactions at the nanoscale^{178–180}. Our results reveal that the xanthophyll cycle pigments, both violaxanthin and zeaxanthin, promote the formation of the protein supramolecular structures, yet show significant difference in the molecular organization of LHCII complexes and their photophysical properties in the environment of lipid membranes. Violaxanthin prevents the self-aggregation of the protein, potentially leading to uncontrolled dissipation of excitation energy of LHCII-bound chlorophylls. However, zeaxanthin promotes the formation of the

aggregated LHCII supramolecular structures characterized by effective chlorophyll excitation quenching. By controlling the supramolecular organization of LHCII, the particular regulatory activity of xanthophyll cycle is formed in the photosynthetic apparatus of the plants.

3.2 Experimental methods

Sample preparation

Monogalactosyldiacylglycerol (MGDG) and digalactosyldiacylglycerol (DGDG) were purchased from Larodan. n-Dodecyl- β -D-maltoside (DM), Tricine and KCl were obtained from Sigma-Aldrich. Crystalline all-*trans* zeaxanthin was purchased from Extrasynthese. Light harvesting pigment-protein complex LHCII was isolated from fresh spinach (*Spinacia oleracea* L.) leaves, as described previously.¹⁸¹ All-*trans* violaxanthin was isolated from *Narcissus jonquilla* L. flowers and purified using the HPLC technique. Xanthophyll purification was carried out using C-18 coated, phase-reserved column (YMC GmbH, Germany, length 250 mm, internal diameter 4.6 mm). A mixture of acetonitrile/methanol/water (72:8:3, v/v/v) was used as mobile phase and elution rate was 0.8 ml/min. All xanthophylls were repurified chromatographically directly before sample preparation.

LHCII-lipid membranes were prepared according to the procedure elaborated and tested previously¹⁸². MGDG and DGDG were dissolved in chloroform (molar ratio of MGDG to DGDG was 2:1). The LHCII complexes were suspended in 20 mM Tricine and 10 mM KCl buffer, pH 7.6, containing 0.03% DM. The mixture of lipids was transferred to glass test tubes and placed in a vacuum (<10⁻⁵ bar) for 30 min. Xanthophyll pigments were dissolved in ethanol and added to the lipid mixture at the beginning of evaporation. The molar ratio of zeaxanthin or violaxanthin to LHCII monomers was 1:1. LHCII complexes were transferred to lipid film and incorporated into lipid membranes through mild sonication in an ultrasonic bath for 30 min. The molar ratio of LHCII complexes to lipids was 1:100. In order to remove detergent molecules, the sample was incubated with Bio-beads adsorbent (from BioRad) at 4°C for 12 h. Multilayers of LHCII and lipid were separated from the sample by centrifugation at 15 000g for 5 min. Next, the pellet was resuspended in 20 mM Tricine and 10 mM KCl buffer.

AFM measurements

An aliquot (20 μ l) of lipoprotein suspension with/without exogenous xanthophyll pigments was deposited on freshly cleaved mica surface at the room temperature and was dried in the vacuum desiccator overnight to enable lipid membranes stacking and forming multilayers containing chloroplast lipid and LHCII complex on the substrate. AFM scanning was operated with Park NX10 (Park Systems, South Korea) in the tapping mode. The cantilevers PPP-NCHR (Park Systems, South Korea) with a nominal spring constant of 42 N/m and a typical tip radius of 7 nm were used. The AFM images were scanned with a resolution of 512 \times 512 or 1024 \times 1024 pixels at a rate of 1 Hz. In order to avoid the defects and imperfections, a regime of weak tip-sample interaction was employed during the scanning by monitoring the tip dithering phase shift within a variation of 5 degrees in the negative region. AFM phase images were untreated, and height images were simply flattened using XEI software (Park Systems) in the first order to minimize potential flatten-induced defects on the images.

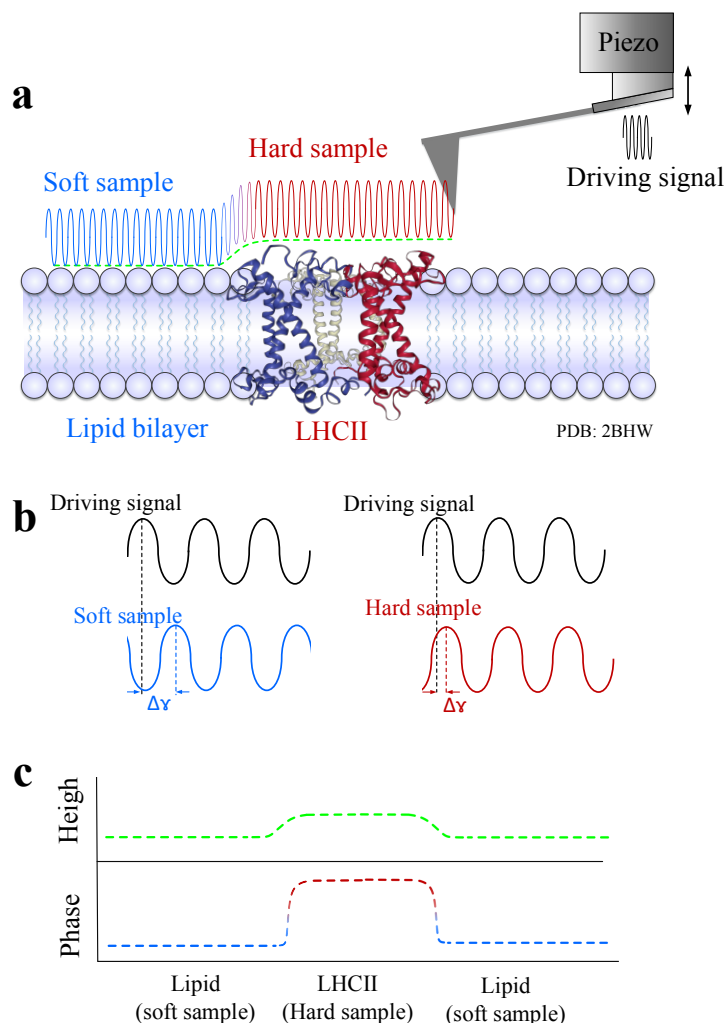


Figure 3.2 Schematic of AFM experiment of LHCII on the lipid bilayers. (a) The principle of the tapping mode imaging. The AFM cantilever is excited to oscillate with a constant amplitude being driven by a piezo to which a sinusoidal signal at around 330 kHz is applied. The scanning with a small interaction force is performed on the lipid bilayer (blue) and embedded LHCII protein (orange) from left to right. The scanned height profile (dashed green line) of the lipid-protein bilayer is barely distinguishable between lipid and protein regions. (b) The phase shift between the driving signal (black) and the AFM-recorded signal on the stiff sample (orange) and on the soft sample (blue). This phase shift changes depending on the sample stiffness and viscous properties. (c) The comparison of the scanned profile on height (up) and phase-contrast (bottom) images. It shows much better distinguishable difference between lipid and LHCII protein on the phase-contrast image.

AFM-IR spectroscopy

An aliquot (20 μ l) suspension of lipoprotein, lipoprotein with violaxanthin and lipoprotein with zeaxanthin, was deposited on the hydrophobic ZnSe single crystal prism at the room temperature. After that, the samples were dried in the vacuum desiccator overnight, and thus the antenna-contained lipid membranes were stacked forming lipoprotein multilayers on ZnSe surface. The islands of the lipoprotein multilayer samples were selected and measured by NanoIR system (Anasys Instruments Inc., USA) that combines AFM and infrared spectroscopy measurements. The AFM scanning was performed in the contact mode with a soft cantilever EX-C450 (Anasys) having a spring constant of ~ 0.2 N/m. The AFM height and IR absorption images were recorded in 5×5 μ m area with a resolution of 512×512 pixels and 8 co-averages at the rate of 0.2 Hz. Each spectrum was collected at a selected position on the AFM image of the sample with the spectral resolution of 1 cm^{-1} and 128 co-averages within the range of 1200 - 1800 cm^{-1} to ensure its reliability. The final spectra were averaged from more than five recorded spectra and no smoothing

process was applied to spectra in order to avoid the potential artifacts. Further processing was realized using Analysis Studio and Origin software.

FLIM measurements

FLIM measurements were performed using a confocal MicroTime 200 (PicoQuant, Germany) system coupled to an inverted microscope OLYMPUS IX71. The samples were excited by a picosecond, 470 nm pulse laser with a repetition rate of 20 MHz. The lifetime resolution was better than 16 ps. Photons were collected with a 60x water immersed objective (NA 1.2, OLYMPUS UPlanSApo). The single focal plane was selected with a pinhole diameter of 50 μm . The scattered light was removed using dichroic ZT473RDC XT (Analysentechnik), 470 notch filter (Chroma Technology) and observation were made through the addition of 630 long pass filter (Semrock). Results of measurements were analyzed using SymPhoTime 64 software.

3.3 Results and discussion

AFM characterization of the architecture of lipid bilayers and LHCII proteins

AFM height imaging is the most widely used AFM technique in many applications as it provides morphological image with a high spatial resolution. However, for the samples with slight topological difference, such as the LHCII embedded in the lipid bilayer (Figure 3.2a), distinguishing their features on the height images becomes challenging. Meanwhile, AFM phase-contrast imaging, which is sensitive to the sample stiffness and adhesion, are also known to give valuable information in analyzing samples, such as polymers, composites and surface coatings, especially those with similar topography¹⁸³⁻¹⁸⁸. This is due to the circumstance that, for the oscillating AFM cantilever excited by the driving piezo (Figure 3.2a) in the tapping mode, different visco-elastic properties of samples result in different tip-sample interactions, shifting accordingly the phase of the cantilever oscillation with respect to the exciting signal (Figure 3.2b). This phase variation can be recorded as the phase-contrast image, that provides more distinguishable contrast between species, especially for those with slightly different topology, than the height image (Figure 3.2c), for analyzing species with different rigidities and mechanical properties¹⁸⁷. Nowadays the phase-contrast imaging becomes an important approach for compositional characterization¹⁸⁸ and high-resolution imaging in the biological field¹⁸⁵.

The surface morphology and phase-contrast AFM images of lipoprotein multilayers in the absence and presence of xanthophylls in our experiments are shown in Figure 3.3 and Figures 3.4-3.5 respectively. although the embedded LHCII have only minimal topological differences with lipid bilayers, the visco-elastic differences between lipid and LHCII protein result in sufficient phase variations enabling to identify them (Figure 3.3b-c). Moreover, our experiments demonstrate that the architecture of such structures is dependent on the presence of xanthophylls, either violaxanthin or zeaxanthin.

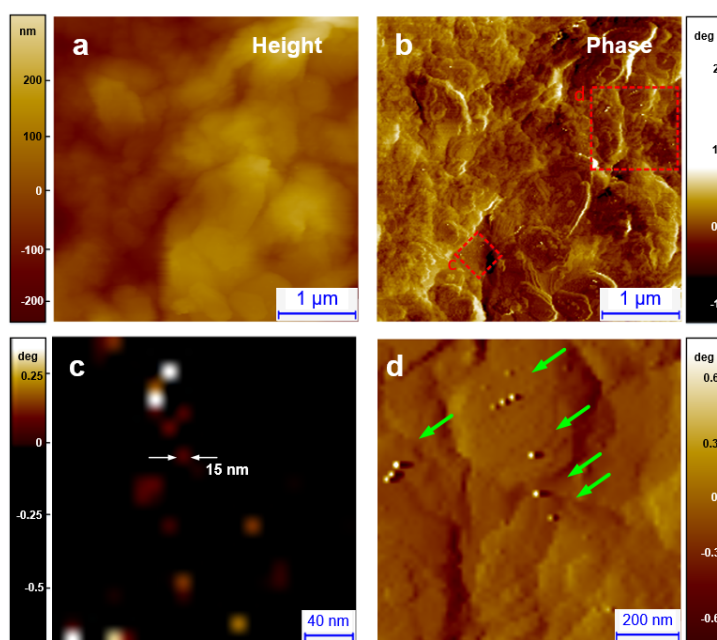


Figure 3.3 AFM measurement on LHCII protein. AFM height (a) and phase-contrast (b) images of the lipid bilayer and LHCII proteins. (c-d) The zoomed images of the particular regions in the phase-contrast image are presented, indicating the evidence of the existence of trimeric LHCII protein indicated by green arrows. From these images, it is indicated that the size of individual LHCII structure is approximately 10-20 nm.

Figure 3.3 presents the LHCII-lipid samples formed in the absence of exogenous xanthophylls. Individual light-harvesting antennas were seen in the phase image (Figure 3.3b). Two specific areas on this image are highlighted in Figures. 3.3c-d, where individual antennas are indicated. It can be seen that the size of the LHCII antenna (Figure 3.3c) is of the same order as LHCII trimers reported in the literature^{189,190}.

AFM height and phase images of the LHCII-lipid multilayers in the presence of violaxanthin are shown in Figure 3.4a-b. Instead of individual proteins, a large number of LHCII supramolecular structures were observed on the phase-contrast image, as indicated by the green arrows in Figure 3.4b. According to the detailed images of these assembled LHCII antennas in Figure 3.4c-d, where the macromolecular organization can be easily seen, these supramolecular structures are believed to be the assemblies of individual LHCII trimers. These LHCII supramolecular structures exhibit heterogeneous shapes, showing a normal dimension in the order of tens of nanometers, and the individual LHCII trimeric structures exhibit a diameter of around 10 nm, in the agreement with that presented in Figure 3.4c. The ability of formation of 2D supramolecular structures of LHCII on a solid support (25-150 nm width), also in the environment of lipids, was recently demonstrated with application of AFM technique¹⁹¹.

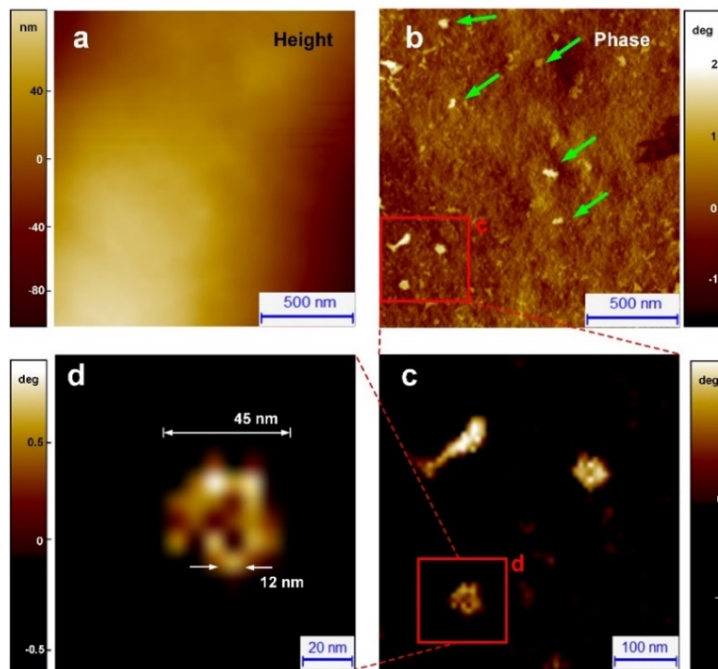


Figure 3.4 AFM measurement on LHCII protein in the presence of the violaxanthin. AFM height (a) and phase-contrast (b) images of the lipid bilayer and LHCII in presence of the violaxanthin. Green arrows indicate the location of the LHCII supramolecular structures. The zoomed images (c-d) reveal that the size of these LHCII supramolecular structures is of the order of tens of nanometers, and the size of individual LHCII trimeric subcomponent is around 10 nm. The macromolecular organization of LHCII supramolecular structures can be seen on these phase images.

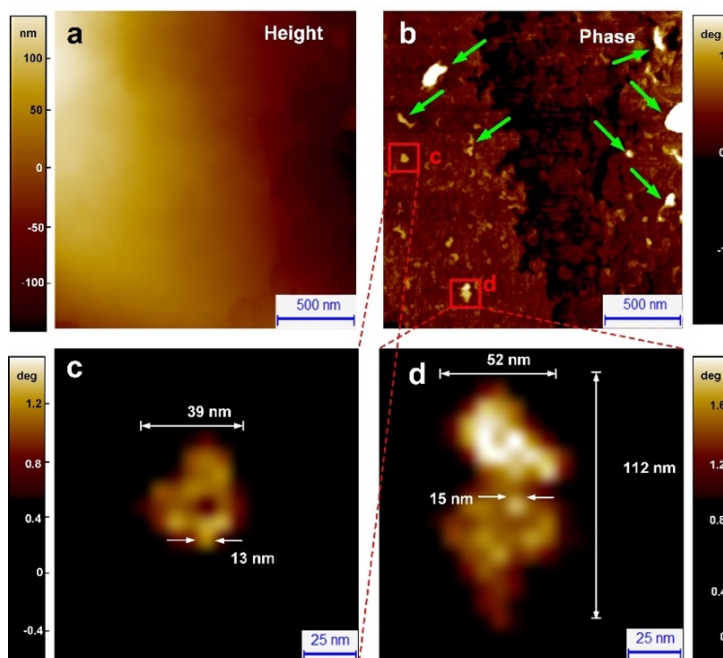


Figure 3.5 AFM measurement on LHCII protein in the presence of the zeaxanthin. AFM height (a) and phase-contrast (b) images of lipid bilayer and LHCII protein in presence of the zeaxanthin. Green arrows indicate the location of LHCII super-complexes. The zoomed phase images (c-d) from the regions identified in the phase-contrast AFM image reveal that oligomeric LHCII supramolecular structures have the sizes ranging from tens to up to one hundred nanometers.

The AFM morphology and phase images of the lipoprotein multilayers formed in the presence of zeaxanthin are exhibited in Figure 3.5a-b while the close shots of particular LHCII supramolecular structures are showed in Figure 3.5c-d. From these images, plenty of supramolecular structures of the light-harvesting antenna are observed on the phase-contrast images (Figure 3.5b). These heterogeneous LHCII assemblies on the chloroplast lipid membranes exhibit the sizes ranging from a few tens to a few hundreds of nanometers (Figure 3.5b), while the diameter of the single LHCII trimer agrees with the previous observations.

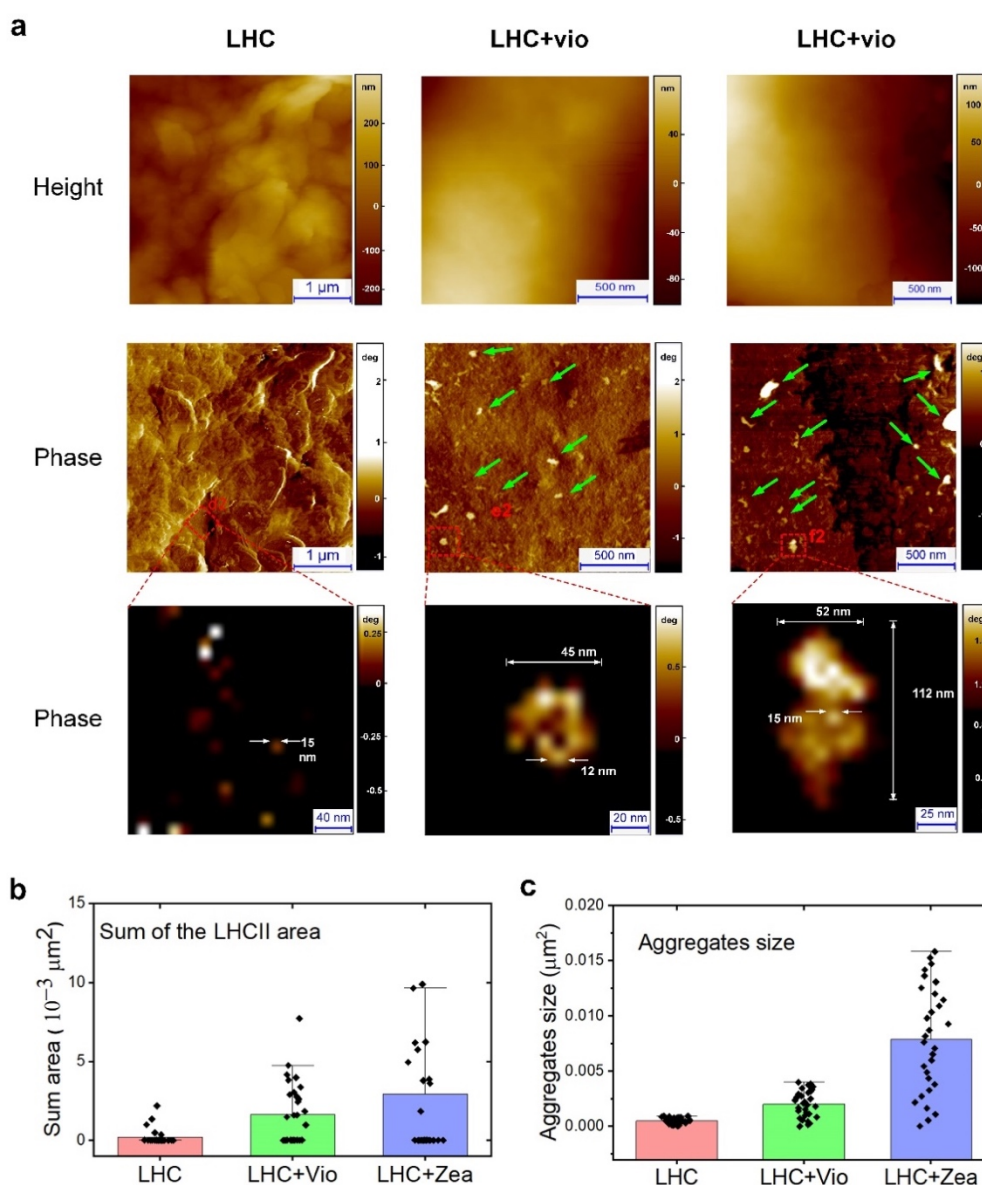


Figure 3.6 The morphological comparison of LHCII in the presence/absence of the xanthophylls. (a) The comparison of the AFM height and phase images among the LHCII, LHCII and violaxanthin, and LHCII and zeaxanthin conditions. The size of the LHCII supramolecular structure are noted. The individual LHCII proteins are seen in the case of LHC II independently, while intermediate size of LHCII supramolecular structure is observed in the case with the presence of violaxanthin and larger supramolecular structure can be seen in the case with zeaxanthin. (b-c) The statistical analysis on the sum area and aggregates size of the supramolecular structures.

Comparison of the images presented in Figures 3.3-3.5 clearly reveals that exogenous xanthophylls influence the molecular organization of LHCII protein in the bilayer membranes. In general, it can be concluded that both violaxanthin and zeaxanthin promote the formation of certain supramolecular LHCII structures observed in largely homogenous protein-lipid phase. The statistical analysis (Figure 3.6) shows that the size of the LHC supramolecular assemblies obtained in the presence of zeaxanthin is generally larger than that yielded in the case of violaxanthin.

AFM-IR nanospectroscopic characterization of LHC proteins

Although our high-resolution AFM measurements show that xanthophylls are capable of assembling LHCII antenna into supramolecular structures, their formation mechanism and possible structural modification of LHCII proteins by xanthophylls are still unknown. Similarly, it remains difficult to identify specific molecular differences of the LHCII supramolecular structures formed in the presence of violaxanthin and zeaxanthin. To study these aspects, we performed the AFM-IR nanospectroscopic measurements¹³. As shown in the schematic (Figure 3.7a), a tunable pulsed infrared laser illuminates the sample and excites certain molecular vibrations by absorbing radiation at particular wavelengths. The absorbed radiation energy rapidly results in the localized thermal expansion of the sample which can be detected by measuring the dithering of AFM cantilever¹¹. Additional details can be found in our previous reports^{40,163,192} and in the Method section.

In the AFM-IR measurement, either IR absorption map in nanoscale or the absorption spectrum at a specific location can be obtained. The IR absorption fingerprints can be used to identify the molecular structures by applying the multi-compositional analysis. For the lipids formed bilayer membranes, typical molecular vibrational transitions are the ester carbonyl group stretching, with the absorption bands in the 1750-1700 cm^{-1} region. For proteins and polypeptides, there are three typical absorption bands (amide I, II and III) but the most informative band for an analysis of the secondary structure and molecular organization of proteins is the amide I, ranging from 1700 to 1600 cm^{-1} . This amide I band combines the C=O stretching, N-H bending and C-N stretching vibration modes, and the combination of them can be used to characterize several basic secondary structures such as α -helical structure (1645-1665 cm^{-1}) and inter/intra-molecular β -structure (1695-1680 and 1635-1615 cm^{-1})¹⁹³. On the IR absorption map (Figure 3.7b), the yellow and red regions represent the accumulation of LHCII proteins. We can see a homogenous distribution of individual LHCII proteins on the lipid membrane in the absence of xanthophylls. However, these LHCII complexes form supramolecular structures which are distributed heterogeneously within the lipid multibilayers in the presence of xan-

thophylls. This suggests again that the xanthophylls are capable of assembling individual LHCII proteins. A stronger absorption was observed on the IR absorption map in the presence of zeaxanthin than that in the case of violaxanthin, indicating that zeaxanthin possesses the stronger ability to assemble LHCII proteins than violaxanthin, which agrees the result on the AFM phase-contrast images.

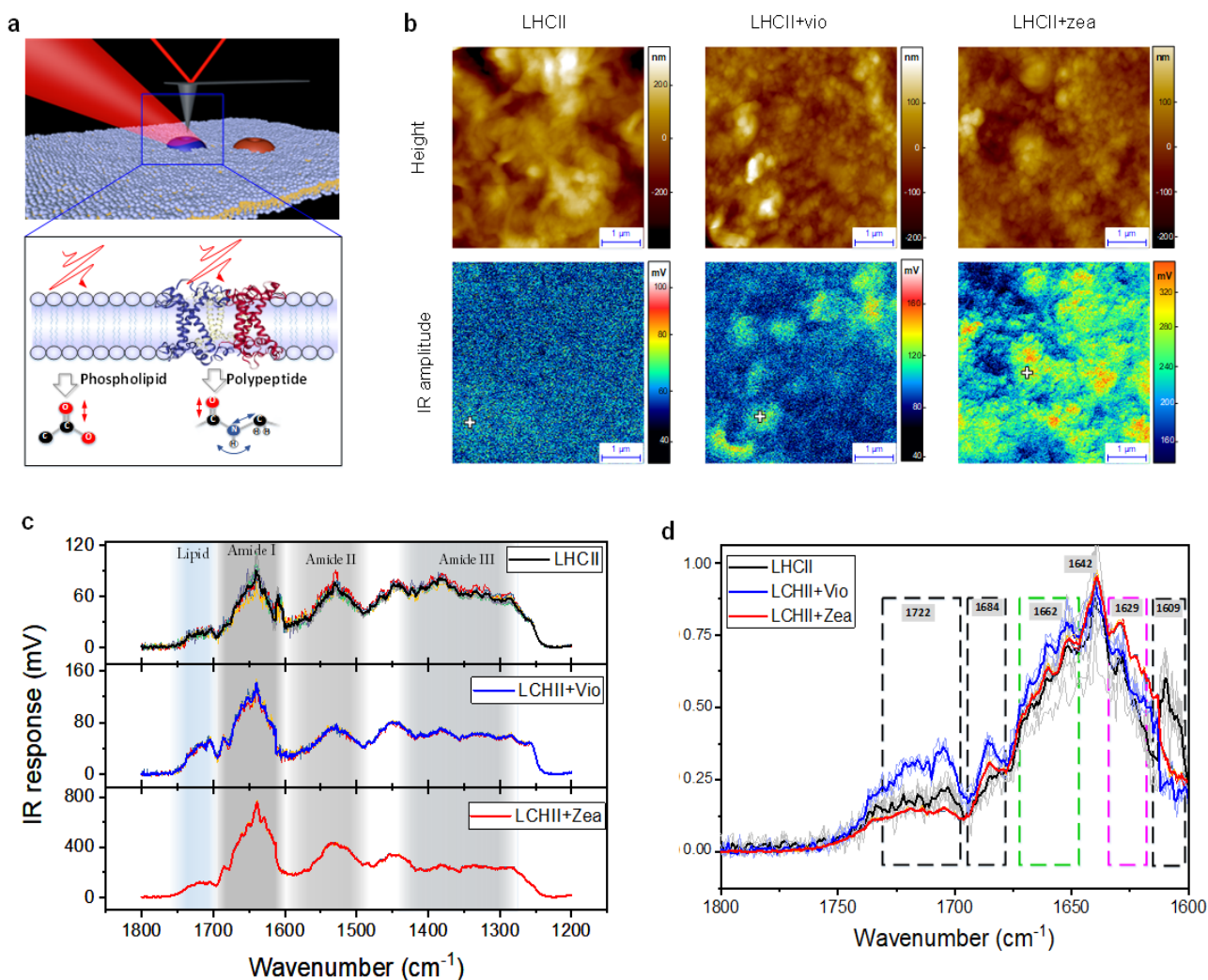


Figure 3.7 AFM-IR characterization of the lipoprotein multilayers in the presence/absence of the xanthophylls. (a) Schematics of the AFM-IR nanospectroscopy. The incident IR radiation is absorbed by the investigated sample at certain wavenumber, inducing the molecular vibrations and photothermal expansion. This local thermal expansion can be detected by the AFM, providing either an IR absorption map or the absorption spectrum at a specific location. (b) The surface morphology images and IR absorption (1645 cm^{-1}) maps of lipoprotein multilayer, consisting of chloroplast lipids and the antenna complex LHCII, in the absence of xanthophylls (left) as well as in the presence of violaxanthin (middle) or zeaxanthin (right). (c) The infrared absorption spectra of the lipoprotein multilayers in the absence of xanthophylls (top), as well as in the presence of violaxanthin (middle) or zeaxanthin (bottom). The spectra ranging $1200\text{--}1800\text{ cm}^{-1}$ were recorded at the locations noted by the cross on the IR absorption maps. The blue area indicates the region of lipid absorption band, while the grey areas indicate the regions of protein amide bands on the IR absorption spectrum. (d) The normalized IR absorption spectra in the protein amide I region ($1600\text{--}1700\text{ cm}^{-1}$), and in the lipid component region ($1700\text{--}1800\text{ cm}^{-1}$). The spectra correspond to the lipid-LHCII multilayers in the absence of xanthophylls (black) and in the presence of violaxanthin (blue) or zeaxanthin (red), showing the conformational differences of LHC supramolecular and lipid structure. The final spectra were averaged from several spectra (grey) and each spectrum was recorded with 128 co-average to ensure its reliability. No smoothing process was applied to minimize the potential artifacts. The magenta dashed frames indicate the bands of β -structural absorption, and green dashed frame refers to the helical absorption region.

The IR absorption spectra of lipoprotein multilayers (Figure 3.7c-d) in both cases, visible in the absence and in the presence of xanthophylls, show two main absorption fingerprint peaks at 1642 and 1722 cm^{-1} . These peaks attest the existence of α -helix-rich domains of LHCII protein and lipid component respectively. This evidence suggests that the xanthophylls assemble LHCII proteins into supramolecular structures, without substantially affecting the secondary structure of lipoprotein embedded in the multilayer.

Figure 3.7d attests that the absorption spectra of lipoprotein multibilayers without xanthophylls (black) and with violaxanthin (blue) are generally overlapped in the range 1650-1610 cm^{-1} . We also found the appearance of a small but noticeable absorption peak at 1629 cm^{-1} in the spectra of lipoprotein multibilayers with zeaxanthin (red). This indicates that zeaxanthin, formed under strong light conditions, links LHCII antenna and maintains the stability of their supramolecular structures by forming inter-molecular β -structures. Such structures can be involved in the formation of quenching centers in the case of excessive excitation, and protect the photosynthetic apparatus against photo-damage. These aggregated structures are not present in the case of violaxanthin (1629 cm^{-1}), which although slightly promotes helical conformation (1662 cm^{-1}), suggesting that violaxanthin is capable of linking LHCII trimers into supramolecular structures and maintaining their native conformational structure of LHCII complex in the supramolecular organization. Thus we believe that violaxanthin packs the LHCII trimers in order to prevent the formation of aggregated structures that potentially may lead to uncontrolled excitation quenching. This may be considered as one of the reasons why violaxanthin is accumulated in the photosynthetic apparatus under low light conditions.

Comparing the spectrum of lipoprotein multibilayers in the presence of zeaxanthin (red) with other spectra, we also see a decrease of absorption at 1722 cm^{-1} . This is due to the circumstance that for this case there are more proteins over lipids on the lipoprotein multilayer in the region of supramolecular structures probed under AFM tip.

Another important observation is the presence of relatively intensive subband, centered at 1609 cm^{-1} in the amide I spectral band, exclusively in the samples formed by lipids and LHCII, without exogenous xanthophylls. Since this particular sub-band can be assigned to the well-ordered molecular aggregated forms of protein, we can conclude that both violaxanthin and zeaxanthin prevent the formation of such structures. Such an effect can be referred to as a “molecular spacer” activity of the xanthophyll cycle pigments protecting against the formation of nonspecific aggregates of LHCII within the membrane, potentially leading to uncontrolled excitation quenching.

FLIM characterization of LHCII embedded in lipid membranes

In order to address the question regarding the possible effect of the xanthophyll-determined molecular organization of LHCII in the lipid membrane environment on photophysical properties of the protein bound chlorophylls, we additionally applied imaging technique based on fluorescence lifetime measurements.

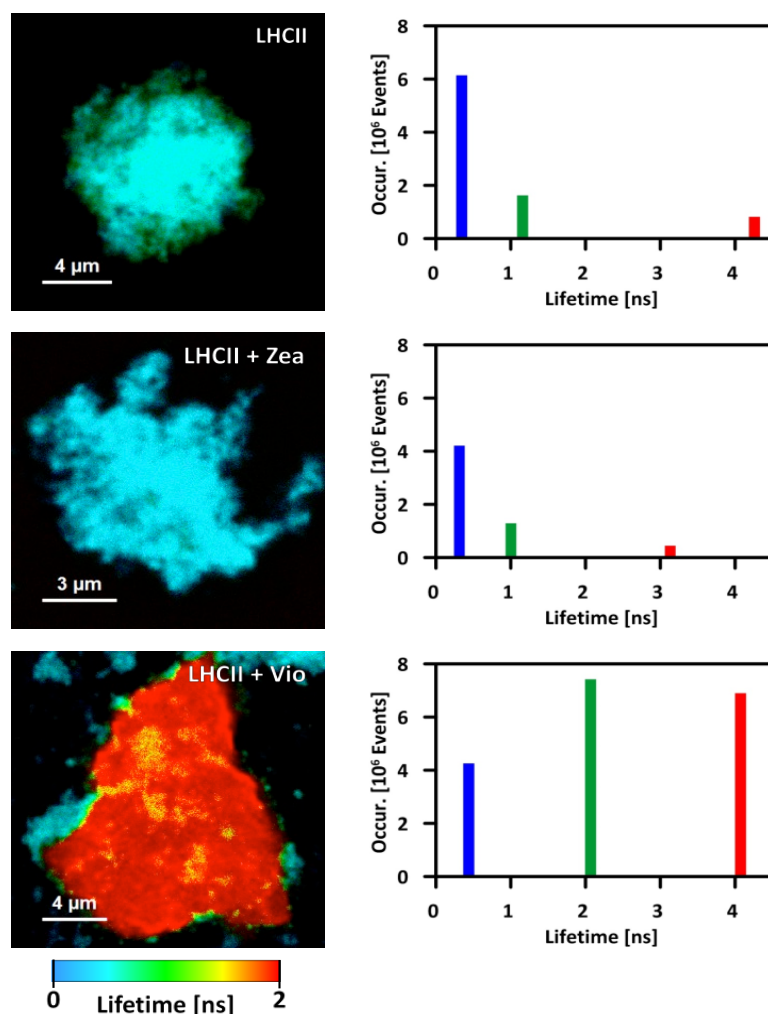


Figure 3.8 FLIM analysis of the LHCII-lipid membrane fragments. Samples were formed in the absence of exogenous xanthophylls (marked as LHCII) and in the presence of exogenous zeaxanthin (LHCII+Zea) or exogenous violaxanthin (LHCII+Vio). Colour codes in images represent FLIM analysis of fluorescence lifetimes. The histograms in the right-hand panel represent the results of the quantitative analysis of fluorescence lifetime components and their amplitudes applied to the images present in the left-hand panel.

FLIM images of the LHCII-lipid membrane fragments (Figure 3.8) show a profound effect of exogenous xanthophylls on fluorescence lifetime of chlorophyll *a* being a constituent of LHCII. Relatively short intensity-averaged fluorescence lifetime (0.72 ns, expressed by green color code) can be observed in the sample formed without exogenous xanthophylls. Very similar lifetimes, in the 0.6-0.9

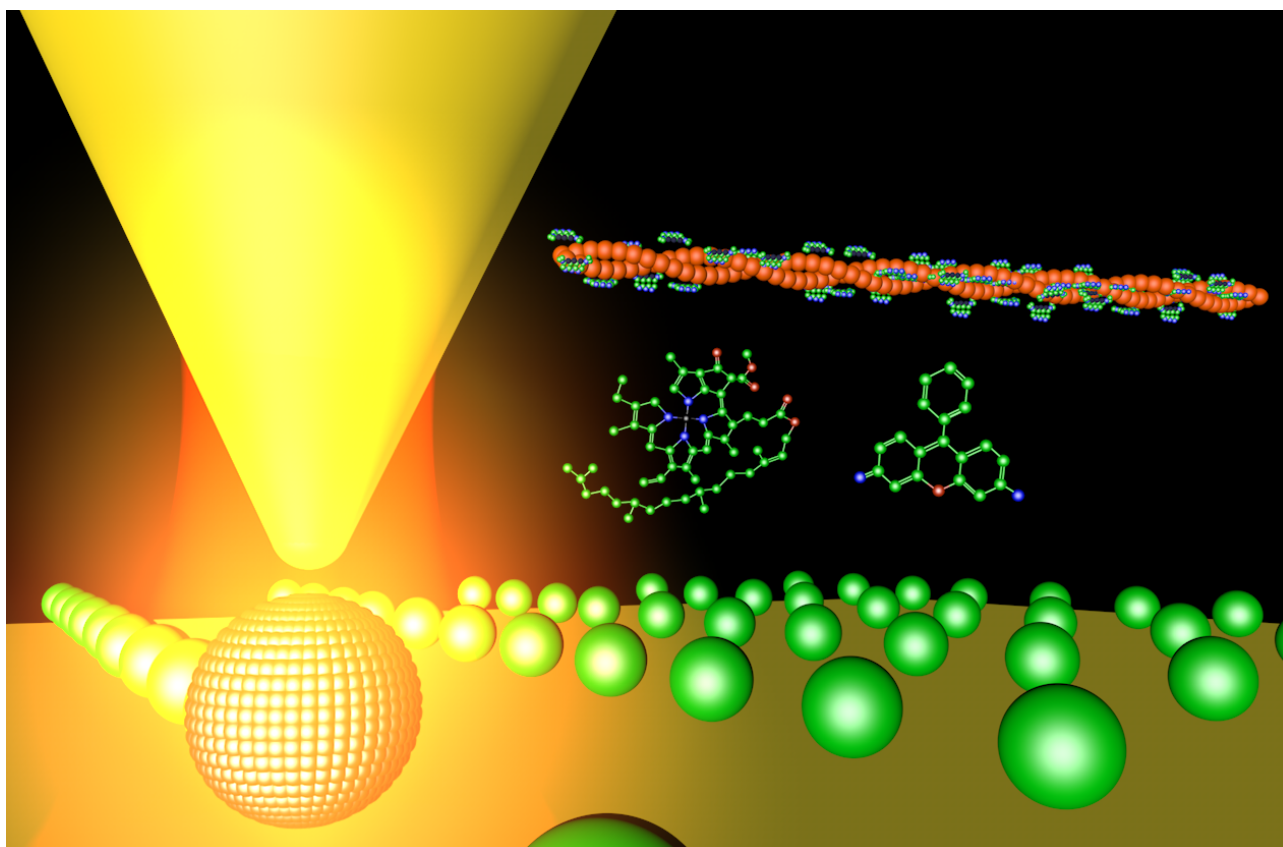
ns range, have been reported for LHCII complexes self-assembled into the 2D-structures in the lipid environment.²⁷ Such a result is consistent with the formation of aggregated structures of LHCII, concluded on the basis of the IR nanospectroscopy of the same samples. Interestingly, the supramolecular structures formed in the presence of zeaxanthin are characterized by even lower fluorescence lifetimes and therefore excitation quenching rates (0.49 ns, expressed by blue color code). Importantly, the supramolecular structures formed in the presence of violaxanthin are characterized by relatively long fluorescence lifetimes (2.14 ns, expressed by red color code). Such a pronounced difference between the effect of violaxanthin and zeaxanthin implies a role of the xanthophyll cycle pigments in shifting the excitation energy dissipation yield towards higher values, under strong light conditions, and towards lower values under low light conditions. The activity of violaxanthin can be interpreted in terms of a “molecular spacer” inhibiting the formation of aggregated structures of LHCII leading to excitation quenching. The picture seems to be more complicated in the case of zeaxanthin. On the one hand, zeaxanthin inhibits self-assembly of LHCII that can be observed in the lipid phase without exogenous carotenoids but, on the other hand, it stabilizes supramolecular structures of LHCII characterized by exceptionally efficient thermal excitation energy dissipation. The question whether such excitation quenching is based upon direct chlorophyll excitation quenching by zeaxanthin (including zeaxanthin cation radical) or is a consequence of the specific molecular organization of the antenna complexes remains open and is to be addressed in future studies. Independently of a current mechanism, the results presented in this work show that the first step of control of regulatory excitation quenching in LHCII, based on zeaxanthin, relays on stabilization of the specific supramolecular structures. This conclusion harmonizes with the findings that in the mechanism of the zeaxanthin-dependent excitation quenching zeaxanthin is acting in between the complexes, helping to create quenching sites¹⁷⁶.

3.4 Conclusion

The results of the combined analysis based on nanoscale AFM imaging, IR nanospectroscopy and fluorescence lifetime imaging microscopy lead to the conclusion that the xanthophyll cycle pigments significantly influence the molecular organization of LHCII in the environment of lipid membranes. Violaxanthin and zeaxanthin promote the formation of the protein supramolecular structures presenting substantially different photophysical properties. Violaxanthin assembles the LHCII proteins while preserving their native conformation in the supramolecular organizations, but zeaxanthin promotes the formation of larger LHCII supramolecular structures with forming aggregated structures in the meantime. The LHCII structures formed in the presence of zeaxanthin are characterized by relatively short fluorescence lifetimes of the protein-bound chlorophyll *a*, indicative of effective excitation

quenching. The opposite effect on excitation quenching can be observed in the LHCII structures formed in the presence of violaxanthin. The results point to a regulatory activity of the xanthophyll cycle, aimed at the adjustment of excitation density in the antenna systems to the capacity of photosynthetic energy conversion. According to the results of the present work, this particular regulatory activity is realized via control of the supramolecular organization of LHCII.

Chapter 4 Gap-plasmon enhanced Photo-Thermal Induced Resonance (PTIR)



This chapter is based on a published work in the journal *Nano Letters*, with the following information:

Jiangtao Zhou, Anton Smirnov, Giovanni Dietler* and Sergey Sekatskii*. **Gap-Plasmon-Enhanced High-Spatial-Resolution Imaging by Photothermal-Induced Resonance in the Visible Range.**

Nano Lett. 19(11), 8278-8286, 2019.

Affiliations:

*Laboratory of Physics of Living Matter, Ecole Polytechnique Fédérale de Lausanne (EPFL),
CH-1015 Lausanne, Switzerland*

Abstract: Chemical characterization at the nanoscale is of significant importance for many applications in physics, analytical chemistry, material science, and biology. Despite the intensive studies in the infrared range, high-spatial-resolution and high-sensitivity imaging for compositional identification in the visible range is rarely exploited. In this work, we present a gap-plasmon-enhanced imaging approach based on photothermal-induced resonance (PTIR) for nanoscale chemical identification. With this approach, we experimentally obtained a high spatial resolution of ~ 5 nm for rhodamine nanohill characterization and achieved mono-layer sensitivity for mapping the single-layer chlorophyll-a islands with the thickness of only 1.9 nm. We also successfully characterized amyloid fibrils stained with methylene blue dye, indicating that this methodology can be also utilized for identification of the radiation-insensitive macromolecules. We believe that our proposed high-performance visible PTIR system can be used to broaden the applications of nanoscale chemical identification ranging from nanomaterial to life science areas.

4.1 Introduction

Nanoscale chemical identification and imaging play a key role in quite various applications spanning the areas of physics, analytical chemistry, material and biological sciences^{13,52,194}. Localized detection of light-matter interaction is one of the most efficient non-destructive and label-free approaches to achieve this, and different related techniques have been developed in this direction, such as scattering near-field scanning optical microscopy (s-NSOM)¹⁹⁵, tip-enhanced Raman spectroscopy (TERS)¹⁹⁶, infrared-mass combined spectrometry¹⁹⁷ and X-ray microscopy¹⁹⁸. Among them, the recently developed Photothermal Induced Resonance (PTIR), which utilizes Atomic Force Microscopy (AFM) to detect the radiation-induced photothermal expansion of investigated sample under the AFM tip, is

currently attracting more and more interest due to its advantages in signal-to-noise ratio (SNR) and spatial resolution^{13,40,155,161,199,200}.

In infrared range, the electromagnetic radiation excites particular vibrational modes of molecules, enabling to establish absorption fingerprints to characterize the molecular compositions^{13,201} and thus, infrared PTIR is becoming more and more popular in the field of material science and biology^{13,155}. In visible range, ultraviolet-visible (UV-vis) spectroscopy is also widely exploited in material science²⁰² and biology, e.g. enzyme kinetics^{133,203}, DNA and protein activities²⁰⁴. However, visible PTIR-based nanoscale imaging is rarely studied²⁰⁵. Visible PTIR has wide potential applications in nanoscale materials characterization, such as e.g. perovskite solar cell^{206–208} and nanoparticles²⁰⁵, and studies of macromolecules in the biological systems, e.g. photosynthesis and subcellular analysis^{200,205}. Of course, there are many challenges here to be overcome. For example, the spatial resolution of existing visible and infrared PTIRs typically is of only 10-40 nm^{199,200,205}, and high-sensitivity visible-PTIR measurements have not been fully exploited.

In this work, we present a gap plasmon-enhanced visible PTIR for imaging and potential chemical identification with high-sensitivity and a few nanometers spatial resolution. Visible radiation is absorbed by the molecules and induces thermal expansion resulting in the mechanical deflection of the soft AFM cantilever. The performance of this framework is enhanced by two factors: the coincidence of the laser pulse repetition rate f_{pulse} with the cantilever dithering resonance frequency f_{reson} , and gap plasmon enhancement of the electromagnetic field between gold-coated tip apex and substrate^{209–211}. The former improves the detection sensitivity and the latter one enhances the light-sample interaction and its photothermal response. This elaborated method achieved a high spatial resolution of ~ 5 nm, which is better than that of the existing PTIR imaging in both infrared and visible range. Besides, the identification of monolayer chlorophyll-a molecules with the thickness of 1.9 nm with a spatial resolution of ~ 7.5 nm is demonstrated showing a monolayer-sensitivity of our PTIR system. We also successfully characterized the visible light-insensitive amyloid fibrils (9-nm-thickness) by taking the advantage of the stained methylene blue (MB) dye, which may shed light on the application of the light-insensitive samples for chemical characterization in nanoscale.

4.2 Experimental methods

Gap plasmon resonance enhanced visible PTIR

Nanosecond (20-50 ns) pulsed laser source (CrystaLaser CRL-QL671-100, USA) with the wavelength of 671 nm and the power of up to 100 mW (at 10 kHz repetition rate) were employed. The repetition rate of pulsed laser is

tunable, ranging from 1 to 200 kHz. It has the vertical 100:1 linear polarization. The laser was focused onto the sample located under the AFM tip at an angle of 45°-70° with the spot size of ca. 80-150 μm if a lens with the focal distance of 10 cm was used, and of ca. 40-60 μm if an optical fiber with a pigtail focuser was used. The ultra-smooth 200-nm-thick template stripped gold-mica (Platypus Technologies, Madison, USA) was used as a substrate, and the sample preparation was implemented immediately after the gold-mica chip is separated from its support.

A commercial AFM (NX10 Park Systems, Korea) operating in contact mode was used. We exploited silicon cantilevers (HQ:CSC17/Cr-Au, Micromasch, Sofia, Bulgaria) having the nominal spring constant of 0.18 N/m and first resonance frequency of 13 kHz. These cantilevers have gold coated tips with an apex radius of less than 35 nm. The scanning was performed with the scan rate of less than 2 Hz in the ambient conditions. The lock-in amplifier SR850 (Stanford Research Instr., Stanford, USA) was used. Further image flattening and processing were done with XEI software (Park Systems, South Korea) and SPIP (Image Metrology, Denmark) software.

AFM cantilever characterization

The characterization of AFM cantilevers was performed in different commercial AFM systems in the ambient condition. The calibration of the spring constant of cantilever was performed using JPK Nanowizard III AFM (Bruker, USA). By using the thermal fluctuation method, we calculated the effective spring constant of each cantilever used in the experiment, and then the characterization of amplitude-frequency response of the cantilevers was carried out using Park AFM (NX10, Korea).

COMSOL simulations

The electromagnetic enhancement of our PTIR system was simulated by COMSOL Multiphysics 5.2a. The gold tip was simulated as a conical tip with half cone angle of 22° and with an apex radius of 25 nm, which are close to the actual parameters of AFM tip used in this experiment. The gap between gold tip and 200-nm-thick gold substrate ($\epsilon \cong -14^{212}$) was 2 nm. A p-polarized laser beam with a wavelength of 671 nm was incident at angle of 60° to the gap region of the PTIR system.

Rhodamine nanohills sample preparation

Laser dye Rhodamine 800 (CAS 137993-41-0, Sigma-Aldrich) was used in the experiments. The powder of Rhodamine 800 was dissolved in the ethanol. After being sonicated for 3 min, 10 μl -droplets of the Rhodamine dye solution at the concentration of 200 μM were deposited onto the cleaved mica substrate, followed by drying in the vacuum desiccator overnight²¹³.

Chlorophyll-a sample preparation

An aliquot (10 μl) of 10% 1,6-Hexanedithiol (CAS 1191-43-1, Sigma) was used to functionalize the template stripped gold-mica substrate for 3 min, followed by rinsing and drying with compressed air. Chlorophyll-a (CAS 479-61-8, Sigma-Aldrich) powder was dissolved in the ethanol, followed by sonication for 3 min. Aliquots (10 μl) of the chlorophyll-a solution at the concentration of ~ 50 μM were deposited onto the functionalized gold substrate for 5 min, and then were rinsed and dried using a gentle nitrogen flow.

Amyloid fibril preparation and staining

Full-length recombinant human α -Synuclein (AnaSpec, USA) was dissolved in the buffer (50 mM Tris:HCl, 150 mM NaCl, pH 7.4) and then filtered with 100 kDa filter. The concentration of this protein solution was determined by ultraviolet absorbance (Nanodrop 2000, ThermoFisher, USA). The α -Syn solution was incubated at a concentration of 45 μ M at 37 °C for 50 days.

Then, the incubated α -Syn solution with amyloid fibrils was mixed with 0.001% w/v methylene blue solution. The mixed solution was filtered with 100 kDa filter, afterwards the retentate was resuspended in order to remove the monomers and unbounded MB particles. An additional filtering and resuspending was repeated twice to obtain the MB stained amyloid fibrils. Then, an aliquot solution of MB stained α -Syn fibrils (10 μ l) was deposited onto the gold-mica substrate for 4 minutes, followed by drying with a gentle nitrogen flow.

Ultraviolet-visible (UV-vis) spectroscopy

The UV-Vis spectroscopic measurement was performed using Perkin-Elmer Lambda 950 spectrophotometer. The sample was tested in disposable plastic cuvette (Sigma-Aldrich) with a path length of 10 mm. The light source of spectrometer was switched on 20 min before measurement to have a stabilized light source. Spectra were acquired in the range 300–800 nm at 1 nm spectral resolution. Further analysis of the spectra was done using Origin Pro software.

4.3 Results

Schematic of our experimental setup is presented in Figure 4.1a. A tunable nanosecond pulsed (20–50 ns) laser in visible range (671 nm) illuminates the sample, and the light absorption induces localized photothermal expansion (Figure 4.1b). The AFM was operated in the contact mode so that the thermal expansion of the sample directly triggers the cantilever deflection. To characterize the oscillatory motion of cantilever, we investigated its frequency response at different conditions. The soft AFM cantilever with a gold-coated tip (Figure 4.1c) was used in this experiment. As indicated in Figure 4.1d, the frequency responses of the cantilever in the free oscillation condition (red) and in the contact conditions with different forces applied are shown. It can be seen that the first resonant frequency of the cantilever's free dithering located at 13 kHz, which almost disappeared when cantilever tip approached substrate and force was applied. Meanwhile, the first resonance peak of the cantilever with larger amplitude appeared at the frequency of \sim 55 kHz, after cantilever tip approached the substrate. This agrees with the simulation of cantilever vibration modes (Figure 4.2). The ratio of these two frequencies is equal to 4.3, which rather well coincides with the theoretical consideration relevant for the resonant frequencies of hinged uniform rectangular beam whose one end is respectively free or supported²¹⁴. In the region of applied forces around 20 nN, which was used in our experiments, the amplitude of the frequency resonance mode is already quite prominent, see Figure 4.1d. The laser

pulses were triggered by lock-in amplifier which worked exactly at this repetition rate (i.e. ~ 55 kHz for this case) to maximize the cantilever resonance amplitude and thus to improve the measurement sensitivity.

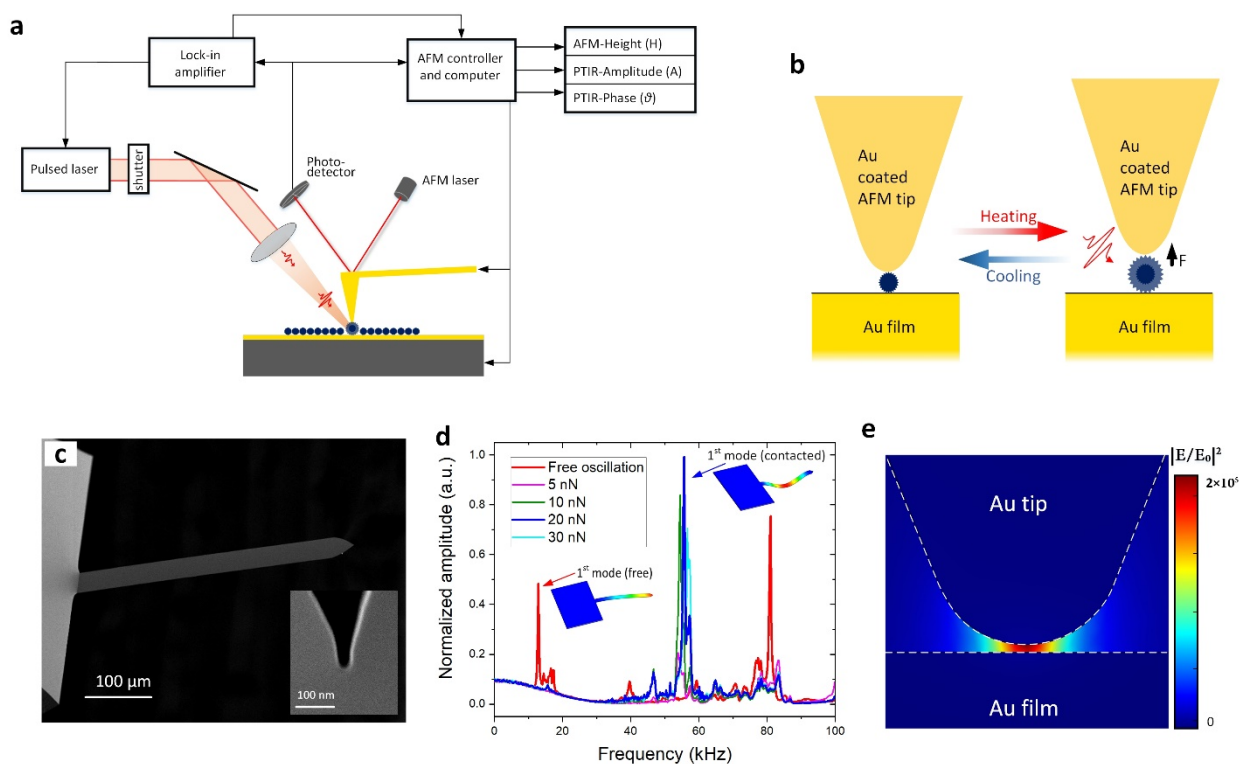


Figure 4.1 Schematic representation and characterization of the visible PTIR setup. (a) The schematic of the visible PTIR system. (b) The process of photothermal expansion of investigated sample molecules under gold tip apex on the gold surface in absence and presence of radiation. (c) The scanning electron microscope (SEM) image of the AFM cantilever and tip (insert). (d) The frequency response of the cantilever in the free oscillation mode (red) and in the contact mode with different forces applied. The free cantilever oscillates at ~ 13 kHz of its first free-oscillating mode, while the first oscillating mode for the tip-contacted oscillation is ~ 55 kHz. This agree with the simulation in the Figure 4.2, and the insert shows the shape of the cantilever beam of the first free and contacted resonance modes. (e) The simulated distribution of electromagnetic field intensity ($|E/E_0|^2$). The 671 nm light was incident in the gap of 2 nm between gold tip and substrate at an angle of 60° in the simulation and an enhancement factor in the order of 10^5 was achieved (see details in Methods section).

There are several factors contributing to the amplification of electromagnetic field in the gold tip-substrate gap region in our experiments. First, the size of gold tip apex used is much smaller than light wavelength, which relaxes the necessity to use special schemes, e.g. the Kretschmann geometry, to excite surface plasmons. Then, the gap plasmon resonances are efficiently excited by laser in visible range to achieve higher sensitivity than that in the infrared range¹⁹⁴, these aspects will be discussed in details later. Note, that the laser used has vertical 100:1 linear polarization, and thus the radiation is strongly *p*-polarized hence suitable for the observation of gap plasmon resonance^{194,215} in the gold tip-substrate region. Thus, for 2 nm thickness tip-substrate gap, the simulated local electrical field with an enhancement factor of as high as 1.6×10^5 is achieved under the AFM tip (Figure 4.1e).

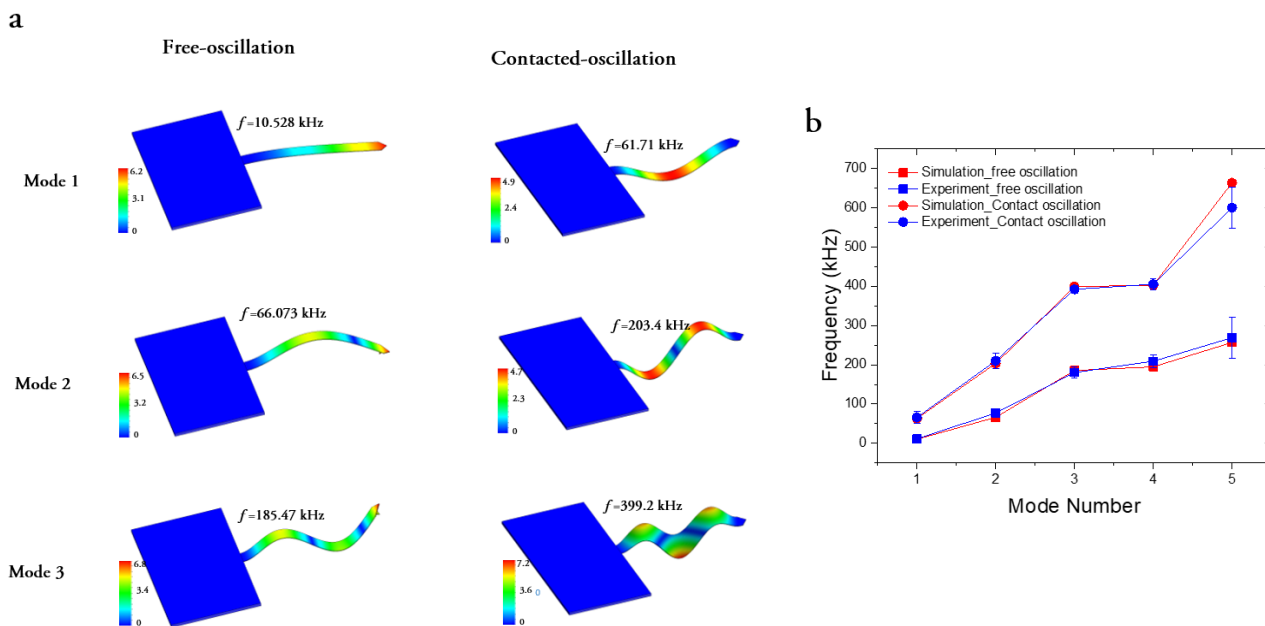


Figure 4.2 The simulation of cantilever resonance. (a) Simulation of cantilever resonance modes and their shape of cantilever beam of the first three resonance modes in the free oscillation condition (up) and in the contact condition (bottom). In the free cantilever condition, the resonance frequencies of the first, second and third resonance modes are 10, 66 and 185 kHz, respectively. Whilst in the contact condition, these resonance frequencies are 61, 203 and 399 kHz respectively. The shape of oscillating cantilever in different oscillating frequencies are showed. (b) The correspondence of the frequencies of first five resonance modes between simulated and experimental results in both free and contact oscillation.

4.3.1 Characterization of Rhodamine 800 dye nanohills

The first trial to test our visible PTIR system was performed with Rhodamine 800 laser dye, which has a strong optical adsorption at 671 nm (Figure 4.3). Nanohill-like clusters of dye molecules with a typical size of 50-500 nm and a height of 20–50 nm were deposited onto the mica surface (Methods section). The AFM and PTIR maps scanned in the contact mode are shown in Figure 4.4. Here, the height and error signals are obtained from AFM feedback loop. They describe respectively the sample topography and precision of the surface tracking during the scanning. The PTIR-amplitude and PTIR-phase signals are obtained from the outputs of the lock-in amplifier, indicating the amplitude of cantilever vibration (hence corresponding to the magnitude of photothermal expansion) and the phase shift of this vibration with respect to the triggering lock-in output signal, respectively.

As shown in Figure 4.4, for 40-nm-high Rhodamine cluster, the PTIR signals disappear when laser irradiation is absent (Figure 4.4c-d), and appear once the laser illuminates the sample (Figure 4.4e-f). Both PTIR-amplitude and PTIR-phase are maximal (Figure 4.4g-h) when the laser repetition frequency matches the cantilever resonance frequency.

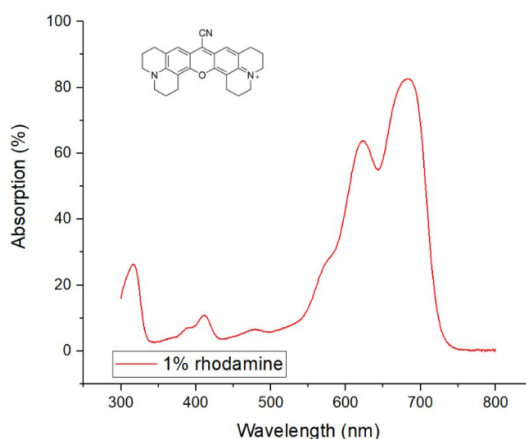


Figure 4.3 The UV-vis absorption spectrum of the 1% Rhodamine 800 dye solution.

Assuming an optical absorption cross section $\sigma \cong 1.2 \times 10^{-16} \text{ cm}^2$ for Rhodamine 800 molecule²¹⁶, for the laser pulse energy of 0.6 μJ and energy flux $J = 1.5 \text{ mJ}/\text{cm}^2$ (50 mW, 80 kHz repetition rate and focal spot of ca. 0.2 mm size), we obtain an estimation of the increase of the temperature during one laser pulse as $\Delta T \cong \frac{\sigma \cdot J \cdot N_A}{C_M} = 200 \text{ K}$. Here N_A is Avogadro number and C_M is a molar heat capacitance of the dye, for which a value $C_M = 550 \text{ J}/\text{K} \cdot \text{mol}$, measured for analogous Rhodamine dye²¹⁷, was applied. In this estimation, we ignore the reflection of laser radiation and the electromagnetic field enhancement by sharp metal-coated tip, as well as different correcting factors related with the shape and refraction index of nanohill-like dye structures²¹⁸.

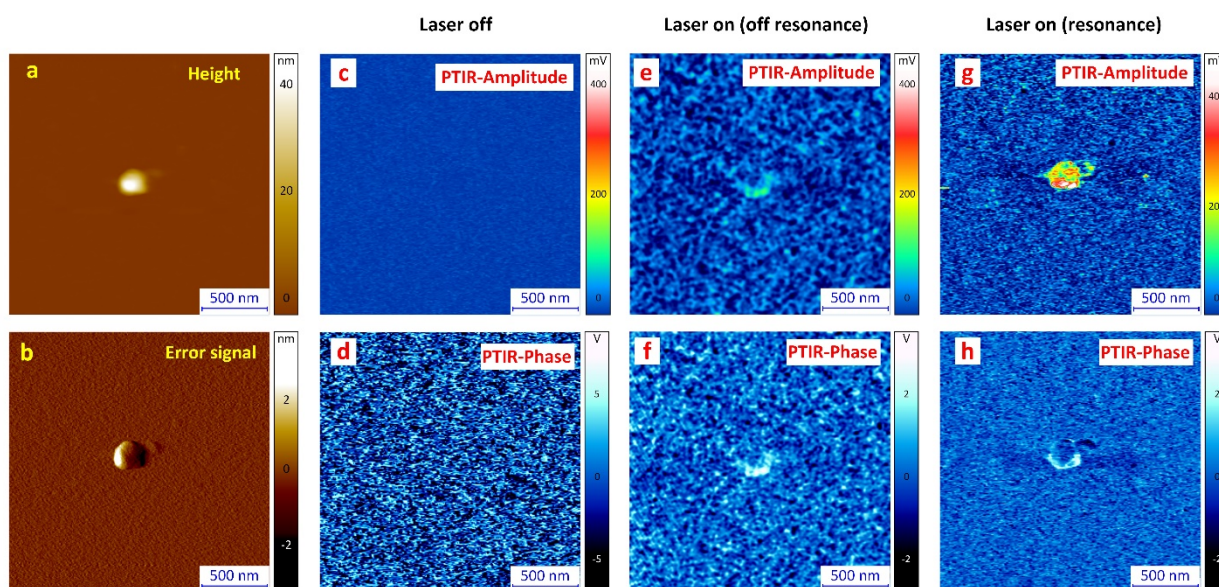


Figure 4.4 The visible PTIR measurements of the nanohill-like Rhodamine cluster. (a-b) The height and error signal of the Rhodamine cluster with a height of 40 nm. (c-h) The PTIR-amplitude (c, e, g) and PTIR-phase (d, f, h) signals obtained while laser is off (c, d), and for laser repetition frequency mismatching (e, f; at $\sim 80 \text{ kHz}$) and matching (g, h; at $\sim 55 \text{ kHz}$) the cantilever resonance frequency.

We suppose that the percentage of light energy absorbed by the Rhodamine nanohill with the height h is small, $\sigma ch \ll 1$, where c is the number of dye molecules per cubic centimeter. This value does correspond to our observations that the samples are not too far from melting during experiment, and thus long-time exposure of laser irradiation should be avoided. Accepting for the dye the thermal expansion coefficient of $\alpha \cong 10^{-4} K^{-1}$, which is characteristic for majority of polymers and plastics, we see a quite large expansion of a 40 nm-nanohill Rhodamine cluster in our experiment: $\delta h = \alpha h \Delta T \cong 0.8 \text{ nm}$. The spring constant related with the elongation of this dye structure with the lateral size $L=200 \text{ nm}$ and height $h=40 \text{ nm}$ is of the order of $k \cong L^2 Y/h \cong 40 \sim 400 \text{ N/m}$, much larger than that of the cantilevers used (0.18 N/m). Here Y is the Young's modulus estimated experimentally as ranging $0.04 - 0.4 \text{ GPa}$ ¹⁴⁴.

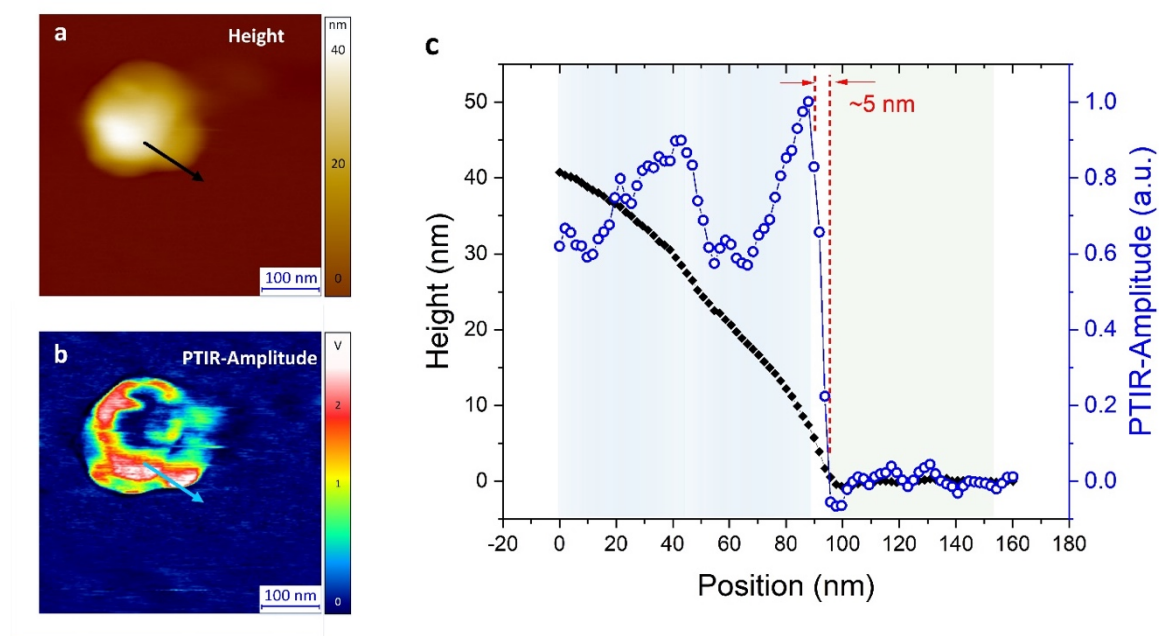


Figure 4.5 The characterization of the nanohill-like Rhodamine cluster. (a-b) The height and PTIR amplitude images of the Rhodamine cluster, scanning at a rate of 2 Hz in the $0.5 \times 0.5 \mu\text{m}^2$ area with 256×256 pixels. (c) The profile of the height and PTIR-amplitude signal of the investigated Rhodamine nanohill along the arrows indicated in the height and PTIR-amplitude maps.

Further characterization of Rhodamine dye was carried out, as shown in Figure 4.5, to better understand the visible-PTIR measurement sensitivity and spatial resolution. The morphology and PTIR-amplitude of nanohill-like Rhodamine cluster are shown in Figure 4.5. The $0.5 \times 0.5 \mu\text{m}^2$ PTIR image is obtained with 256×256 pixels with a scanning rate of 2 Hz, and thus each pixel corresponding to $2 \times 2 \text{ nm}^2$ area represents the average signal of 110-160 pulses of the laser. As seen, more structural details can be found on the PTIR-amplitude map, compared with the height image. Here, a high spatial resolution of $\sim 5 \text{ nm}$ is achieved, which, to the best of our knowledge, is the highest spatial resolution

achieved in the existing PTIR studies^{199,205,219} and approaches best resolution of TERS in ambient conditions (2-15 nm^{52,220}). In comparison with infrared PTIR where the best lateral resolution is around 20 nm^{199,200}, the better performance in visible range is believed to be due to the larger molecular absorption coefficient of visible radiation and higher light intensity caused by the possibility of better focused spot of incident light. Certainly, the enhancement of electromagnetic field in this PTIR system also plays an important role. This result is also slightly better than that (lateral resolution of 8.3 nm) obtained in the recent study of visible PTIR using an uncoated sharper AFM tip²⁰⁵.

4.3.2 Characterization of monolayers of Chlorophyll-a

Detection and imaging of monolayers of organic molecules are of great importance in many research fields. Still in most cases, PTIR investigations target only an averaged information pertinent for a large accumulation of molecules, while working with monolayer molecules is certainly more challenging²²¹ and it is rarely studied. This is due to smaller photothermal expansion and lower SNR generated by the monolayer molecules with the typical height of a few nanometers.

To testify the monolayer-sensitivity of our visible PTIR experiments, we investigated 2-nm-thick monolayer of chlorophyll-a molecules^{222,223}, deposited on the 1,6-Hexanedithiol functionalized gold surface (Figure 4.6a and Methods section). The chlorophyll-a molecules show strong absorption in the band 1650-1680 nm (Figure 4.6b). To enhance the PTIR signal, in addition to the matching of resonance frequencies, we targeted also the gap plasmon resonance-based field enhancement of the PTIR signal.

The topology and PTIR maps of investigated monolayer are shown in the Figure 4c-j. The “island” of chlorophyll-a, in the middle of Figures 4.6c-e, with the height of 1.9 nm (Figure 4.6j) strongly absorbs the visible radiation and thus induces thermal expansion, which was detected in our visible PTIR system. The zoom-in characterization can be seen in Figure 4.6f-h. A considerable improvement of the spatial resolution was achieved according to Figure 4.6j: PTIR-amplitude and height maps exhibit a spatial resolution of ~7.5 nm and ~28 nm respectively. Meanwhile, the PTIR-amplitude maps (Figures 4d and 4g) show a clear difference between chlorophyll-a and substrate, which is better than that of AFM height image. Besides, note that the 3-nm-thick structure indicated with the magenta dash line in Figures 4.6c-e, shows no signal of photothermal expansion (Figure 4.6d and 4.6i), which is believed to be other chemicals or artifacts formed during sample preparation. This is a clear demonstration of the chemical selectivity attained in our experiments.

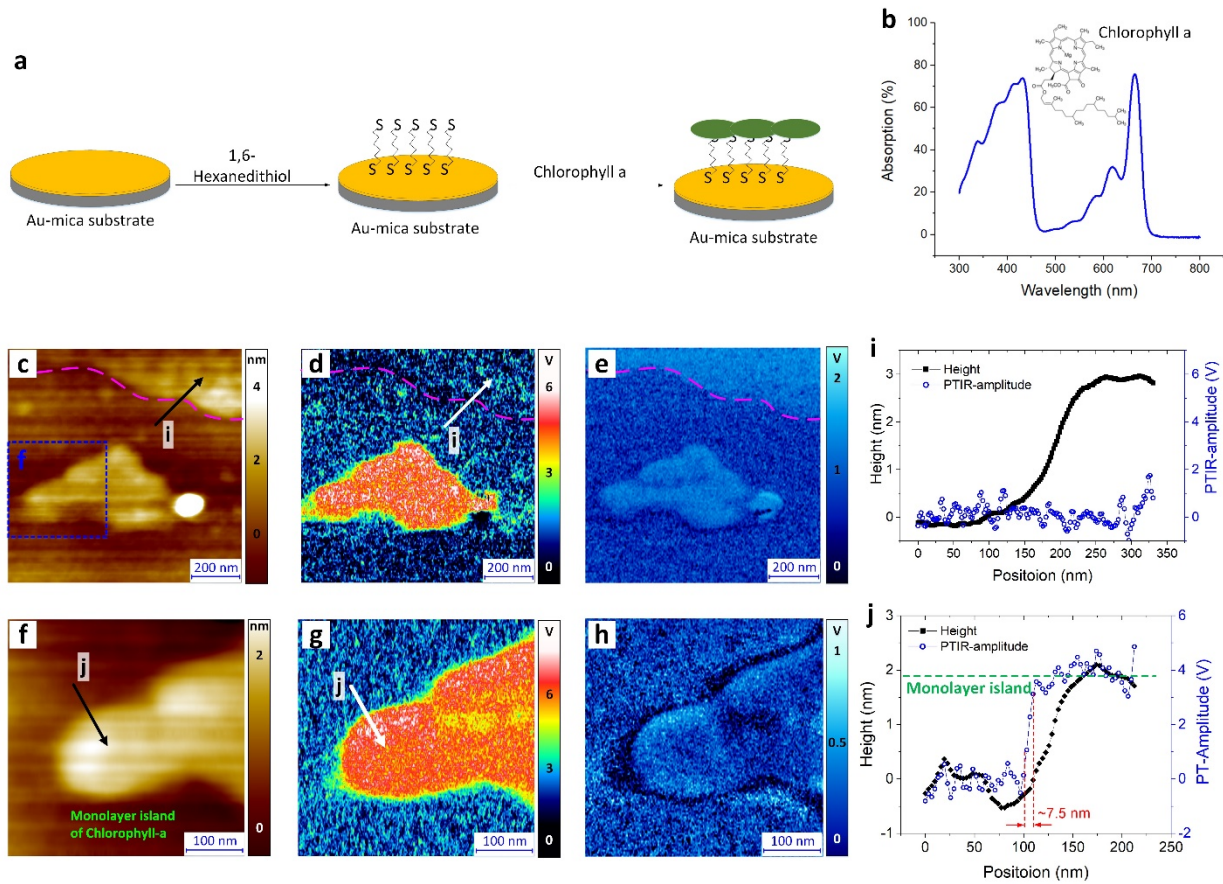


Figure 4.6 The visible PTIR characterization of chlorophyll-a monolayer. (a) The workflow procedure of preparing chlorophyll-a monolayer on the gold substrate. (b) UV-vis absorption spectrum of chlorophyll-a molecules. (c-e) The height (c), PTIR-amplitude (d) and PTIR-phase (e) of chlorophyll-a monolayer island. (f-h) The height (f), PTIR-amplitude (g) and PTIR-phase (h) of the zoom-in area indicated (c) on the chlorophyll-a monolayer island. (i) The profile of height and PTIR-amplitude signal of the island in (c, d) along the arrow. (j) The profile of height and PTIR-amplitude signal of the island in (f, g) along the arrow. The green dash line indicates the approximate height of single chlorophyll-a molecule which shows a dimension of around 1.9 nm, and the spatial resolution of chlorophyll-a monolayer on the PTIR-amplitude map is up to ~ 7.5 nm.

Let us describe gap plasmon resonance (also named plane-sphere structure plasmon resonance) field enhancement in more details. This resonance is a hybrid resonance between metal-coated AFM tip, approximating as a sphere with the real part of the dielectric permittivity $\varepsilon_1'(\omega)$, and semi-infinite space occupied by the metal with the real part of the dielectric permittivity $\varepsilon_2'(\omega)$. The resonance condition^{214,215} is

$$\frac{\varepsilon}{\varepsilon_1'(\omega)} + \frac{\varepsilon}{\varepsilon_2'(\omega)} = -\left(n + \frac{1}{2}\right) \sqrt{\frac{2d}{R}} \quad (1)$$

where $n=0, 1, 2, \dots$, ε is dielectric permittivity of the environment, R is the radius of the tip apex and d is the gap size. The formula (1) can be understood as a tool to determine the resonant gap distances d for any given frequency:

$$d = \frac{R}{2(n+1/2)^2} \left(\frac{\varepsilon}{\varepsilon_1'(\omega)} + \frac{\varepsilon}{\varepsilon_2'(\omega)} \right)^2 \quad (2).$$

In the middle IR spectral range, the distances d for which the resonance takes place for small values of n are very small. For example, at the wavelength of 2.48 μm (which is ca. 4000 cm^{-1} so that excitation of almost all characteristic molecular vibrations needs this or longer wavelength), where $\varepsilon_1' = \varepsilon_2' = -405^{224}$, even for blunt tip with $R=100 \text{ nm}$, $\varepsilon = 2.3$ and $n=0$, we obtain $d \cong 0.03 \text{ nm}$. This value rapidly drops further with the increase of the wavelength. If d is much larger, as this takes place in our and other experiments¹⁹⁹, we still can formally have a kind of resonance at large values of n , but then it does not make a great sense to speak about “gap plasmon” and there is no hybridization between sphere and plane. Certainly, in some cases the excitation of vibrational overtones in near IR might be useful, but already for twice smaller wavelength of 1.24 μm we have $\varepsilon_1' = \varepsilon_2' = -102^{224}$ and thus $d \cong 0.4 \text{ nm}$, so that submonolayer sensitivity is needed to realize resonant conditions. This might be problematic given the small optical absorption cross sections for vibrational overtones.

Situation is quite different for the visible light, i.e. in the case of our experiments. Although this is difficult to obtain reliable estimations of the dielectric permittivity for the gold tip at wavelength of 671 nm in the literature, we can still estimate this values as ranging from $\varepsilon_1' \cong -24^{224}$ to $\varepsilon_1' = -13^{225}$. Correspondingly, then for $n=0$, $\varepsilon = 2.3^{226}$ and $R=30 \text{ nm}$, which is close to the actual parameter of the gold-coated tips used in this experiment, we get the resonant gap distance ranging from $d \cong 2.2 \text{ nm}$ to $d \cong 7.5 \text{ nm}$. Thus, this does not seem surprising that at certain conditions plasmon gap resonance can be excited for the thicknesses close to 2 nm (Figure 4.6). In addition, the simulation shows an enhancement factor of the order of 10^5 for the electric field under the tip during the characterization of 2-nm-thick monolayer. Indeed, the excitation of the gap plasmon resonance and its utility for Scanning Probe Microscopy (apertureless s-NSOM for the case) have been demonstrated already²⁰¹, also in the visible range at 633 nm . Note also that the effect of the field enhancement is localized in transversal x-y directions on the subtip scale with the size around $\sqrt{2dR}$; that is of the order of 10 nm for our case (accepting $\varepsilon'_{1,2} = -24$). In relation with this, it is worthwhile to underline

again the experimentally observed better resolution in PTIR channel than that in AFM topographical one (Figure 4.6j).

With gold-coated tip and substrate, not only the light absorption of the chlorophyll-a, but that of the gold is also important. At the wavelength used we have for the corresponding absorption coefficient $\alpha \cong 8 \cdot 10^5 \text{ cm}^{-1224,225}$, which means that both gold coatings involved absorb light quite efficiently. This definitely enlarges the characteristic thermal expansions realized in our experiments, much further than sub-angstrom values which follow from the consideration given above.

4.3.3 Characterization of amyloid fibrils stained with MB dye

With the advantage of molecular sensitivity in our visible-PTIR system, the following attempt is to characterize non-absorbing nanostructures stained with small light-absorbing molecules. For this, we utilized the methylene blue dye, which quite efficiently absorbs at the 671 nm, to study visible light-insensitive amyloid fibrils (Figure 4.7) using our visible PTIR system.

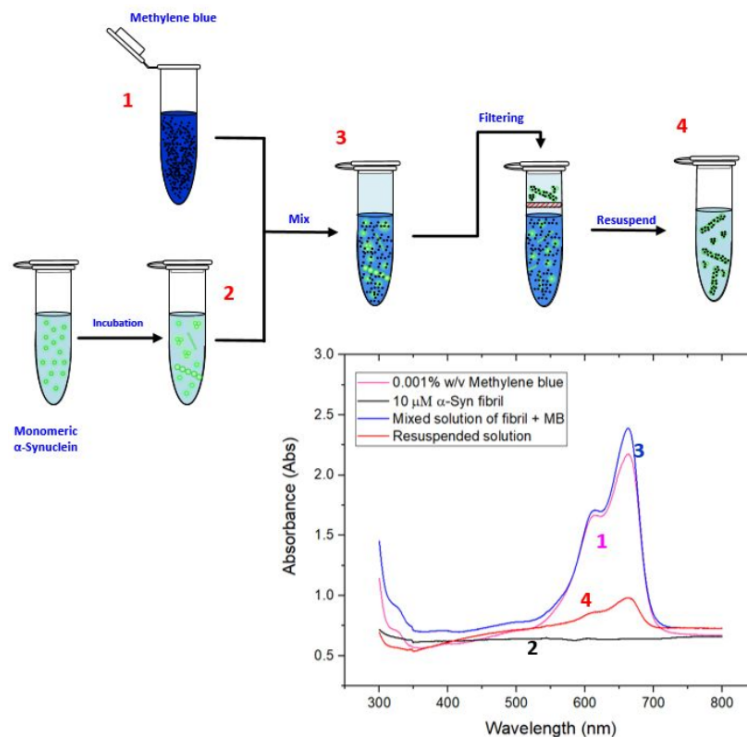


Figure 4.7 The preparation of MB stained α -Synuclein fibrils. The workflow (up) shows the procedure of the preparation of stained α -Synuclein fibrils. The methylene blue solution (spectrum 1) was mixed with the visible light-insensitive α -Syn fibril solution (spectrum 2), which was obtained after the incubation of $45 \mu\text{M}$ α -Synuclein monomers for 50 days (see the Method section). After mixing, the solution (spectrum 3) was filtered with 100 kDa filter, then the retentate was resuspended in order to remove the monomers and unbound MB molecules. The solution with MB-stained fibrils and oligomers are then obtained, and used for the following deposition on the substrate. Compared with visible light-insensitive α -Syn fibril solution (spectrum 2), this solution of stained fibrils shows a relatively weak absorption peak at 670 nm (spectrum 4). For further detailed see the Method section.

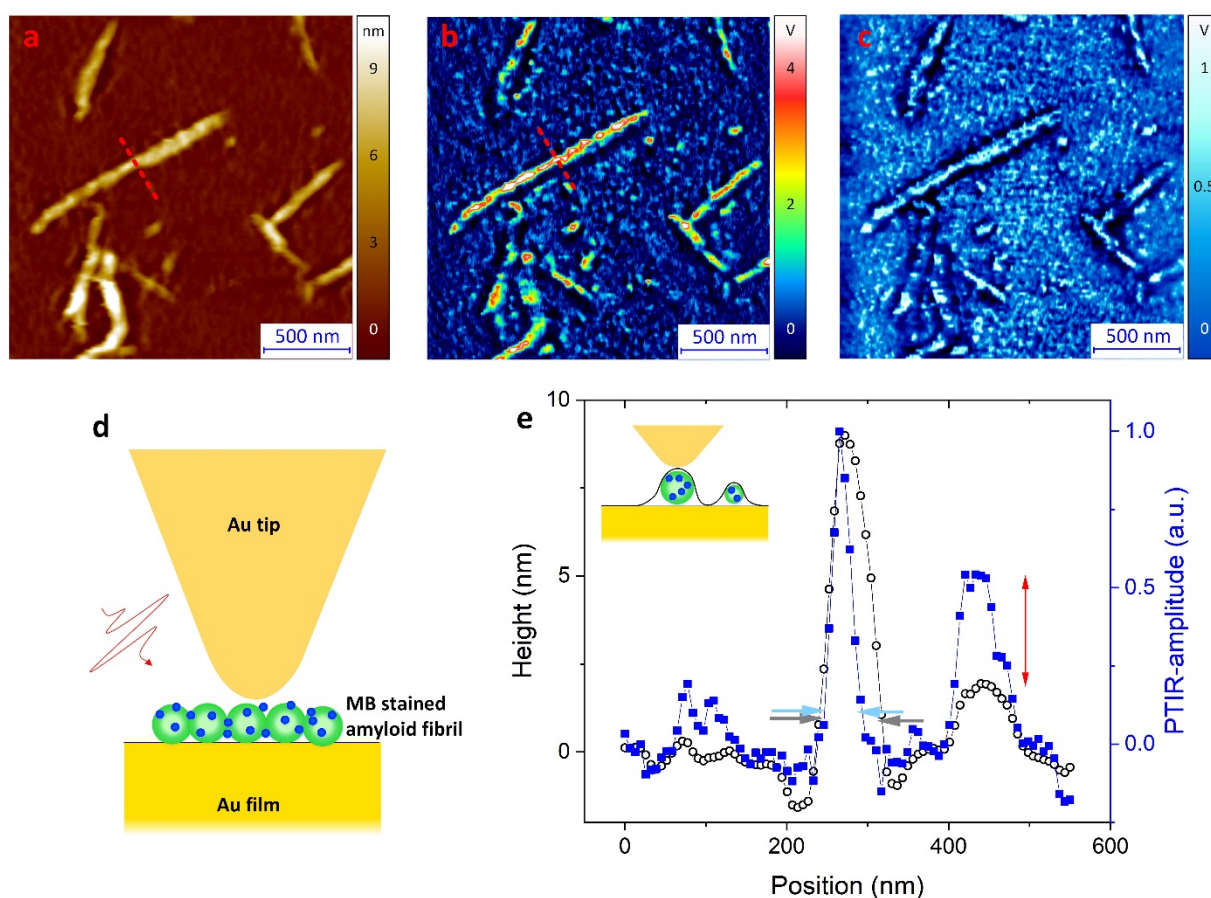


Figure 4.8 The visible PTIR characterization of methylene blue stained amyloid fibrils. (a-c) The height (a), PTIR amplitude (b) and PTIR phase (c) signal of visible-PTIR scanning on the MB-stained amyloid fibrils. (d) The schematic of PTIR study on the MB molecules (blue dots) stained amyloid fibril (green linear assembly). (e) The height (black) and normalized PTIR amplitude (blue) signals of the cross-section of amyloid fibril and oligomer indicated by the red dash line.

Amyloid fibrils are the aggregates of amyloidogenic proteins and methylene blue (MB) has been proved to be able of inhibiting protein aggregation, including α -Syn^{227–229}, Tau²³⁰ and β -amyloid²³¹. The mechanism by which MB acts as inhibitor is not clear, but it may depend on its interaction with aggregates to reduce protein-protein binding²³⁰. As a result, there is a focus of interest in the potential MB-treatment in the protein aggregation related neurodegenerative disorders, such as Parkinson's and Alzheimer's disease. A-Synuclein (α -Syn) fibril is a characteristic pathological feature of synucleinopathies and Parkinson's disease, and the preparation details of MB stained α -Syn fibrils are given (Methods section and Figure 4.7). The AFM and PTIR data are presented in Figure 4.8. The study of height distribution along the fiber shows that we have a case of twisted fibrils¹³⁶ here (Figure 4.9). As can be seen, the fibrillar and oligomeric aggregates with the height of 5-10 nm are clearly observed in the PTIR images.

In Figure 4.8e, we present the height and normalized PTIR amplitude signals of the cross-section of amyloid fibril indicated in Figure 4.8a-b. The PTIR amplitude is maximized at the top of the 9-nm-thick fibril and it is noticeable that the fibril width of 64 nm on the AFM topological data (grey arrow) is reduced to 45 nm (blue arrow) in the PTIR signal. This again demonstrates that the photothermal expansion can provide more precise detection for sample characterization. Besides, we see that the fibrils in the PTIR-amplitude map are not as smooth as the same fibrils in the height image, which we believe is, among others, due to the additional contrast caused by heterogeneous distribution of MB molecules on the amyloid fibril surface (Figure 4.9).

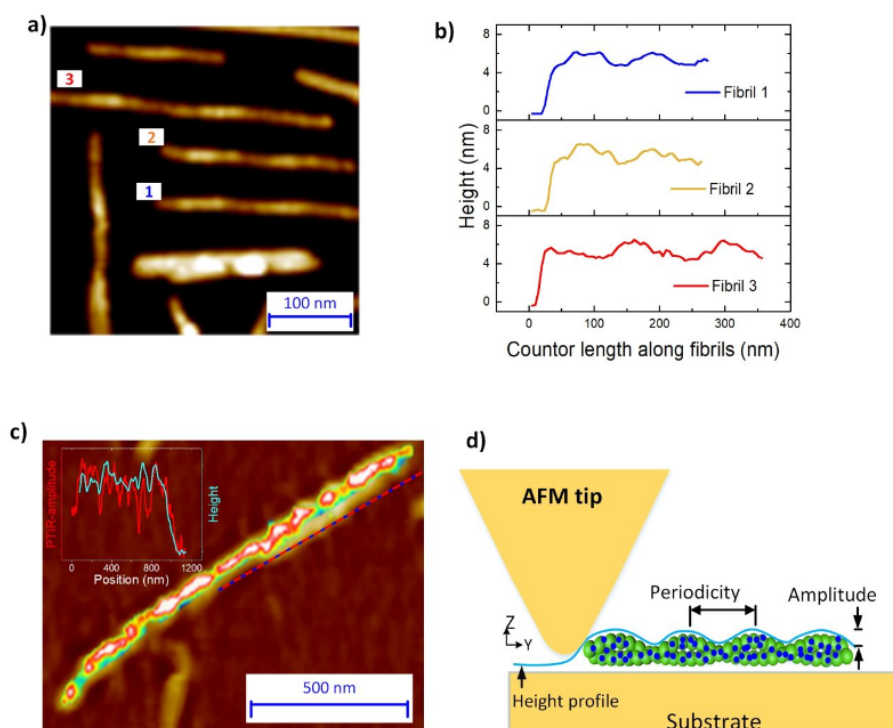


Figure 4.9 The characterization of α -Synuclein fibrils. (a-b) The AFM image of non-stained α -Synuclein fibrils: the majority of fibrils have twisted morphology with fluctuated height profile. The height profiles of the fibrils 1, 2 and 3, as indicated in (a), are shown in (b). (c) The overlapped map of morphological and PTIR amplitude images of MB-stained amyloid fibril from Figure 4.8a-b, where the fluctuated shape along the axis of the MB stained fibril is clearly seen. The insert shows the profiles of height and PTIR-amplitude along the axis of this fibril. (d) The schematic representation of AFM scanning of twisted amyloid fibril and MB distribution along the fibril. The thicker region accumulates more MB molecules, thus gives a stronger response in the PTIR measurement. This also partly explains the larger fluctuated contrast on the PTIR-amplitude profile over that on the height profile (c).

Moreover, the structure with a height of 2.1 nm indicated by the red arrow in Figure 4.8e, which can be clearly seen on the PTIR-amplitude map, is believed to be MB-stained α -Syn oligomer. The ratio of heights between the fibril and oligomer is equal to 0.22, and this value increases to 0.5 on the PTIR curve. In our opinion, this might be due to the difference of the electromagnetic field enhancement for different gap sizes, as it should be for the case of gap plasmon resonance. The dielectric constant

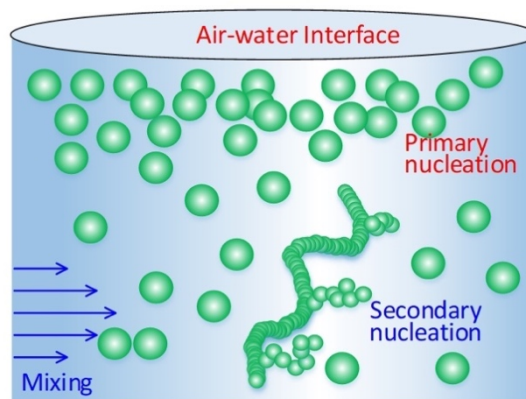
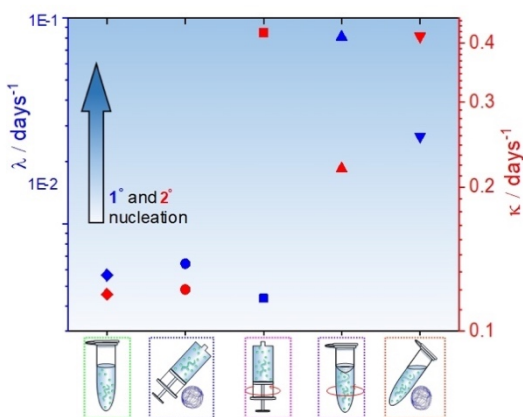
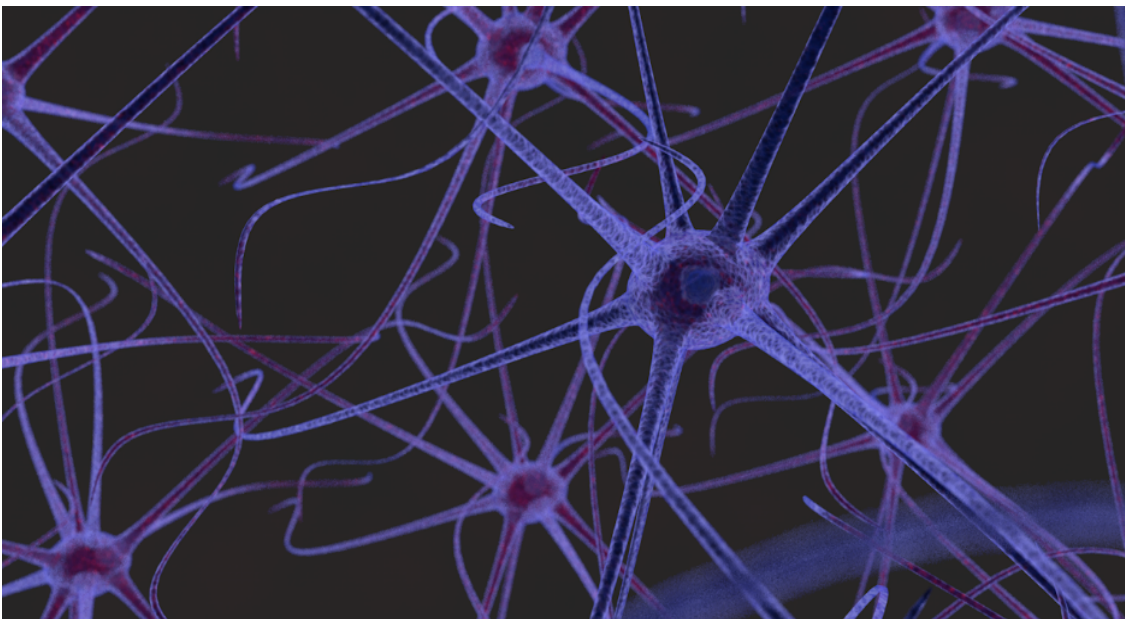
of amyloid fibrils²³² is close to that of Chlorophyll, so we obtain the size of resonant gap ranging 2-8 nm, and our experimental data suggest that actually this value is more close to the lower end of the range. It seems that this effect can greatly benefit the ultrasensitive imaging and characterization of small nanostructures, of the order of nanometers.

4.4 Conclusion

In summary, we presented a PTIR system in the visible range, achieving chemical identification with the spatial resolution of ~ 5 nm and monolayer sensitivity (~ 2 nm). These advantages result from two factors exploited in our experiments: matching the laser pulse repetition rate with the resonance frequency of AFM cantilever, and gap plasmon resonance enhancement. The former improves the sensitivity by making the detection of the cantilever vibration induced by sample expansion much more effective. The latter enhances the approach by amplifying the acting electromagnetic field. For the radiation spectral range used, the values of the tip-substrate distance d , corresponding to efficient plasmon gap resonance, lie in the range of a few nanometers. This fits very well with the practically interesting range of monolayer coatings, nanomaterials, bio-macromolecules, and many others. This also means that the small variations of the sample thickness can lead to large changes of the EM field amplification drastically improving the resolution and contrast of the images.

We believe that our proposed visible PTIR system, given the achieved spatial resolution and sensitivity level, will be quite useful for compositional identification at nanoscale for various samples and molecules absorbing radiation in the visible range. Also, the imaging of MB-stained amyloid fibrils suggests that those macromolecules which are not sensitive to incident radiation may also be studied and characterized utilizing an appropriate modification with light-absorbing chemical compounds. Applications ranging from nanomaterial science, analytical chemistry, optoelectronic industry to biological macromolecules can be envisaged.

Chapter 5 Effect of sedimentation, micro-gravity, hydrodynamic mixing and air-water interface on protein aggregation



This chapter is based on an accepted paper in the Journal *Chemical Science*, with the following information:

Jiangtao Zhou,^{1†} Francesco S. Ruggeri,^{2,3†*} Manuela R. Zimmermann,² Georg Meisl,² Giovanni Longo,⁴ Sergey K. Sekatskii,¹ Tuomas P. J. Knowles^{2,3*} and Giovanni Dietler^{1*}. ***Effects of sedimentation, microgravity, hydrodynamic mixing and air-water interface on α -synuclein amyloid formation.*** *Chem. Sci.* 2020, 11, 3687-3693.

Affiliations:

1. *Laboratory of Physics of Living Matter, École Polytechnique Fédérale de Lausanne (EPFL), CH-1015 Lausanne, Switzerland*
2. *Department of Chemistry, University of Cambridge, Lensfield Road, Cambridge CB2 1EW, UK*
3. *Centre for Misfolding Diseases, Department of Chemistry, University of Cambridge, Lensfield Road, Cambridge CB2 1EW, UK*
4. *Istituto di Struttura della Materia, CNR, Via del Fosso del Cavaliere 100, 00133, Roma, Italy*

† *These authors contributed equally to this work*

Abstract. The formation of amyloid fibrils is a characterizing feature of a range of protein misfolding diseases, including Parkinson's disease. The propensity of native proteins to form such amyloid fibril, both in vitro and in vivo, is highly sensitive to the surrounding environment, which can alter the aggregation kinetics and fibrillization mechanisms. Here, we investigate systematically the influence of several representative environmental stimuli on α -synuclein aggregation, including hydrodynamic mixing, the presence of an air-water interface and sedimentation. Our results show that hydrodynamic mixing and interfacial effects are critical in promoting several microscopic steps of α -synuclein aggregation and amyloid fibril formation. The presence of an air-water interface under agitation significantly promoted primary nucleation. Secondary processes were facilitated by hydrodynamic mixing, produced by 3D rotation and shaking either in the presence or in the absence of an air-water interface. Effects of sedimentation, as investigated in a microgravity incubator, of α -synuclein lead only to minor changes on the aggregation kinetics rates in comparison to static conditions. These results forward the understanding of α -synuclein fibrillization, paving the way for the development of high-throughput assays for the screening of pharmacological approaches targeting Parkinson's disease.

5.1 Introduction

The formation of pathological fibrillar amyloid aggregates is associated with several protein misfolding diseases, including many neurodegenerative disorders.^{57,58,60} Within this class of diseases, Parkinson's diseases^{82,233,234} is fundamentally linked at the molecular level with the misfolding and aggregation of the α -synuclein protein.

The mechanistic link between α -synuclein amyloid formation and disease onset is still elusive and to date no treatments to delay or cure Parkinson's disease are available. This knowledge gap in part originates in a lack of comprehensive understanding of the energy landscape and the kinetics of the transition from soluble native monomers to insoluble amyloid fibrils. Further limiting factors are related to the poor reproducibility of the kinetics of aggregation, as well as a high degree of polymorphism, which reflects on the weak tendency of α -synuclein to spontaneously aggregate in vitro. These effects hamper the accurate study of α -synuclein aggregation required for high-throughput for biotechnology and drug discovery purposes.^{141,144}

The aggregation kinetics of α -synuclein is routinely accelerated by exploiting the effect of solution conditions or other external factors, including pH,²³⁵ temperature²³⁵ and ionic strength,²³⁵⁻²³⁷ as well as seed aggregates,^{235,238,239} nanoparticles²⁴⁰ and lipid vesicles²⁴¹. Moreover, a variety of hydrodynamic mixing approaches, including stirring^{235,242}, shaking²⁴³ and shearing²⁴⁴ are employed. In particular, hydrodynamic mixing plays a critical role in protein aggregation^{235,240,245} and it has been previously shown that the strength of the hydrodynamic flow may be critical for accelerating fibril formation.^{235,246} Further fundamental but elusive factors, which have been shown to influence protein aggregation kinetics are the phenomena of sedimentation during incubation and the interaction with air-water interfaces.^{235,243,245} The poorly controlled presence of hydrophobic interfaces can cause uncertainty and variability in the kinetics of aggregation, as well as a high degree of polymorphism.^{245,247-251} Furthermore, many biological activities are gravity-dependent,²⁵² such as lipid membrane fluidity²⁵³⁻²⁵⁵ and ion channels,²⁵⁶ and it has been reported that microgravity and hyper-gravity conditions with under/over-sedimentation effect can promote or hinder the aggregation process respectively.²⁵⁷ However the gravitational influence on protein aggregation is still not fully understood^{257,258} and the understanding of the combined phenomena of sedimentation, hydrodynamic mixing and interaction with air-water interfaces on protein aggregation remains elusive.

In the present work, we undertake a systematic characterization of α -synuclein aggregation in static, microgravity and orbital shaking condition to investigate and unravel the influence of sedimentation,

hydrodynamic mixing and air-water interfaces on the microscopic steps of primary nucleation and secondary processes of α -synuclein aggregation. To characterize the process of aggregation, we exploited a combination of Thioflavin T (ThT) based kinetics assays^{141,241,259}, circular dichroism (CD) spectroscopy^{141,260}, high-resolution atomic force microscopy (AFM) imaging^{141,163,261} and the theoretical platform offered by chemical kinetics^{70,71}.

5.2 Experimental methods

Expression and purification of α -Synuclein

Recombinant wild type α -synuclein was expressed by *E. coli* and then purified as described previously²⁶².

Experimental setup and aggregation assay

Purified monomeric α -synuclein protein was dissolved in buffer (50 mM Tris·HCl, 150 mM NaCl, pH 7.4), and filtered through a 100 kDa filter. The α -synuclein concentration in the solution was determined by ultraviolet absorbance (Nanodrop 2000). An aliquot (1 mL) of α -synuclein solution was sealed either in a low protein-binding syringe while gently removing the gas vesicle inside or in an Eppendorf tube. The α -synuclein solution was incubated at 37 °C in static, orbital shaking, and RPM-induced microgravity conditions.

In static condition, the protein solution samples were statically incubated in the incubator at 37 °C. In orbital shaking condition, the α -synuclein solutions in both the Eppendorf tube and the syringe were vertically fixed and agitated in the horizontal plane at the speed of 400 rpm. The microgravity environment was simulated by using a self-build random position machine (RPM) with the reported protocol²⁵⁵. This RPM system was realized by employing 3D-clinostat configuration^{263–265} to rotate three-dimensionally the sample with well-controlled speed and acceleration. This RPM system contains two independent high-precision motors to give a random rotation orientation and gravity vector on the sample, providing a simulated microgravity condition for protein aggregation. For the condition of microgravity, the α -synuclein solution was sealed in the syringe and incubated in the chamber of the RPM system at 37 °C. The sample solutions were placed in the rotational center of the RPM system to maintain an average null gravity vector and to minimize residual gravity artifacts during the experiment^{255,266}. Due to the size of the syringe used, the protein samples experienced a free-fall with small spherical trajectories, resulting in a good approximation of a microgravity environment ranging from 0 g to 0.2 g^{255,267}. During the experiment, a constant speed of ~30 rpm was applied on both axes. This relatively fast speed was chosen to generate the simulated microgravity and to maintain the centrifugal force minimal. For the 3-dimensional (3D) shaking condition, the α -synuclein solutions in the Eppendorf tube were also incubated in the RPM system. However, instead of generating microgravity, the agitation in random direction generated 3-dimensional liquid turbulence in the Eppendorf tube. This effect provoked the influence of hydrodynamic mixing and interaction between protein and air-water interface, on the protein aggregation in the bulk solution in the Eppendorf tube.

AFM measurement

An aliquot (10 μl) of diluted α -synuclein solution (10 μM) was prepared before each AFM measurement. Freshly cleaved mica was functionalized with an aliquot (10 μl) of 0.5% (3-Aminopropyl) triethoxysilane (APTES) for 1.5 min at room temperature, and was then rinsed and dried with a compressed gas flow. Then, an aliquot (10 μl) of the α -synuclein solution at a concentration of 10 μM was deposited on the functionalized mica for 4 min, which was immediately rinsed with mili-Q water and dried by a gentle flow of nitrogen gas. AFM imaging was operated by Park NX10 AFM (Park Systems, South Korea) in non-contact mode in ambient conditions. PPP-NCHR cantilevers were used, they have a typical spring constant of 42 N/m and a tip radius of less than 7 nm. A stable and weak tip-sample interaction was applied during scanning with a phase variation of $\pm 5^\circ$ in the negative region for a consistent measurement of fibrillar cross-sectional dimensions¹⁶³. AFM images were flattened using XEI software (Park Systems, South Korea). The statistical analysis of amyloid fibrils on the AFM images was carried out by SPIP software (Image Metrology, Denmark). The average height of amyloid fibrils was measured by averaging the cross section of the fibrillar structure. More than 100 fibrils on multiple random scanned locations were measured in each condition. The volume of fibrils was characterized by using SPIP software and compared between the fibrils from different $4 \times 4 \mu\text{m}^2$ AFM images and six random-selected areas were calculated in each condition.

CD spectroscopy

An aliquot (40 μL) of diluted α -synuclein solution (15 μM) was analyzed with a Jasco J-815 CD spectrometer in the range of 190-280 nm in each measurement at room temperature. A high-quality quartz cuvette with an optical path length of 1.0 mm was employed and spectra were collected every 0.2 nm in continuous scanning mode at a speed of 40 nm/min. Further smoothing of spectra was processed with a Savitzky-Golay filter (10 points, 2nd order).

ThT fluorescence assay

Fresh ThT solution was prepared from stock solution before each measurement at a concentration of 100 μM . An aliquot of α -synuclein solution was diluted by ThT solution and Milli-Q water to reach a final concentration of 3 μM and a ThT concentration of 10 μM in every experiment. An aliquot of prepared α -synuclein solution (70 μl) in each condition was measured in a Bucher Analyst AD plate reader. ThT measurements were performed at an excitation wavelength of 450 nm and an emission wavelength of 485 nm.

Quantitative analysis of ThT assays

The ThT assays were analyzed using the online fitting software AmyloFit, following the referred guidelines⁷¹. In summary, the normalized data were fitted to the general model ‘secondary nucleation dominated, unseeded’. Each fitting parameter was constraint to have identical values for a given experimental condition. The fitted lines are shown in Figure 5.9 (first column). The fitting results were converted into the rate of primary nucleation, λ , and secondary processes, κ , according to

$$\lambda = \sqrt{2 k_+ k_n m_0^{n_c}} \text{ and } \kappa = \sqrt{2 k_+ k_2 m_0^{(n_2+1)}}$$

respectively, where the parameters $k+k_n$, n_c , $k+k_2$ and n_2 were obtained from fitting. The values for the intermediate concentration of 30 μM are plotted in Figure 5.10e in the main text. The half-times shown in Figure 5.10d in the main text were extracted from the normalized curves of the ThT assays using the ‘Half Time Plotter’ functionality of AmyloFit.

Further mechanistic investigation

An alternative approach to investigate which microscopic step is most likely affected by a change in the experimental conditions is to describe the observed effects by allowing variation of only one specific microscopic step and then compare which scenario best describes the data. This analysis was also performed using the online fitting software amylofit, and the general model ‘secondary nucleation dominated, unseeded’. To study effects on primary nucleation, the fitting parameters related to primary nucleation, i.e. k_+ and n_c were allowed to vary with the experimental conditions, whereas the remaining fitting parameters were constrained to one global value for all conditions.

The rate of primary nucleation, λ , was then calculated as before using $\lambda = \sqrt{2 k_+ k_n m_0^{n_c}}$, where m_0 indicated the monomer concentration. The effects on secondary processes were studied analogously, i.e. the fitting parameters related to secondary processes, namely k_+ and n_c , were allowed to vary with the experimental conditions, whereas the remaining fitting parameters were constrained to one global value for all conditions. The rate of secondary processes, κ , was then evaluated according to $\kappa = \sqrt{2 k_+ k_2 m_0^{(n_2+1)}}$ where m_0 denoted again the monomer concentration. Finally, effects on the elongation reaction were studied analogously, but utilizing the model ‘secondary nucleation dominated’, which allows to decouple the rate constant of elongation, k_+ , from the rate constant of primary nucleation or secondary processes respectively. The fitting results are shown in Figures 5.9 (primary nucleation, secondary processes and elongation). Panel a in these figures shows the variation of the parameter allowed to vary with condition. The mean squared errors obtained when allowing different parameters to vary were comparable, and therefore none of the scenarios could be ruled out, i.e. it could not be determined whether the altered experimental conditions mainly affected primary nucleation, secondary processes or elongation. This indicated that the tested experimental conditions influenced the aggregation of α -synuclein in a more complex manner than just one single process. Indeed, the fits represented the data better when changes in both primary nucleation and secondary processes were allowed (compare fits to global fits in the first column of Figure 5.9). This is not surprising given that this study encompasses the effects of several distinct experimental features. The way in which the tested experimental conditions likely affect primary nucleation and secondary processes is discussed in the main text.

5.3 Results

We selected six distinct conditions to study the influence of sedimentation, hydrodynamic mixing and the presence of an air-water interface on the aggregation of α -synuclein, as shown in Figure 5.1 left. The protein solution was studied in three different dynamic conditions: 1) *static*; 2) *orbital shaking*, achieved by shaking at 400 rpm (rotations per minute) on a circular orbit on the horizontal plane;

3) *microgravity environment*, implemented by using a random position machine (RPM) with a 3D-tiltostat configuration, rotating at ~ 30 rpm^{255,267}. Additionally, for each dynamic condition, the protein solution was sealed and incubated either in an Eppendorf tube in the presence of an air-water interface or in a syringe in the absence of any air-water interface. The experiments were performed at pH 7.4, at 37 °C and at a variable initial monomeric concentration between 20 and 65 μM . Aliquots were taken at different time points and characterized by AFM, CD and ThT assays.

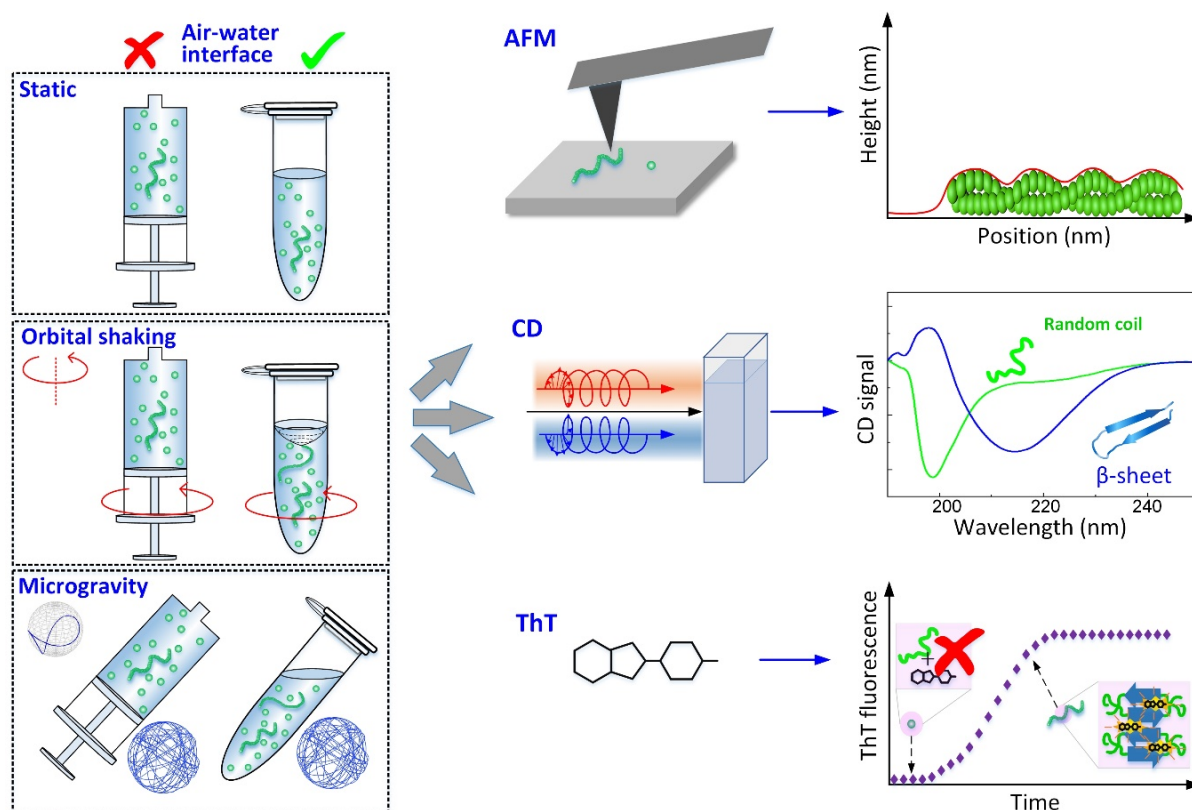


Figure 5.1 Schematic of the experimental approach. Left: The time course of α -synuclein aggregation was studied under a combination of distinct dynamic conditions (static, orbital shaking and microgravity²⁶⁸) and in the presence or absence of an air-water interface, as implemented in Eppendorf tubes or syringes respectively. Right: Experimental methods used to characterize α -synuclein aggregates and aggregation kinetics: high-resolution AFM microscopy to assess aggregates morphology and formation (Top), CD spectroscopy to investigate changes in secondary structure (Middle), and ThT fluorescence assay to study aggregation kinetics (Bottom).

In the static syringe (Static-Syr), the aggregation was subject only to sedimentation effects, while in the Eppendorf tube (Static-Epp) an additional static air-water interface was present. Orbital shaking introduced hydrodynamic mixing effects in the agitated syringe (OShaking-Syr), whereas, in the case of agitated Eppendorf tube (OShaking-Epp), it provoked a combination of hydrodynamic flow and interfacial interaction with a moving air-water interface. In the simulated microgravity environment, the sample sealed in the syringe (microgravity-Syr) experienced less sedimentation compared with the static condition. Whereas the protein solution under microgravity in an Eppendorf tube (microgravity-Epp) was exposed to a continuous 3D rotation of the air-water interface.

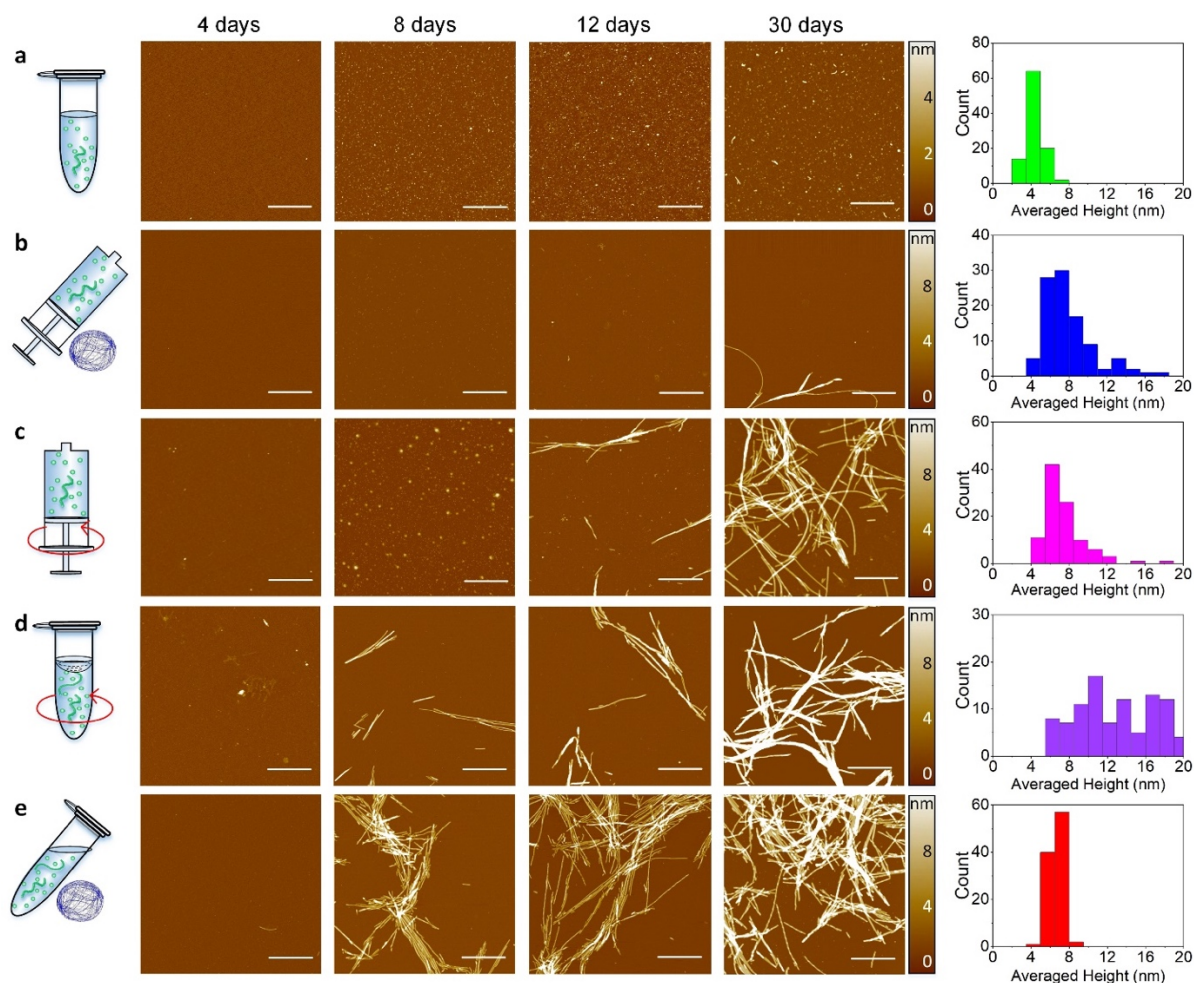


Figure 5.2 High-resolution imaging of amyloid fibrils formation by AFM. Time points of aggregation at 4, 8, 12, 16 and 30 days in static-Eppendorf (static-Epp) (a), microgravity-Syringe (microgravity-Syr) (b), Orbital Shaking-Syringe (OShaking-Syr) (c), Orbital Shaking-Eppendorf (OShaking-Epp) (d) and microgravity-Eppendorf (microgravity-Epp) (e) conditions at initial monomeric concentration of 45 μ M. Scale bar is 1 μ m. The histograms (right) show the statistical distribution of the cross-sectional height of fibrillar aggregates after 30 days.

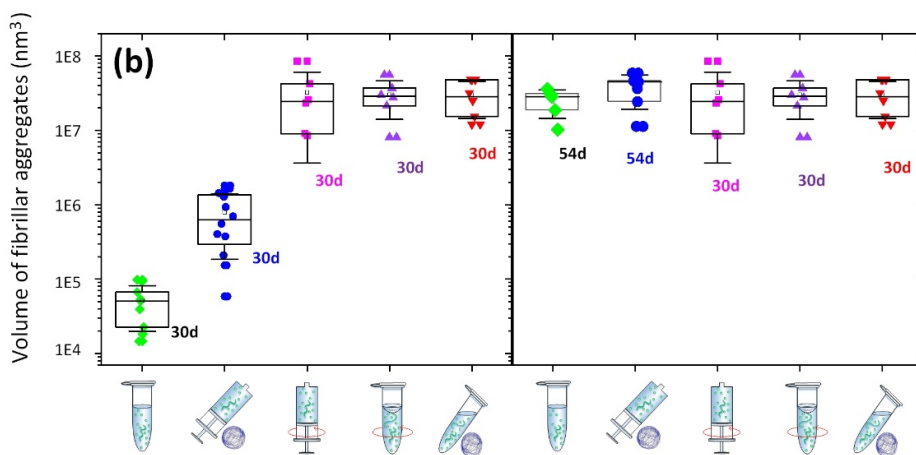


Figure 5.3 Statistical data of the volume of fibrillar aggregates. Fibrils obtained after 30-days incubation (left) and of the mature fibrils obtained in the plateau phase of aggregation. It is clear that, after 30-d incubation, the fibrillar aggregates formed in the Static-Epp and microgravity-Syr conditions were two orders lower than that of other conditions. In comparison, these values of mature fibrils are in the same order of magnitude, indicating that the initiating monomeric protein could yield the similar amount of fibrillar aggregates in the final plateau stage under different studied conditions.

5.3.1 Nanoscale imaging of α -synuclein amyloid formation

To unravel the process of protein fibrillization at the single aggregate scale, we used high-resolution AFM imaging of the 3D morphology of individual protein assemblies (Figure 5.2). To improve adsorption of the negatively charged α -synuclein species on the surface, we exploited the positive chemical functionalization of mica by APTES (Methods section). For each of the conditions shown in Figure 5.1, we collected an aliquot of the aggregating solution after 4, 8, 12, 16 and 30 days of incubation, which were then deposited on the positive functionalized mica. This approach enabled to monitor the process of aggregation at high spatial resolution and at the single aggregate level.

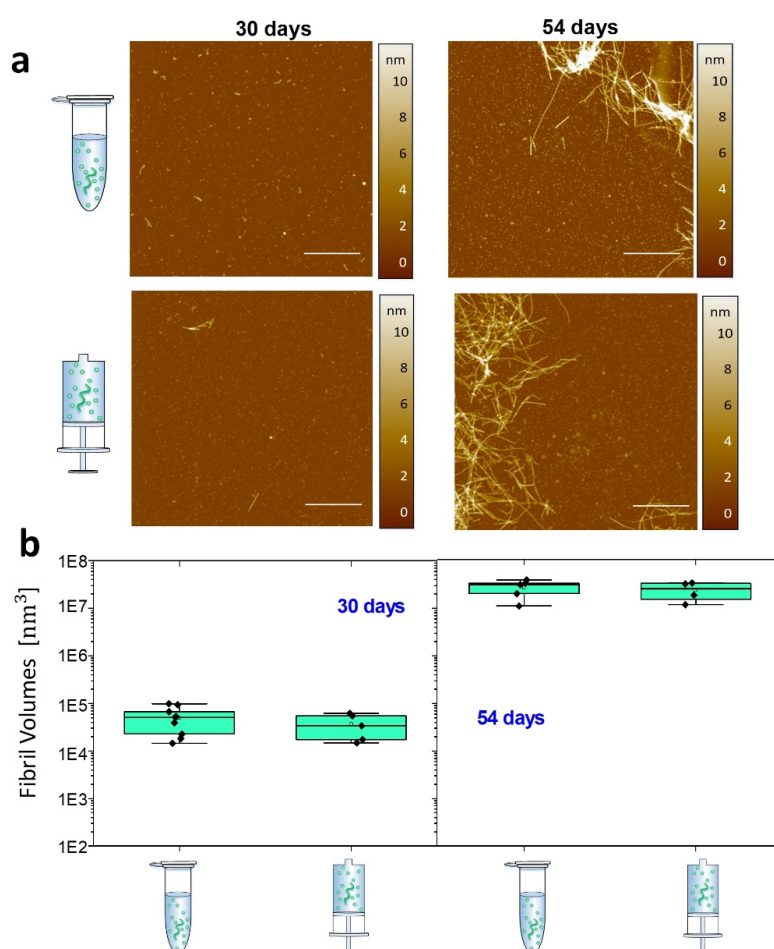


Figure 5.4 Comparison of amyloid formation in static conditions in Eppendorf tubes with an air-water interface and syringes without an air-water interface. (a) AFM images of protein aggregates obtained in Static-Epp and Static-Syr conditions after 30 and 54 days of incubation. The scale bar is 1 μ m. (b) Statistical analysis of the volume of the formed fibrillar aggregates after 30 days (left) and 54 days (right) of static incubation for Eppendorf and syringe incubation. This result indicates that a similar speed of fibrillar aggregates formation in these two conditions.

A qualitative observation of the aggregation in each condition of incubation demonstrates that protein aggregated slower in static and microgravity syringe conditions. In static conditions in both the absence and presence of an air-water interface only very few and short protofibrils with typical fibril

cross-sectional diameter of 4 ± 2 nm were formed after 30 days (Figure 5.2a). The formation of mature amyloid fibrils occurred both in the presence and absence of an air-water interface only after 54 days. Remarkably, in static conditions, the presence of the air-water interface did not significantly affect the process of amyloid formation. In microgravity-Syr conditions, mature fibrillar aggregates with cross-sectional diameter above 6 nm were observed already after 16 days, they increased in abundance after 30 days incubation, and the formation of abundant mature amyloid fibrils was observed after 54 days. In contrast, OShaking-Epp conditions lead to the formation of mature fibrillar aggregates after only 16 days of incubation. In the presence of a moving air-water interface (OShaking-Epp and microgravity-Epp), abundant mature fibrillar aggregates were formed already after 8 days of incubation. These aggregates had typical lengths of few micrometers and a cross-sectional height above 6 nm.

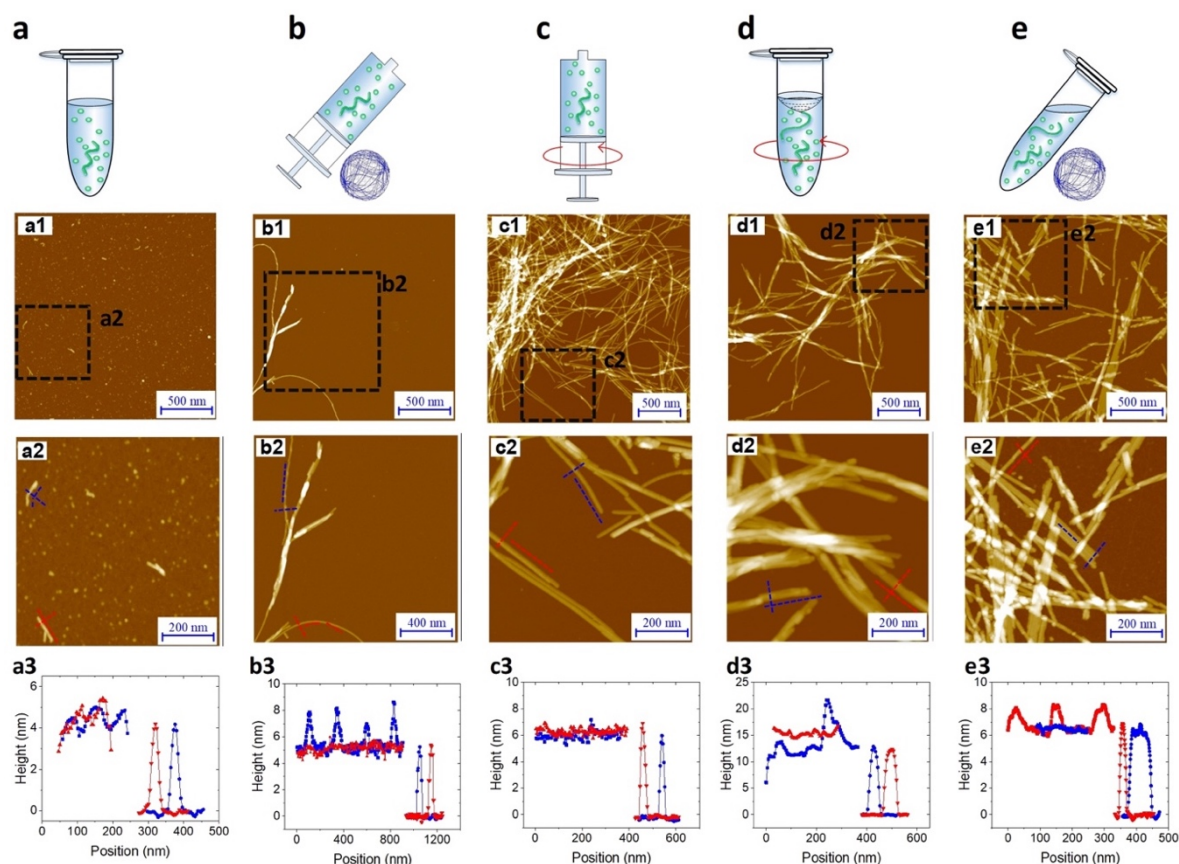


Figure 5.5 Morphological characterization of amyloid fibrils after 30 days of incubation. (Left) AFM images of fibrils formed after 30 days. (Middle) The zoom-in AFM image in the area indicated in (a1-e1) to show the detailed shape of fibrils. (Right) The fibril height profiles along the dashed lines indicated in the AFM images.

We confirmed these observations by measuring quantitatively the volume of fibrillar aggregates formed at different time points under each condition (Figure 5.3). After 30 days of incubation, less fibrillar mass was formed under static and microgravity-Syr conditions in comparison to all other

incubation conditions. In both static conditions, i.e. irrespective of the presence or absence of an air-water interface, we observed a similar speed of aggregation and similar amounts of fibrils formed (Figure 5.4). After 54 days of incubation, a similar volume of fibrillar aggregates was produced in all conditions (Figure 5.3). The data indicates that sedimentation has the capability to slower the aggregation kinetics and that reduced sedimentation effects in a microgravity environment slightly increases the speed of amyloid formation. Moreover, we observed that the amyloid fibrils formed in each condition showed a high degree of polymorphism (Figures 5.5 and 5.6).

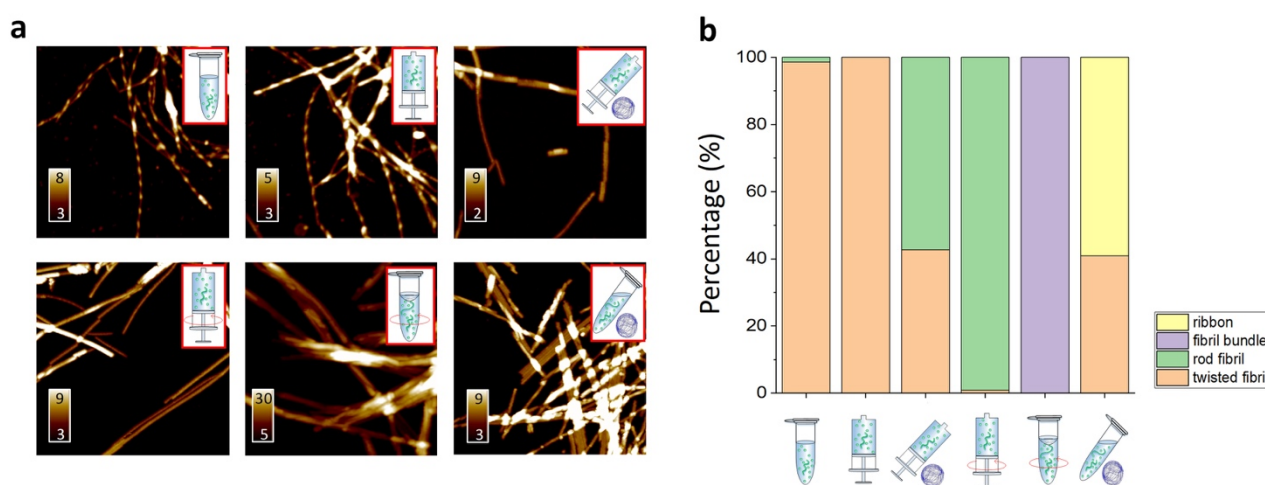


Figure 5.6 Polymorphism of mature amyloid fibrils produced in each condition. Statistical analysis of fibril morphology in each condition. The result shows that the dominating twisted fibrils was found in the static conditions, while homogeneous rod fibrils and fibril bundles were observed in the OShaking-Syr and OShaking-Epp conditions respectively. However, heterogeneous fibrils, including rod fibril and twisted fibril, were revealed in the microgravity-Syr condition, and the coexistence of ribbon and twisted fibril was observed from microgravity-Epp condition.

5.3.2 Correlation of CD spectroscopy and ThT fluorescence to characterize aggregation

CD spectroscopy was used to monitor the secondary structural transition from the disordered native form of monomeric α -synuclein to the amyloid cross- β sheet conformation. Random coil and cross- β sheet show typical absorptions at 198 nm and 220 nm, respectively (Figure 5.1). In all the experimental conditions studied in the present work, aliquots of the aggregation reaction were collected to acquire CD spectra as a function of the incubation time. The CD spectra recorded at a concentration of 45 μ M are shown in Figure 5.7 left. For all the studied conditions, the gradual shift of the minimum of the CD spectrum at 198 nm to 220 nm indicated the formation of cross- β sheet conformation as a function of the incubation time.

The ThT dye shows a specific fluorescence signal upon binding to cross- β sheet aggregates^{67,269}, and can be used to monitor the aggregation kinetics of α -synuclein. We studied the aggregation process at the initial monomeric concentrations of 20, 30, 45, 55, 60 μ M (Figure 5.7 and 5.8).

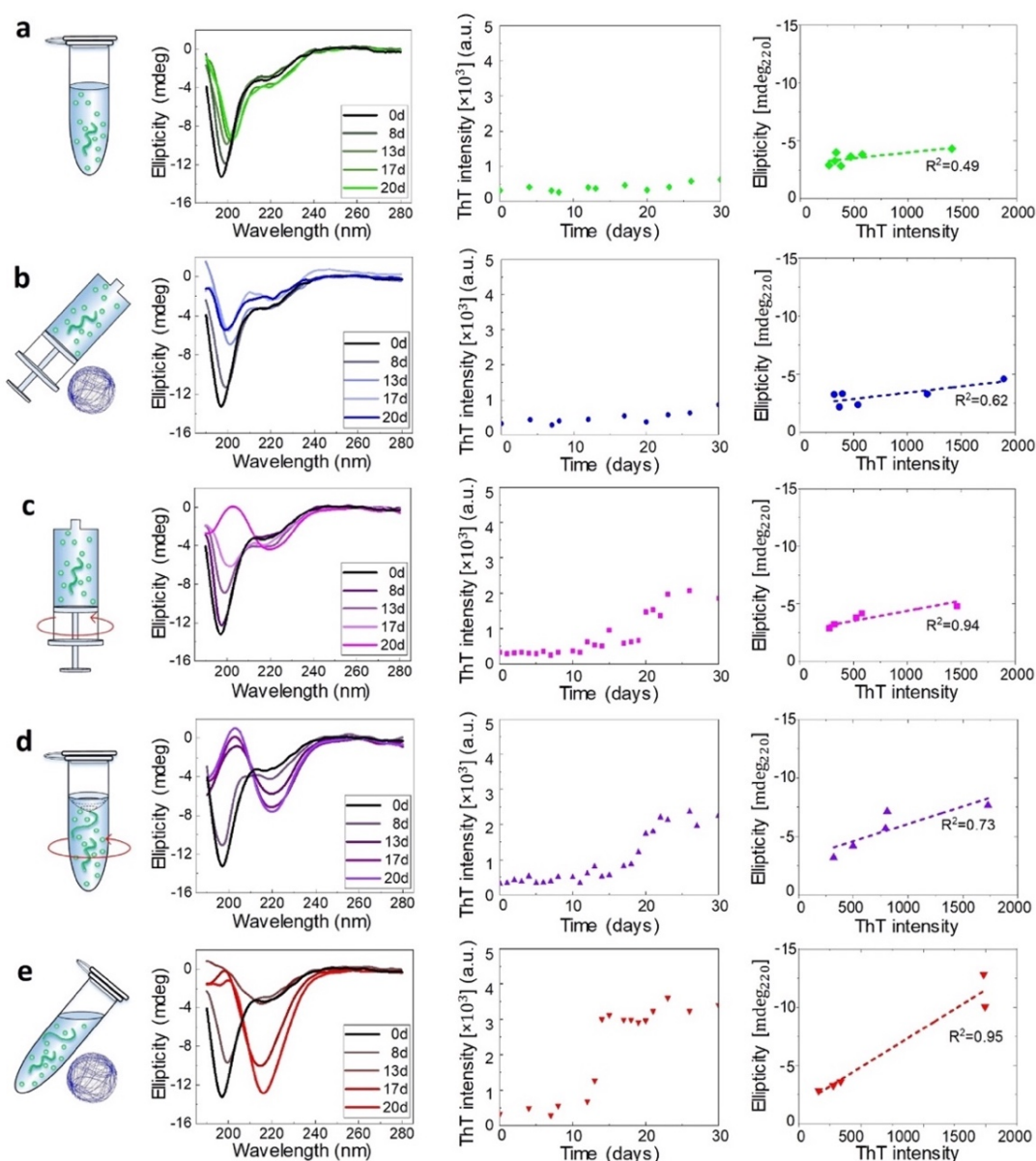


Figure 5.7 CD and ThT characterization of α -synuclein aggregation at $45 \mu\text{M}$. For each experimental condition defined in Figure 1, we show as a function of the incubation time the CD spectra (Left), the ThT assay (Middle) and the correlation at each time point between ThT intensity and CD signal at 220 nm (Right). The dashed lines are the best linear fits to the scattering plots.

In each condition defined in our work, we then quantitatively evaluated the propensity of α -synuclein to form cross- β sheet amyloid fibrils as a function of the incubation time by correlating at each time point the increase of ThT fluorescence versus the structural change measured at 220 nm ^{260,270}. In **Figure 5.7** middle, the kinetic curves of aggregation in each condition at $45 \mu\text{M}$ are presented. A steeper curve indicates faster kinetics of aggregation. Then, in Figure 5.8 right, we show a plot of the intensity of ThT fluorescence versus the absolute value of CD intensity, where the slope of the linear fitting of the ThT vs. CD data was used to characterize the tendency to form cross- β sheet fibrillar protein (**Figure 5.10a-b**).

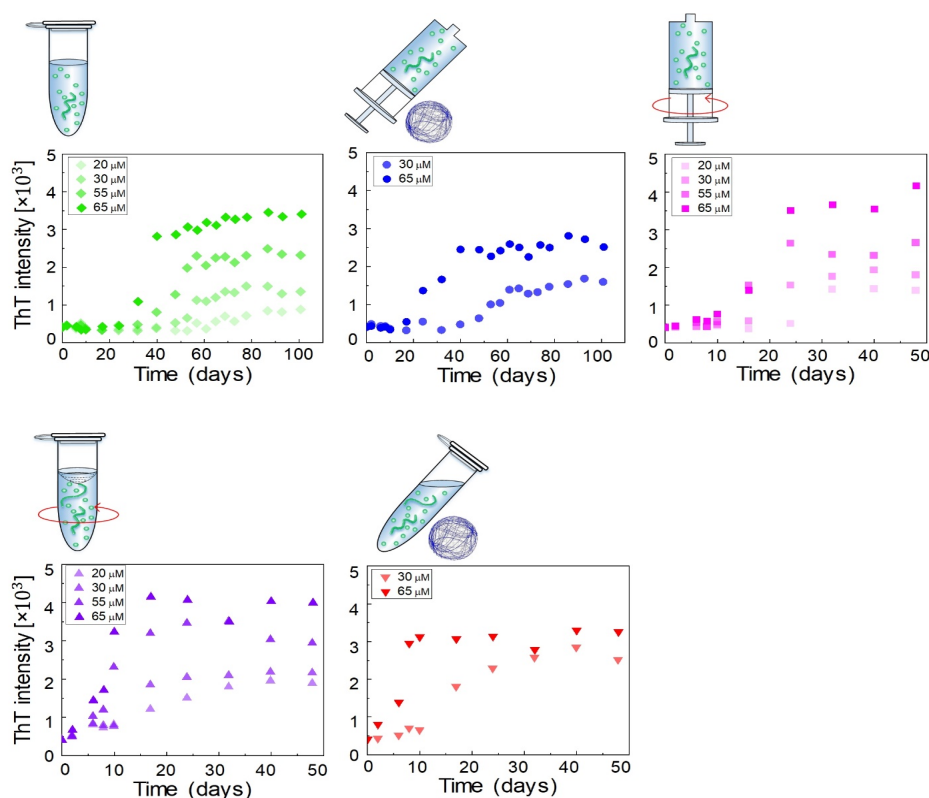


Figure 5.8 ThT assay of α -synuclein at different concentrations in each condition. The ThT fluorescence measurement of α -Synuclein of monomeric protein concentration of 20, 30, 55, 65 μM in the static-Epp, OShaking-Syr, OSaking-Epp conditions. Another two assays were performed of initiating protein concentration of 30 and 65 μM in the microgravity-Syr and microgravity-Epp conditions. Only two measurements were performed in the microgravity condition due to the limited space on the rotating plate of the RPM system, since placing the sample away from the rotational center, would not allow to have average low gravity vector during the experiment^{255,266}.

The data indicated that the kinetics of aggregation and structural transition to fibrillar amyloid cross- β sheet of α -synuclein in static (Static-Epp and Static-Syr) and microgravity-Syr conditions are significantly slower than the kinetics of aggregation in the presence of strong hydrodynamic mixing and a moving (OShaking-Epp) and 3D rotating (microgravity-Epp) air-water interface. Aggregation of α -synuclein under OShaking-Epp conditions showed intermediate kinetics of aggregation and cross- β sheet formation. The spectroscopic and kinetic data were in excellent agreement with the AFM quantification of the volume of formed fibrillar aggregates as measured by AFM as a function of the incubation time (Figure 5.9). The described trends of relative aggregation rates were also reflected in the aggregation half-times $t_{1/2}$ measured in the ThT assays (Figure 5.10). Interestingly, reduced gravitational effects seemed to alter the concentration dependence of the relative overall aggregation rate as compared to ambient conditions. This indicated that the different experimental conditions tested influence the aggregation of α -synuclein in a complex manner, likely effecting more than one microscopic step.

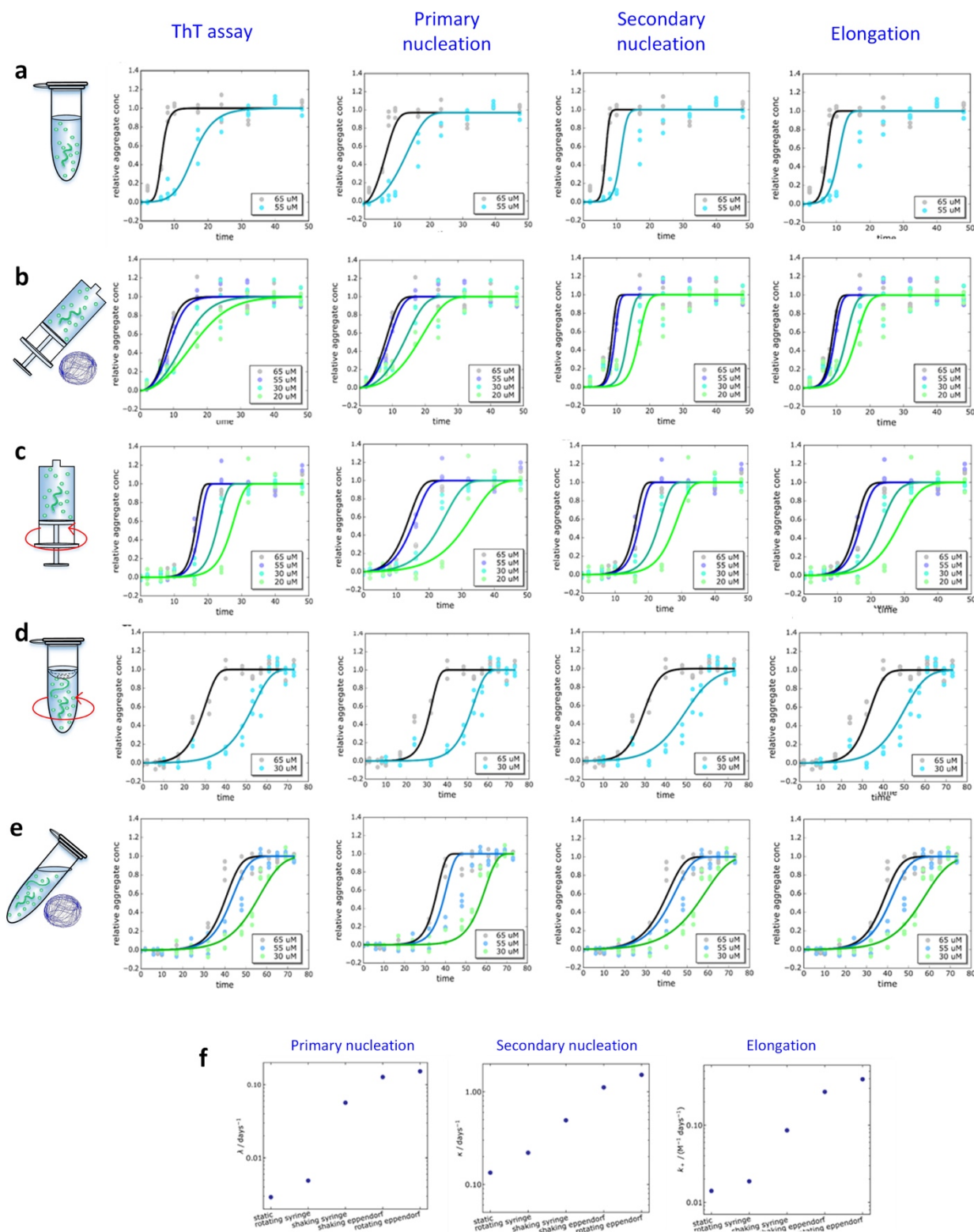


Figure 5.9 Global fitting of ThT assay and fitting results. (a-e) Global fitting of the ThT aggregation assay, and the global fitting results assuming that the tested experimental conditions mainly affected primary nucleation, secondary nucleation and elongation of α -synuclein aggregation, in the a) microgravity-Epp, b) OShaking-Epp, c) OShaking-Syr, d) microgravity-Syr and e) Static-Epp experimental conditions. All curves of the ThT assays were fitted simultaneously, but they are plotted separately for each condition to improve clarity. (f) Rate of primary nucleation, secondary processes and elongation against tested experimental conditions.

5.3.3 Chemical kinetics analysis

We have established that the different experimental conditions tested affect the overall rate of aggregation of α -synuclein in distinct ways. To understand the origin of these effects, a chemical kinetics analysis was performed (Figure 5.9). The underlying principle of this analysis is to map the differences in the aggregation curves to changes in the rate constants of the individual microscopic steps. For α -synuclein, the reaction network of microscopic steps consists of primary nucleation, i.e. the spontaneous formation of new aggregates, growth or elongation of existing fibrils and secondary processes, in which existing aggregates facilitate the formation of additional fibrils^{70,271,272}. The rate constants and rates of each microscopic step can be obtained from global fitting of a measurement of the aggregate concentration over time, as recorded in ThT assays, to an integrated rate law (see Methods section)^{71,273}.

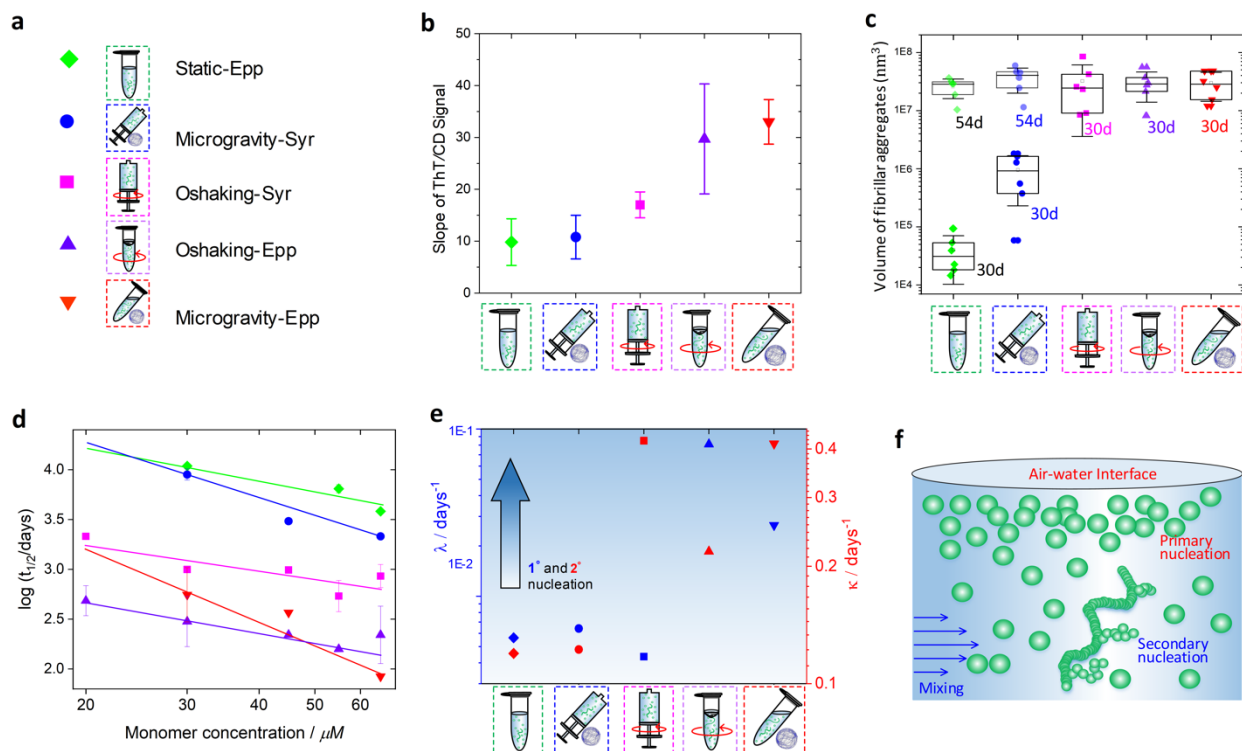


Figure 5.10 Effects of environmental stimuli on α -Syn microscopic steps of aggregation. (a) Legend of the condition of incubation used in the present work. (b) Slope of the ThT vs. CD signal at $45 \mu\text{M}$. (c) Correlation between formed fibril volume and the slope of CD vs. ThT measurements. (c) Volume of the fibrillar aggregates formed under incubation in each condition after 30 days (solid points) and 54 days (transparent points). (d) A double logarithmic plot of the half time of aggregation versus initial protein concentration. (e) Rates of primary nucleation (blue) and secondary (red) processes at $30 \mu\text{M}$ monomer concentration obtained from global fitting of the aggregation kinetics at the different conditions to an integrated rate law. (f) Schematic representation of the effect of hydrodynamic mixing and air-water interface on primary nucleation and secondary process during aggregation of α -synuclein. Primary nucleation is significantly increased in the presence of a moving air-water interface, whereas secondary processes are increased by rotating in the presence of an air-water interface or shaking.

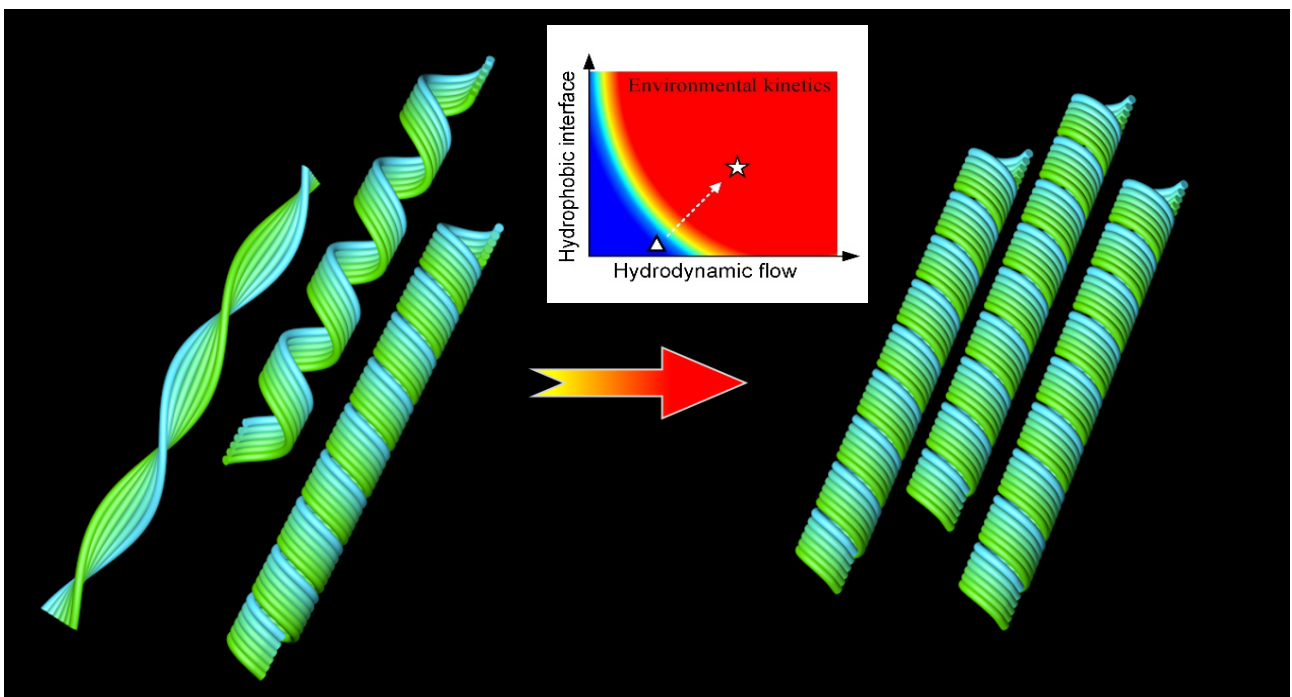
In Figure 5.10e, the rates of primary nucleation, λ , and secondary processes, κ , are plotted against the tested experimental conditions. Sedimentation effects, as probed by the microgravity-Syr condition, did not significantly affect the rates of primary nucleation or secondary processes of α -synuclein as compared to the reference, static-Epp. We found that primary nucleation was significantly increased in the presence of a moving air-water interface (OShaking-Epp and microgravity-Epp). This result agrees with previous studies of the interactions between α -Syn aggregates and hydrophobic interfaces such as lipid membranes^{271,274}. A plausible explanation is the accumulation of monomeric proteins onto the air-water interface due to interactions with hydrophobic protein domains^{251,275,276}. Secondary processes, on the other hand, were facilitated by rotating in the presence of an air-water interface or shaking. This indicates that agitation promotes secondary processes, but the accelerating effect differs with the agitation approach, i.e. with the type of the flow field and intensity^{240,244}.

5.4 Conclusion

In summary, we present a comprehensive study that explores the influence of several environmental factors on α -synuclein aggregation, including microgravity-induced under-sedimentation, hydrodynamic mixing and interactions of the air-water interface.

Our results reveal that microgravity-induced under-sedimentation shows minor differences when compared to slow aggregation in static conditions, independent of the presence of a static air-water interface. Inhibition of sedimentation by microgravity results in only a slight promotion of aggregation and mature fibril formation, which is consistent with previous reports^{257,277,278}, but it exhibits no significant difference on the rates of primary nucleation nor secondary processes. Hydrodynamic mixing highly promotes the formation of amyloid fibrils, both in the presence and absence of an air-water interface. Under orbital shaking and in the absence of an air-water interface, the presence of hydrodynamic mixing increases the rate of secondary process during the aggregation, an effect that has been observed for other amyloid forming systems and was there attributed to increased fragmentation²⁷⁹. In the presence of a moving air-water interface, a further increase of the rate of primary nucleation is observed, as shown in **Figure 5.10e-f**. This increased rate of primary nucleation may be a result of the interaction of monomeric proteins at the air-water interface. Overall, these observations enrich the understanding of the influence of environmental stimuli on the microscopic steps determining the phenomenon of α -synuclein amyloid formation. Environmental factors are not only critical in promoting fibril formation, but are of great importance for the comprehension of α -synuclein aggregation and amyloid formation, which is fundamental for attempting high-throughput assays and seeking pharmacological treatments for Parkinson's disease.

Chapter 6 Environmental control of amyloid polymorphism and order-order transition among fibril polymorphs



This chapter contains a manuscript in preparation:

Jiangtao Zhou¹, Francesco S. Ruggeri^{2,3}, Leonardo Venturelli¹, Ludovic Keiser⁴, Sergey Sekatskii¹, François Gallaire⁴, Sandor Kasas¹, Giovanni Longo⁵, Tuomas P. J. Knowles^{2,3} and Giovanni Dietler¹. *Environmental control of amyloid polymorphism and order-order transition among fibril polymorphs*. In preparation.

Affiliations:

1. *Laboratory of Physics of Living Matter, Ecole Polytechnique Fédérale de Lausanne (EPFL), CH-1015 Lausanne, Switzerland*
2. *Department of Chemistry, University of Cambridge, Lensfield Road, Cambridge CB2 1EW, UK*
3. *Centre for Misfolding Diseases, Department of Chemistry, University of Cambridge, Lensfield Road, Cambridge CB2 1EW, UK*
4. *Laboratory of Fluid Mechanics and Instabilities, Ecole Polytechnique Fédérale de Lausanne (EPFL), CH1015 Lausanne, Switzerland*
5. *Istituto di Struttura della Materia, CNR, Via del Fosso del Cavaliere 100, 00133, Roma, Italy*

Abstract. The phenomenon of amyloid polymorphism is known as one of the key features of protein aggregation. Unravelling the underlying mechanism of this phenomenon is critical for understanding pathways of pathological amyloid fibrillization that associated with various neurodegenerative diseases, as well as the amyloid-based biomaterial and biotechnological applications. However, the origin of amyloid polymorphism and the interplay among the polymorphs are still elusive. In this work, we established an unprecedented association between fibril polymorphism and the strength of environmental kinetics originating from hydrophobic air-water interface and hydrodynamic flow. Our results reveal that polymorphic fibrils, including twisted, helical and rod-like fibrils, were observed in the environmentally low-kinetic conditions, whereas homogeneous rod-like fibrils were generated under the high-kinetic condition. Remarkably, the transition from twisted and helical fibrils to rod-like fibril by mediating the environmental kinetics shows that the evolutionary mechanism of amyloid polymorphs due to their difference on the free-energy map. These results may enrich our understanding on the polymorphic origin of pathological fibrils, and also shine a light on the controlled manufacturing of homogeneous amyloids for biomaterial applications.

6.1 Introduction

Pathological amyloid formation is a significant feature of a number of neurodegenerative disorders such as Alzheimer's and Parkinson's diseases^{58,60,83}. Moreover, functional amyloid fibrils, due to their exceptional mechanical properties, have been gaining increasing interests in biotechnological applications, such as biosensor, biomimetic material and drug delivery^{280,281,115}.

Amyloid polymorphism, referring to the diversity of fibril architectures such as twisted and rod-like fibrils, is a wide-spread phenomenon in the amyloid fibrillization both *in vitro* and *in vivo*^{78,93,94,96,282}. Understanding the underlying mechanism of this phenomenon is of fundamental significance for studying both pathological and functional amyloid fibrillization pathways. For the former case, the pathological fibrils with various polymorphs *in vivo*^{90,94} has been proved to show distinct biological effects on living systems, e.g. prion strain and cytotoxicity^{78,283}. For the latter case, homogenous fibril with less diversity in mesoscale structure is crucial in their material performance^{85,93,95,282,284}, e.g. mechanical properties. Environmental control is an efficient mediating tool in the biological system²⁸⁵⁻²⁸⁷ and nevertheless, the knowledge of environmental controlling fibril morphological differentiation is not enough. Protein aggregation kinetics can be varied by the environmental factors such as pH^{235,288}, ionic strength^{235,289}, interfaces²⁹⁰, and agitation²³⁵. It was noted that fibril polymorphism is correlated with kinetic origin²⁹¹ and the ionic strength^{237,282} and pH values^{284,288,292} exhibited the potential to control twisted fibril periodicity. Remarkably, the transition between heterogeneous fibrils during their self-fibrillization was observed^{93,96,97}, indicating the interplay between distinct polymorphs. However, the underlying mechanism of polymorphic fibril formation and its correlation with environmental factors remain unclear.

In this work, we present the α -Synuclein (α -Syn) fibril polymorphism under the control of the strength of environmental kinetics, originated from air-water interface and hydrodynamic flow. Hydrophobic air-water interface^{247,293,294}, as a typical hydrophobic-hydrophilic interface that includes lipid membrane^{241,295} and polymeric nanoparticles²⁴⁰, exhibits an adsorption effect on the protein assemblies^{247,251,294} and thus significantly impacts on the aggregation kinetics^{247,269}, secondary-structure^{293,296} and morphology²⁵¹, such as triggering primary nucleation^{240,297} and forming spontaneous curved fibrils²⁵¹. On the other hand, hydrodynamic flow has been proved to influence the aggregation kinetics by promoting protein-protein interaction^{235,244} and secondary nucleation^{240,244,297}, and this influence mainly depends on the strength and the types (shear or extensional) of the flow^{236,244,298}. Remarkably, hydrodynamic and interfacial effects also show synergetic environmental impacts in

many physiological circumstances^{240,299,300} ranging from the bloodstream to cerebrovascular system^{301,302}.

Our results reveal that the environmental kinetics is capable of varying fibrillization mechanisms and determining the polymorphism of fibril architectures. Low environmental kinetics may generate polymorphic fibrils, whereas high environmental kinetics could yield homogeneous rod-like fibrils. Remarkably, we observed the order-order transition from heterogeneous fibrils to uniform rod-like fibrils by modulating the environmental kinetics, confirming that fibril polymorphs hold distinct free-energy levels. These results might not only shine a light on understanding the origin of amyloid polymorphism in the physiological condition, but also open a window for controlling fibril polymorphism and for generating homogeneous fibrils for the functional material applications.

6.2 Experimental methods

Sample preparation

Full-length recombinant human α -Synuclein (AnaSpec, USA) was dissolved in buffer (50 mM Tris·HCl, 150 mM NaCl, pH 7.4) and filtered with 100 kDa filter. The concentration of α -Syn solution was measured by ultraviolet absorbance (Nanodrop 2000). An aliquot (1 mL) of α -Syn solution was sealed in five sterilized low protein binding wall syringes incubated in different conditions at a concentration of 30 μ M at 37 °C. Three syringes were incubated with large, small and none bubble in the oscillating conditions, and another syringe with small bubble was statically incubated. In the cases of large and small bubbles, the volume ratio of the protein solution and air bubble in the L-bubble and S-bubble conditions was maintained 2:1 and 4:1 respectively in the experiment. The size of air-water interface in the L-bubble conditions were roughly 2-3 times larger than that in the S-bubble conditions.

Rotating bioreactor system

The three oscillating syringes with different sizes of bubbles were incubated on the platform of an in-house developed random positioning machine (RPM) at 37 °C. The rotation of the platform was regulated by two independent motors in three dimensions, which enables the rotation in random direction. The samples were fixed at the center of the RPM machine. The rotation speed of RPM was considerably slow, approximately 5 rpm, to maintain a gentle bubble oscillation in the syringe.

CFD simulation

To quantify the hydrodynamics generated by bubble motion, we performed a computational fluid dynamics (CFD) simulation using the finite elements method. The oscillating bubble generates a hydrodynamic flow in the capillary and its flow field could be decomposed in two contributions: the strain rate and the shear rate (Figure 6.2), referring to the extensional flow and shearing flow field, respectively. In which, however, the strain rate (elongational) is known to be crucial for protein aggregation due to its ability of stretching protein molecules and to increase protein

kinetics compared with the shear rate²⁴⁴. In Figure 6.1b, the strain rate maximized, of the order of 10 s^{-1} , at the rear and at the front side of bubble, due to an intermediate Reynolds number ($\text{Re}=60$) of the protein solution. Meanwhile, no significant difference of flow field and strain rate values were observed between the Oscillating L-bubble and the Oscillating S-bubble conditions (Figure 6.2).

The CFD simulations were carried out by using the laminar flow module of the finite element method (FEM) solver Comsol (COMSOL Inc., MA, USA). To account for the flow created by the buoyancy-driven bubble oscillation in the experiments, we performed the simulation in the frame of the bubble. The dimensions of the capillary were $1 \times 16 \text{ cm}$ while the height of the bubble was 7 mm . The no-slip boundary condition was applied to the walls of the capillary, and the interface of this air bubble was considered to be shear-free (full slip) as a reasonable assumption for air-liquid interfaces. A flow of constant flow rate $q = V * d$ was injected from the left of the capillary, where d is the capillary width and V is the mean velocity of the flow. Here we took $V = 10 \text{ mm/s}$ to meet the velocity of bubble motion in the experiment, which corresponds to a Reynolds number:

$$\text{Re} = \rho V d / \mu = 60$$

where ρ and μ are the density and viscosity of protein solution respectively. We neglected the orientation variation of the oscillatory flow as the hydrodynamic flow can be represented in each cycle and the strain rate distributes mainly due to the expansion of the flow independent from bubble oscillation. Navier-Stokes equations were solved in bidimensional domain composed of 18433 mesh elements and 801 boundary elements (corresponding to 28854 degrees of freedom solved). The simulations converged and doubling the number of mesh elements led to the same results. The shear rate (sh) and strain rate (st) are defined in the following as

$$sh = \sqrt{\left(\frac{\partial u}{\partial y}\right)^2 + \left(\frac{\partial v}{\partial x}\right)^2}, \text{ and } st = \sqrt{\left(\frac{\partial u}{\partial x}\right)^2 + \left(\frac{\partial v}{\partial y}\right)^2}.$$

where u and v respectively represent the velocity field component in the x and y direction. The shear rate is defined as the norm of the gradient of the hydrodynamic flow velocity in the direction normal to the streamline that indicates the shearing flow field. The strain rate is characterized by the norm of the gradient of the flow velocity in the direction parallel to the streamline that corresponds to the extensional flow field. This choice for the formula enabled to provide a close estimation of the force to which protein oligomers and aggregates are subjected.

CD spectroscopy

An aliquot of diluted α -Syn solution ($15 \mu\text{M}$) was analyzed at room temperature with a Jasco J-815 CD spectrometer in the range of 190-280 nm in each measurement. A high-quality quartz cuvette with an optical path length of 1.0 mm was employed and spectra were collected with the resolution of 0.2 nm in continuous scanning mode. Further smoothing of spectra was processed with a Savitzky-Solay filter in OriginPro (OriginLab, MA, USA).

ThT Assay

Fresh ThT solution was prepared from stock solution before each measurement at the ThT concentration of 100 μM . An aliquot of $\alpha\text{-Syn}$ solution was diluted by ThT solution and Milli-Q water to reach a final protein concentration of 3 μM and ThT concentration of 10 μM in every experiment. An aliquot of prepared $\alpha\text{-Syn}$ solution (70 μl) in each experiment was measured three times in a Bucher Analyst AD plate reader. ThT fluorescence reading was performed at an excitation wavelength of 450 nm and an emission wavelength of 485 nm. The signal of fluorescence intensity was fitted with a sigmoidal model according to:

$$y(t) = \frac{A}{1 + e^{-(t-t_{50})/\tau}}$$

where A is the difference of fluorescence intensity between plateau and baseline on ThT curve, t is the incubation time, t_{50} is the time at which the signal reaches half of the average value of the plateau and baseline and $1/\tau$ is the rate of fibril growth^{137,235,247}.

AFM measurement

Aliquots of $\alpha\text{-Syn}$ solution (30 μM) were collected each time point and diluted to 10 μM before each AFM measurement. Freshly cleaved mica was functionalized by an aliquot (10 μl) of freshly prepared 1% (3-Aminopropyl) triethoxysilane (APTES) for 1.5 minutes, and then rinsed with Milli-Q water and dried using gentle air flux. Then, an aliquot (10 μl) of $\alpha\text{-Syn}$ solution was deposited on the mica for 4 minutes, followed by a smooth rinsing of Milli-Q water and a gentle flow of nitrogen gas. AFM measurements were operated by Park NX10 AFM (Park Systems, South Korea) in the non-contact mode using NCHR cantilevers (Nanosensors, Switzerland), which processes a nominal spring constant of 42 N/m and a typical tip radius of less than 7 nm. A weak tip-sample interaction was applied during scanning by monitoring the scanning phase within a variation of 5° for accurate scanning. AFM images were simply flattened using XEI software (Park Systems, South Korea) in the first order to minimize the potential defects.

AFM statistical analysis

The statistical analysis of flattened AFM images was carried out using the DNA-trace software developed before³⁰³. The profile of amyloid fibrils was traced along amyloid fibrils by selecting the maximal height point in every cross-section. The statistical determination of the fibril length was obtained by measuring the contour length of each fibril. However, the average height and smoothness was recorded by retracing each fibril by avoiding the overlapping regions. The average height was calculated by averaging the height value of all points along fibril profile and smoothness was measured by counting 80% of the variation of all height values vs. the average height.

QI-AFM imaging

QI-AFM imaging was performed by using JPK Nanowizard III microscope (Bruker, USA) with a high-sensitivity cantilever (PPP-CONTSCAuD, Nanosensors) with a nominal spring constant of 0.2 N/m and a typical tip radius of less than 7 nm. The spring constant and deflection sensitivity of used cantilever were calibrated before each measurement. All acquired images had size of 5 \times 5 μm^2 and we used the Quantitative imaging (QITM) mode with a

resolution of 256×256 pixels. Each force-distance (FD) curve was recorded as a single pixel in the QI-AFM image. The data acquisition rate was 50,000 Hz and the maximum force was set to 10 nN with an indentation length of 500 nm. A complete FD curve (extension and retraction) was recorded in 10 ms. At least five QI-AFM images were collected for each sample for a total of 327'680 FD curves. Image processing was carried out using the JPK Data Processing software (Bruker, USA). The force curve batch was processed with the following steps: calibration of spring constant and deflection sensitivity, correction of baseline offset and tilt, determination of contact point, and elasticity fitting. The Young's modulus is determined by fitting extend FD curve to avoid the influence of plastic deformation, with an assumption of Derjaguin-Müller-Toporov (DMT) model and sphere tip shape. A Poisson ratio of 0.3 was used in the calculation as a reasonable assumption for amyloid fibrils^{304,305}.

A threshold filter of Matlab (MathWorks Inc., CA, USA) script was developed to allow us to precisely evaluate the image and distinguish amyloid fibrils from substrate background. Further calculation and statistical analysis were realized in OriginPro (OriginLab Corporation, MA, USA).

6.3 Results

6.3.1 *Experimental setup and hydrodynamics simulation*

The study of α -Syn aggregation with the synergetic influence of hydrodynamic flow and air-water interface was performed by controlling the motion of the air bubble in the syringes sealed with the protein solution (Figure 6.1a-b). In the hydrodynamic case, the protein incubation was carried out in a random positioning machine (RPM)^{255,268,306} bioreactor that allows a gentle reciprocating motion of the bubble in the syringe (see Methods). Three syringes of α -Syn solution at $30\mu\text{M}$ were prepared with different bubble sizes: large bubble (Oscillating L-bubble), small bubble (Oscillating S-bubble) and no bubble (Oscillating non-bubble), as shown in Figure 6.1c. The volume ratio of liquid-bubble in the large and small bubble conditions were maintained 2:1 and 4:1 respectively. Besides, another syringe with a small bubble in the static condition (Static S-bubble) was incubated.

In the hydrodynamic cases, the gentle reciprocating movement of the bubble (Figure 6.1a) led to a combined environmental kinetics originated from interface and hydrodynamic flow. To quantify the hydrodynamic effect, we performed a computational fluid dynamics (CFD) simulation (Figure 6.1b and Methods), indicating two main hydrodynamic contributions: the strain rate and the shear rate (Figure 6.2) that refer to the elongational flow and shearing flow field, respectively. This result showed that no significant difference of flow field and strain rate values were observed between Oscillating L-bubble and Oscillating S-bubble conditions (Figure 6.2), but only a slight difference in the shearing flow field. Therefore, in addition to a slight hydrodynamic difference, the main difference between in the Oscillating L-bubble and Oscillating S-bubble conditions was the interfacial effect,

where the volume of the air bubble in the former case was maintained twice larger than that of later case in this experiment.

By contrast, the protein solution in the Oscillating non-bubble condition suffered no air-water interface but a much lower magnitude of hydrodynamics generated by dissolved microbubbles^{307,308} and insoluble protein aggregates. Besides, the protein solution in the static condition (Static S-bubble) was only exposed to the air-water interfacial effect.

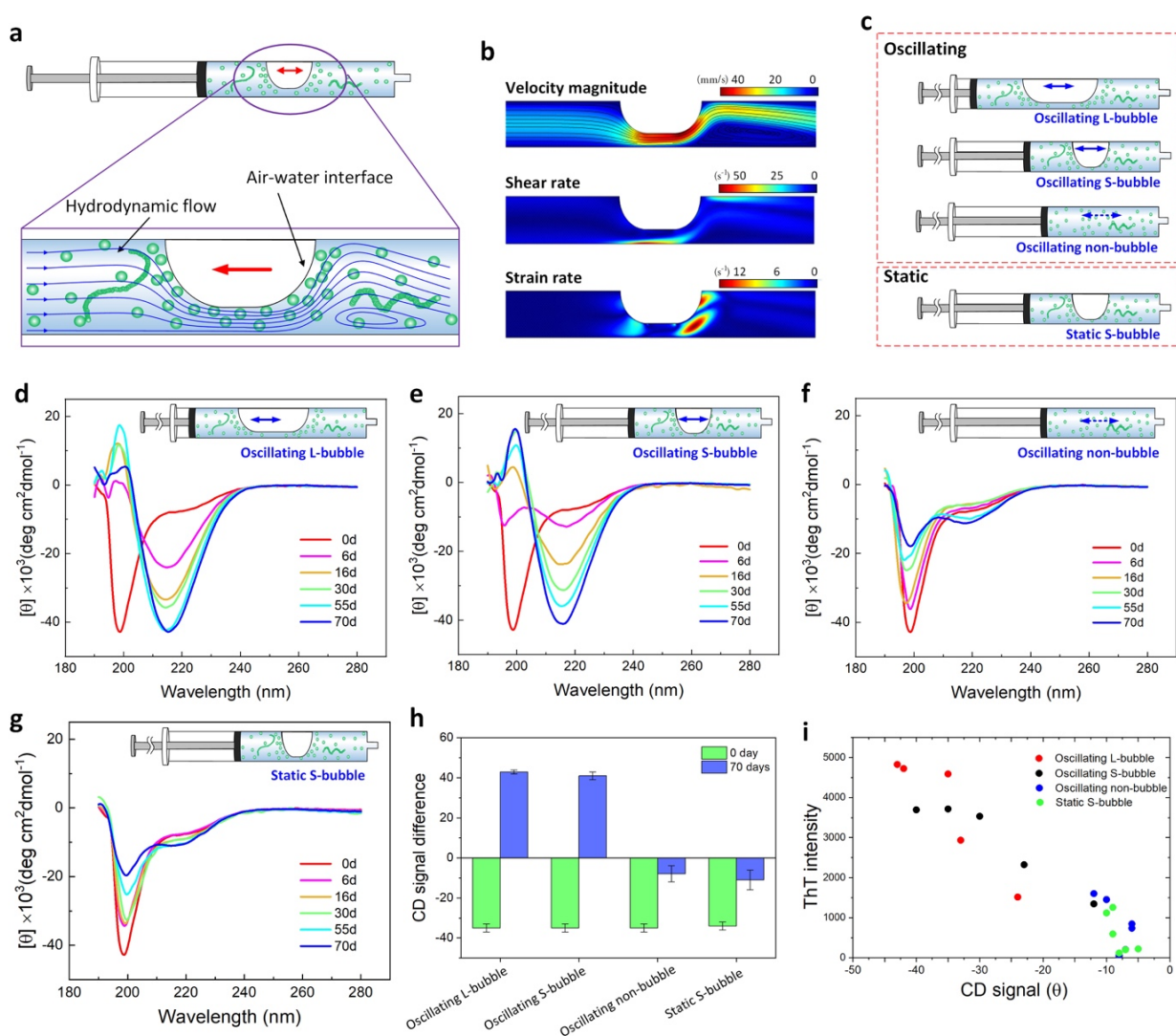


Figure 6.1 Experimental setup and CD measurement. (a) Schematics of the oscillating bubble in the syringe of protein solution at the concentration of $30\mu\text{M}$ that exposed to both hydrodynamic and interfacial effects. (b) CFD simulation of Oscillating S-bubble condition shows the hydrodynamic flow, shear and strain rate distribution. (c) The schematics of experimental setup in the oscillating and static conditions. (e-g) Evolution of CD spectra under the Oscillating L-bubble (c), Oscillating S-bubble (d), Oscillating non-bubble (e) and Static S-bubble (f) conditions. (h) CD signal difference between α -helix and β -sheet after 0 and 70 days incubation. (i) Correlation of the CD and ThT fluorescence measurement on the protein aggregation.

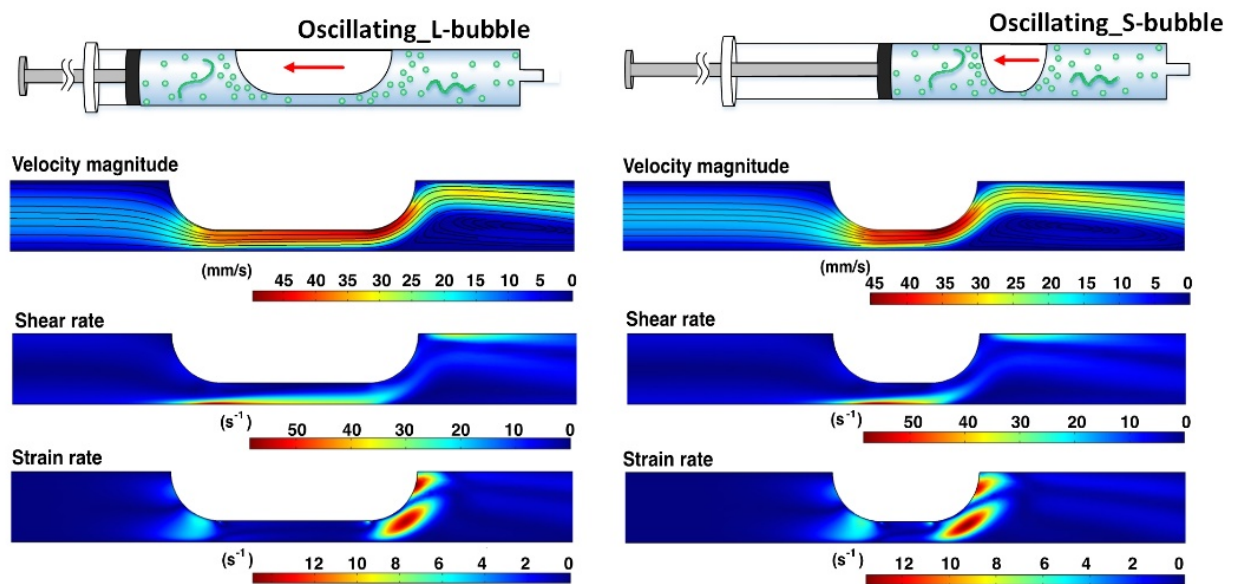


Figure 6.2 Hydrodynamics of the conditions with different sizes of bubble. Comparison of the hydrodynamic flow in the protein solution generated by two different sizes of the bubble in the strong hydrodynamic conditions (oscillating L-bubble (left) and oscillating S-bubble (right)) by using CFD analysis. This numerical simulation enables to obtain the velocity magnitude and streamlines of hydrodynamic flow (top), as well as the shear rate (middle) and strain rate (bottom) in the capillary. This CFD simulation suggests that no major difference exists in terms of strain rate comparing the long and short bubbles, but only slight difference lies in the shearing flow field.

6.3.2 Conversion of secondary structure of α -Syn aggregates

The structural evolution of α -Syn aggregates was investigated by circular dichroism (CD) spectroscopy that fingerprints the features of their secondary structures, such as random coil, α -helix and β -sheet. In this experiment, prior to incubation, α -Syn showed a characteristic absorption at 199 nm, indicating an intrinsically disordered random-coil structure.

In Oscillating L-bubble condition (Figure 6.1d), the absorption dips on the spectrum showed an immediate disappearance at 199 nm and a rapid drop at 218 nm, suggesting a quick conversion from random coil to β -sheet conformation. The aggregates formed substantial β -sheet-rich content only after 6 days. Similarly, the structural transition in Oscillating S-bubble (Figure 6.1e) condition showed an analogous but slightly slower trend, exhibiting a steady transition from random coil to β -sheet that showed with a strong absorption at 218 nm.

By contrast, the spectral variations in the Oscillating non-bubble (Figure 6.1f) and Static S-bubble (Figure 6.1g) conditions were obviously slower. A gradual and steady increase at 199 nm and a slight decrease at 218 nm were simultaneously observed on the evolution of the absorption spectra. The final spectra showed dual absorption peaks indicating co-existence of helical and β -sheet conformations.

The CD results show that the secondary structural transition from random coil to β -sheet in the conditions with hydrodynamic agitation and bubble are considerably rapid and enormous after 70 days incubation (Figure 6.1h), while the conversion in the weaker hydrodynamic condition and the static-bubble condition exhibit a slower trend. These results were confirmed by Thioflavin T (ThT) fluorescence assay that shows ThT signals reached final plateau after only 25 days in the Oscillating L/S-bubble conditions and after 50 days in the Oscillating non-bubble and static S-bubble conditions (Figure 6.3). The correlation of the intensity of ThT fluorescence versus the CD intensity (Figure 6.1i) indicates this agreement and verifies the tendency of forming cross- β sheet-rich aggregates in each condition.

6.3.3 Aggregation kinetics of α -Syn fibrillization.

The α -Syn aggregation kinetics was characterized by Thioflavin T (ThT) fluorescence assay, where ThT signal typically shows a sigmoidal curve as a function of time with three steps of fibrillization that describes aggregation kinetics^{67,269}. The result of ThT measurement are shown in Figure 6.3, and half-time (t_{50}) and growth rate ($1/\tau$) of fibril formation were obtained by using sigmoidal equation^{137,235,247} (see Methods section) from the fitted ThT curves.

ThT curves in the Oscillating L-bubble and Oscillating S-bubble conditions exhibited an exponential increase immediately after incubation. This might be attributed to positive feedback from secondary nucleation and fragmentation due to the hydrodynamic flow^{137,235,240,309,310}. The ThT signals reached final plateau after only 25 days with a short half-time (10 d) and a fast growth rate (0.22 d^{-1}). The main differences between the Oscillating L-bubble and the Oscillating S-bubble conditions are the slightly higher aggregation kinetics and the final ThT intensity at equilibrium phase in Oscillating L-bubble condition. By contrast, the Oscillating non-bubble and Static S-bubble conditions exhibited slower aggregation kinetics. After longer lag phases, the ThT signals gradually rose with a medium rate (0.07 d^{-1}) reaching the plateau after 50 days.

The ThT study on α -Syn aggregation kinetics is in good agreement with the CD measurements. These results show how the environmental kinetics influences α -Syn aggregation. Notably, the Oscillating L-bubble and Oscillating S-bubble conditions clearly exhibited the highest environmental effect on protein aggregation, which show a much less impact in the Oscillating non-bubble and Static S-bubble conditions.

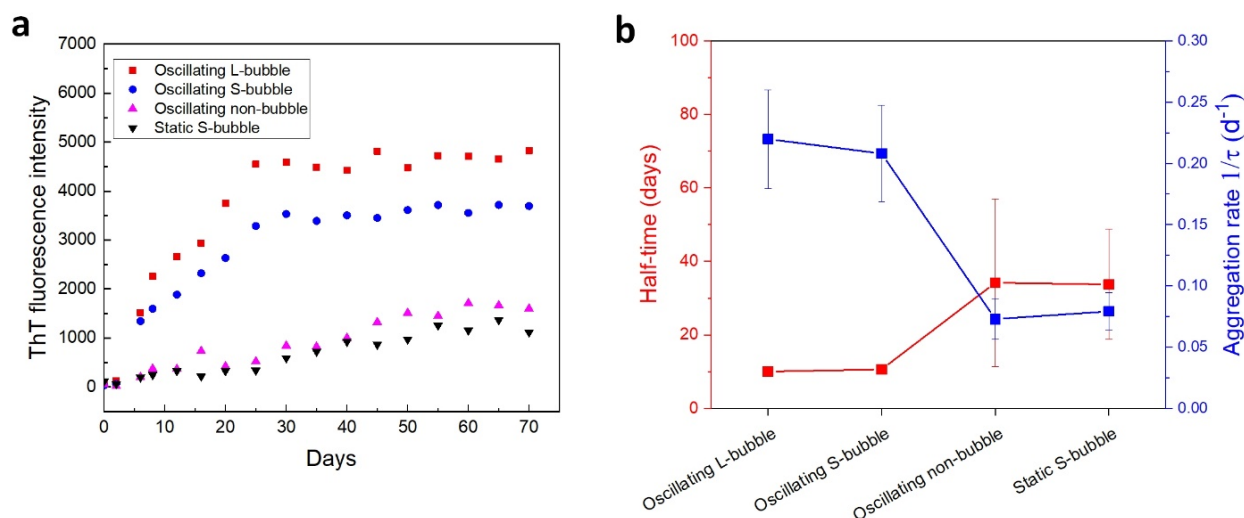


Figure 6.3 The α -Synuclein aggregation kinetics revealed by ThT fluorescence assay. (a) ThT fluorescence curves of α -Synuclein solution incubated under the conditions of oscillating L-bubble (red), oscillating S-bubble (blue), oscillating non-bubble (magenta), static non-bubble (purple) and static S-bubble (black) at the initial monomeric concentration of $30\mu M$. (b) Half-time (t_{50}) and fibril growth rate ($1/\tau$) are obtained from the fitted ThT data. It is clearly showed that under oscillating L/S-bubble conditions the α -Syn aggregation kinetics is faster than that of the oscillating non-bubble and static S-bubble conditions.

6.3.4 The nanoscale characterization of polymorphic amyloid fibrils

Investigating amyloid fibril morphology is of great importance due to its significance in the both pathological and functional applications. The amyloid fibrillar architectures may suggest the underlying association between the multiple aggregation pathways and amyloid polymorphism. This morphological differentiation had been proved to be critical in the biological and material applications, such as cytotoxicity^{78,283} and mechanical properties³¹¹.

In this experiment, we employed atomic force microscopy (AFM) to assess morphological features of amyloid fibrils at single-aggregate level. Prior to incubation, α -Syn protein were detected as homogeneous monomers and oligomers. As incubating, both early fibril in the growing time and mature fibrils in each condition were presented in Figure 6.4a-d. On the AFM topographic maps, several representative morphological features of mature fibrils were extracted, including fibril smoothness, flexibility and Young's modulus, as plotted in Figure 6.4f-h. More morphological properties, e.g. length and average height, are shown in Figure 6.5. Fibril smoothness describes the surface roughness of fibril. Fibril flexibility, characterized by the ratio between the contour length s and end-to-end length l_e (s/l_e), correlates with the protofilament configuration of the mature fibril and nanomechanical properties^{136,312,313}. A lower value of flexibility indicates a rigid fibril, while a large value corresponds to a soft and flexible fibril. The Young's modulus of mature fibril indicating the mechanical properties of fibrils, were measured by performing AFM nanoindentation measurement (Figure 6.6).

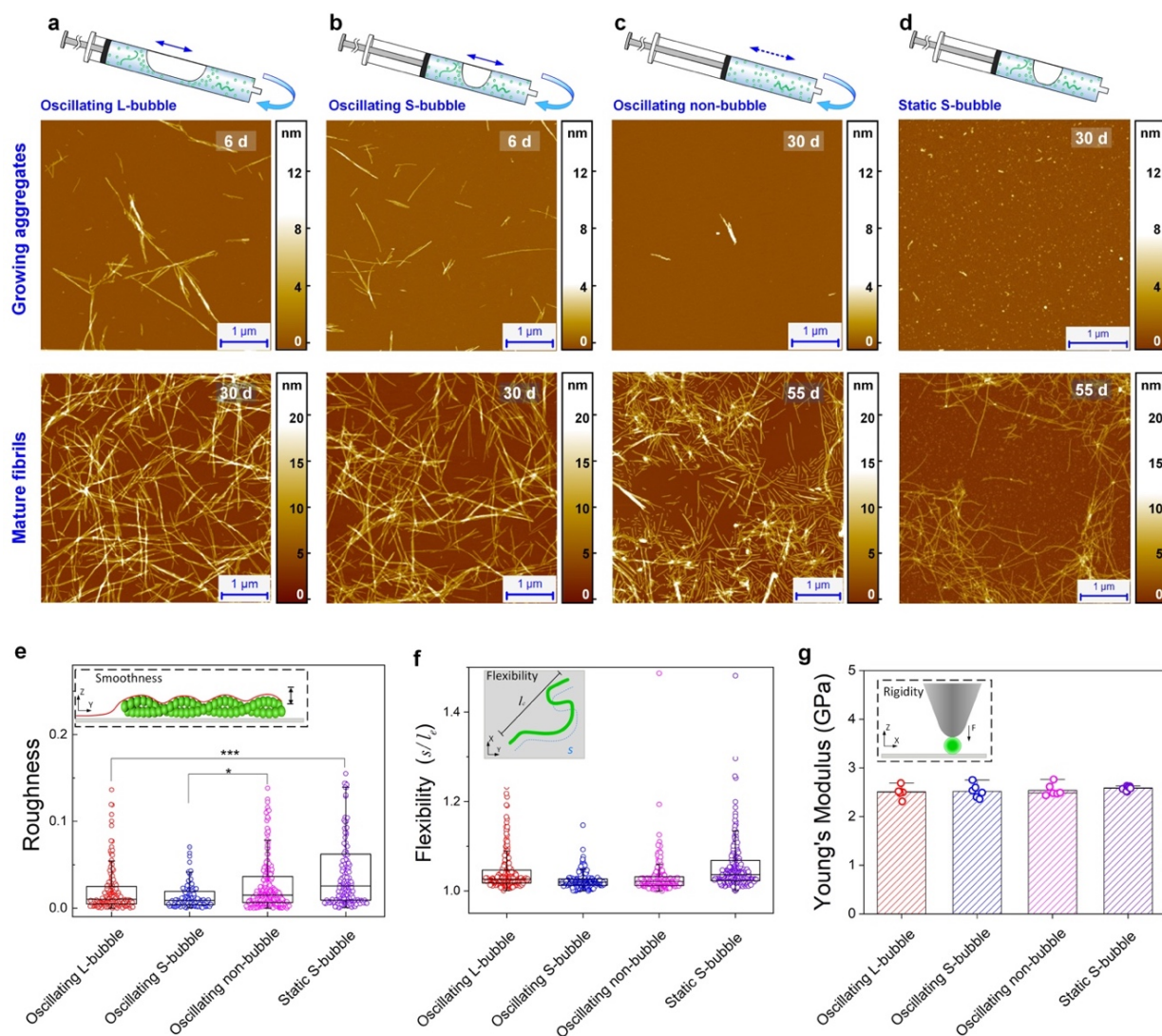


Figure 6.4 AFM images and statistical analysis on the amyloid fibril features. (a-d) AFM images of growing aggregates and mature fibrils from each condition. (e-g) Statistical investigation on the morphological and mechanical properties of fibrils, including roughness (e), flexibility (f) and Young's modulus (g).

In the Oscillating L-bubble condition (Figure 6.4 and red plots in Figure 6.4e-g), early fibrils were found only after 6 days, while abundant mature fibrils with a relatively long shape were obtained after 30d incubation. Similarly, the Oscillating S-bubble condition (Figure 6.4b and blue plots in Figure 6.4f-i) promoted the similar trend of fibril formation and plenty of mature fibrils were detected after 30 days incubation. Interestingly, the morphology of mature fibrils yielded in these high-hydrodynamic conditions are relatively comparable, maintaining similar thickness and length (9 nm and 0.5 μm respectively, Figure 6.5), as well as a low flexibility and a low roughness (Figure 6.4e-f). This high smoothness is due to the mature fibril profile, exhibiting a homogeneous rod-like shape (Figures 7a-b and 7e-f) in both Oscillating L-bubble and Oscillating S-bubble conditions.

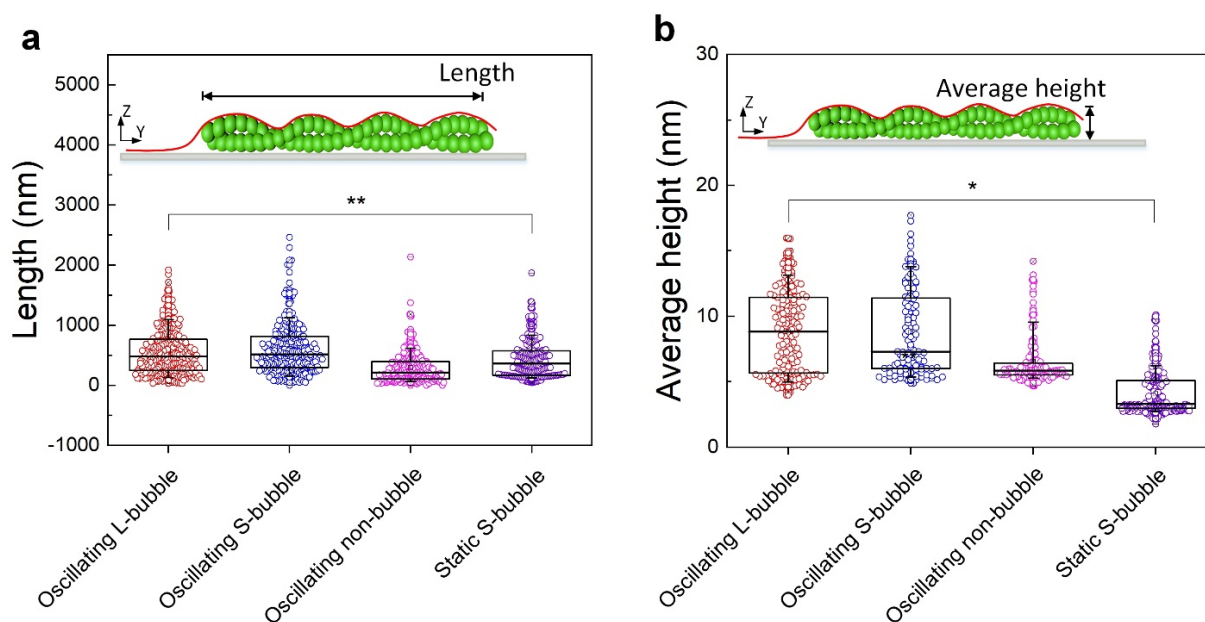


Figure 6.5 The fibril height and length distribution. The statistics of the length (a) and the average height (b) of mature amyloid fibrils yielded in the Oscillating L-bubble, Oscillating S-bubble, Oscillating non-bubble and Static S-bubble conditions.

In the Oscillating non-bubble condition (Figure 6.4c and magenta plots in Figure 6.4e-g), the process of fibril formation was significantly slower. Early and mature fibrils were detected with 30 and 55 days incubation respectively. It is noticeable that these mature fibrils were highly rough and rigid (Figure 6.4e-f), with relatively short profile and uniform average height (Figure 6.5). Remarkably, the polymorphic fibrils in the Oscillating non-bubble condition were found, including rod-like^{78,95}, and twisted and helical^{85,95} fibrils (Figure 6.7c and 6.7g).

By contrast, the Static S-bubble condition (Figure 6.4d and purple plots in Figure 6.4e-g) promoted the formation of seed-like protofibrils in the initiating phase, which then evolved into fibrils with a high roughness and flexibility. The average height of fibrils shows two clustering groups, peaking at 3.1 and 5.2 nm (Figure 6.5), refer to single protofilament and double stranded mature fibril respectively^{78,314}.

The QI-AFM images of the Young's modulus of the amyloid fibrils are presented in Figure 6.6. Contrary to fibril flexibility (Figure 6.4f) that depends on the intrinsically configurational property in the fibril axial direction, fibril nanomechanical property is associated with their inter-protofilaments arrangements in the perpendicular to fibril axis. The nanomechanical property is characterized by Young's modulus (E), which normally gives values in the range of GPa with the AFM nano-indentation techniques^{120,141,315,316}. In order to better evaluate the fibril stiffness, we applied a threshold filter on QI-AFM images (Figure 6.6 a2-d2) to distinguish two separated normal distributions: one for amyloid fibrils and the other for the substrate (Figure 6.6 a3-d3). As shown, the Young's modulus for

the measured substrates in each condition were around 3.2 GPa (Figure 6.6e), indicating the reliability of the nanomechanical measurement. The Young's moduli of homogeneous rod-like fibrils from the oscillating L-bubble and the Oscillating S-bubble conditions exhibited comparable values around 2.5 GPa, close to the heterogeneous fibrils from oscillating non-bubble conditions. However, this value for polymorphic fibrils obtained in static S-bubble condition rises to 2.58 GPa with no significant variation. These results confirm that both hydrodynamic flows and hydrophobic effect can yield slight effect on the mechanical properties of the formed amyloid fibrils.

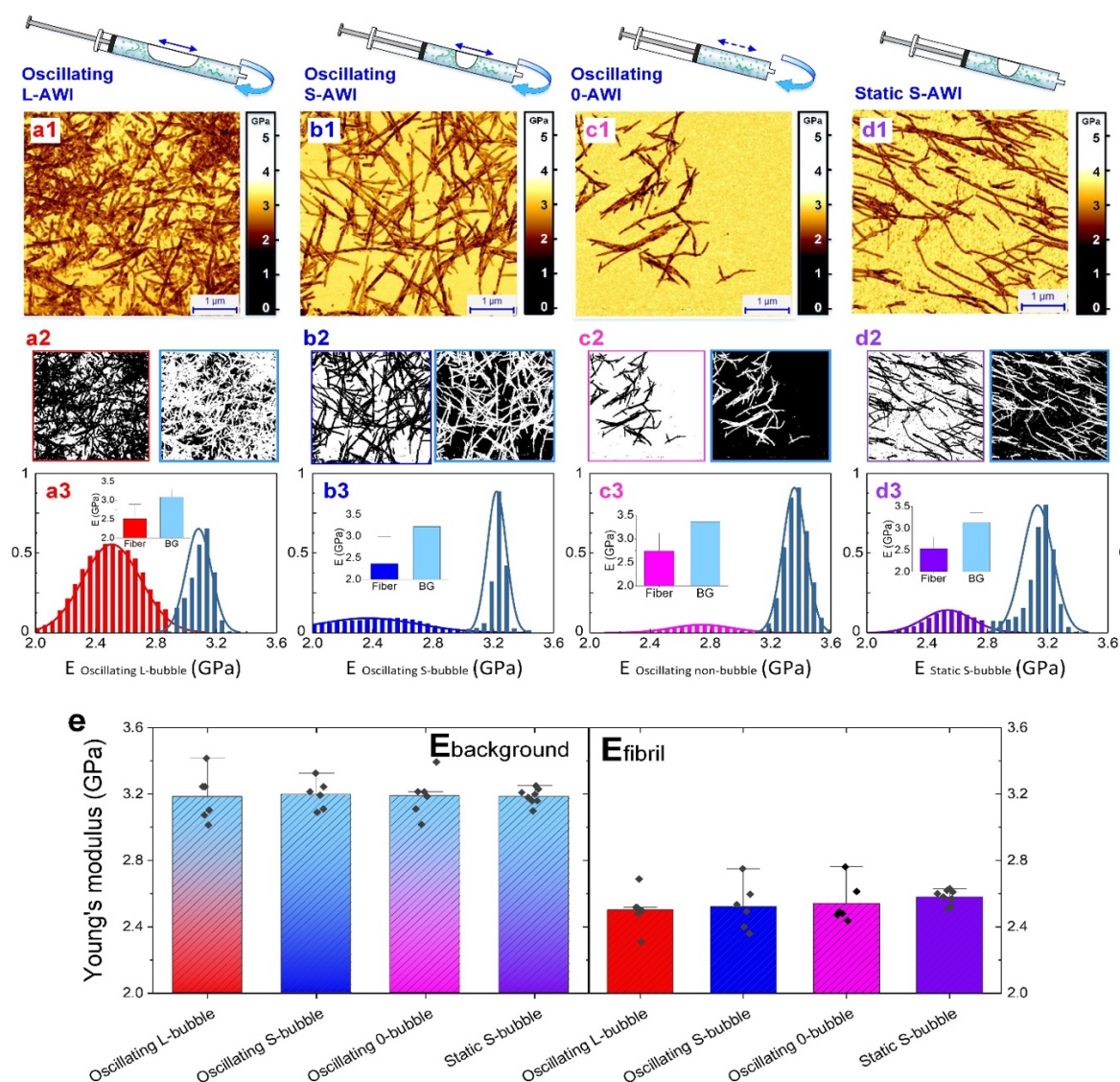


Figure 6.6 Nanomechanical properties of amyloid fibrils under each condition. (a1-d1) Representative QI-AFM images of amyloid fibrils from the oscillating L-bubble, oscillating S-bubble, oscillating non-bubble and static S-bubble conditions, respectively. (a2-d2) The threshold filter designed to distinguish fibrils and substrate on each QI-AFM image. (a3-d3) The normal distribution of the Young's modulus value of the fibrils and the substrate on each QI-AFM image and Gaussian fitting of each histogram to extracting the average Young's modulus of both fibril and substrate. (e) Statistical diagram of Young's modulus of both fibril (right) and substrate (left) from multiple QI-AFM images in each experimental condition.

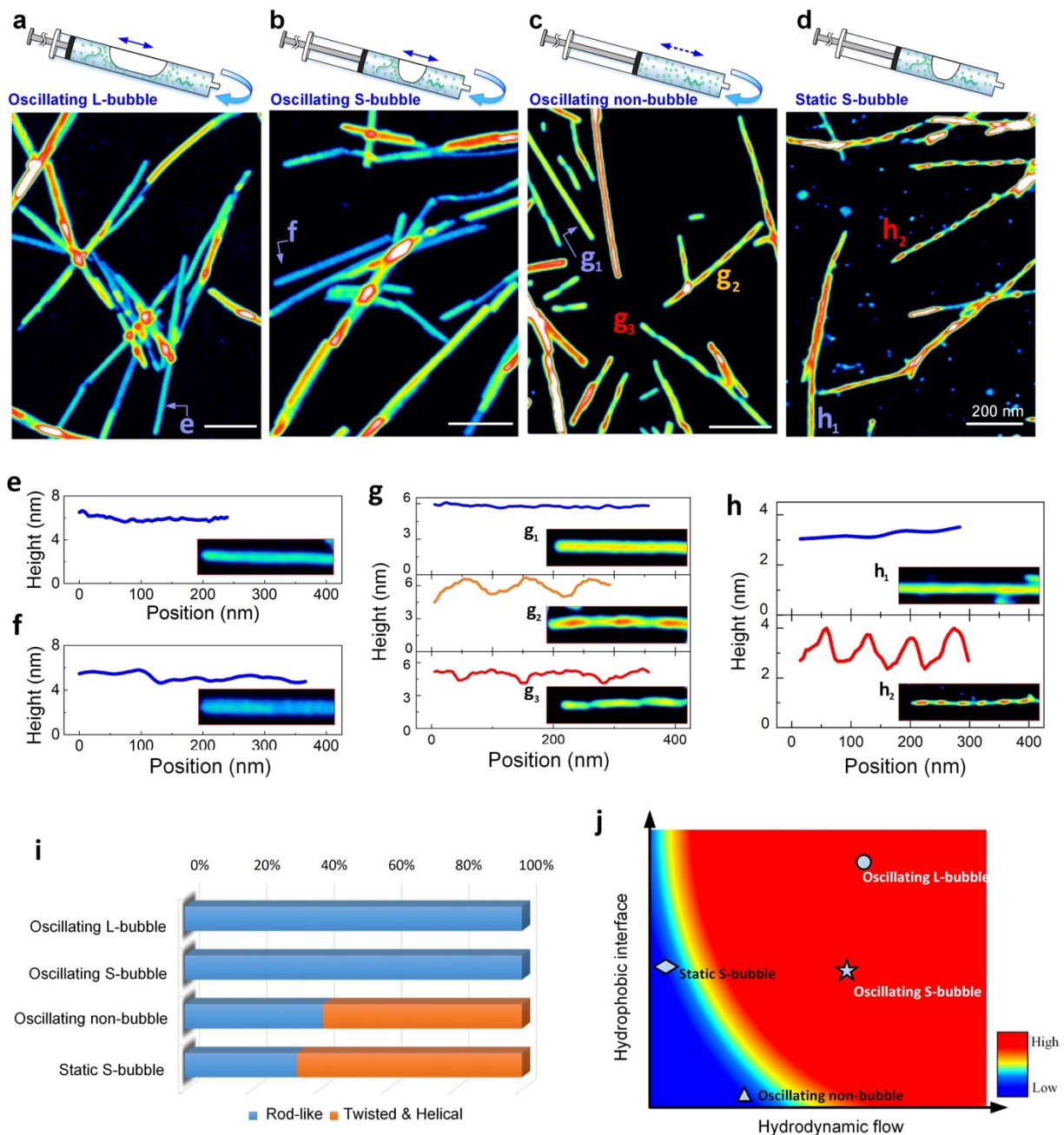


Figure 6.7 Fibril polymorphism and its correlation with environmental kinetics. (a-h) AFM images of homogeneous rod-like fibrils formed in the Oscillating L-bubble (a) and Oscillating L-bubble (b) conditions, with typical rod-like fibril (e, f) in each condition. AFM images of polymorphic fibrils yielded in the Oscillating non-bubble (c) and Static S-bubble (d) conditions with representative twisted, helical and rod-like fibrils (g, h) in each condition. (e) The statistics on the amyloid polymorphism in each condition. (f) The environmental kinetics map, composed by contribution of hydrodynamic flow and interface, indicates the correlation between fibril polymorphism and environmental kinetics.

Then, we performed the statistical investigation on amyloid fibril polymorphism (Figure 6.7i), confirming that the Oscillating L/S-bubble conditions promoted the formation homogeneous rod-like fibril while the Oscillating non-bubble and Static S-bubble conditions generated the coexistence of rod-like, helical and twisted fibrils. This agrees the observation on the AFM images (Figure 6.7a-h), as well as the statistical roughness measurement (Figure 6.4e) due to the difference in the roughness

between rod-like and periodically fluctuated fibrils. The nanoindentation measurements shows that Young's modulus of these fibrils is in the range of GPa (Figures 6.4g and 6.6), indicating that these fibrils are mature fibril, in agreement with the result of the ThT assay (Figure 6.3).

According to the environmental kinetics in each condition, it is interesting to note that the conditions with high environmental kinetics generated homogeneous rod-like fibril, while the conditions with a weak kinetics, either oscillation or interface, could lead to polymorphic fibrils. This result agrees with previous optical microscopic observation in the microfluidic study³¹⁷. Thus, a possible interpretation for the origin of the amyloid polymorphic phenomenon in each condition is the environmental kinetics. Since the multiple pathways of protein aggregation provide the possibility of forming heterogeneous configurations of amyloid fibrils, the environmental kinetics could be one of the potential approaches to control the aggregation pathways^{237,282,284,291}. In this experiment, the environmental kinetics in the Oscillating non-bubble and the Static S-bubble condition, due to the hydrodynamics and interfacial effect respectively, were relatively weak, as shown on the environmental kinetics map (Figure 6.7j). This weak kinetics allows multiple fibrillization pathways and thus yields polymorphic fibrils, including twisted, helical and rod-like fibrils. Nevertheless, the overwhelming environmental kinetics in the Oscillating L-bubble and Oscillating S-bubble conditions were considerably high that occupy a high dynamic level, leading to the formation of homogeneous rod-like fibrils.

6.3.5 Order-order transition among fibril polymorphs

To verify the hypothesized correlation between environmental kinetics and fibril polymorphism, we employed the protein solution with heterogeneous mature fibrils, obtained after 70 days incubation in the Oscillating non-bubble condition, and further incubated the solution in the Oscillating S-bubble condition, as shown in Figure 6.8a. This approach was to enhance the environmental kinetics of protein solution from low to high kinetics (Figure 6.8b). As seen, prior to the further incubation, we observed the coexistence of twisted and rod-like fibrils, which were confirmed as mature fibrils due to its ThT signal was in the plateau phase (Figure 6.3). However, after 5 days in the Oscillating S-bubble condition, we noted a clear morphological transition to homogeneous rod-like fibrils on the AFM image, as well as statistical investigation (Figure 6.8c).

Thus, we verified that the fibril polymorphism is associated with environmental kinetics. This environmental kinetics is crucial for the generation of polymorphic or homogeneous fibrils in this experiment. Lower environmental kinetics allows multiple aggregation pathways and morphological dif-

ferentiation of amyloid fibrils. Higher environmental kinetics condition may also allow multiple aggregation pathways but the high-kinetics could enable the transition from twisted and helical fibril to rod-like fibril, from polymorphic fibrils to homogenous fibrils (Figure 6.8d). These results also confirm that the strength of environmental kinetics could be one of the key factors to modulate the amyloid fibril polymorphism.

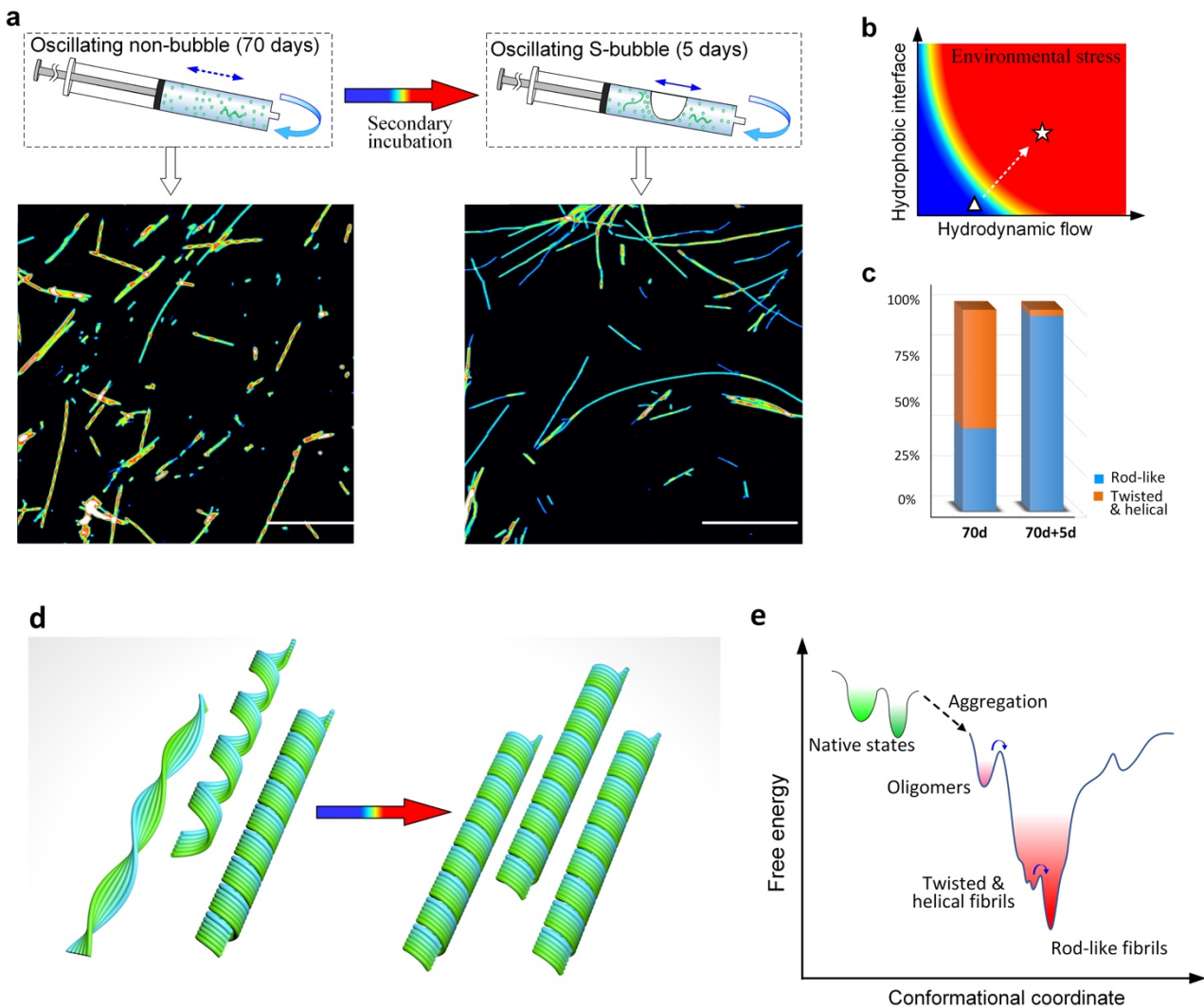


Figure 6.8 Order-order transition of amyloid fibril by enhancing environmental kinetics. (a) The protein solution incubated 70 days in the Oscillating non-bubble condition, was further incubated for 5 days in the Oscillating S-bubble condition. AFM images of amyloid fibrils before and after the further incubation. (b-c) The variation of the environmental kinetics (b) and the statistical transition on fibril polymorphs (c) before and after the further incubation. (e) Schematics of the morphological transition from polymorphic fibrils to homogeneous rod-like fibril. (f) Funnel-like energy landscape of the amyloid polymorphs in this experiment.

From an energetic point of view, the environmental kinetics depended transition from twisted fibril to rod-like fibril suggests that, fibrils polymorphs in this experiment may hold unique levels of free energy and structural stability, as shown energy landscape in Figure 6.8e. The twisted and helical

fibril is the metastable and transformable species that possess a relatively low level on the energy landscape that could transit to other forms under the environmental-kinetic control²⁹¹. This transition is confirmed by the observation on the uncontrolled fibril evolution^{93,96,318,319}. In this experiment, rod-like fibrils formed under high-dynamic condition are the most thermodynamically stable form with a free-energy minimum^{96,97,99,311,318}.

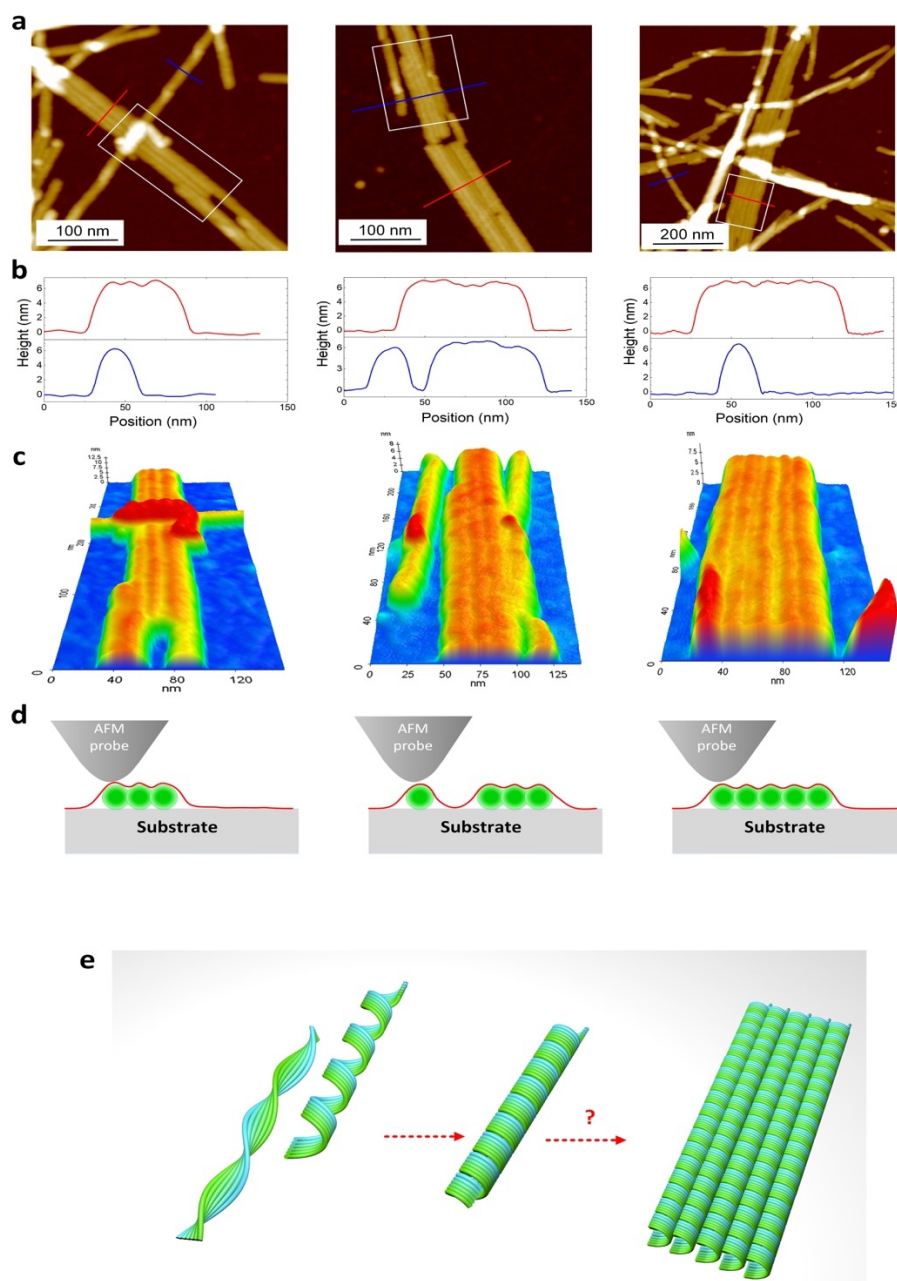


Figure 6.9 The formation multi-stranded ribbon in the experiment. AFM images (a) and height profiles (b) of illustrated examples of multi-stranded ribbon obtained under the high-kinetic conditions with long-time incubation. (c-d) The 3D-AFM images (c) and schemes (d) of the fibrils vividly show parallel-packing arrangements and the number of rod-like fibril in the multi-stranded ribbon. (e) The schematics to show the possible transition from rod-like fibril to multi-stranded ribbon.

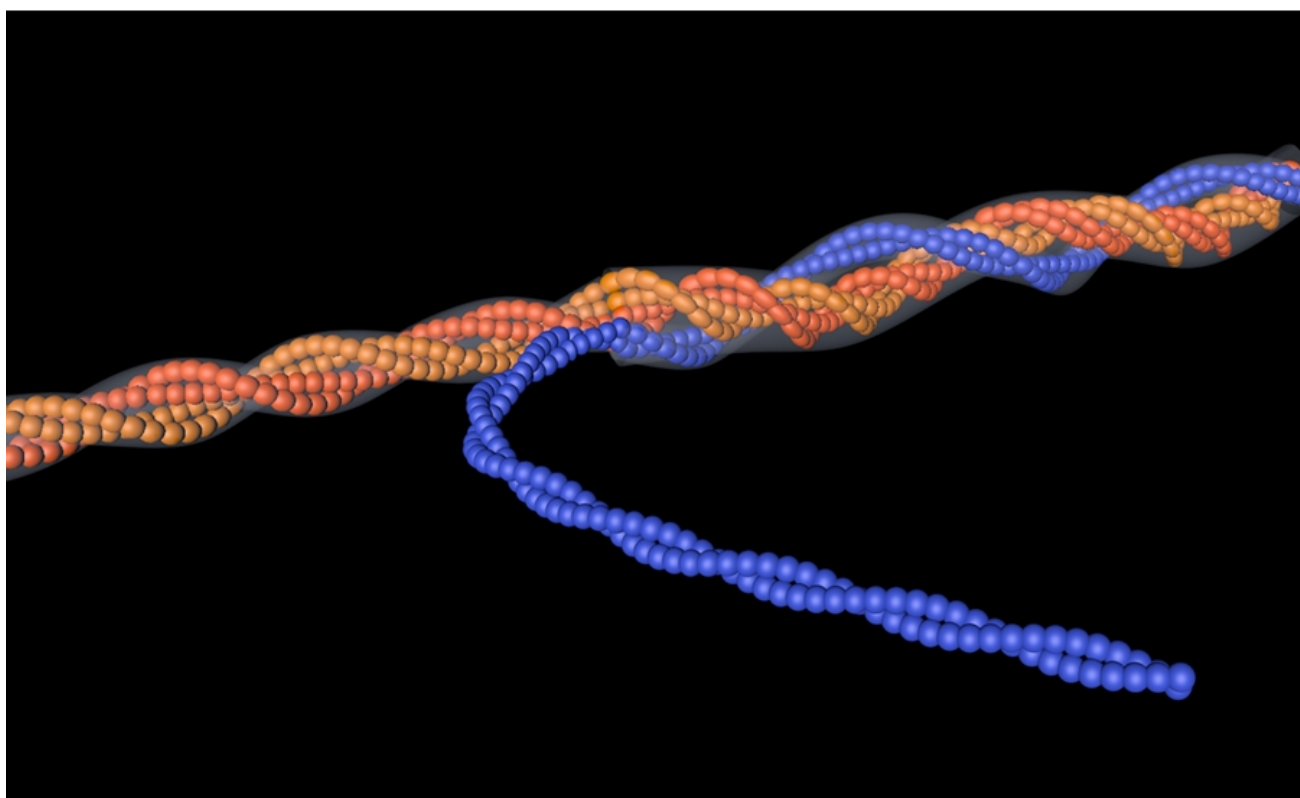
In addition, the parallel stacked rod-like fibril, termed multi-stranded ribbon, were observed occasionally in the high environmental-kinetic conditions with long-term incubation. As seen in Figure 6.9, the height profile and 3D images of the illustrated multi-stranded ribbon clearly shows the parallel-stacking scheme of multiple rod-like fibrils. Since it was obtained with long-term and high-kinetic incubation, despite of the rare observation, we hypothesize this multi-stranded ribbon may hold the similar or even lower free energy level compared to rod-like fibril⁹³. However, there is not enough evidence to support it in this experiment, but it could be an interesting topic to target in the future.

6.4 Conclusion

In summary, our experimental results underline the correlation between fibril polymorphism and the environmental kinetics which is the combination of hydrophobic interface and hydrodynamic flow in this experiment. On one hand, depending on the strength of environmental kinetics, we observed that polymorphic fibrils were formed in the low environmental-kinetic conditions, while homogeneous rod-like fibrils were yielded in the high environmental-kinetic conditions. On the other hand, the environmental control allows the transition from polymorphic fibrils to homogeneous fibrils, from twisted and helical fibrils to rod-like fibrils. Correspondingly, it is clear that the fibril polymorphs hold distinct levels on the energy landscape. Twisted fibrils are metastable fibrils could transit to other energetic-favorable forms with lower free energy level, whereas rod-like fibril maintains the most thermodynamically stable configuration in this experiment.

We believe that these results could contribute to a better understanding on fibril polymorphism phenomenon, including the mechanism of polymorphic fibril formation, the influence of environmental factors and the evolution of fibril polymorphs, to appreciate the pathological origin of α -Syn related diseases. Remarkably, on the other hand, the transition from fibril polymorphism to homogeneity by mediating environmental kinetics indicates the unprecedented environmental control on amyloid polymorphs. This shows a great potential in forming homogeneous amyloid-based functional biomaterials, as well as developing the wide applications in the biotechnological and biomedical fields.

Chapter 7 Interprotofilament interaction and configurational identification of hierarchically twisted amyloid fibrils



This chapter contains a manuscript in preparation:

Jiangtao Zhou¹, Salvatore Assenza², Francesco S. Ruggeri^{3,4}, Ioana M. Ilie⁵, Eugene L. Starostin⁶, Sergey K. Sekatskii¹, Amedeo Caflisch⁵, Tuomas P. J. Knowles^{3,4} and Giovanni Dietler¹. *Interprotofilament interaction and configurational identification of hierarchically twisted amyloid fibrils*. In preparation.

Affiliations:

1. *Laboratory of Physics of Living Matter, Ecole Polytechnique Fédérale de Lausanne (EPFL), CH-1015 Lausanne, Switzerland*
2. *Departamento de Física Teórica de la Materia Condensada, Universidad Autónoma de Madrid, Madrid, Spain.*
3. *Department of Chemistry, University of Cambridge, Lensfield Road, Cambridge CB2 1EW, UK*
4. *Centre for Misfolding Diseases, Department of Chemistry, University of Cambridge, Lensfield Road, Cambridge CB2 1EW, UK*
5. *Department of Biochemistry, University of Zürich, 8057 Zürich, Switzerland*
6. *Department of Civil, Environmental & Geomatic Engineering, University College London, Gower Street, London WC1E 6BT, UK*

Abstract. Amyloids are insoluble fibrillar aggregates of proteins that are considered to be an important pathological hallmark of various neurodegenerative diseases^{57,58,320}. The diversity of aggregation pathways drives the interaction among heterogeneous protein particles, such as monomers and protofibrils, and leads to the formation of polymorphic fibrils^{60,93,137}. However, the underlying interactions between individual protofilaments and protofibrils is rarely discussed and their role in forming mature fibril remains poorly understood. Here, we investigated the significance of interprotofilament interactions in the fibrillization process and their impacts on the fibrillization mechanisms of twisted fibrils with hierarchical polymorphic configurations. By means of atomic force microscopy (AFM) with Ångström-level vertical resolution and comprehensive statistical analysis, we identified the packing arrangement of multi-protofilaments bricked fibrils, including twisted-ribbon and random-twisted fibrils, as a result of parallel-packing and random-intertwining model respectively. Our experiments provide evidence of novel mechanisms of amyloid fibrillization driven by random-intertwining of protofilaments, allowing the quantitative evaluation the role of intermolecular protofilaments interactions on aggregation pathways and fibrillization configurations. This study advances the fundamental understanding of fibrillization mechanisms, from protofilaments to higher-ordered mature fibrils, and enriches the multifaceted set of protein aggregation pathways.

7.1 Introduction

Pathological amyloid formation is associated with many neurodegenerative diseases, such as Alzheimer's and Parkinson's diseases^{57,58,320}. Hence, understanding their complex aggregation mechanisms is of fundamental significance for exploring for both pathological and functional roles of amyloid fibrils. Interactions between amyloidogenic proteins are fundamental in the formation of the aberrant fibrillar aggregates. In the initiating phase, the monomers undergo structural rearrangements and aggregate into oligomers. Then, the misfolded oligomeric and monomeric building blocks form linear β -sheet-rich protofilaments that stabilize by a dense network of H-bonds^{60,79,321} in the elongation phase. Meanwhile, secondary mechanisms, such as fragmentation, secondary nucleation and inter-fibril interactions, play a critical role in determining the aggregation kinetics and fibrillization mechanisms. This eventually results in a wide diversity of fibril morphologies, such as twisted^{95,99,136,322,323}, helical^{85,95} and crystal-like fibrils^{85,95,323}. However, the inter-protofilament interaction, referring to the intermolecular reaction between protofilaments and protofilaments-based protofibrils, to form higher-ordered mature fibrils, is rarely discussed and its role in the fibrillization mechanisms remains unclear.

In this work, we investigated the fibrillization of full-length insulin as a representative model^{324,240,70} to explore the impact of interprotofilament interaction on the fibrillization mechanisms and to reveal the protofilament packing configurations of the polymorphic twisted fibrils. We performed high resolution atomic force microscopy (AFM) to monitor the morphological evolution of fibrillar aggregates and developed novel statistical analysis which successfully classified hierarchically twisted fibrils and identified their multi-stranded configurations. AFM is a powerful technique for studying amyloid fibrils because of its precision in morphological characterization of individual aggregates at nanoscale and because of its ability of quantitatively evaluating heterogeneous aggregates during their evolution process^{85,96,136,318,325,326}. However, AFM tip convolution effects largely limit its horizontal resolution, and thus hampering a precise description of fibrils with nanometer-sized diameters. This difficulty is here surpassed by taking advantage of the high AFM vertical resolution (2 Å) in conjunction with comprehensive statistical analytics, which enabled unraveling the configurational features of multi-stranded twisted fibrils. Further observation revealed two types of protofilament packing arrangement, corresponding to twisted-ribbon and random-twisted fibrils. These results highlight the influence of interprotofilament interactions in the fibrillization process, and bridges the gap of the mechanisms for amyloid evolution, from single protofilaments to mature twisted fibrils.

7.2 Experimental methods

Preparation of insulin fibrils.

Full-length bovine insulin (Sigma Aldrich, Dorset, UK) was obtained from bovine pancreas, and all other chemicals were from Sigma Aldrich. Insulin powder was dissolved in the salt-free buffer (pH 1.6, 25 mM HCl) to 2 mM as fresh stock solutions. The formation of twisted fibrils was highly reproducible in this acidic environment without strong ionic strength. Before each experiment, the stock solution was agitated for 2 min and then purified with 0.22 μm filter. Then the stock solutions were diluted to a concentration of 200 μM . After centrifuging (Microcon I8 centrifuge) at 4 °C with 100 kDa centrifugal filter at 12k r.p.m. for 5 min, the protein concentration was averaged from three measurements by UV absorption (Nanodrop 2000 spectrophotometer) at 280 nm using an extinction coefficient of 1 for 1.0 mg/ml. All the processes above were performed at 4 °C. The insulin solution was incubated at 70 °C and immediately diluted after each sample collection. An aliquot solution (30 μL) was diluted 10 times with buffer solution and stored at 4 °C, to minimize unexpected protein assembly.

Atomic force microscope (AFM) measurements.

An aliquot (10 μL) of freshly incubated solution (10 μM) was deposit on the freshly cleaved bare mica for 4 min. Due to surface charge, these insulin aggregates can easily attach with negatively charged mica. Then, the mica was rinsed by 500 μL Mili-Q water. After fast removing the droplet subtly by kimwipes, the mica was quickly dried by a gentle flow of nitrogen gas under ambient condition to avoid introducing morphological turbulence during deposition. Further drying was done by leaving sample in the vacuum desiccator.

AFM images were scanned by NX-10 Atomic Force Microscopy (Park Systems, South Korea) using the non-contact Amplitude Modulation (NC-AM) in ambient condition. The AFM images with the resolution of 1024 \times 1204 pixels were scanned by using the non-contact cantilevers (PPP-NCHR, Park) with resonance frequency of 330 kHz and force constant of 42 N/m. Knowing that an appropriate controlling of cantilever plays a key role in the statistical analysis of each AFM height measurement, a weak tip-sample interaction is carefully achieved by monitoring AFM phase images in the negative range with an amplitude less than $\pm 5^\circ$. AFM images were flattened by XEI software (Park System, South Korea). To avoid artifacts induced in flattening and to compare data between different measurements, every AFM image was flattened by plane in first order. The reliability of AFM scanning was monitored by controlling the roughness of mica surface less than 0.2 nm.

Statistical analysis.

The flattened AFM images were analyzed with DNA trace software. This allows to trace the height profile of the ridge of amyloid fibrils along their contour length, by either extracting the maximum point or using Gaussian fit in each cross-section of the amyloid fibril. To normalize the extracted data, a constant sampling step of 1 nm was used in each extraction of height profiles. To avoid artifacts and average the statistical data, we only take the fibrils with minimal length of 150 nm into account while cross section between fibrils were strictly excluded. The features including the height value and position of peaks and dips on the fluctuated height profile were extracted, to normalize the average height, maximal and minimal height, amplitude and periodicity.

CD spectroscopy.

An aliquot (70 μL) of insulin solution at the initiating monomeric concentration of 30 μM was analyzed at room temperature with a Jasco J-815 CD spectrometer. A high-quality quartz cuvette with an optical path length of 1.0 mm was used and spectra were collected with a step 0.2 nm in continuous scanning mode in the range of 190-280 nm in each measurement. The spectra were smoothed with a Savitzky-Solay filter in Origin.

ThT Assay.

An aliquot of insulin solution was diluted by freshly prepared ThT solution to reach a final initiating protein concentration of 3 μM and ThT concentration of 10 μM in every experiment. An aliquot of diluted insulin solution (70 μl) in each experiment was measured three times in a Bucher Analyst AD plate reader and ThT fluorescence reading was performed at an excitation wavelength of 450 nm and an emission wavelength of 485 nm. The signal of fluorescence intensity was fitted with a sigmoidal model.

Infrared nanospectroscopy.

An aliquot (5 μl) of diluted insulin solution (20 μl) was deposited on hydrophobic ZnSe monocrystal prism at the room temperature and was dried by evaporation in the vacuum desiccator overnight to form monolayer of insulin aggregates on ZnSe surface. The freshly prepared sample were measured by nanoIR system (Anasys Instruments Inc., USA) that combines AFM and infrared spectroscopy measurements^{13,40} and enables chemical analysis in nanoscale. A soft cantilever (EX-C450, Anasys) with spring constant of 0.2 N/m was used and the spectra were collected with a sampling rate of 1 cm^{-1} and 128 co-average in the range of 1200-1800 cm^{-1} and further nominalization were realized in Analysis Studio (Analysis). The analysis of secondary structural composition in the amide I (1600-1700 cm^{-1}) were performed in Origin according to the correlations between protein structures and Amide I frequency indicated before¹⁹⁷. The spectra were processed according to previous methods⁴⁰, and sub-bands in the Amide I region (1600-1700 cm^{-1}) were revealed by multiple Gaussian fitting¹⁹⁷, including helical and turn-like (1648-1685 cm^{-1}) structure, β -sheet and antiparallel β -sheet (1610-1640 and 1685-1695 cm^{-1}) structure and random coil (1640-1650 cm^{-1}) structure.

Theoretical modelling of fibril morphologies.

The morphologies of randomly-twisted fibrils were modeled via the Hierarchical Assembly Model (HAM), as described in the main text. For each fibril, the composing protofilaments and protofibrils were modeled as intertwining tubular objects with constant diameters. In the case of protofilaments, the diameter was set as $b = 1.2$ nm, while for protofibrils the enveloping tube was considered, corresponding to a diameter equal to $n \cdot b$, where n is the number of protofilaments within the protofibril. As mentioned in the main text, a better agreement with experimental data is achieved by assuming increased diameters for protofibrils involved in the formation of larger fibrils. This was done in practice by setting the diameter to $n \cdot b + dh_n$. The value of dh_n was set to 0.84 nm, 1.76 nm and 2.5 nm for $n = 3, 4, 5$ respectively; for $n = 1, 2$ no increase was considered. The intertwining of two protofilaments/protofibrils was implemented by imposing that the corresponding tubular axes follow a helix described by

$$\left(x, R_n \cdot \cos\left(\frac{2\pi x}{p} + \phi_0\right), R_n \cdot \sin\left(\frac{2\pi x}{p} + \phi_0\right) \right) \quad (\text{S1})$$

where R_n and p are the radius and periodicity of the helix, respectively. The values of ϕ_0 of the two helices were set in antiphase. As shown below, IMH and amplitude are independent of p , so for simplicity we set $p = 100$ nm for all fibrils, roughly corresponding to twice the average values of peak-to-peak distances found in the experiments. Assuming that the composing protofibrils are made of n and m protofilaments, the corresponding helices radii were set as $R_n = \frac{mb}{2}$ and $R_m = \frac{nb}{2}$, which correspond to the values set by minimizing the bending energy (see below). Nevertheless, as shown in the next section, the theoretical IMH and amplitude are independent of the particular choice made for R_n and R_m , as long as the condition $R_n + R_m = \frac{n+m}{2}b$ is satisfied. Therefore, the values of R_n and R_m were set only to allow drawing the cartoons reported in Table 7.1. When protofibrils with increased diameters were considered, the same formulae were applied by substituting $n \rightarrow n + dh_n/b$ and/or $m \rightarrow m + dh_m/b$. In the case of twisted ribbons, the same description was implemented by Assenza et al³²⁷: the n protofilaments forming the ribbon were labeled as $i = -\frac{n-1}{2}, \dots, \frac{n-1}{2}$ and the axis of the i -th protofilament was imposed to follow a helix with radius $i \cdot b$ and periodicity p . For representation purposes, in all the cartoons reported in Table 7.1 the radius of the tubes was increased by a factor of five.

Theoretical AFM profiles.

Assuming that the fibrils are sufficiently soft to adapt their conformation to the substrate (that is, there is always a contact point with the surface), at each point the theoretical AFM height can be computed as the difference between the maximum and the minimum of the fibril conformation at that point. Under this assumption, for randomly-twisted fibrils the AFM profile is independent of the particular choice of weights given to the radii of the composing protofibrils, as we show in the following. Without loss of generality, let us assume $n \geq m$ and that the height of each helix is given by its y coordinate. Moreover, let w be the weight of the radius of the protofibril made of n protofilaments, thus $R_n = w \frac{(n+m)b}{2}$ and $R_m = (1-w) \frac{(n+m)b}{2}$. Starting from Eq.(S1), the maximum and minimum of each protofibril are then given by $max_n = w \frac{(n+m)b}{2} \cos\left(\frac{2\pi x}{p} + \phi_0\right) + \frac{nb}{2}$; $min_n = w \frac{(n+m)b}{2} \cos\left(\frac{2\pi x}{p} + \phi_0\right) - \frac{nb}{2}$; $max_m = -(1-w) \frac{(n+m)b}{2} \cos\left(\frac{2\pi x}{p} + \phi_0\right) + \frac{mb}{2}$; $min_m = -(1-w) \frac{(n+m)b}{2} \cos\left(\frac{2\pi x}{p} + \phi_0\right) - \frac{mb}{2}$. In each of the previous formulae, the second term accounts for the thickness of the tube; moreover, the minus sign in the first term of max_m and min_m originates from the phase difference (equal to π) between the two helices. The overall maximum and minimum heights are obtained as $H_{Max} = \max(max_n, max_m)$ and $H_{Min} = \min(min_n, min_m)$, respectively. It is straightforward to show that $(H_{Max}, H_{Min}) = (max_n, min_n)$ for $\left|\cos\left(\frac{2\pi x}{p} + \phi_0\right)\right| < \frac{n-m}{n+m}$; moreover, $(H_{Max}, H_{Min}) = (max_m, min_m)$ for $\cos\left(\frac{2\pi x}{p} + \phi_0\right) < -\frac{n-m}{n+m}$ and $(H_{Max}, H_{Min}) = (max_n, min_m)$ for $\cos\left(\frac{2\pi x}{p} + \phi_0\right) > \frac{n-m}{n+m}$. The AFM height is computed as $H_{AFM} = H_{Max} - H_{Min}$ and is thus equal to:

$$H_{AFM}^{random}(x) = \begin{cases} nb & \text{if } \left|\cos\left(\frac{2\pi x}{p} + \phi_0\right)\right| < \frac{n-m}{n+m} \\ \frac{(n+m)b}{2} \left[1 + \left|\cos\left(\frac{2\pi x}{p} + \phi_0\right)\right|\right] & \text{otherwise} \end{cases} \quad (S2)$$

Note that the AFM height is independent of the particular choice of w . Eq.(S2) was employed to plot the theoretical profiles of randomly-twisted fibrils reported in Figure 7.10 and Table 7.1. Remembering the assumption $n \geq m$, it is evident that the maximum and minimum AFM heights are $(n+m)b$ and nb , thus giving an amplitude equal to mb , as

expected. The average height can be computed by integration of Eq. (S2) over one period, i.e. $\frac{1}{p} \int_0^p H_{AFM}^{random}(x) dx$, which gives for the IMH:

$$\text{IMH}_{\text{random}} = \frac{1}{p} \int_0^p H_{AFM}^{random}(x) dx + \frac{m \cdot b}{2} = \left(\frac{n+m}{2} + \frac{2}{\pi} \sqrt{n \cdot m} + \frac{n-m}{\pi} \arcsin \frac{n-m}{n+m} \right) b + \frac{m \cdot b}{2} \quad (\text{S3})$$

In the case of a twisted ribbon, the maximum and minimum height of the fibril conformation are easily obtained as $\pm \left(\frac{(n-1)b}{2} \left| \cos \left(\frac{2\pi x}{p} + \phi_0 \right) \right| + \frac{b}{2} \right)$, i.e. $H_{AFM}^{ribbon}(x) = (n-1)b \left| \cos \left(\frac{2\pi x}{p} + \phi_0 \right) \right| + b$. The maximum and minimum AFM heights are thus $n \cdot b$ and b , respectively, hence resulting in an amplitude equal to $(n-1)b$. Integration of the AFM profile gives for the IMH

$$\text{IMH}_{\text{ribbon}} = \frac{2}{\pi} (n-1)b + \frac{n+1}{2} b \quad (\text{S4})$$

All the previous formulae hold also for protofibrils with increased diameters, provided that the substitutions $n \rightarrow n + dh_n/b$ and/or $m \rightarrow m + dh_m/b$ are performed.

Theoretical modelling of fibrils bending.

Assuming that protofibrils do not possess a spontaneous curvature, the bending induced by a helical conformation has an energetic cost U_{bending} which can be described via the Wormlike-Chain model³²⁸:

$$\frac{U_{\text{bending}}}{k_B T} = \frac{1}{2} l_p \int_0^\Gamma \left(\frac{d\hat{t}}{ds} \right)^2 ds \quad (\text{S5})$$

In the previous formula, $k_B T$ is the thermal energy, l_p the persistence length of the protofibril, s the arc-length parameterization of the helix, Γ its total contour length, and \hat{t} the unit vector tangent to the helix at position s . From equation (S1), the tangent vector can be obtained by differentiating with respect to x and normalizing. We note that the arc-length parameter is related to x via $s = \sqrt{1 + \frac{4\pi^2 R_n^2}{p^2}} x$. Nevertheless, numerical substitution shows that $2\pi R_n \ll p$ (at most one has $2\pi R_5 \approx 20$ nm, which is about one fifth of the experimental p), thus from Eq.(S1) $\left(\frac{d\hat{t}}{ds} \right)^2 \approx \left(\frac{d\hat{t}}{dx} \right)^2 = \left(\frac{4\pi^2 R_n}{p^2} \right)^2$ independently of s . Hence, after the trivial integration of this constant value Eq.(S5) becomes

$$\frac{U_{\text{bending}}}{k_B T} = \frac{1}{2} l_p \left(\frac{4\pi^2 R_n}{p^2} \right)^2 L \quad (\text{S6})$$

Where $L = \Gamma / \sqrt{1 + \frac{4\pi^2 R_n^2}{p^2}} \approx \Gamma$ is the total length along the helical axis. The persistence length can be computed as $l_p = EI_n / k_B T$, where $E = 3.3$ GPa is the Young's modulus of the protofibril³²⁹ and I_n its area moment of inertia. For a protofibril made of n laterally-associated protofilaments, the cross section is a rectangle with sides b and nb , to which correspond principal moments of inertia equal to $\frac{1}{12} n^3 b^4$ and $\frac{1}{12} n b^4$. Assuming that the protofilaments within a protofibril are distributed along the radius of the enveloping tube, the two sides of the rectangle are oriented along the binormal (side of length b) and normal (side of length nb) of the helix. As a consequence, the second bending mode is the one being stimulated, that is $I_n = \frac{1}{12} n b^4$. Substitution into Eq.(S6) and further rearrangement of the result gives:

$$\frac{U_{\text{bending}}}{k_B T} = \frac{2}{3} \pi^4 \frac{E}{k_B T} \frac{b^4 R_n^2 L}{p^4} n \quad (\text{S7})$$

Assuming that R_n and R_m are solely determined by bending, one can obtain the most elastically-favorable morphology by minimizing the bending energy of the system under the constraint $R_n + R_m = \frac{(n+m)b}{2}$. Starting from Eq.(S7), the quantity to be minimized is thus $nR_n^2 + m\left(\frac{(n+m)b}{2} - R_n\right)^2$, which gives $R_n = \frac{m}{n+m} \frac{(n+m)b}{2} = \frac{mb}{2}$ and $R_m = \frac{nb}{2}$. Note that electrostatics is likely to play a role in determining the actual values of R_n and R_m , thus we stress that the formulae provided here were obtained.

Theoretical modelling of fibrils energetics.

From an energetic perspective, fibrils formation is mainly driven by the combination of electrostatics and lateral association. Elasticity is likely to play a minor role due to the difference in magnitude between the radius and periodicity, as typical elastic contributions involve large powers of the ratio $\frac{b}{p}$ (see for instance Eq.(S7)). In contrast, electrostatics plays a major role in fibrils formation. Indeed, the strongly acidic environment employed in the experiments (pH=1.6) results in a large linear charge density of protofilaments and fibrils, whose competition with lateral association ultimately determines the fate of the aggregation process. The key role of electrostatics is further indicated by the control experiments performed in the presence of 150 mM of salt, i.e. when significant screening of electrostatics is present (see Figure 7.5). In this case, the adhesion forces become overwhelmingly stronger than electrostatic interaction, and as a result uncontrolled aggregation takes place.

For a fibril made of n protofilaments, the free energy is thus written as:

$$F(n) = F_{electro}(n) + F_{lateral}(n) \quad (S8)$$

As a simple model for the lateral association, we assume that $n - 1$ lines of contact are present, to which a certain linear energy density $-q$ is associated (in units of $k_B T$), with the minus sign indicating attraction. For a fibril of length L , the lateral association free energy thus reads:

$$\frac{F_{lateral}(n)}{k_B T} = -q(n - 1)L \quad (S9)$$

The electrostatic free energy counts on two contributions: interaction between charges along the fibril and loss of configurational entropy of counterions. The latter is due to the confinement of a finite fraction of counterions in a region in close proximity of a highly-charged polyelectrolyte, a phenomenon known as Manning condensation³³⁰. To estimate the total electrostatic free energy $F_{electro}$, we consider the fibril as a uniformly-charged cylinder of radius $\frac{nb}{2}$ and employ a formula proposed by Manning³³¹:

$$\frac{F_{electro}(n)}{k_B T} = \left[-\left(2 - \frac{1}{\sigma'(n)}\right) \ln k\ell - 1 + \frac{1}{\sigma'(n)} \right] \lambda(n)L \quad (S10)$$

In the previous equation, k is the inverse of the Debye length; ℓ is a certain microscopic length which will be detailed below; $\lambda(n)$ is the linear charge density of the fibril; L is the length of the fibril; $\sigma' \equiv \sigma/\sigma_c(n)$, where σ is the surface charge density of the fibril and $\sigma_c(n)$ a critical surface charge density that needs to be exceeded for counterion condensation to take place (i.e., Eq.(S10) holds for $\sigma' > 1$). We now proceed to describe in detail the various quantities appearing in Eq.(S10). The inverse of the Debye length is computed as $k = \sqrt{8\pi N_{av} l_B I} \simeq \frac{1}{1.92 \text{ nm}}$, where $N_{av} = 6.022 \cdot 10^{23} \text{ mol}^{-1}$ is Avogadro's constant, $I = 25 \text{ mM}$ the ionic strength corresponding to the pH conditions and $l_B = \frac{e^2}{4\pi\epsilon_0\epsilon_r k_B T} \simeq 0.72 \text{ nm}$

is the Bjerrum length, with $e = 1.6 \cdot 10^{-19}$ C being the elementary charge, $\epsilon_0 = 8.859 \cdot 10^{-12}$ F/m the permittivity of vacuum and $\epsilon_r = 78$ the relative permittivity of water. To calculate $\lambda(n)$, we first estimated the charge of an insulin dimer at pH=1.6 by considering the crystallographic structure of bovine insulin (PDB: 2zp6) and using PROPKA^{332,333}, obtaining a total charge of $11.8e$. Importantly, the estimated charge did not change when considering the folded or unfolded structure, suggesting that the molecular rearrangement of insulin dimers should not affect their total charge. Further, we assumed that the fibrils being considered here have a similar structure as the proposed model for human insulin fibrils^{81,322}, thus the spacing between two consecutive dimers was fixed at 0.47 nm. This gives for the linear charge density $\lambda(n) = n \cdot \frac{11.8e}{0.47 \text{ nm}} \simeq n \cdot \frac{25e}{nm} \simeq n \cdot 4.02 \frac{C}{nm}$, where the factor n is included to account for the n protofilaments forming the fibril. The surface charge density σ is directly related to λ by the formula $\sigma = \frac{\lambda(n)}{2\pi \frac{n}{b}} \simeq 6.66 \frac{C}{nm^2}$, independently of n . The microscopic length ℓ is expected to be related to the typical distance of condensed counterions from the polyelectrolyte. In this regard, we note that Manning further defines an internal partition function of the condensed counterions as $Q = \frac{8\pi \exp(1)}{\gamma} l_B \ell^2 \theta$, where $\gamma = \exp(-kl_B/2) \simeq 0.83$ is the activity coefficient of the counterions and θ is the fraction of polyelectrolyte charges neutralized by the condensed counterions found within a certain distance r_c from the polyelectrolyte surface. This partition function accounts for the change in free energy per Bjerrum length induced by the localization of condensed counterions and can be approximately written as $Q = V_{cc} \theta$, where V_{cc} is the confining volume. We estimate this volume as the cylindrical annulus around a protofilament with outer radius equal to $r_M = r_c + \frac{b}{2}$, i.e. $V_{cc} = \pi r_M^2 l_B - \pi \left(\frac{b}{2}\right)^2 l_B$. The quantity r_M is known as the Manning radius and can be obtained as³³⁴ $r_M = 0.9[\lambda(1)l_B - 1]^{0.22} + \frac{b}{2} \simeq 2.28$ nm. Comparing the formulas for the partition function Q enables obtaining $\ell = \sqrt{\frac{\gamma}{8 \exp(1)} \left[r_M^2 - \left(\frac{b}{2}\right)^2 \right]} \simeq 0.43$ nm. Finally, the critical surface charge density reads $\sigma'(n) = \frac{-e \ln k \ell}{2\pi l_B \frac{nb}{2} \cdot f\left(k \cdot \frac{nb}{2}\right)}$, where $f(x) = \frac{K_0(x)}{x K_1(x)}$ with $K_i(x)$ being the modified Bessel functions of the second kind.

Starting from Eq.(S9) and Eq.(S10), one can then estimate the propensity of two protofibrils to form a mature fibril by computing the total change in free energy as:

$$\frac{\Delta F_{total}(n,m)}{k_B T} = \frac{\Delta F_{electro}(n,m)}{k_B T} + \frac{\Delta F_{lateral}(n,m)}{k_B T} \quad (S11)$$

In Eq.(S11), $\Delta F_{electro}(n, m) = F_{electro}(n + m) - F_{electro}(n) - F_{electro}(m)$ and $\Delta F_{lateral}(n, m) = F_{lateral}(n + m) - F_{lateral}(n) - F_{lateral}(m) = -k_B T \cdot qL$. Note that the gain in lateral-association energy is simply $-qL$, as in the present model only a single line of contact is added upon aggregation.

7.3 Results

7.3.1 Morphological evolution of the insulin amyloids

The morphological evolution of the insulin aggregates has been monitored over a duration of ten hours under acidic condition (Figure 7.1). At an early stage, the initiating monomeric protein (Figure 7.1a) formed amorphous pre-fibrillar nuclei (Figure 7.1b), which gradually vanished once protofilaments appeared. Individual protofilaments were observed after 1-hour incubation (Figure 7.1c), followed by an increasing amount of protofibrils (Figure 1d-f). In this period of fibrillization, we observed plenty of evidences of interfibril interaction and combination, as indicated by the arrows. In the following incubation, the matured fibrils were gradually formed (Figure 7.1 g-h). These mature fibrils showed a considerable increase in the length and thickness compared with the protofibrils, as well as the quantity of fibrils.

Besides, we utilized three independent techniques to verify the trend of protein aggregation. ThT fluorescence assay was performed to show the aggregation kinetics (Figure 7.2a), confirming the lag phase over a duration of about 5 hours, followed by a shorter elongation phase and the saturation phase after ca. 10-hour incubation. Circular dichroism experiments and infrared nanospectroscopy measurements (Figure 7.3b-c) were performed that shows a clear gradual transition from α -helix structure to the β -sheet rich conformation of the protein aggregates.

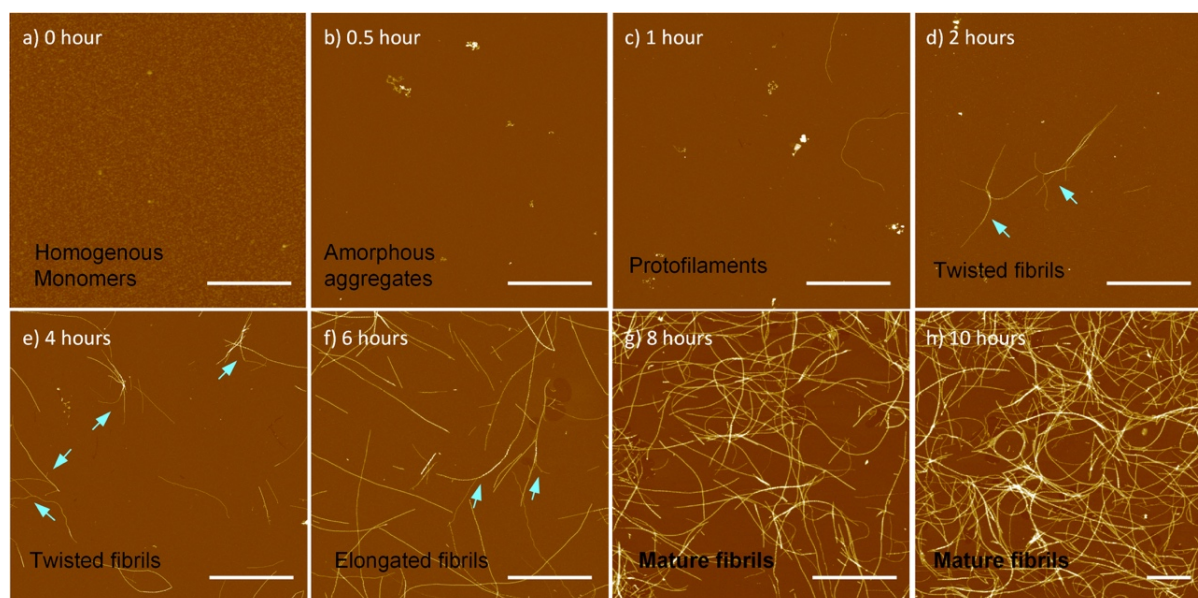


Figure 7.1 The morphological evolution of full-length insulin aggregates at acidic pH. (a-h) AFM images of full-length insulin self-assembly incubated at pH 1.6 for 0, 0.5, 1, 2, 4, 6, 8 and 10 hours, respectively. These AFM images show (a) homogeneous monomeric insulin; (b) amorphous pre-fibrillar aggregates; (c-f) protofilaments and protofibrils; (g-h) mature fibrils. Interfibrillar interactions are indicated by arrows. Scale bars are 2 μ m.

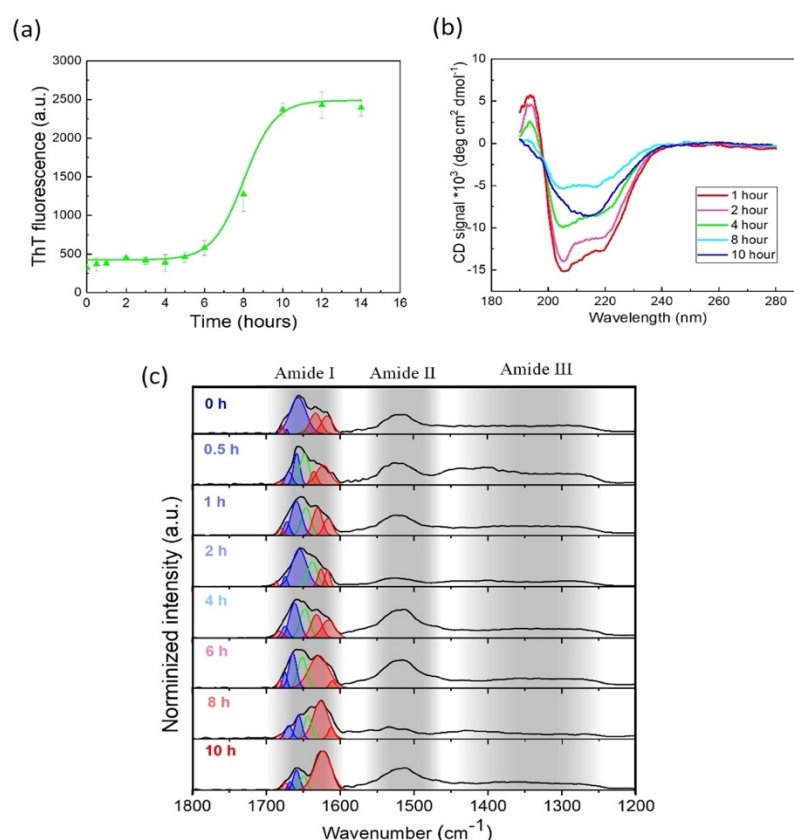


Figure 7.2 Aggregation kinetics and secondary-structure transition of insulin self-assembly. (a) Aggregation kinetics revealed by the evolution of ThT fluorescence as a function of incubation time. (b) CD spectra of insulin solution incubated for 1, 2, 4, 8 and 10 hours. The dips on the spectrum at 208 and 220 nm (α -helical conformation) show a gradual shrinking in the first 8 hours and transferring to 218 nm (β -sheet content) in the following 2 hours. (c) NanoIR infrared absorption spectra of the formed aggregates from 0 to 10 hours incubation in the range 1200–1800 cm^{-1} . The band of amide I, II and III are indicated with grey background. The details of multi-composition analysis are shown in method section. The blue Gaussian bands represent helical and turn-like (1648–1685 cm^{-1}) structure, red Gaussian bands refer to β -sheet and antiparallel β -sheet (1610–1640 and 1685–1695 cm^{-1}) structure and green peak indicates the random coil (1640–1650 cm^{-1}) structure.

It is interesting to note that, except for the single protofilaments in the beginning of incubation, these protofibrils and mature fibrils showed homogeneously-fluctuated height profiles (Figure 7.3), and this regular height fluctuations were maintained during the whole aggregation process. This twisted geometry is believed result from the incubation condition, especially pH and ionic strength^{322,326}, and it indicated that an acidic pH environment enlarges the high surface charge of insulin fibrils and favors the formation of twisted configurations^{81,322,324,335}.

According to the statistical measurement on the average height of the protein aggregates and twisted fibrils, it is also worth to note that the average height of the fibrils shows an overall increasing trend as a function of incubation time (Figure 7.4a-g), from the monomers (1 nm) before the incubation to the fibrils with height ranging from 2 to 8 nm. Remarkably, we observed that the average height of the protofibrils in each incubation time showed multi-peaked distribution, and these peaks saw an overall increase along the incubation (Figure 7.4h). This trend of morphological evolution suggested

the fibrillization mechanism of hierarchical assembly by stacking of protofilaments and protofibrils, as a result of the interprotofilament interaction, as indicated in Figure 7.1d-f.

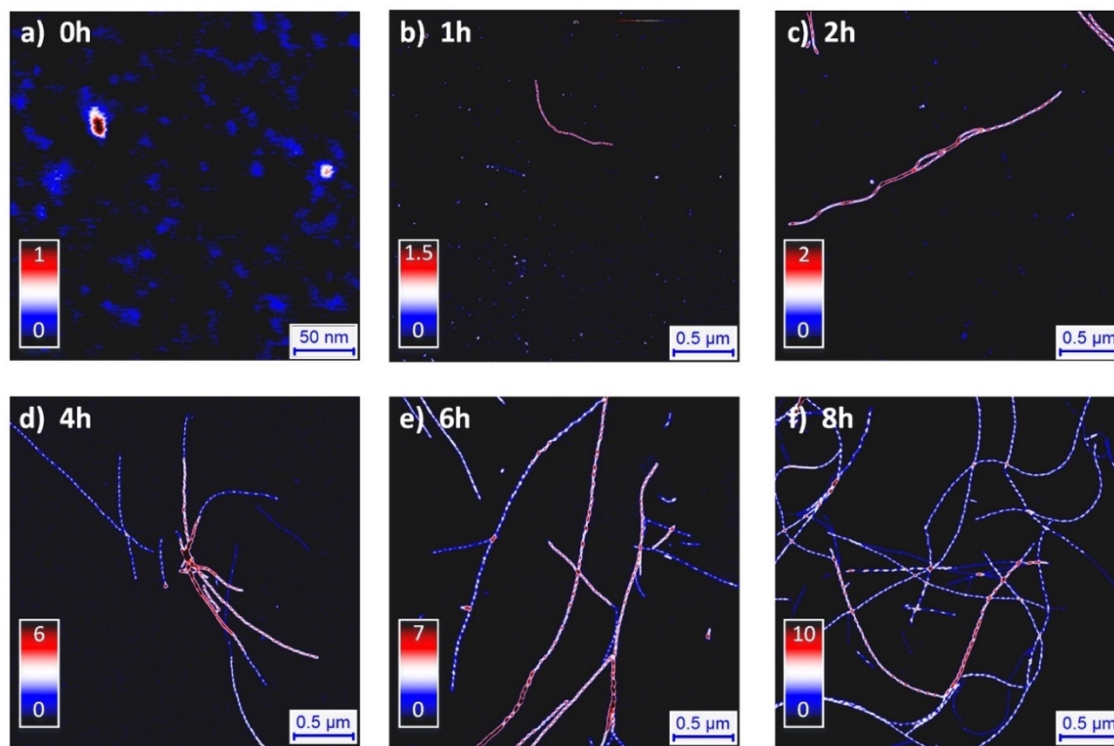


Figure 7.3 High-resolution AFM images of insulin aggregates throughout fibrillization. (a-f) The AFM images show insulin monomers (a), protofilaments (b) and fibrils with fluctuating height (c-f) after 0, 1, 2, 4, 6 and 8 hours incubation. The insulin monomers (a) show a height of around 1 nm and the protofilaments appeared after 1-hour incubation also have a height of 1 nm with no significant fluctuations along the profile. The protofibrils and mature fibrils formed in the following incubation display a homogeneously-fluctuating height profile together with an overall increase of fibril height.

Thus, it is clear to focus the study on the intertwining phenomenon among protofilaments and protofibrils. This phenomenon was intensively observed in the during the lag and elongation phases of the aggregation process, which evidences the key role played by interprotofilament interaction in the fibrillization process. First, to visualize this interaction in the initiating stage, we isolated early fibrillar aggregates from protein solution after 1-2 hours incubation. We captured a nanoracket-shaped self-folded protofilament (Figure 7.6a) with a height of 1.2 nm, close to the diameter of an insulin monomer. This geometry was considered as mesoscale building blocks of entangled plaques³³⁶. Further evidences of fibril-fibril intertwining are shown in Figure 7.6b, suggesting the existence of a widespread mechanism knitting protofilaments to form higher-ordered multi-stranded fibrils with complex configurations. We reason that the origin of the interprotofilament interaction is the surface adhesion^{336,337} as a consequence of the hydrophobic and polar interactions, between insulin fibrillar aggregates. This intertwining effect might not attribute to the electrostatic force as we proved that an enhanced electrostatic force by modulating ionic strength induced the gathering of fibrils and the formation of massive fibril bundles (Figure 7.5).

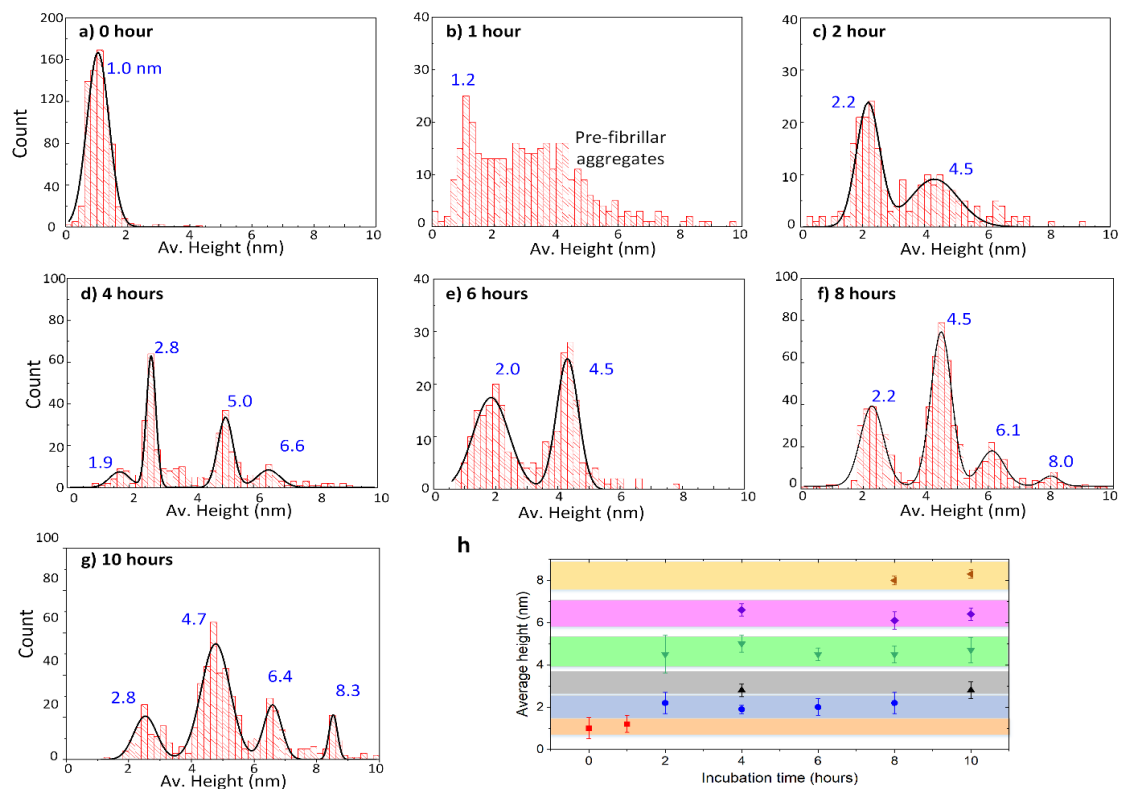


Figure 7.4 Statistical analysis of the average height of insulin aggregates. (a) The height distribution of insulin proteins before incubation shows an average height of 1.0 nm, indicating homogeneous monomeric proteins under acidic conditions²³⁵. (b) Height distribution of protein aggregates incubated for 1 hour. The distribution of average height of protofilaments is located at 1.2 nm, but another cluster of height distribution (1-8 nm) was found because of the existence of amorphous pre-fibrillar aggregates. (c-g) The height distributions of protofibrils and fibrils obtained after 2-8 hours incubations show multiple peaks, indicating the presence of distinct families. (h) Evolution of average height of twisted fibrils for each family as a function of incubation time, showing the tendency of thickening the fibrils as enlarging the incubation time.

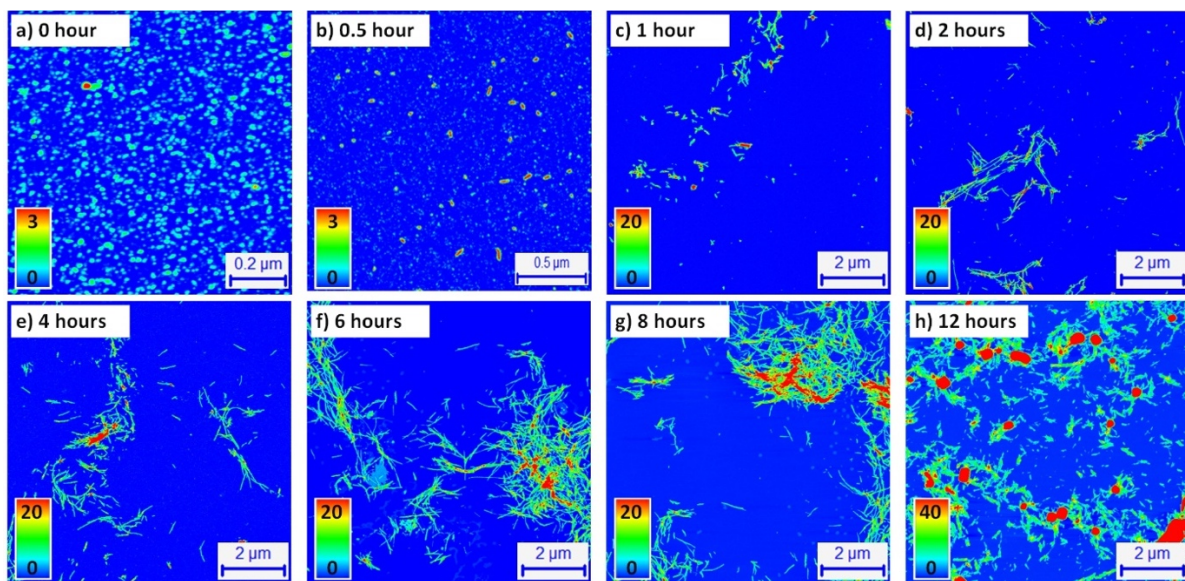


Figure 7.5 The morphological evolution of insulin aggregates under large ionic-strength conditions. (a-h) AFM images of insulin aggregates obtained in the presence of 150mM NaCl after 0, 0.5, 1, 2, 4, 6, 8 and 12 hours of incubation, respectively.

7.3.2 Statistical analysis on the morphological features of twisted fibrils

To further characterize the effect of inter-protofilament interaction on fibril polymorphism, it is essential to access the stacking arrangement of protofilaments within these fibrils. Due to convolution effects, AFM tips have not enough horizontal resolution to detect the inner configurations of fibrils, whose diameters are in the order of a few nanometers (Figure 1.9).

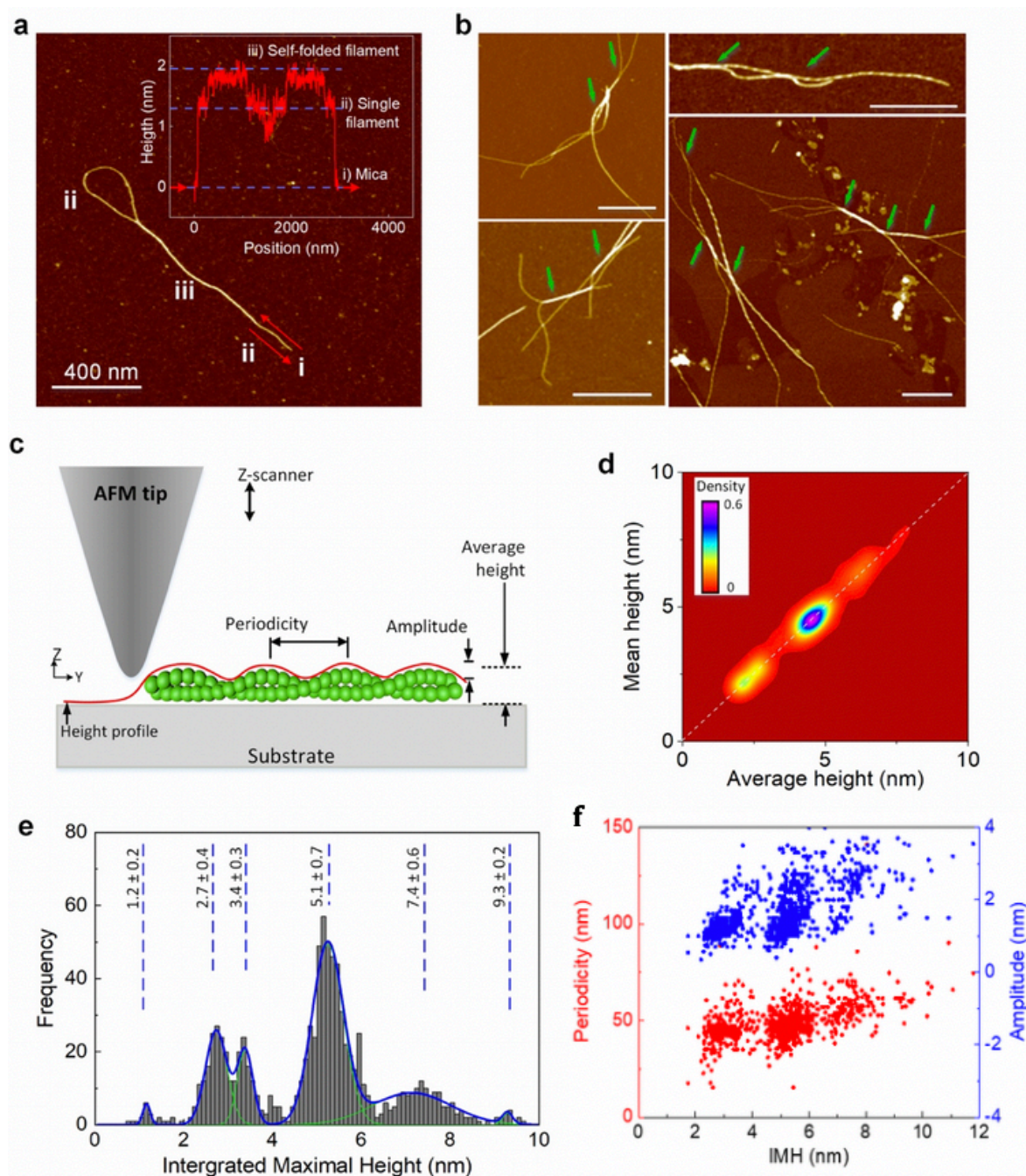


Figure 7.6 Snapshots of fibril-fibril interaction and statistical analysis on fibril morphologies. (a) AFM image of a self-folded protofilament with the nanorocket shape. The insert shows the height profile along the ridge of the protofilament following the direction of red arrows. The height of i) mica, ii) single protofilament and iii) self-folded protofilament are clearly indicated. (b) AFM snapshots of the intertwining protofilaments and protofibrils isolated from solution in the early stage, as indicated by the arrows. The scale bar is $0.5\mu\text{m}$. (c) Schematic representation of a twisted amyloid fibril scanned by an AFM tip. The height profile (red) along the fibril is extracted by tracing along the ridge of the fibril. Average height,

periodicity and amplitude of the fluctuating height profile are indicated. Considering the flexibility of the protofibrils, the lower surface of these protofibrils were believed on the substrate. (d) The density map distribution of average height against mean height of all twisted fibrils. The equilibrium of distribution suggests the correspondence between extracted extrema and average height, and thus the reliability of extracted IMH and amplitude. (e) The IMH distribution of the twisted fibrils obtain in the experiment, that features six distinct families peaked at 1.2 ± 0.2 , 2.7 ± 0.4 nm, 3.4 ± 0.3 , 5.1 ± 0.7 , 7.4 ± 0.6 and 9.4 ± 0.4 nm. (f) Scatter plot of the periodicity and amplitude vs. IMH. The clustered distribution indicates that the correlation between amplitude and periodicity of twisted fibrils with their IMH height.

However, this limitation can be circumvented by employing the high vertical resolution (2 \AA) AFM to access the precise features of the height profile, e.g. height, pitch and amplitude, of the twisted fibrils, as illustrated in Figure 7.6c. Firstly, we traced the ridge of fibrils along the contour length to obtain their height profiles, illustrated as the red curve in Figure 7.6c. Then, several features from this height profile were extracted: the average height was obtained as $H_{Av.} = \frac{1}{n} \sum_{k=1}^n H_k$, where H_k refers to the height value of each pixel on the height profile of the fibril; the periodicity P was defined as the distance between consecutive peaks; the maximum (H_{max}) and minimum height (H_{min}) were computed as the heights corresponding to peaks and wells, respectively. Note that P , H_{max} and H_{min} were averaged over the whole trace. Finally, the amplitude was defined as $A = H_{max} - H_{min}$.

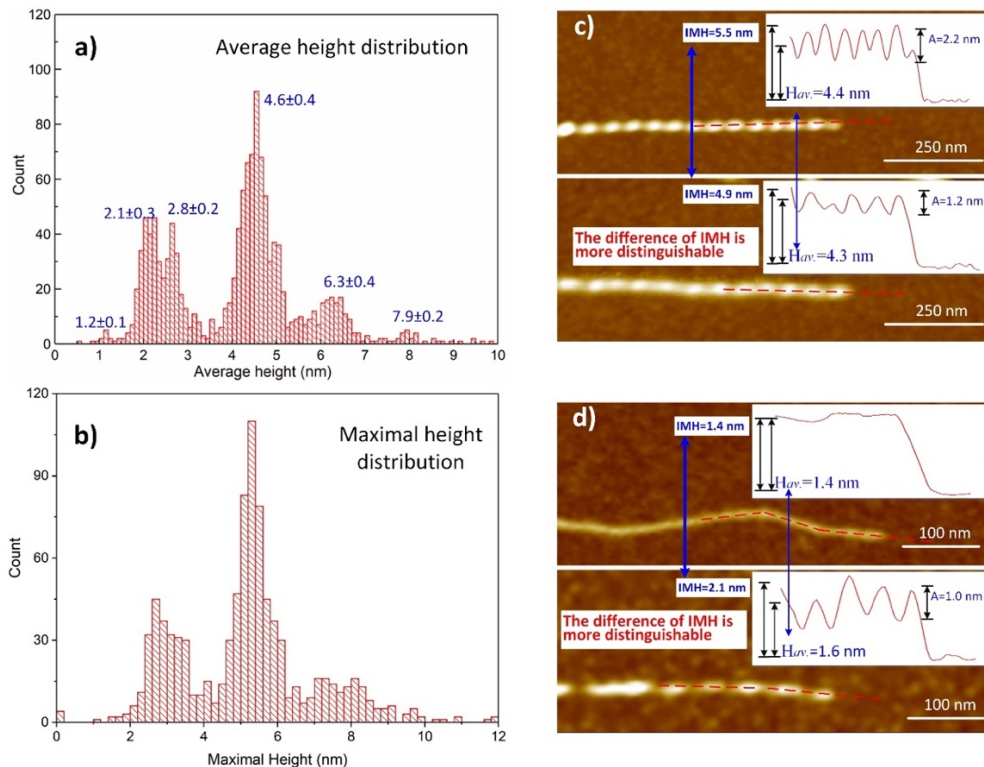


Figure 7.7 Assessment of average and maximal height of hierarchically twisted fibrils. (a) Distribution of average fibril height acquired by averaging all height values traced along the amyloid fibril. (b) Distribution of maximal height acquired by averaging all peaks on height profile of fibrils, which shows only three main peaks. (c) Two twisted fibrils with different amplitudes, implying distinct configurations, shows similar average height, but indicates different values of IMH, which thus allows distinguishing them from each other. (d) A protofilament shows an average height similar to another twisted fibril, while there is a marked difference in IMH. These two examples (c-d) epitomize the advantages derived from employing the IMH over the average height to characterize hierarchical twisted fibrils.

The average height of twisted fibrils obtained throughout the whole incubation period are displayed a multimodal distribution (Figure 7.7a) with six distinguishable fibril families peaked at 1.2 ± 0.1 , 2.1 ± 0.3 , 2.8 ± 0.2 , 4.6 ± 0.4 , 6.3 ± 0.4 and 7.9 ± 0.2 nm. This feature has been previously reported for amyloid fibrils^{95,324,338–340} and is believed to be due to the combination of different amount of protofilaments^{324,338}. As mentioned above, larger families were favored at longer incubation times, supporting a hierarchical building process (Figure 7.5h). Thus, it is reasonable that higher-ordered fibrils were obtained by intertwining two smaller components under the hierarchical assembly model (HAM)^{324,341–344}. This argument is further reinforced by the observation of ubiquitous protofibril-intertwining events (Figure 7.6b). Therefore, we assume that the various peaks in the average height distribution correspond to different amounts (from one to six) of protofilaments.

However, despite its popularity in characterizing amyloid fibril^{40,85,235,339,342}, average height might be misleading because configurational information is missing in the averaging process. Indeed, as illustrated in Figure 7.7c-d, qualitatively-different packing arrangements can result in similar average height. In contrast, the maximal height can in principle discriminate between different configurations, yet its distribution does not satisfactorily capture the various families (Figure 7.7b). In order to better characterize the various populations of polymorphic twisted fibrils, we therefore introduce a novel feature, namely the *Integrated Maximal Height* (IMH), defined as:

$$H_{IMH} = H_{Av} + \frac{1}{2}A,$$

where H_{Av} refers to average height of twisted fibril and A is the amplitude of the fluctuation in the height profile. Before further characterization, we evaluated the stability and comparability of IMH and amplitude. By comparing mean height ($H_{mean} = \frac{1}{2}(H_{max} + H_{min})$) and average height in Figure 7.6d, we found the equilibrium distribution that confirms the consistency between average height and extracted features from height profile, and thus proves the reliability of IMH and amplitude. Contrary to the maximal height, IMH captures the presence of the six-fibril families (Figure 7.6e), peaked at the values 1.2 ± 0.2 , 2.7 ± 0.4 nm, 3.4 ± 0.3 , 5.1 ± 0.7 , 7.4 ± 0.6 and 9.4 ± 0.4 nm. This is comparable to the results obtained via the average height distribution, but with the advantage of clearly distinguishing qualitatively-different configurations (Figure 7.7a), suggesting that the various peaks correspond to a different number (from one to six) of protofilaments.

Then, we address the relation between the IMH and the other geometrical features of polymorphic twisted fibrils. In Figure 7.7f, we report a scatter plot showing the variation of periodicity and amplitude as a function of IMH. The tendency of clustering of the data suggests the dependence of both

periodicity and amplitude of twisted fibrils on their IMH height. Thus, we analyzed the periodicity and amplitude of these twisted fibrils from each family (Figure 7.6e) classified by IMH distribution.

For the periodicity, we found a single-peak distribution in each family, exhibiting an overall linear increase of average periodicity as a function of IMH (Figure 7.8a-g), consistent with previous observations^{85,136,345}. However, this increase as a function of protofilament number is not consistent with the prediction based on a twisted-ribbon model where twisting is driven by electrostatics³²⁷. Moreover, there is an obvious overlap of periodicities among different fibril families (Figure 7.8g) and the direct inspection shows a high degree of disagreement of the periodicities and IMH among different illustrated examples (Figure 7.8h), indicating that periodicity is not a good candidate for reliable characterization of twisted fibrils.

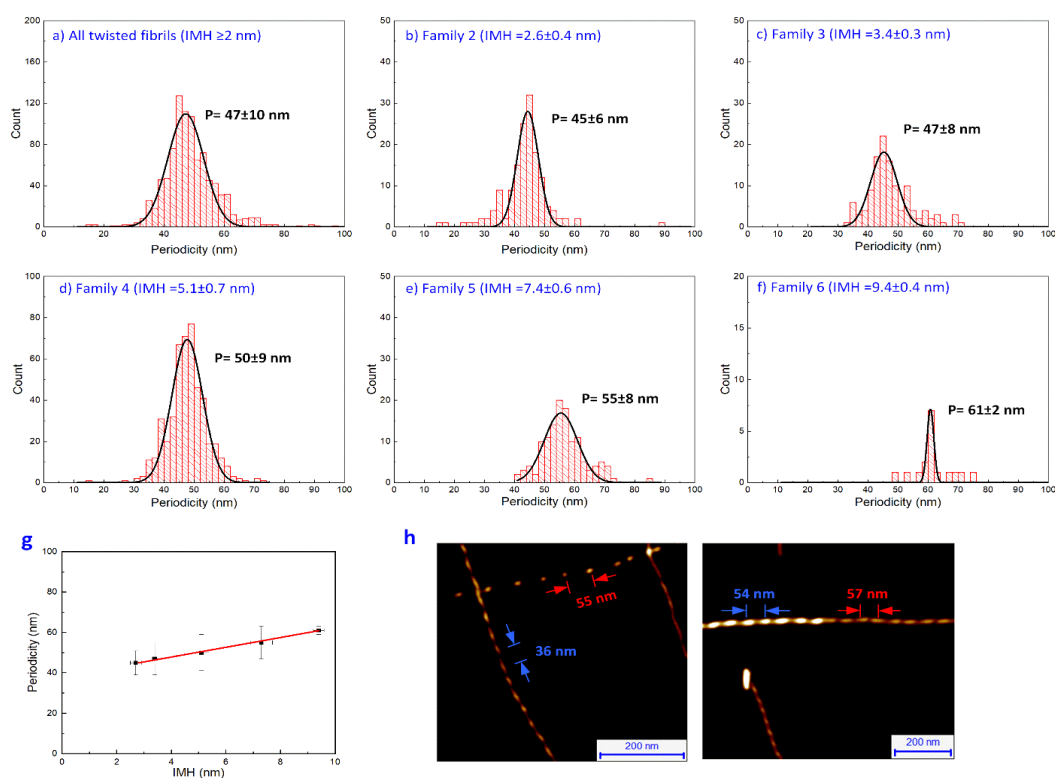


Figure 7.8 Evaluation of the periodicity of twisted fibrils. (a) Histogram of periodicity distribution of all twisted fibrils with an IMH height of more than 2 nm. (b-f) Distribution of periodicity with amyloid fibrils from each IMH family, where it is clearly seen that only one dominant peak was found in each family. (g) Fibril periodicity in each family shows a linear dependence on IMH. (h) Some examples of irregular features of fibril periodicity. Left: Two twisted fibrils with similar height (color scale) show considerable differences in their periodicity. Right: Two twisted fibrils with obviously different IMH show the same periodicity. The lack of a clear relationship between height and periodicity indicates that the fibril periodicity does not provide a reliable characterization of twisted fibrils.

For amplitude, in contrast, we found the amplitude distribution within each IMH family (Figure 7.9a) shows multiple regularly located peaks (1.3 ± 0.4 , 2.5 ± 0.4 and 3.4 ± 0.2 nm), which correspond to the IMH of fibrils with one (1.2 ± 0.2 nm), two (2.7 ± 0.4 nm) and three (3.4 ± 0.2 nm) protofilaments respectively (Figure 7.6e). These findings reinforce the hypothesis that twisted fibrils are hierarchically

built by intertwining one strand of protofilament or protofibril with another. Since the high lateral flexibility of amyloid fibril, it is believed that the surface of twisted fibril is in contact with flat mica substrates (Figure 7.6c). Thus, it is clear that the IMH of twisted fibrils corresponds to the IMH sum of two strands of intertwining sub-protofibrils, whereas the amplitude corresponds to the IMH diameter of the thinner sub-strand.

Based on this ansatz, we conceptualized all possible packing arrangements of twisted fibrils according to their IMH and amplitude, as illustrated in Figure 7.9. For example, the fibrils with IMH of 2.7 ± 0.4 nm (Figure 4a-ii), corresponding to those fibrils consisting of two protofilaments, show only one peak located at 1.2 ± 0.2 nm, close to the IMH of a single protofilament. This agrees with the only possible intertwining pattern of two protofilaments. In contrast, the fibrils containing four protofilaments (IMH 5.1 ± 0.7 nm) show three amplitude peaks (Figure 4a-iv) corresponding to three different packing arrangements: one-to-three (4^A), two-to-two (4^B) and twisted-ribbon (4^C) fibrils (Figure 7.9b). In this way, we can interpret the amplitude distribution in each family and thus identify different classes of twisted fibrils. It is worth noting that our proposed configurations include as particular cases insulin fibril configurations solved by cryoEM in the literature^{81,322,335}, which also supports the reliability and reproducibility of our results.

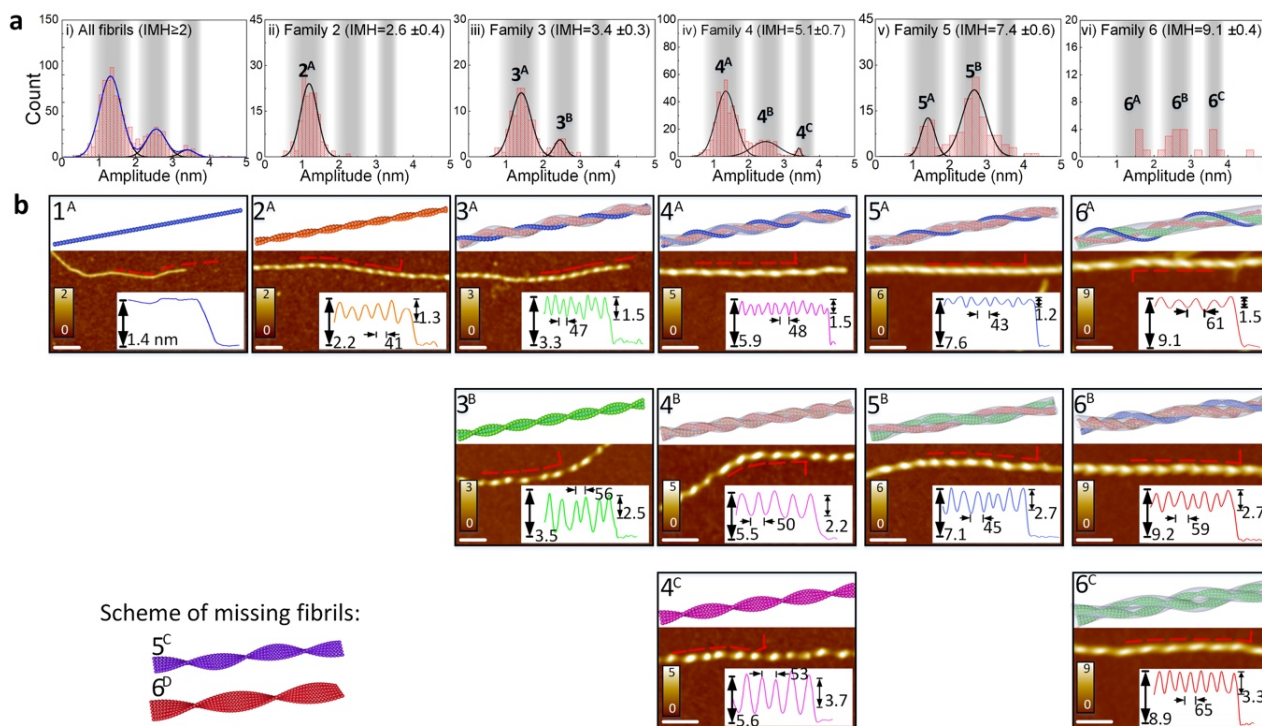


Figure 7.9 Statistical analysis of amplitude distribution and conformational identification of hierarchically twisted fibrils. (a) Histogram of amplitude distribution of all twisted fibrils with IMH height of more than 2 nm (i) and fibrils from each classified IMH family (ii-vi). Coloured regions (light, medium and deep grey) refer to the IMH value of fibrils with 1, 2 and 3 protofilaments respectively. The labels on the peaks represent different types of fibril arrangement: the digits refer to the number of protofilaments in the fibrils, and letters A, B, C and D stand for increasing values of the amplitude, corresponding

to 1,2,3,4 protofilaments, respectively. All the peaks observed in each IMH family are located in the grey regions, suggesting that each peak originates from the size of a smaller protofibril involved in the formation of the fibril at hand. (b) Schematic models of all possible configurations of twisted fibrils made of up to 6 protofilaments, with corresponding examples of AFM scanned fibrils. The inset in each scheme shows the height profile of the fibril along the red dashed line, for which the IMH, periodicity and amplitude are reported. The scale bar in the AFM image corresponds to 100 nm.

7.3.3 Morphological modelling of twisted fibrils

Besides, we also modeled the geometry of the protofilament-based structure of these identified fibrils. As shown in Figure 7.10a-b, we illustrated the AFM tip and the comparison between the real morphology of the protofilament-based fibrils and the modeled AFM-scanned fluctuated height profile. By applying a diameter of single protofilament of 1.2 nm, we obtained the IMH and amplitude of all these modeled height profiles, and matched these modeled data with experimental data (Table 7.1). We found an overall agreement from this comparison (green values), despite of slight mismatch on the IMH values of the thick fibrils (red values).












No.	Modelling of protofilament arrangement	Modelling (IMH/amp.)	Experiment (IMH/amp.)
2		2.6/1.3	2.6±0.4/1.3±0.4
3A		3.8/1.3	3.4±0.4/1.3±0.4
3B		3.8/2.5	3.4±0.4/2.5±0.4
4A		5.1/1.2	5.1±0.7/1.3±0.4
4B		5.1/2.1	5.1±0.7/2.5±0.4
4C		5.1/3.8	5.1±0.7/3.4±0.2
5A		6.6/1.2	7.4±0.6/1.3±0.4
5B		6.6/2.6	7.4±0.6/2.5±0.4
6A		7.8/1.2	9.1±0.4/1.3±0.4
6B		7.8/2.9	9.1±0.4/2.5±0.4
6C		7.8/3.2	9.1±0.4/3.4±0.2

Table 7.1 The protofilament-based modelling on fibril geometry. The modelled schemes and their IMH and amplitude of each modelled height profiles with a diameter of protofilament of 1.2 nm. The correlation between these modelled data with experimental data shows an overall agreement (green values), despite of slight mismatch on the IMH values of the thicker fibrils (red values).

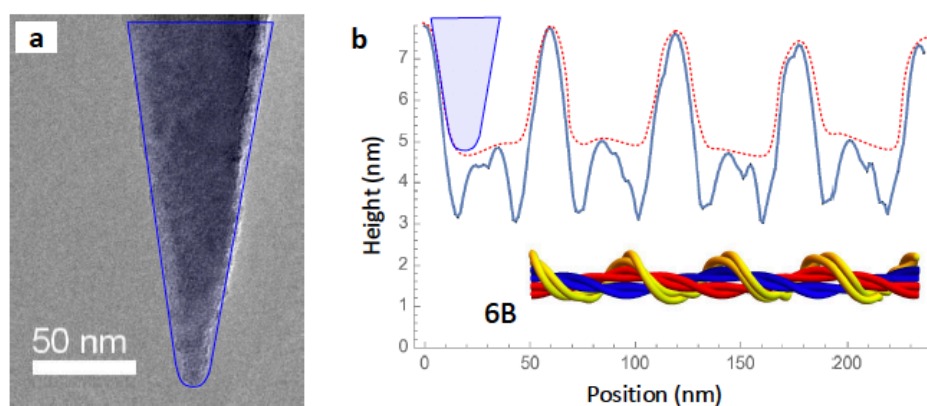


Figure 7.10 The AFM tip fitting on the modelled fibril geometry. (a) The size of experimental AFM tip (b) The correlation between the modelled morphology (blue) of the protofilament-based fibrils and the fitted AFM result on fibril height profile.

In general, we classify the fibril configurations into two categories: twisted ribbons and randomly-twisted fibrils. On one hand, the twisted ribbons are constructed by parallel-stacking of protofilaments, which straightforwardly give the measured amplitude by recognizing the maximum and minimum profile height as corresponding to the difference of the height of vertically-adsorbed protofilaments and single protofilament, respectively^{99,136,237}. Indeed, in this case the maximum and minimum height are $n \cdot b$ and b , respectively, where $b \simeq 1.2$ nm is the diameter of a protofilament and n is the number of protofilaments within the ribbon. This results in an amplitude equal to $(n - 1) \cdot b$, in excellent agreement with the experimental data (structures 2^A, 3^B and 4^C in Figure 7.9b).

On the other hand, the random-twisted fibrils containing more complex architecture can be rationalized with the aid of the hierarchical assembly model (HAM)^{19,33–36}. This model prescribes the intertwining of two-cylinders enveloping the protofilaments or protofibrils composing the fibril, and therefore a protofibril made of n protofilaments is represented as a cylinder of diameter $n \cdot b$. For instance, in Figure 7.11a, we sketch the HAM model of fibril 3^A, composed by twisting a protofilament around a scaffolding 2^A fibril. A theoretical AFM profile is also reported assuming that small deformations of the fibril ensure its homogeneous adsorption onto the substrate (Figure 7.6c). Note that for representation purposes the sketch in Figure 7.11a shows significantly larger diameter/periodicity ratios than the experimental data. From the theoretical AFM profile, both the IMH and amplitude could be analytically computed and compared well with the experimental results (Figure 7.11a). A better agreement with the data for the thickest fibrils could be achieved by assuming that protofibrils involved in the formation of a fibril have larger diameters than when they are considered alone (Figure 7.11b-c). For instance, the diameter of 3^A equals to 3.6 nm when the protofibril is considered alone, while it becomes 4.4 nm when 3^A is used as a scaffold to form 5^B or 6^C. This increase might be due to the presence of dangling ends along the protofibrils, i.e. disordered sequences decorating the

core^{81,82}. Indeed, when a protofibril is considered alone, the disordered nature of the dangling ends may prevent their detection by the AFM tip. In contrast, when the protofibril is providing the scaffold to form a larger fibril, the second intertwining protofibril/protofilament may “tie” the dangling ends to the core, thus making them visible to the AFM tip.

We interpret that the appearance of random-twisted and twisted-ribbon fibrils is due to different origins of driving forces. On one hand, the adhesion forces^{321,336,346}, consisting of hydrophobic and polar interaction, between individual fibrillar aggregates in the bulk solution, to form the HAM polymorphic fibrils with random intertwining of protofilaments and protofibrils^{324,336,341–343}. On the other hand, insulin protein, containing two well-characterized fibril-forming segments (LYQLEN and VEALYL), can induce steric zipper^{79–81,322} to parallel stack protofilaments and thus form twisted-ribbon^{136,237} fibrils. Thus, the combined effect results in the coexistence of twisted-ribbon model and random-twisted fibrils^{85,95,322,323,344}, which therefore affect amyloid formation propensity. From energetic point of view, the origin of this intertwining is to reduce the free energy and form mechanically robust fibril configuration^{98,99,318}, as well as the competition among the twisted fibril polymorphs.

Interestingly, our data show a non-monotonic behavior of populations as a function of number of protofilaments. Fibrils with four protofilaments ($n = 4$, where n is the number of protofilaments) are the most common configuration (Figure 7.6e). Moreover, thin fibrils ($n \leq 4$) tend to progressively combine with single protofilaments, so that fibrils 3^A and 4^A dominate each family (Figure 7.9a iii-iv). In contrast, mature fibrils ($n > 4$) are mostly formed by recruiting protofilament pairs ($n = 2$), thus fibrils 5^B and 6^B are the majority in their family.

However, not all possible protofibril packing arrangements were found in this experiment, in particular the higher-ordered twisted-ribbons (5^C and 6^D) as shown in Figure 7.9b. As early twisted ribbons (3^B and 4^C) were formed less frequently in each family (Figure 7.9a iii-iv) upon the increase of the number of protofilaments, we reason that the decreasing concentration of monomers in time prevented the formation of thicker twisted ribbons due to exhaustion of available protofilaments (compare Figure 7.5h).

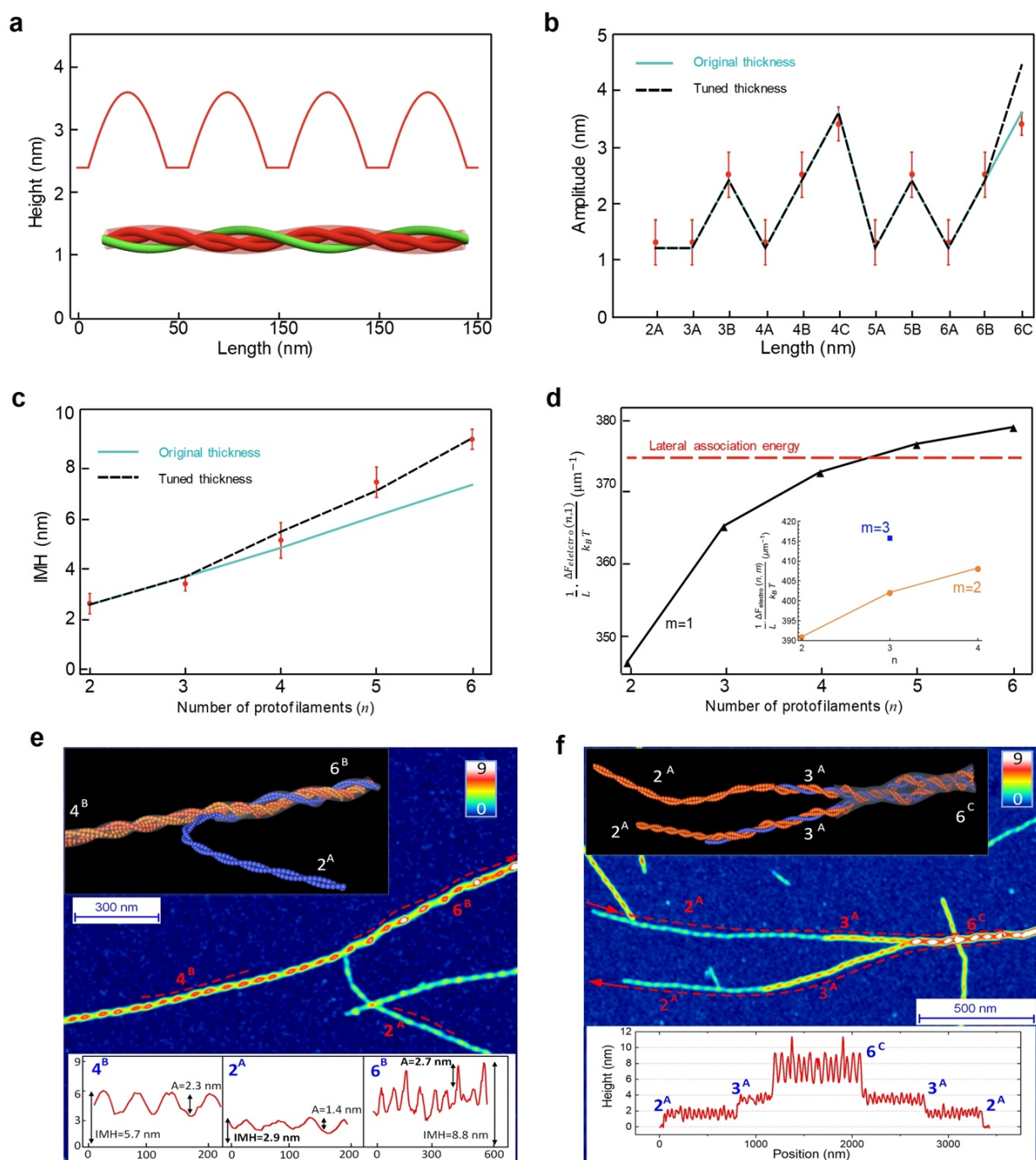


Figure 7.11 Modeling of fibril morphologies and energetics and the configurational interpretation of twisted fibrils. (a) The representation of HAM model of fibril 3A, that shows the conformation with the intertwining of two-cylinders protofilaments or protofibrils. (b-c) The comparison of experimental amplitude (b) and IMH (c) of the fibrils, shown as red dots, with these modelling data with protofilament-based HAM model (aqua curve) and with HAM model with tuned thickness of single protofilament (dashed black curve). (d) The modeling of fibril energetics in the intertwining fibril. It shows the energy in the intertwining as a function of number of protofilament in one strand of protofibril (n), for the number in the other strand (m). (e) AFM snapshot of 2A and 4B protofibrils partially intertwined to form 6B, where the fibril profiles before and after entangling are showed in the bottom inset with indicated IMH height and amplitude. (f) AFM snapshot showing formation of two 3A protofibrils via aggregation of 2A and protofilaments, followed by their intertwining to generate a higher-ordered fibril (6C). The insets show schematic representations of the intertwining steps reported in the AFM images.

The proposed HAM twisting hypothesis is further illustrated by the snapshots of the intertwining fibrils. In Figure 7.11e, we show the merging of two protofibrils, which are identified as fibril 2^A and

4^B families according to the features on their height profiles, to form a higher-order twisted fibril family 6^B . It is noteworthy that this formed mature fibril (6^B) is especially in the entangling region so that its height profile shows two clear envelope levels, where the lower envelope corresponds to the IMH of fibril 4^B and the amplitude equals to IMH of fibril 2^B , respectively. However, in the direction away from intertwining, the lower envelope became gradually less obvious, suggesting that two strands of protofibrils knit individually, independent of their inner configurations, on the basis of HAM model^{322,324}. This observation again directly proves the hypothesis that random-twisted fibrils are obtained from intertwining of protofibrils and protofilaments. Similarly, Figure 7.11b shows the formation of mature fibril 6^C by intertwining two protofibrils 3^A , which are themselves obtained as a combination of fibril 2^A and a protofilament, and the morphological features of these fibrils are in perfect agreement with the scheme reported.

This non-trivial picture is compatible with two possible physical scenarios. One of them relies on the observation of the progressive disappearance of single protofilaments from the system (see Figure 7.5h). Within this scenario, addition of a single protofilament is always more energetically favorable than combination with thicker protofibrils. At the early stages of aggregation, thin fibrils are then formed by progressively attaching single protofilaments, which explains the dominance of 3^A and 4^A for $n \leq 4$. Nevertheless, further formation of n^A fibrils is suppressed due to the disappearance of protofilaments, so that alternative aggregation routes are pursued. In the second scenario, this suppression is instead due to the competition between electrostatics and lateral association. The control experiment with screened electrostatics shows that large aggregates are formed (Figure 7.5), indicating that electrostatics opposes the aggregation process and suggesting larger electrostatic energies for thicker fibrils. It is thus possible that at a critical thickness ($n = 4$) the electrostatic repulsion becomes stronger than lateral attraction, thus suppressing further recruitment of protofilaments. We further note that the two scenarios are not incompatible, and both protofilament depletion and electrostatics strengthening may be acting at the same time.

7.3.4 Energetics modelling of the twisted fibrils

In order to rationalize these arguments, we considered a simple model of fibrils energetics. At the simplest level, combining two protofibrils of length L adds a line of lateral contacts between them, which contribute an energy $\Delta F_{lateral}(n, m) = -k_B T q L$ independently of the number of protofilaments n and m of the composing protofibrils, where $k_B T$ is the thermal energy and q the linear energy density of lateral attraction. In a previous work, based on the analysis of torsional correlations along fibrils, it was estimated that $q \geq 310 k_B T / \mu\text{m}$ ³⁴⁷. The electrostatic free energy is obtained as a

combination of two effects. First, repulsion of the various charges decorating the surface of a fibril. Second, due to the large linear charge density of a fibril (see Method), counterion condensation is expected to take place, which has a cost in terms of counterions configurational entropy. Following previous study³³¹, we compute the electrostatic free energy of a fibril made of n protofilaments as $F_{electro}(n) = k_B T \left[- \left(2 - \frac{1}{\sigma'(n)} \right) \ln k\ell - 1 + \frac{1}{\sigma'(n)} \right] \lambda(n)L$, where k is the inverse of the Debye length; $\ell \simeq 0.43$ nm is a microscopic length related to the confining volume of condensed counterions; $\sigma'(n)$ is the surface charge density of the fibril normalized by a critical value; $\lambda(n)$ is the corresponding linear charge density (see Methods). The free-energy change induced by the combination of two protofibrils with n and m protofilaments is then computed as $\Delta F_{electro}(n, m) = F_{electro}(n + m) - F_{electro}(n) - F_{electro}(m)$. Finally, the total change in free energy is computed as $\Delta F_{total}(n, m) = \Delta F_{lateral}(n, m) + \Delta F_{electro}(n, m)$. In Figure 7.11d, we report $\frac{1}{L} \frac{\Delta F_{electro}(n, m)}{k_B T}$ as a function of n for $m = 1, 2, 3$. We note that $\Delta F_{electro}(n, m) > 0$ for all n, m , i.e. the electrostatic energy increases upon addition of protofilaments, in agreement with our conclusions above based on the control experiment in the presence of salt (Figure 7.5).

If the physics of the system is governed by the first scenario, aggregation is always favored. As a consequence, $\Delta F_{total}(n, m) < 0$ for all n, m . This condition imposes a lower boundary to the value of q . Particularly, by reckoning that the maximum value of the electrostatic free-energy difference is attained for $n = m = 3$ (inset in Figure 7.11d), one has $q \geq \Delta F_{electro}(3, 3) \simeq 415 k_B T / \mu\text{m}$, which is in agreement with the condition $q \geq 310 k_B T / \mu\text{m}$ established before³⁴⁷.

Similar results are obtained in the case of the second scenario, where the change in the relative strength between electrostatics and lateral association is responsible for the anomalous populations distribution. The feasibility of this scenario is secured by the steady increase of $\Delta F_{electro}(n, m)$ with the number of protofilaments; in other terms, it costs more energy to add a protofilament to thicker fibrils. Imposing that $n = 4$ is the most populated family for $m = 1$ gives for the parameter q the condition $\Delta F_{electro}(3, 1) \leq q \leq \Delta F_{electro}(4, 1)$, i.e. $q \simeq 375 k_B T / \mu\text{m}$, again in good agreement with the previous estimation³⁴⁷. Nevertheless, the model predicts that for thicker fibrils the aggregation of one protofilament is still more favorable than adding a two-stranded protofibril (compare main plot and inset in Figure 7.11d), in contrast with the experimental results. This does not necessarily mean that this scenario should be discarded: it is possible that adding a single line of contact may be reductive in the case of combination between multistranded protofibrils. We have numerically checked that increasing the lines of contact by a small portion while keeping the same value of q significantly enhances the strength of lateral attraction. For instance, 1.1 lines of contact are sufficient for the

addition of two-stranded fibrils to become energetically favorable (i.e. $\Delta F_{total} < 0$), while 1.2 lines are needed for the case of three-stranded fibrils. As a final note, we stress that the quantitative estimation of q depends on the value chosen for the quantity ℓ ; nonetheless, we have checked that the qualitative behavior reported in Figure 7.11d does not change in the interval $0.1 \text{ nm} \leq \ell \leq 0.7 \text{ nm}$.

7.4 Conclusion

In summary, this work provides a comprehensive study on the influence of interprotofilament interaction on mature fibril conformation and fibrillization propensity. By statistical analysis of high-resolution AFM images, we successfully identified and unraveled the polymorphic structures of insulin fibrils, showing a set of hierarchically-built conformations of either twisted-ribbon or random-twisting packing arrangements. The latter architecture is generated through a novel HAM mechanism that enables the intertwining of protofibrils in the fibrillization process to form the higher-ordered fibrils. The modelling of the geometry and energetics of the fibrils was introduced to rationalize the experimental results and provided new insights on the magnitude of the lateral attraction holding the protofilaments together. Our results shed light on the mesoscopic mechanisms of fibril formation and advance the understanding of the role of interprotofilament interaction among various aggregation reactions during the formation of functional and pathological amyloid fibrils.

Chapter 8 Conclusion and future perspective

8.1 The conclusion on the experimental results in the thesis

In the framework of this PhD thesis, we presented several works concerning the investigation of biomacromolecule and amyloid fibrils, by using the AFM-related methodologies and several conventional techniques, such as ThT assay and CD spectroscopy, for studying protein aggregation.

As indicated in the introduction, AFM, as a versatile tool for nanoscale investigation of the specimen, shows a wide diversity of application fields, ranging from material science and physics, to chemistry and biological systems. In this thesis, we performed AFM measurements on distinct samples to access their various properties, including morphologies, mechanical properties and secondary structure with a high spatial resolution. With these experimental data, one can distinguish the nanoscale structure, follow the morphological evolution and monitor the transition of structural conformation that is crucial to understand the significance in the biological processes.

The first two studies in the main section target at the investigation of the role of xanthophyll cycle in the regulation LHCII protein and the development of the novel high-sensitivity AFM for chemical analysis at nanoscale in the visible range:

- First, the study of the xanthophyll cycle and its regulation on the supramolecular organization and structural conformation of LHCII on the chloroplast lipid was performed. With the high-resolution AFM and AFM-IR measurement, we successfully identified the LHCII on the chloroplast lipid membrane and detected the morphological and conformational difference of the LHCII and LHCII aggregates.
- The second research section is the plasmon-enhanced vis-PTIR investigation on the morphological and chemical analysis on multiple samples, including Rhodamine nanohills and single-layer molecules. This methodology is enhanced by both the gap plasmon and the instrumentation resonance, that has the potential to be widely applied in the high-spatial resolution and ultra-sensitivity chemical analysis applications.

Amyloid fibril is the main research target in this thesis. The second chapter of the introduction gives an overview of the amyloid fibril and protein aggregation. The amyloid formation is the widespread phenomenon of various neurodegenerative diseases, such as Alzheimer's and Parkinson's diseases. This association enables the continuously increasing interest worldwide on the biophysical and biochemical investigation on amyloid formation, fibrillization pathways, molecular structure, cytotoxicity and the attempts of inhibiting aggregation or reducing the toxicity. Despite of the increasing knowledge on amyloids, the achieved progress is still limited and does not enable to fully solve the scientific questions regarding the amyloid formation mechanism and cytotoxicity. In this introduction, we discuss the current situation of the several representative neurodegenerative diseases, current understanding on the protein aggregation pathways and aggregation kinetics, molecular structure of amyloid fibrils, biomaterial applications of amyloid fibrils, as well as the various technologies for characterizing amyloid fibril formation.

The following three sections all focus on studying the aggregation mechanisms of amyloid fibrils, in terms of the fibrillization pathways and aggregation kinetics, with multiple interesting conclusions that might promote our understanding on amyloid fibrillization.

- The first investigation on amyloid fibrils is to study the influence of several representative environmental factors, including microgravity, sedimentation, hydrodynamic mixing and the air-water interface, on the α -synuclein aggregation. With the analysis on ThT data, we obtained that the hydrodynamic mixing increases the secondary process during the aggregation, and the air-water interface under agitation significantly promoted primary nucleation.
- In addition, we investigated the association between fibril polymorphism and environmental kinetics originating from hydrophobic air-water interface and hydrodynamic flow. We revealed that polymorphic fibrils and homogeneous rod-like fibrils were observed in the environmentally high-kinetic and low-kinetic conditions, respectively. The order-order transition from twisted to rod-like fibril was observed by mediating the environmental kinetics.
- Moreover, we investigated the packing arrangement of multi-protofilaments twisted fibrils, including twisted-ribbon and random-twisted fibrils, and evidenced the novel fibrillization mechanisms driven by random-intertwining of protofilaments. This study advances the fundamental understanding of fibrillization mechanisms, from protofilaments to higher-ordered mature fibrils, and enriches the understanding on protein aggregation pathways and fibrillization mechanisms.

Overall, these investigations on the amyloid aggregation may play a fundamental significance in, for example, to enrich the understanding on the fibrillization mechanisms, reveal the origin of polymorphic fibril formation, and discover the influence of environmental factors on the aggregation kinetics. These results might also show the potential in the novel amyloids-based biomaterials for the biomedical and biotechnological applications.

8.2 Future developments

This thesis demonstrates the capability of AFM-based technologies for the nanoscale investigation of macromolecules and amyloid fibrils. On one hand, from a technological point of view, further investigations should be concentrated on developing advanced AFM-techniques and on combining the AFM-techniques with other cutting-edge technologies, such as cryoEM and super-resolution microscopy. With the improvement on the instrumentation, more details on the experimental result could be released and more challenging experiment can be expected.

On the other hand, for the research targets, the presented experimental results in the thesis show great scientific significance and meanwhile highlight great potential in the relevant research. Here, we raise several interesting questions that deserved to be conquered in the future.:

1. The mechanism of multi-stranded ribbon formation

The multi-stranded ribbon is the parallel-stacked rod-like fibril that formed in the long-term and high environmental-kinetic incubation, as indicated in Chapter 6. The detail of their formation is one of the pending questions in this thesis, and it definitely would be an interesting research topic. Although less frequently observed, this multi-stranded ribbon may hold the similar or even lower free energy level over rod-like fibril. It was proved that the short peptide generates rod-like fibrils, which could even lower its free energy by transiting to crystal. This phenomenon, however, was not observed in the aggregation of the full-length protein. It is assumed that the multi-stranded ribbon might be the crystal aggregate for full-length protein, and how to obtain the multi-stranded ribbon by modulating the environmental kinetics is still unknown. This research might better enrich our understanding on fibrillization mechanism and also show potential biomaterial applications.

2. Hydrogel-amyloid interaction

The formation of amyloid plaques in the environment of neuron networks suggests the idea of studying the impact of a biomimetic network on the amyloid formation, where hydrophilic hydrogel can be good candidate. Due to their good biocompatibility and desirable physical

characteristics close to the physiological conditions, hydrogel has been widely used in many biomedical applications. The AFM-IR technology and super-resolution microscopy can be applied simultaneously to monitor the fibril growth in solution and structural evolution, because of their ability to analyze and distinguish the sample at nanoscale. In addition, the biodegradability of the hydrogel allows the assessment of amyloid fibril with conventional AFM to obtain the morphological details and mechanical properties. The combination of these results is believed to provide a more comprehensive conclusion on the influence of 3D hydrogel network on amyloid formation.

3. Optical fiber based nanomotion sensor

Another interesting project is the combination of AFM techniques with another cutting-edge technology. An example is the optical fiber sensing is a popular technique for commercial high-sensitive sensing the physical and chemical features, such as temperature and refractive index. The possibility of combining optical fiber sensing and cantilever nanomotion technology is attracting our research interests. With the structure shown in Figure 8.1, we could design the optical fiber based nanomotion sensor by using the interfering light. This approach might be the more sensitive as the Young's modulus of the 3D-printed polymerized cantilever could be much lower than that of the conventional cantilever and thus the spring constant could be lower. Also, this optical fiber-based sensor can be very compact and easy to be replaced in the commercial usages. We expected that this research might have wide applications of disease diagnosis, and drug discovery, such as antibiotic susceptibility/resistance test.

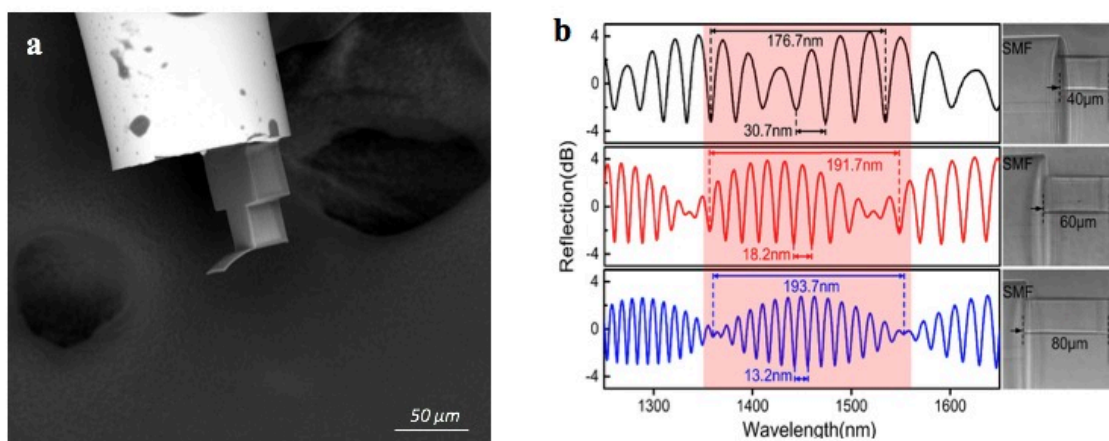


Figure 8.1 The represented optical fiber based nanomotion sensor. (a) The SEM image of the fiber-based nanomotion sensor with 3D-printed cantilever on the endface. (b) The reflected interference spectra with different cavity length.

We believe that the advance of the technology and the combination with multiple technologies could enable the great promotion of the investigation and the exploration on diverse properties of various specimens, including biomolecules and amyloid fibrils. In terms of the amyloid-related research, the achievements on these methodologies are crucial to better address the scientific questions, for example, to solve the conformational transition at the molecular level, and probe the detailed mechanism of fibrillization process and polymorphic fibril formation. Such conclusion is believed to be of significant importance in developing pharmacological treatments of neurodegenerative diseases, as well as designing novel biomaterials for the biomedical and biotechnological applications.

References

- (1) Eaton, P.; West, P. *Atomic Force Microscopy*; Oxford University Press, 2010. <https://doi.org/10.1093/acprof:oso/9780199570454.001.0001>.
- (2) Burgain, J.; Petit, J.; Scher, J.; Rasch, R.; Bhandari, B.; Gaiani, C. Surface Chemistry and Microscopy of Food Powders. *Progress in Surface Science* **2017**, *92* (4), 409–429. <https://doi.org/10.1016/j.progsurf.2017.07.002>.
- (3) Voigtländer, B. *Atomic Force Microscopy*, 2nd ed.; NanoScience and Technology; Springer International Publishing, 2019. <https://doi.org/10.1007/978-3-030-13654-3>.
- (4) Churnside, A. B.; Sullan, R. M. A.; Nguyen, D. M.; Case, S. O.; Bull, M. S.; King, G. M.; Perkins, T. T. Routine and Timely Sub-PicoNewton Force Stability and Precision for Biological Applications of Atomic Force Microscopy. *Nano Lett.* **2012**, *12* (7), 3557–3561. <https://doi.org/10.1021/nl301166w>.
- (5) Pavliček, N.; Gross, L. Generation, Manipulation and Characterization of Molecules by Atomic Force Microscopy. *Nat Rev Chem* **2017**, *1* (1), 1–11. <https://doi.org/10.1038/s41570-016-0005>.
- (6) Pavliček, N.; Mistry, A.; Majzik, Z.; Moll, N.; Meyer, G.; Fox, D. J.; Gross, L. Synthesis and Characterization of Triangulene. *Nature Nanotech* **2017**, *12* (4), 308–311. <https://doi.org/10.1038/nnano.2016.305>.
- (7) Scheuerer, P.; Patera, L. L.; Simbürger, F.; Queck, F.; Swart, I.; Schuler, B.; Gross, L.; Moll, N.; Repp, J. Charge-Induced Structural Changes in a Single Molecule Investigated by Atomic Force Microscopy. *Phys. Rev. Lett.* **2019**, *123* (6), 066001. <https://doi.org/10.1103/PhysRevLett.123.066001>.
- (8) Fatayer, S.; Albrecht, F.; Zhang, Y.; Urbonas, D.; Peña, D.; Moll, N.; Gross, L. Molecular Structure Elucidation with Charge-State Control. *Science* **2019**, *365* (6449), 142–145. <https://doi.org/10.1126/science.aax5895>.
- (9) Binnig, G.; Rohrer, H.; Gerber, Ch.; Weibel, E. Tunneling through a Controllable Vacuum Gap. *Appl. Phys. Lett.* **1982**, *40* (2), 178–180. <https://doi.org/10.1063/1.92999>.
- (10) Binnig, G.; Rohrer, H.; Gerber, Ch.; Weibel, E. Surface Studies by Scanning Tunneling Microscopy. *Phys. Rev. Lett.* **1982**, *49* (1), 57–61. <https://doi.org/10.1103/PhysRevLett.49.57>.
- (11) Binnig, G.; Rohrer, H.; Gerber, Ch.; Weibel, E. 7×7 Reconstruction on Si(111) Resolved in Real Space. *Phys. Rev. Lett.* **1983**, *50* (2), 120–123. <https://doi.org/10.1103/PhysRevLett.50.120>.
- (12) Binnig, G.; Quate, C. F.; Gerber, Ch. Atomic Force Microscope. *Phys. Rev. Lett.* **1986**, *56* (9), 930–933. <https://doi.org/10.1103/PhysRevLett.56.930>.
- (13) Dazzi, A.; Prater, C. B. AFM-IR: Technology and Applications in Nanoscale Infrared Spectroscopy and Chemical Imaging. *Chem. Rev.* **2017**, *117* (7), 5146–5173. <https://doi.org/10.1021/acs.chemrev.6b00448>.
- (14) Lee, J.; Crampton, K. T.; Tallarida, N.; Apkarian, V. A. Visualizing Vibrational Normal Modes of a Single Molecule with Atomically Confined Light. *Nature* **2019**, *568* (7750), 78–82. <https://doi.org/10.1038/s41586-019-1059-9>.
- (15) Ruf, A.; Abraham, M.; Lacher, M.; Mayr, K.; Zetterer, T. A Miniaturised Fabry Perot AFM Sensor. In *Proceedings of the International Solid-State Sensors and Actuators Conference - TRANSDUCERS '95*; 1995; Vol. 1, pp 660–663. <https://doi.org/10.1109/SENSOR.1995.717316>.
- (16) Peng, Z.; West, P. Crystal Sensor for Microscopy Applications. *Appl. Phys. Lett.* **2004**, *86* (1), 014107. <https://doi.org/10.1063/1.1846156>.
- (17) Tortonese, M.; Yamada, H.; Barrett, R. C.; Quate, C. F. Atomic Force Microscopy Using a Piezoresistive Cantilever. In *TRANSDUCERS '91: 1991 International Conference on Solid-State Sensors and Actuators. Digest of Technical Papers*; 1991; pp 448–451. <https://doi.org/10.1109/SENSOR.1991.148908>.
- (18) Dukic, M.; Adams, J. D.; Fantner, G. E. Piezoresistive AFM Cantilevers Surpassing Standard Optical Beam Deflection in Low Noise Topography Imaging. *Sci Rep* **2015**, *5* (1), 1–11. <https://doi.org/10.1038/srep16393>.
- (19) Sader, J. E.; Chon, J. W. M.; Mulvaney, P. Calibration of Rectangular Atomic Force Microscope Cantilevers. *Review of Scientific Instruments* **1999**, *70* (10), 3967–3969. <https://doi.org/10.1063/1.1150021>.
- (20) Hutter, J. L.; Bechhoefer, J. Calibration of Atomic-force Microscope Tips. *Review of Scientific Instruments* **1993**, *64* (7), 1868–1873. <https://doi.org/10.1063/1.1143970>.
- (21) Trtik, P.; Kaufmann, J.; Volz, U. On the Use of Peak-Force Tapping Atomic Force Microscopy for Quantification of the Local Elastic Modulus in Hardened Cement Paste. *Cement and Concrete Research* **2012**, *42* (1), 215–221. <https://doi.org/10.1016/j.cemconres.2011.08.009>.

- (22) Su, C. Mapping Quantitative Mechanical Properties at Molecular Scale Using Peak Force Tapping AFM. *Microscopy and Microanalysis* **2010**, *16* (S2), 364–365. <https://doi.org/10.1017/S1431927610057132>.
- (23) Forchheimer, D.; Forchheimer, R.; Haviland, D. B. Improving Image Contrast and Material Discrimination with Nonlinear Response in Bimodal Atomic Force Microscopy. *Nature Communications* **2015**, *6*, 6270. <https://doi.org/10.1038/ncomms7270>.
- (24) Benaglia, S.; Gisbert, V. G.; Perrino, A. P.; Amo, C. A.; Garcia, R. Fast and High-Resolution Mapping of Elastic Properties of Biomolecules and Polymers with Bimodal AFM. *Nat Protoc* **2018**, *13* (12), 2890–2907. <https://doi.org/10.1038/s41596-018-0070-1>.
- (25) Kocun, M.; Labuda, A.; Meinhold, W.; Revenko, I.; Proksch, R. Fast, High Resolution, and Wide Modulus Range Nanomechanical Mapping with Bimodal Tapping Mode. *ACS Nano* **2017**, *11* (10), 10097–10105. <https://doi.org/10.1021/acsnano.7b04530>.
- (26) Tang, J.; Yang, G.; Zhang, Q.; Parhat, A.; Maynor, B.; Liu, J.; Qin, L.-C.; Zhou, O. Rapid and Reproducible Fabrication of Carbon Nanotube AFM Probes by Dielectrophoresis. *Nano Lett.* **2005**, *5* (1), 11–14. <https://doi.org/10.1021/nl048803y>.
- (27) Ma, X.; Zhu, Y.; Kim, S.; Liu, Q.; Byrley, P.; Wei, Y.; Zhang, J.; Jiang, K.; Fan, S.; Yan, R.; Liu, M. Sharp-Tip Silver Nanowires Mounted on Cantilevers for High-Aspect-Ratio High-Resolution Imaging. *Nano Lett.* **2016**, *16* (11), 6896–6902. <https://doi.org/10.1021/acs.nanolett.6b02802>.
- (28) Lee, J. S.; Song, J.; Kim, S. O.; Kim, S.; Lee, W.; Jackman, J. A.; Kim, D.; Cho, N.-J.; Lee, J. Multifunctional Hydrogel Nano-Probes for Atomic Force Microscopy. *Nat Commun* **2016**, *7* (1), 1–14. <https://doi.org/10.1038/ncomms11566>.
- (29) Wain, A. J.; Cox, D.; Zhou, S.; Turnbull, A. High-Aspect Ratio Needle Probes for Combined Scanning Electrochemical Microscopy — Atomic Force Microscopy. *Electrochemistry Communications* **2011**, *13* (1), 78–81. <https://doi.org/10.1016/j.elecom.2010.11.018>.
- (30) Dufrêne, Y. F.; Martínez-Martín, D.; Medalsy, I.; Alsteens, D.; Müller, D. J. Multiparametric Imaging of Biological Systems by Force-Distance Curve-Based AFM. *Nature Methods* **2013**, *10* (9), 847–854. <https://doi.org/10.1038/nmeth.2602>.
- (31) Müller, D. J.; Dufrêne, Y. F. Atomic Force Microscopy as a Multifunctional Molecular Toolbox in Nanobiotechnology. *Nature Nanotech* **2008**, *3* (5), 261–269. <https://doi.org/10.1038/nnano.2008.100>.
- (32) Krieg, M.; Fläschner, G.; Alsteens, D.; Gaub, B. M.; Roos, W. H.; Wuite, G. J. L.; Gaub, H. E.; Gerber, C.; Dufrêne, Y. F.; Müller, D. J. Atomic Force Microscopy-Based Mechanobiology. *Nature Reviews Physics* **2019**, *1* (1), 41. <https://doi.org/10.1038/s42254-018-0001-7>.
- (33) Müller, D. J.; Helenius, J.; Alsteens, D.; Dufrêne, Y. F. Force Probing Surfaces of Living Cells to Molecular Resolution. *Nature Chemical Biology* **2009**, *5* (6), 383–390. <https://doi.org/10.1038/nchembio.181>.
- (34) Li, H.; Linke, W. A.; Oberhauser, A. F.; Carrion-Vazquez, M.; Kerkvliet, J. G.; Lu, H.; Marszalek, P. E.; Fernandez, J. M. Reverse Engineering of the Giant Muscle Protein Titin. *Nature* **2002**, *418* (6901), 998–1002. <https://doi.org/10.1038/nature00938>.
- (35) Hu, X.; Li, H. Force Spectroscopy Studies on Protein–Ligand Interactions: A Single Protein Mechanics Perspective. *FEBS Letters* **2014**, *588* (19), 3613–3620. <https://doi.org/10.1016/j.febslet.2014.04.009>.
- (36) Kelchtermans, M.; Lo, M.; Dillon, E.; Kjoller, K.; Marcott, C. Characterization of a Polyethylene–Polyamide Multilayer Film Using Nanoscale Infrared Spectroscopy and Imaging. *Vibrational Spectroscopy* **2016**, *C* (82), 10–15. <https://doi.org/10.1016/j.vibspec.2015.11.004>.
- (37) Dazzi, A.; Prater, C. B.; Hu, Q.; Chase, D. B.; Rabolt, J. F.; Marcott, C. AFM–IR: Combining Atomic Force Microscopy and Infrared Spectroscopy for Nanoscale Chemical Characterization. *Appl Spectrosc* **2012**, *66* (12), 1365–1384. <https://doi.org/10.1366/12-06804>.
- (38) Clède, S.; Lambert, F.; Sandt, C.; Kascakova, S.; Unger, M.; Harté, E.; Plamont, M.-A.; Saint-Fort, R.; Deniset-Besseau, A.; Gueroui, Z.; Hirschmugl, C.; Lecomte, S.; Dazzi, A.; Vessières, A.; Policar, C. Detection of an Estrogen Derivative in Two Breast Cancer Cell Lines Using a Single Core Multimodal Probe for Imaging (SCoMPI) Imaged by a Panel of Luminescent and Vibrational Techniques. *Analyst* **2013**, *138* (19), 5627–5638. <https://doi.org/10.1039/C3AN00807J>.
- (39) Policar, C.; Waern, J. B.; Plamont, M.-A.; Clède, S.; Mayet, C.; Prazeres, R.; Ortega, J.-M.; Vessières, A.; Dazzi, A. Subcellular IR Imaging of a Metal–Carbonyl Moiety Using Photothermally Induced Resonance. *Angewandte Chemie International Edition* **2011**, *50* (4), 860–864. <https://doi.org/10.1002/anie.201003161>.
- (40) Ruggeri, F. S.; Longo, G.; Faggiano, S.; Lipiec, E.; Pastore, A.; Dietler, G. Infrared Nanospectroscopy Characterization of Oligomeric and Fibrillar Aggregates during Amyloid Formation. *Nature Communications* **2015**, *6*, 7831. <https://doi.org/10.1038/ncomms8831>.

Reference

- (41) Stupar, P.; Opota, O.; Longo, G.; Prod'hom, G.; Dietler, G.; Greub, G.; Kasas, S. Nanomechanical Sensor Applied to Blood Culture Pellets: A Fast Approach to Determine the Antibiotic Susceptibility against Agents of Bloodstream Infections. *Clinical Microbiology and Infection* **2017**, *23* (6), 400–405. <https://doi.org/10.1016/j.cmi.2016.12.028>.
- (42) Villalba, M. I.; Stupar, P.; Chomicki, W.; Bertacchi, M.; Dietler, G.; Arnal, L.; Vela, M. E.; Yantorno, O.; Kasas, S. Nanomotion Detection Method for Testing Antibiotic Resistance and Susceptibility of Slow-Growing Bacteria. *Small* **2018**, *14* (4), 1702671. <https://doi.org/10.1002/sml.201702671>.
- (43) Stupar, P.; Chomicki, W.; Maillard, C.; Mikeladze, D.; Kalauzi, A.; Radotić, K.; Dietler, G.; Kasas, S. Mitochondrial Activity Detected by Cantilever Based Sensor. *Mechanical Sciences* **2017**, *8* (1), 23–28. <https://doi.org/10.5194/ms-8-23-2017>.
- (44) Kasas, S.; Ruggeri, F. S.; Benadiba, C.; Maillard, C.; Stupar, P.; Tourno, H.; Dietler, G.; Longo, G. Detecting Nanoscale Vibrations as Signature of Life. *PNAS* **2015**, *112* (2), 378–381. <https://doi.org/10.1073/pnas.1415348112>.
- (45) Longo, G.; Alonso-Sarduy, L.; Rio, L. M.; Bizzini, A.; Trampuz, A.; Notz, J.; Dietler, G.; Kasas, S. Rapid Detection of Bacterial Resistance to Antibiotics Using AFM Cantilevers as Nanomechanical Sensors. *Nature Nanotechnology* **2013**, *8* (7), 522–526. <https://doi.org/10.1038/nnano.2013.120>.
- (46) Gross, L.; Mohn, F.; Moll, N.; Liljeroth, P.; Meyer, G. The Chemical Structure of a Molecule Resolved by Atomic Force Microscopy. *Science* **2009**, *325* (5944), 1110–1114. <https://doi.org/10.1126/science.1176210>.
- (47) Hanssen, K. Ø.; Schuler, B.; Williams, A. J.; Demissie, T. B.; Hansen, E.; Andersen, J. H.; Svenson, J.; Blinov, K.; Repisky, M.; Mohn, F.; Meyer, G.; Svendsen, J.-S.; Ruud, K.; Elyashberg, M.; Gross, L.; Jaspars, M.; Isaksson, J. A Combined Atomic Force Microscopy and Computational Approach for the Structural Elucidation of Breifussin A and B: Highly Modified Halogenated Dipeptides from *Thuiaria Breifussi*. *Angewandte Chemie International Edition* **2012**, *51* (49), 12238–12241. <https://doi.org/10.1002/anie.201203960>.
- (48) Gross, L.; Mohn, F.; Moll, N.; Meyer, G.; Ebel, R.; Abdel-Mageed, W. M.; Jaspars, M. Organic Structure Determination Using Atomic-Resolution Scanning Probe Microscopy. *Nature Chem* **2010**, *2* (10), 821–825. <https://doi.org/10.1038/nchem.765>.
- (49) Schuler, B.; Collazos, S.; Gross, L.; Meyer, G.; Pérez, D.; Guitián, E.; Peña, D. From Perylene to a 22-Ring Aromatic Hydrocarbon in One-Pot. *Angewandte Chemie International Edition* **2014**, *53* (34), 9004–9006. <https://doi.org/10.1002/anie.201403707>.
- (50) Lee, H.; Lee, H.; Park, J. Y. Direct Imaging of Surface Plasmon-Driven Hot Electron Flux on the Au Nanoprism/TiO₂. *Nano Lett.* **2019**, *19* (2), 891–896. <https://doi.org/10.1021/acs.nanolett.8b04119>.
- (51) Riss, A.; Wickenburg, S.; Gorman, P.; Tan, L. Z.; Tsai, H.-Z.; de Oteyza, D. G.; Chen, Y.-C.; Bradley, A. J.; Ugeda, M. M.; Etkin, G.; Louie, S. G.; Fischer, F. R.; Crommie, M. F. Local Electronic and Chemical Structure of Oligo-Acetylene Derivatives Formed Through Radical Cyclizations at a Surface. *Nano Lett.* **2014**, *14* (5), 2251–2255. <https://doi.org/10.1021/nl403791q>.
- (52) Verma, P. Tip-Enhanced Raman Spectroscopy: Technique and Recent Advances. *Chem. Rev.* **2017**, *117* (9), 6447–6466. <https://doi.org/10.1021/acs.chemrev.6b00821>.
- (53) Zrimsek, A. B.; Chiang, N.; Mattei, M.; Zaleski, S.; McAnally, M. O.; Chapman, C. T.; Henry, A.-I.; Schatz, G. C.; Van Duyne, R. P. Single-Molecule Chemistry with Surface- and Tip-Enhanced Raman Spectroscopy. *Chem. Rev.* **2017**, *117* (11), 7583–7613. <https://doi.org/10.1021/acs.chemrev.6b00552>.
- (54) Kodera, N.; Yamamoto, D.; Ishikawa, R.; Ando, T. Video Imaging of Walking Myosin V by High-Speed Atomic Force Microscopy. *Nature* **2010**, *468* (7320), 72–76. <https://doi.org/10.1038/nature09450>.
- (55) Ando, T. High-Speed AFM Imaging. *Current Opinion in Structural Biology* **2014**, *28*, 63–68. <https://doi.org/10.1016/j.sbi.2014.07.011>.
- (56) Heath, G. R.; Scheuring, S. High-Speed AFM Height Spectroscopy Reveals Ms-Dynamics of Unlabeled Biomolecules. *Nat Commun* **2018**, *9* (1), 1–11. <https://doi.org/10.1038/s41467-018-07512-3>.
- (57) Christopher M., D. Protein Folding and Misfolding. *Nature* **2003**, *426*, 884. <https://doi.org/10.1038/nature02261>.
- (58) Chiti, F.; Dobson, C. M. Protein Misfolding, Functional Amyloid, and Human Disease. *Annual Review of Biochemistry* **2006**, *75* (1), 333–366. <https://doi.org/10.1146/annurev.biochem.75.101304.123901>.
- (59) Wechalekar, A. D.; Gillmore, J. D.; Hawkins, P. N. Systemic Amyloidosis. *The Lancet* **2016**, *387* (10038), 2641–2654. [https://doi.org/10.1016/S0140-6736\(15\)01274-X](https://doi.org/10.1016/S0140-6736(15)01274-X).
- (60) Knowles, T. P. J.; Vendruscolo, M.; Dobson, C. M. The Amyloid State and Its Association with Protein Misfolding Diseases. *Nature Reviews Molecular Cell Biology* **2014**, *15* (6), 384. <https://doi.org/10.1038/nrm3810>.

- (61) Riek, R.; Eisenberg, D. S. The Activities of Amyloids from a Structural Perspective. *Nature* **2016**, *539* (7628), 227–235. <https://doi.org/10.1038/nature20416>.
- (62) Bendor, J. T.; Logan, T. P.; Edwards, R. H. The Function of α -Synuclein. *Neuron* **2013**, *79* (6), 1044–1066. <https://doi.org/10.1016/j.neuron.2013.09.004>.
- (63) Cabin, D. E.; Shimazu, K.; Murphy, D.; Cole, N. B.; Gottschalk, W.; McIlwain, K. L.; Orrison, B.; Chen, A.; Ellis, C. E.; Paylor, R.; Lu, B.; Nussbaum, R. L. Synaptic Vesicle Depletion Correlates with Attenuated Synaptic Responses to Prolonged Repetitive Stimulation in Mice Lacking α -Synuclein. *J Neurosci* **2002**, *22* (20), 8797–8807. <https://doi.org/10.1523/JNEUROSCI.22-20-08797.2002>.
- (64) Adamcik, J.; Mezzenga, R. Proteins Fibrils from a Polymer Physics Perspective. *Macromolecules* **2012**, *45* (3), 1137–1150. <https://doi.org/10.1021/ma202157h>.
- (65) Thirumalai, D.; Reddy, G. Protein Thermodynamics: Are Native Proteins Metastable? *Nature Chemistry* **2011**, *3* (12), 910–911. <https://doi.org/10.1038/nchem.1207>.
- (66) Iannuzzi, C.; Maritato, R.; Irace, G.; Sirangelo, I. Misfolding and Amyloid Aggregation of Apomyoglobin. *International Journal of Molecular Sciences* **2013**, *14* (7), 14287–14300. <https://doi.org/10.3390/ijms140714287>.
- (67) Arosio, P.; J. Knowles, T. P.; Linse, S. On the Lag Phase in Amyloid Fibril Formation. *Physical Chemistry Chemical Physics* **2015**, *17* (12), 7606–7618. <https://doi.org/10.1039/C4CP05563B>.
- (68) K. Shoffner, S.; Schnell, S. Estimation of the Lag Time in a Subsequent Monomer Addition Model for Fibril Elongation. *Physical Chemistry Chemical Physics* **2016**, *18* (31), 21259–21268. <https://doi.org/10.1039/C5CP07845H>.
- (69) Ferrone, F. [17] Analysis of Protein Aggregation Kinetics. In *Methods in Enzymology; Amyloid, Prions, and Other Protein Aggregates*; Academic Press, 1999; Vol. 309, pp 256–274. [https://doi.org/10.1016/S0076-6879\(99\)09019-9](https://doi.org/10.1016/S0076-6879(99)09019-9).
- (70) Knowles, T. P. J.; Waudby, C. A.; Devlin, G. L.; Cohen, S. I. A.; Aguzzi, A.; Vendruscolo, M.; Terentjev, E. M.; Welland, M. E.; Dobson, C. M. An Analytical Solution to the Kinetics of Breakable Filament Assembly. *Science* **2009**, *326* (5959), 1533–1537. <https://doi.org/10.1126/science.1178250>.
- (71) Meisl, G.; Kirkegaard, J. B.; Arosio, P.; Michaels, T. C. T.; Vendruscolo, M.; Dobson, C. M.; Linse, S.; Knowles, T. P. J. Molecular Mechanisms of Protein Aggregation from Global Fitting of Kinetic Models. *Nature Protocols* **2016**, *11* (2), 252–272. <https://doi.org/10.1038/nprot.2016.010>.
- (72) Astbury, W. T.; Dickinson, S.; Bailey, K. The X-Ray Interpretation of Denaturation and the Structure of the Seed Globulins. *Biochem J* **1935**, *29* (10), 2351–2360.1.
- (73) Sunde, M.; Serpell, L. C.; Bartlam, M.; Fraser, P. E.; Pepys, M. B.; Blake, C. C. F. Common Core Structure of Amyloid Fibrils by Synchrotron X-Ray Diffraction. Edited by F. E. Cohen. *Journal of Molecular Biology* **1997**, *273* (3), 729–739. <https://doi.org/10.1006/jmbi.1997.1348>.
- (74) Fitzpatrick, A. W. P.; Debelouchina, G. T.; Bayro, M. J.; Clare, D. K.; Caporini, M. A.; Bajaj, V. S.; Jaroniec, C. P.; Wang, L.; Ladizhansky, V.; Müller, S. A.; MacPhee, C. E.; Waudby, C. A.; Mott, H. R.; Simone, A. D.; Knowles, T. P. J.; Saibil, H. R.; Vendruscolo, M.; Orlova, E. V.; Griffin, R. G.; Dobson, C. M. Atomic Structure and Hierarchical Assembly of a Cross- β Amyloid Fibril. *PNAS* **2013**, *110* (14), 5468–5473. <https://doi.org/10.1073/pnas.1219476110>.
- (75) Sachse, C.; Fändrich, M.; Grigorieff, N. Paired β -Sheet Structure of an A β (1–40) Amyloid Fibril Revealed by Electron Microscopy. *PNAS* **2008**, *105* (21), 7462–7466. <https://doi.org/10.1073/pnas.0712290105>.
- (76) Petkova, A. T.; Ishii, Y.; Balbach, J. J.; Antzutkin, O. N.; Leapman, R. D.; Delaglio, F.; Tycko, R. A Structural Model for Alzheimer's β -Amyloid Fibrils Based on Experimental Constraints from Solid State NMR. *Proceedings of the National Academy of Sciences* **2002**, *99* (26), 16742–16747. <https://doi.org/10.1073/pnas.262663499>.
- (77) Tycko, R. Solid-State NMR Studies of Amyloid Fibril Structure. *Annual Review of Physical Chemistry* **2011**, *62* (1), 279–299. <https://doi.org/10.1146/annurev-physchem-032210-103539>.
- (78) Li, B.; Ge, P.; Murray, K. A.; Sheth, P.; Zhang, M.; Nair, G.; Sawaya, M. R.; Shin, W. S.; Boyer, D. R.; Ye, S.; Eisenberg, D. S.; Zhou, Z. H.; Jiang, L. Cryo-EM of Full-Length α -Synuclein Reveals Fibril Polymorphs with a Common Structural Kernel. *Nature Communications* **2018**, *9* (1), 3609. <https://doi.org/10.1038/s41467-018-05971-2>.
- (79) Nelson, R.; Sawaya, M. R.; Balbirnie, M.; Madsen, A. Ø.; Riek, C.; Grothe, R.; Eisenberg, D. Structure of the Cross- β Spine of Amyloid-like Fibrils. *Nature* **2005**, *435* (7043), 773–778. <https://doi.org/10.1038/nature03680>.
- (80) Sawaya, M. R.; Sambashivan, S.; Nelson, R.; Ivanova, M. I.; Sievers, S. A.; Apostol, M. I.; Thompson, M. J.; Balbirnie, M.; Wiltzius, J. J. W.; McFarlane, H. T.; Madsen, A. Ø.; Riek, C.; Eisenberg, D. Atomic Structures of Amyloid Cross- β Spines Reveal Varied Steric Zippers. *Nature* **2007**, *447* (7143), 453–457. <https://doi.org/10.1038/nature05695>.

Reference

- (81) Ivanova, M. I.; Sievers, S. A.; Sawaya, M. R.; Wall, J. S.; Eisenberg, D. Molecular Basis for Insulin Fibril Assembly. *Proceedings of the National Academy of Sciences* **2009**, *106* (45), 18990–18995.
- (82) Rodriguez, J. A.; Ivanova, M. I.; Sawaya, M. R.; Cascio, D.; Reyes, F. E.; Shi, D.; Sangwan, S.; Guenther, E. L.; Johnson, L. M.; Zhang, M.; Jiang, L.; Arbing, M. A.; Nannenga, B. L.; Hattne, J.; Whitelegge, J.; Brewster, A. S.; Messerschmidt, M.; Boutet, S.; Sauter, N. K.; Gonen, T.; Eisenberg, D. S. Structure of the Toxic Core of α -Synuclein from Invisible Crystals. *Nature* **2015**, *525* (7570), 486–490. <https://doi.org/10.1038/nature15368>.
- (83) Eisenberg, D.; Jucker, M. The Amyloid State of Proteins in Human Diseases. *Cell* **2012**, *148* (6), 1188–1203. <https://doi.org/10.1016/j.cell.2012.02.022>.
- (84) Radamaker, L.; Lin, Y.-H.; Annamalai, K.; Huhn, S.; Hegenbart, U.; Schönland, S. O.; Fritz, G.; Schmidt, M.; Fändrich, M. Cryo-EM Structure of a Light Chain-Derived Amyloid Fibril from a Patient with Systemic AL Amyloidosis. *Nat Commun* **2019**, *10* (1), 1–8. <https://doi.org/10.1038/s41467-019-09032-0>.
- (85) Zhang, S.; Andreasen, M.; Nielsen, J. T.; Liu, L.; Nielsen, E. H.; Song, J.; Ji, G.; Sun, F.; Skrydstrup, T.; Besenbacher, F.; Nielsen, N. C.; Otzen, D. E.; Dong, M. Coexistence of Ribbon and Helical Fibrils Originating from HIAPP20–29 Revealed by Quantitative Nanomechanical Atomic Force Microscopy. *PNAS* **2013**, *110* (8), 2798–2803. <https://doi.org/10.1073/pnas.1209955110>.
- (86) Hughes, M. P.; Sawaya, M. R.; Boyer, D. R.; Goldschmidt, L.; Rodriguez, J. A.; Cascio, D.; Chong, L.; Gonen, T.; Eisenberg, D. S. Atomic Structures of Low-Complexity Protein Segments Reveal Kinked β Sheets That Assemble Networks. *Science* **2018**, *359* (6376), 698–701. <https://doi.org/10.1126/science.aan6398>.
- (87) Guerrero-Ferreira, R.; Taylor, N. M.; Mona, D.; Ringler, P.; Lauer, M. E.; Riek, R.; Britschgi, M.; Stahlberg, H. Cryo-EM structure of alpha-synuclein fibrils <https://elifesciences.org/articles/36402/figures> (accessed Jan 20, 2020). <https://doi.org/10.7554/eLife.36402>.
- (88) Boyer, D. R.; Li, B.; Sun, C.; Fan, W.; Sawaya, M. R.; Jiang, L.; Eisenberg, D. S. Structures of Fibrils Formed by α -Synuclein Hereditary Disease Mutant H50Q Reveal New Polymorphs. *Nat Struct Mol Biol* **2019**, *26* (11), 1044–1052. <https://doi.org/10.1038/s41594-019-0322-y>.
- (89) Gremer, L.; Schölzel, D.; Schenk, C.; Reinartz, E.; Labahn, J.; Ravelli, R. B. G.; Tusche, M.; Lopez-Iglesias, C.; Hoyer, W.; Heise, H.; Willbold, D.; Schröder, G. F. Fibril Structure of Amyloid- β (1–42) by Cryo-Electron Microscopy. *Science* **2017**, *358* (6359), 116–119. <https://doi.org/10.1126/science.aao2825>.
- (90) Fitzpatrick, A. W. P.; Falcon, B.; He, S.; Murzin, A. G.; Murshudov, G.; Garringer, H. J.; Crowther, R. A.; Ghetti, B.; Goedert, M.; Scheres, S. H. W. Cryo-EM Structures of Tau Filaments from Alzheimer's Disease. *Nature* **2017**, *547* (7662), 185–190. <https://doi.org/10.1038/nature23002>.
- (91) Tuttle, M. D.; Comellas, G.; Nieuwkoop, A. J.; Covell, D. J.; Berthold, D. A.; Kloepper, K. D.; Courtney, J. M.; Kim, J. K.; Barclay, A. M.; Kendall, A.; Wan, W.; Stubbs, G.; Schwieters, C. D.; Lee, V. M. Y.; George, J. M.; Rienstra, C. M. Solid-State NMR Structure of a Pathogenic Fibril of Full-Length Human α -Synuclein. *Nat Struct Mol Biol* **2016**, *23* (5), 409–415. <https://doi.org/10.1038/nsmb.3194>.
- (92) Jiang, L.; Liu, C.; Leibly, D.; Landau, M.; Zhao, M.; Hughes, M. P.; Eisenberg, D. S. Structure-Based Discovery of Fiber-Binding Compounds That Reduce the Cytotoxicity of Amyloid Beta. *eLife* **2013**, *2*, e00857. <https://doi.org/10.7554/eLife.00857>.
- (93) Adamcik, J.; Mezzenga, R. Amyloid Polymorphism in the Protein Folding and Aggregation Energy Landscape. *Angewandte Chemie International Edition* **2018**, *57* (28), 8370–8382. <https://doi.org/10.1002/anie.201713416>.
- (94) Annamalai, K.; Gührs, K.-H.; Koehler, R.; Schmidt, M.; Michel, H.; Loos, C.; Gaffney, P. M.; Sigurdson, C. J.; Hegenbart, U.; Schönland, S.; Fändrich, M. Polymorphism of Amyloid Fibrils In Vivo. *Angewandte Chemie International Edition* **2016**, *55* (15), 4822–4825. <https://doi.org/10.1002/anie.201511524>.
- (95) Reynolds, N. P.; Adamcik, J.; Berryman, J. T.; Handschin, S.; Zanjani, A. A. H.; Li, W.; Liu, K.; Zhang, A.; Mezzenga, R. Competition between Crystal and Fibril Formation in Molecular Mutations of Amyloidogenic Peptides. *Nature Communications* **2017**, *8* (1), 1338. <https://doi.org/10.1038/s41467-017-01424-4>.
- (96) Usov, I.; Adamcik, J.; Mezzenga, R. Polymorphism Complexity and Handedness Inversion in Serum Albumin Amyloid Fibrils. *ACS Nano* **2013**, *7* (12), 10465–10474. <https://doi.org/10.1021/nn404886k>.
- (97) Adamcik, J.; Castelletto, V.; Bolisetty, S.; Hamley, I. W.; Mezzenga, R. Direct Observation of Time-Resolved Polymorphic States in the Self-Assembly of End-Capped Heptapeptides. *Angewandte Chemie International Edition* **2011**, *50* (24), 5495–5498. <https://doi.org/10.1002/anie.201100807>.

- (98) Aggeli, A.; Nyrkova, I. A.; Bell, M.; Harding, R.; Carrick, L.; McLeish, T. C. B.; Semenov, A. N.; Boden, N. Hierarchical Self-Assembly of Chiral Rod-like Molecules as a Model for Peptide β -Sheet Tapes, Ribbons, Fibrils, and Fibers. *PNAS* **2001**, *98* (21), 11857–11862. <https://doi.org/10.1073/pnas.191250198>.
- (99) Volpatti, L. R.; Vendruscolo, M.; Dobson, C. M.; Knowles, T. P. J. A Clear View of Polymorphism, Twist, and Chirality in Amyloid Fibril Formation. *ACS Nano* **2013**, *7* (12), 10443–10448. <https://doi.org/10.1021/nn406121w>.
- (100) Balchin, D.; Hayer-Hartl, M.; Hartl, F. U. In Vivo Aspects of Protein Folding and Quality Control. *Science* **2016**, *353* (6294), aac4354. <https://doi.org/10.1126/science.aac4354>.
- (101) Kim, Y. E.; Hipp, M. S.; Bracher, A.; Hayer-Hartl, M.; Ulrich Hartl, F. Molecular Chaperone Functions in Protein Folding and Proteostasis. *Annu. Rev. Biochem.* **2013**, *82* (1), 323–355. <https://doi.org/10.1146/annurev-biochem-060208-092442>.
- (102) Fichman, G.; Guterman, T.; Damron, J.; Adler-Abramovich, L.; Schmidt, J.; Kesselman, E.; Shimon, L. J. W.; Ramamoorthy, A.; Talmon, Y.; Gazit, E. Spontaneous Structural Transition and Crystal Formation in Minimal Supramolecular Polymer Model. *Science Advances* **2016**, *2* (2), e1500827. <https://doi.org/10.1126/sciadv.1500827>.
- (103) Fletcher, J. M.; Harniman, R. L.; Barnes, F. R. H.; Boyle, A. L.; Collins, A.; Mantell, J.; Sharp, T. H.; Antognozzi, M.; Booth, P. J.; Linden, N.; Miles, M. J.; Sessions, R. B.; Verkade, P.; Woolfson, D. N. Self-Assembling Cages from Coiled-Coil Peptide Modules. *Science* **2013**, *340* (6132), 595–599. <https://doi.org/10.1126/science.1233936>.
- (104) Gonen, S.; DiMaio, F.; Gonen, T.; Baker, D. Design of Ordered Two-Dimensional Arrays Mediated by Noncovalent Protein-Protein Interfaces. *Science* **2015**, *348* (6241), 1365–1368. <https://doi.org/10.1126/science.aaa9897>.
- (105) E. Hauser, C. A.; Maurer-Stroh, S.; C. Martins, I. Amyloid-Based Nanosensors and Nanodevices. *Chemical Society Reviews* **2014**, *43* (15), 5326–5345. <https://doi.org/10.1039/C4CS00082J>.
- (106) Maji, S. K.; Schubert, D.; Rivier, C.; Lee, S.; Rivier, J. E.; Riek, R. Amyloid as a Depot for the Formulation of Long-Acting Drugs. *PLOS Biology* **2008**, *6* (2), e17. <https://doi.org/10.1371/journal.pbio.0060017>.
- (107) Silva, R. F.; Araújo, D. R.; Silva, E. R.; Ando, R. A.; Alves, W. A. L-Diphenylalanine Microtubes As a Potential Drug-Delivery System: Characterization, Release Kinetics, and Cytotoxicity. *Langmuir* **2013**, *29* (32), 10205–10212. <https://doi.org/10.1021/la4019162>.
- (108) Li, C.; Born, A.-K.; Schweizer, T.; Zenobi-Wong, M.; Cerruti, M.; Mezzenga, R. Amyloid-Hydroxyapatite Bone Biomimetic Composites. *Advanced Materials* **2014**, *26* (20), 3207–3212. <https://doi.org/10.1002/adma.201306198>.
- (109) Meier, C.; Welland, M. E. Wet-Spinning of Amyloid Protein Nanofibers into Multifunctional High-Performance Biofibers. *Biomacromolecules* **2011**, *12* (10), 3453–3459. <https://doi.org/10.1021/bm2005752>.
- (110) Li, C.; Adamcik, J.; Mezzenga, R. Biodegradable Nanocomposites of Amyloid Fibrils and Graphene with Shape-Memory and Enzyme-Sensing Properties. *Nature Nanotechnology* **2012**, *7* (7), 421–427. <https://doi.org/10.1038/nnano.2012.62>.
- (111) Solin, N.; Inganäs, O. Protein Nanofibrils Balance Colours in Organic White-Light-Emitting Diodes. *Israel Journal of Chemistry* **2012**, *52* (6), 529–539. <https://doi.org/10.1002/ijch.201100113>.
- (112) Rizzo, A.; Solin, N.; Lindgren, L. J.; Andersson, M. R.; Inganäs, O. White Light with Phosphorescent Protein Fibrils in OLEDs. *Nano Lett.* **2010**, *10* (6), 2225–2230. <https://doi.org/10.1021/nl1012008>.
- (113) G. Bäcklund, F.; Wigenius, J.; Westerlund, F.; Inganäs, O.; Solin, N. Amyloid Fibrils as Dispersing Agents for Oligothiophenes: Control of Photophysical Properties through Nanoscale Templating and Flow Induced Fibril Alignment. *Journal of Materials Chemistry C* **2014**, *2* (37), 7811–7822. <https://doi.org/10.1039/C4TC00692E>.
- (114) Herland, A.; Thomsson, D.; Mirzov, O.; Scheblykin, I. G.; Inganäs, O. Decoration of Amyloid Fibrils with Luminescent Conjugated Polymers. *J. Mater. Chem.* **2007**, *18* (1), 126–132. <https://doi.org/10.1039/B712829K>.
- (115) Knowles, T. P. J.; Mezzenga, R. Amyloid Fibrils as Building Blocks for Natural and Artificial Functional Materials. *Advanced Materials* **2016**, *28* (31), 6546–6561. <https://doi.org/10.1002/adma.201505961>.
- (116) Rothmund, P. W. K. Folding DNA to Create Nanoscale Shapes and Patterns. *Nature* **2006**, *440* (7082), 297–302. <https://doi.org/10.1038/nature04586>.
- (117) Liu, X.; Zhang, F.; Jing, X.; Pan, M.; Liu, P.; Li, W.; Zhu, B.; Li, J.; Chen, H.; Wang, L.; Lin, J.; Liu, Y.; Zhao, D.; Yan, H.; Fan, C. Complex Silica Composite Nanomaterials Templated with DNA Origami. *Nature* **2018**, *559* (7715), 593–598. <https://doi.org/10.1038/s41586-018-0332-7>.
- (118) Chao, J.; Wang, J.; Wang, F.; Ouyang, X.; Kopperger, E.; Liu, H.; Li, Q.; Shi, J.; Wang, L.; Hu, J.; Wang, L.; Huang, W.; Simmel, F. C.; Fan, C. Solving Mazes with Single-Molecule DNA Navigators. *Nature Mater* **2019**, *18* (3), 273–279. <https://doi.org/10.1038/s41563-018-0205-3>.

Reference

- (119) Fratzl, P.; Weinkamer, R. Nature's Hierarchical Materials. *Progress in Materials Science* **2007**, *52* (8), 1263–1334. <https://doi.org/10.1016/j.pmatsci.2007.06.001>.
- (120) Knowles, T. P. J.; Buehler, M. J. Nanomechanics of Functional and Pathological Amyloid Materials. *Nature Nanotechnology* **2011**, *6* (8), 469–479. <https://doi.org/10.1038/nnano.2011.102>.
- (121) Vollrath, F.; Knight, D. P. Liquid Crystalline Spinning of Spider Silk. *Nature* **2001**, *410* (6828), 541–548. <https://doi.org/10.1038/35069000>.
- (122) Collins, S. R.; Douglass, A.; Vale, R. D.; Weissman, J. S. Mechanism of Prion Propagation: Amyloid Growth Occurs by Monomer Addition. *PLOS Biology* **2004**, *2* (10), e321. <https://doi.org/10.1371/journal.pbio.0020321>.
- (123) Bolisetty, S.; Mezzenga, R. Amyloid–Carbon Hybrid Membranes for Universal Water Purification. *Nature Nanotech* **2016**, *11* (4), 365–371. <https://doi.org/10.1038/nnano.2015.310>.
- (124) Kasai, S.; Ohga, Y.; Mochizuki, M.; Nishi, N.; Kadoya, Y.; Nomizu, M. Multifunctional Peptide Fibrils for Biomedical Materials. *Peptide Science* **2004**, *76* (1), 27–33. <https://doi.org/10.1002/bip.10565>.
- (125) Reynolds, N. P.; Charnley, M.; Mezzenga, R.; Hartley, P. G. Engineered Lysozyme Amyloid Fibril Networks Support Cellular Growth and Spreading. *Biomacromolecules* **2014**, *15* (2), 599–608. <https://doi.org/10.1021/bm401646x>.
- (126) Howie, A. J.; Brewer, D. B.; Howell, D.; Jones, A. P. Physical Basis of Colors Seen in Congo Red-Stained Amyloid in Polarized Light. *Lab Invest* **2008**, *88* (3), 232–242. <https://doi.org/10.1038/labinvest.3700714>.
- (127) Vassar, P. S.; Culling, C. F. Fluorescent Stains, with Special Reference to Amyloid and Connective Tissues. *Arch Pathol* **1959**, *68*, 487–498.
- (128) Wolfe, L. S.; Calabrese, M. F.; Nath, A.; Blaho, D. V.; Miranker, A. D.; Xiong, Y. Protein-Induced Photophysical Changes to the Amyloid Indicator Dye Thioflavin T. *PNAS* **2010**, *107* (39), 16863–16868. <https://doi.org/10.1073/pnas.1002867107>.
- (129) Biancalana, M.; Makabe, K.; Koide, A.; Koide, S. Molecular Mechanism of Thioflavin-T Binding to the Surface of β -Rich Peptide Self-Assemblies. *J Mol Biol* **2009**, *385* (4), 1052–1063. <https://doi.org/10.1016/j.jmb.2008.11.006>.
- (130) Biancalana, M.; Koide, S. Molecular Mechanism of Thioflavin-T Binding to Amyloid Fibrils. *Biochimica et Biophysica Acta (BBA) - Proteins and Proteomics* **2010**, *1804* (7), 1405–1412. <https://doi.org/10.1016/j.bbapap.2010.04.001>.
- (131) Miles, A. J.; Wallace, B. A. Synchrotron Radiation Circular Dichroism Spectroscopy of Proteins and Applications in Structural and Functional Genomics. *Chemical Society reviews* **2006**, *35* (1), 39–51. <https://doi.org/10.1039/b316168b>.
- (132) Miles, A. J.; Wallace, B. A. Circular Dichroism Spectroscopy of Membrane Proteins. *Chem. Soc. Rev.* **2016**, *45* (18), 4859–4872. <https://doi.org/10.1039/C5CS00084J>.
- (133) Schmid, F.-X. Biological Macromolecules: UV-Visible Spectrophotometry. In *eLS*; American Cancer Society, 2001. <https://doi.org/10.1038/npg.els.0003142>.
- (134) Jo, E.; McLaurin, J.; Yip, C. M.; George-Hyslop, P. S.; Fraser, P. E. α -Synuclein Membrane Interactions and Lipid Specificity. *J. Biol. Chem.* **2000**, *275* (44), 34328–34334. <https://doi.org/10.1074/jbc.M004345200>.
- (135) Micsonai, A.; Wien, F.; Kernya, L.; Lee, Y.-H.; Goto, Y.; Réfrégiers, M.; Kardos, J. Accurate Secondary Structure Prediction and Fold Recognition for Circular Dichroism Spectroscopy. *PNAS* **2015**, *112* (24), E3095–E3103. <https://doi.org/10.1073/pnas.1500851112>.
- (136) Adamcik, J.; Jung, J.-M.; Flakowski, J.; Rios, P. D. L.; Dietler, G.; Mezzenga, R. Understanding Amyloid Aggregation by Statistical Analysis of Atomic Force Microscopy Images. *Nature Nanotechnology* **2010**, *5* (6), 423. <https://doi.org/10.1038/nnano.2010.59>.
- (137) Jeong, J. S.; Ansaloni, A.; Mezzenga, R.; Lashuel, H. A.; Dietler, G. Novel Mechanistic Insight into the Molecular Basis of Amyloid Polymorphism and Secondary Nucleation during Amyloid Formation. *Journal of Molecular Biology* **2013**, *425* (10), 1765–1781. <https://doi.org/10.1016/j.jmb.2013.02.005>.
- (138) Azouz, M.; Cullin, C.; Lecomte, S.; Lafleur, M. Membrane Domain Modulation of $A\beta$ 1–42 Oligomer Interactions with Supported Lipid Bilayers: An Atomic Force Microscopy Investigation. *Nanoscale* **2019**, *11* (43), 20857–20867. <https://doi.org/10.1039/C9NR06361G>.
- (139) Watanabe-Nakayama, T.; Ono, K.; Itami, M.; Takahashi, R.; Teplow, D. B.; Yamada, M. High-Speed Atomic Force Microscopy Reveals Structural Dynamics of Amyloid B1–42 Aggregates. *PNAS* **2016**, *113* (21), 5835–5840. <https://doi.org/10.1073/pnas.1524807113>.

- (140) Knowles, T. P.; Fitzpatrick, A. W.; Meehan, S.; Mott, H. R.; Vendruscolo, M.; Dobson, C. M.; Welland, M. E. Role of Intermolecular Forces in Defining Material Properties of Protein Nanofibrils. *Science* **2007**, *318* (5858), 1900–1903. <https://doi.org/10.1126/science.1150057>.
- (141) Ruggeri, F. S.; Adamcik, J.; Jeong, J. S.; Lashuel, H. A.; Mezzenga, R.; Dietler, G. Influence of the β -Sheet Content on the Mechanical Properties of Aggregates during Amyloid Fibrillization. *Angewandte Chemie* **2015**, *127* (8), 2492–2496. <https://doi.org/10.1002/ange.201409050>.
- (142) Meersman, F.; Cabrera, R. Q.; McMillan, P. F.; Dmitriev, V. Compressibility of Insulin Amyloid Fibrils Determined by X-Ray Diffraction in a Diamond Anvil Cell. *High Pressure Research* **2009**, *29* (4), 665–670. <https://doi.org/10.1080/08957950903350975>.
- (143) Sachse, C.; Grigorieff, N.; Fändrich, M. Nanoscale Flexibility Parameters of Alzheimer Amyloid Fibrils Determined by Electron Cryo-Microscopy. *Angewandte Chemie International Edition* **2010**, *49* (7), 1321–1323. <https://doi.org/10.1002/anie.200904781>.
- (144) Ruggeri, F. S.; Benedetti, F.; Knowles, T. P. J.; Lashuel, H. A.; Sekatskii, S.; Dietler, G. Identification and Nanomechanical Characterization of the Fundamental Single-Strand Protofilaments of Amyloid α -Synuclein Fibrils. *PNAS* **2018**, *115* (28), 7230–7235. <https://doi.org/10.1073/pnas.1721220115>.
- (145) Andersen, C. B.; Yagi, H.; Manno, M.; Martorana, V.; Ban, T.; Christiansen, G.; Otzen, D. E.; Goto, Y.; Rischel, C. Branching in Amyloid Fibril Growth. *Biophys J* **2009**, *96* (4), 1529–1536. <https://doi.org/10.1016/j.bpj.2008.11.024>.
- (146) Harris, J. R. Cholesterol Binding to Amyloid- β Fibrils: A TEM Study. *Micron* **2008**, *39* (8), 1192–1196. <https://doi.org/10.1016/j.micron.2008.05.001>.
- (147) Dobashi, M.; Yuda, F.; Masuda, A.; Terashima, K. Electron Microscopic Study on Amyloid Fibril Formation in Human Lymph Nodes. *13*.
- (148) Tagliavini, F.; Giaccone, G.; Verga, L.; Ghiso, J.; Frangione, B.; Bugiani, O. Alzheimer Patients: Preamyloid Deposits Are Immunoreactive with Antibodies to Extracellular Domains of the Amyloid Precursor Protein. *Neuroscience Letters* **1991**, *128* (1), 117–120. [https://doi.org/10.1016/0304-3940\(91\)90773-M](https://doi.org/10.1016/0304-3940(91)90773-M).
- (149) Petkova, A. T.; Leapman, R. D.; Guo, Z.; Yau, W.-M.; Mattson, M. P.; Tycko, R. Self-Propagating, Molecular-Level Polymorphism in Alzheimer's β -Amyloid Fibrils. *Science* **2005**, *307* (5707), 262–265. <https://doi.org/10.1126/science.1105850>.
- (150) Cheng, Y.; Grigorieff, N.; Penczek, P. A.; Walz, T. A Primer to Single-Particle Cryo-Electron Microscopy. *Cell* **2015**, *161* (3), 438–449. <https://doi.org/10.1016/j.cell.2015.03.050>.
- (151) Jiménez, J. L.; Guijarro, J. I.; Orlova, E.; Zurdo, J.; Dobson, C. M.; Sunde, M.; Saibil, H. R. Cryo-Electron Microscopy Structure of an SH3 Amyloid Fibril and Model of the Molecular Packing. *EMBO J* **1999**, *18* (4), 815–821. <https://doi.org/10.1093/emboj/18.4.815>.
- (152) Fitzpatrick, A. W.; Saibil, H. R. Cryo-EM of Amyloid Fibrils and Cellular Aggregates. *Current Opinion in Structural Biology* **2019**, *58*, 34–42. <https://doi.org/10.1016/j.sbi.2019.05.003>.
- (153) Schmidt, A.; Annamalai, K.; Schmidt, M.; Grigorieff, N.; Fändrich, M. Cryo-EM Reveals the Steric Zipper Structure of a Light Chain-Derived Amyloid Fibril. *PNAS* **2016**, *113* (22), 6200–6205. <https://doi.org/10.1073/pnas.1522282113>.
- (154) Wasmer, C.; Lange, A.; Melckebeke, H. V.; Siemer, A. B.; Riek, R.; Meier, B. H. Amyloid Fibrils of the HET-s(218–289) Prion Form a β Solenoid with a Triangular Hydrophobic Core. *Science* **2008**, *319* (5869), 1523–1526. <https://doi.org/10.1126/science.1151839>.
- (155) Centrone, A. Infrared Imaging and Spectroscopy Beyond the Diffraction Limit. *Annual Rev. Anal. Chem.* **2015**, *8* (1), 101–126. <https://doi.org/10.1146/annurev-anchem-071114-040435>.
- (156) Felts, J. R.; Kjoller, K.; Lo, M.; Prater, C. B.; King, W. P. Nanometer-Scale Infrared Spectroscopy of Heterogeneous Polymer Nanostructures Fabricated by Tip-Based Nanofabrication. *ACS Nano* **2012**, *6* (9), 8015–8021. <https://doi.org/10.1021/nn302620f>.
- (157) Felts, J. R.; Cho, H.; Yu, M.-F.; Bergman, L. A.; Vakakis, A. F.; King, W. P. Atomic Force Microscope Infrared Spectroscopy on 15 Nm Scale Polymer Nanostructures. *Review of Scientific Instruments* **2013**, *84* (2), 023709. <https://doi.org/10.1063/1.4793229>.
- (158) Brown, P. S.; Bhushan, B. Durable, Superoleophobic Polymer–Nanoparticle Composite Surfaces with Re-Entrant Geometry via Solvent-Induced Phase Transformation. *Sci Rep* **2016**, *6* (1), 1–11. <https://doi.org/10.1038/srep21048>.

Reference

- (159) Dong, R.; Fang, Y.; Chae, J.; Dai, J.; Xiao, Z.; Dong, Q.; Yuan, Y.; Centrone, A.; Zeng, X. C.; Huang, J. High-Gain and Low-Driving-Voltage Photodetectors Based on Organolead Triiodide Perovskites. *Advanced Materials* **2015**, *27* (11), 1912–1918. <https://doi.org/10.1002/adma.201405116>.
- (160) Yuan, Y.; Chae, J.; Shao, Y.; Wang, Q.; Xiao, Z.; Centrone, A.; Huang, J. Photovoltaic Switching Mechanism in Lateral Structure Hybrid Perovskite Solar Cells. *Advanced Energy Materials* **2015**, *5* (15), 1500615. <https://doi.org/10.1002/aenm.201500615>.
- (161) Kim, S. Y.; Khanal, D.; Kalionis, B.; Chrzanowski, W. High-Fidelity Probing of the Structure and Heterogeneity of Extracellular Vesicles by Resonance-Enhanced Atomic Force Microscopy Infrared Spectroscopy. *Nature Protocols* **2019**, *14* (2), 576. <https://doi.org/10.1038/s41596-018-0109-3>.
- (162) Dazzi, A.; Prazeres, R.; Glotin, F.; Ortega, J. M.; Al-Sawaftah, M.; de Frutos, M. Chemical Mapping of the Distribution of Viruses into Infected Bacteria with a Photothermal Method. *Ultramicroscopy* **2008**, *108* (7), 635–641. <https://doi.org/10.1016/j.ultramic.2007.10.008>.
- (163) Ruggeri, F. S.; Vieweg, S.; Cendrowska, U.; Longo, G.; Chiki, A.; Lashuel, H. A.; Dietler, G. Nanoscale Studies Link Amyloid Maturity with Polyglutamine Diseases Onset. *Sci Rep* **2016**, *6*. <https://doi.org/10.1038/srep31155>.
- (164) Meier, B. H.; Riek, R.; Böckmann, A. Emerging Structural Understanding of Amyloid Fibrils by Solid-State NMR. *Trends in Biochemical Sciences* **2017**, *42* (10), 777–787. <https://doi.org/10.1016/j.tibs.2017.08.001>.
- (165) Wüthrich, K. NMR Studies of Structure and Function of Biological Macromolecules (Nobel Lecture). *Angewandte Chemie International Edition* **2003**, *42* (29), 3340–3363. <https://doi.org/10.1002/anie.200300595>.
- (166) Wälti, M. A.; Ravotti, F.; Arai, H.; Glabe, C. G.; Wall, J. S.; Böckmann, A.; Güntert, P.; Meier, B. H.; Riek, R. Atomic-Resolution Structure of a Disease-Relevant A β (1–42) Amyloid Fibril. *PNAS* **2016**, *113* (34), E4976–E4984. <https://doi.org/10.1073/pnas.1600749113>.
- (167) Chmeliov, J.; Gelzinis, A.; Songaila, E.; Augulis, R.; Duffy, C. D. P.; Ruban, A. V.; Valkunas, L. The Nature of Self-Regulation in Photosynthetic Light-Harvesting Antenna. *Nature Plants* **2016**, *2* (5), 1–7. <https://doi.org/10.1038/nplants.2016.45>.
- (168) Jahns, P.; Latowski, D.; Strzalka, K. Mechanism and Regulation of the Violaxanthin Cycle: The Role of Antenna Proteins and Membrane Lipids. *Biochimica et Biophysica Acta (BBA) - Bioenergetics* **2009**, *1787* (1), 3–14. <https://doi.org/10.1016/j.bbabi.2008.09.013>.
- (169) Niyogi, K. K.; Grossman, A. R.; Björkman, O. Arabidopsis Mutants Define a Central Role for the Xanthophyll Cycle in the Regulation of Photosynthetic Energy Conversion. *The Plant Cell* **1998**, *10* (7), 1121–1134. <https://doi.org/10.1105/tpc.10.7.1121>.
- (170) Frank, H. A.; Bautista, J. A.; Josue, J. S.; Young, A. J. Mechanism of Nonphotochemical Quenching in Green Plants: Energies of the Lowest Excited Singlet States of Violaxanthin and Zeaxanthin. *Biochemistry* **2000**, *39* (11), 2831–2837. <https://doi.org/10.1021/bi9924664>.
- (171) Holt, N. E.; Zigmantas, D.; Valkunas, L.; Li, X.-P.; Niyogi, K. K.; Fleming, G. R. Carotenoid Cation Formation and the Regulation of Photosynthetic Light Harvesting. *Science* **2005**, *307* (5708), 433–436. <https://doi.org/10.1126/science.1105833>.
- (172) Ruban, A. V.; Phillip, D.; Young, A. J.; Horton, P. Carotenoid-Dependent Oligomerization of the Major Chlorophyll a/b Light Harvesting Complex of Photosystem II of Plants. *Biochemistry* **1997**, *36* (25), 7855–7859. <https://doi.org/10.1021/bi9630725>.
- (173) Johnson, M. P.; Goral, T. K.; Duffy, C. D. P.; Brain, A. P. R.; Mullineaux, C. W.; Ruban, A. V. Photoprotective Energy Dissipation Involves the Reorganization of Photosystem II Light-Harvesting Complexes in the Grana Membranes of Spinach Chloroplasts. *The Plant Cell* **2011**, *23* (4), 1468–1479. <https://doi.org/10.1105/tpc.110.081646>.
- (174) Welc, R.; Luchowski, R.; Grudzinski, W.; Puzio, M.; Sowinski, K.; Gruszecki, W. I. A Key Role of Xanthophylls That Are Not Embedded in Proteins in Regulation of the Photosynthetic Antenna Function in Plants, Revealed by Monomolecular Layer Studies. *J. Phys. Chem. B* **2016**, *120* (51), 13056–13064. <https://doi.org/10.1021/acs.jpcc.6b10393>.
- (175) Gruszecki, W. I.; Grudzinski, W.; Gospodarek, M.; Patyra, M.; Maksymiec, W. Xanthophyll-Induced Aggregation of LHCII as a Switch between Light-Harvesting and Energy Dissipation Systems. *Biochimica et Biophysica Acta (BBA) - Bioenergetics* **2006**, *1757* (11), 1504–1511. <https://doi.org/10.1016/j.bbabi.2006.08.002>.
- (176) Xu, P.; Tian, L.; Kloz, M.; Croce, R. Molecular Insights into Zeaxanthin-Dependent Quenching in Higher Plants. *Sci Rep* **2015**, *5* (1), 1–10. <https://doi.org/10.1038/srep13679>.
- (177) Qi, J.; Wu, B.; Feng, S.; Lü, S.; Guan, C.; Zhang, X.; Qiu, D.; Hu, Y.; Zhou, Y.; Li, C.; Long, M.; Jiao, Y. Mechanical Regulation of Organ Asymmetry in Leaves. *Nature Plants* **2017**, *3* (9), 724. <https://doi.org/10.1038/s41477-017-0008-6>.

- (178) Ruban, A. V.; Johnson, M. P. Visualizing the Dynamic Structure of the Plant Photosynthetic Membrane. *Nature Plants* **2015**, *1* (11), 15161. <https://doi.org/10.1038/nplants.2015.161>.
- (179) Mari, S. A.; Wegmann, S.; Tepper, K.; Hyman, B. T.; Mandelkow, E.-M.; Mandelkow, E.; Müller, D. J. Reversible Cation-Selective Attachment and Self-Assembly of Human Tau on Supported Brain Lipid Membranes. *Nano Lett.* **2018**, *18* (5), 3271–3281. <https://doi.org/10.1021/acs.nanolett.8b01085>.
- (180) Axmann, M.; Sezgin, E.; Karner, A.; Novacek, J.; Brodessa, M. D.; Röhr, C.; Preiner, J.; Stangl, H.; Plochberger, B. Receptor-Independent Transfer of Low Density Lipoprotein Cargo to Biomembranes. *Nano Lett.* **2019**. <https://doi.org/10.1021/acs.nanolett.9b00319>.
- (181) Krupa, Z.; Huner, N. P. A.; Williams, J. P.; Maissan, E.; James, D. R. Development at Cold-Hardening Temperatures: The Structure and Composition of Purified Rye Light Harvesting Complex II. *Plant Physiology* **1987**, *84* (1), 19–24. <https://doi.org/10.1104/pp.84.1.19>.
- (182) Janik, E.; Bednarska, J.; Zubik, M.; Puzio, M.; Luchowski, R.; Grudzinski, W.; Mazur, R.; Garstka, M.; Maksymiec, W.; Kulik, A.; Dietler, G.; Gruszecki, W. I. Molecular Architecture of Plant Thylakoids under Physiological and Light Stress Conditions: A Study of Lipid–Light-Harvesting Complex II Model Membranes. *The Plant Cell* **2013**, *25* (6), 2155–2170. <https://doi.org/10.1105/tpc.113.113076>.
- (183) Melcher, J.; Carrasco, C.; Xu, X.; Carrascosa, J. L.; Gómez-Herrero, J.; Pablo, P. J. de; Raman, A. Origins of Phase Contrast in the Atomic Force Microscope in Liquids. *PNAS* **2009**, *106* (33), 13655–13660. <https://doi.org/10.1073/pnas.0902240106>.
- (184) Fang, F. Z.; Xu, Z. W.; Dong, S. Study on Phase Images of a Carbon Nanotube Probe in Atomic Force Microscopy. *Meas. Sci. Technol.* **2008**, *19* (5), 055501. <https://doi.org/10.1088/0957-0233/19/5/055501>.
- (185) Raman, A.; Trigueros, S.; Cartagena, A.; Stevenson, A. P. Z.; Susilo, M.; Nauman, E.; Contera, S. A. Mapping Nanomechanical Properties of Live Cells Using Multi-Harmonic Atomic Force Microscopy. *Nature Nanotechnology* **2011**, *6* (12), 809–814. <https://doi.org/10.1038/nnano.2011.186>.
- (186) Legleiter, J.; Park, M.; Cusick, B.; Kowalewski, T. Scanning Probe Acceleration Microscopy (SPAM) in Fluids: Mapping Mechanical Properties of Surfaces at the Nanoscale. *PNAS* **2006**, *103* (13), 4813–4818. <https://doi.org/10.1073/pnas.0505628103>.
- (187) Herruzo, E. T.; Perrino, A. P.; Garcia, R. Fast Nanomechanical Spectroscopy of Soft Matter. *Nature Communications* **2014**, *5*, 3126. <https://doi.org/10.1038/ncomms4126>.
- (188) Payam, A. F.; Ramos, J. R.; Garcia, R. Molecular and Nanoscale Compositional Contrast of Soft Matter in Liquid: Interplay between Elastic and Dissipative Interactions. *ACS Nano* **2012**, *6* (6), 4663–4670. <https://doi.org/10.1021/nn2048558>.
- (189) Liu, Z.; Yan, H.; Wang, K.; Kuang, T.; Zhang, J.; Gui, L.; An, X.; Chang, W. Crystal Structure of Spinach Major Light-Harvesting Complex at 2.72 Å Resolution. *Nature* **2004**, *428* (6980), 287. <https://doi.org/10.1038/nature02373>.
- (190) Standfuss, J.; Scheltinga, A. C. T. van; Lamborghini, M.; Kühlbrandt, W. Mechanisms of Photoprotection and Nonphotochemical Quenching in Pea Light-harvesting Complex at 2.5 Å Resolution. *The EMBO Journal* **2005**, *24* (5), 919–928. <https://doi.org/10.1038/sj.emboj.7600585>.
- (191) Adams, P. G.; Vasilev, C.; Hunter, C. N.; Johnson, M. P. Correlated Fluorescence Quenching and Topographic Mapping of Light-Harvesting Complex II within Surface-Assembled Aggregates and Lipid Bilayers. *Biochimica et Biophysica Acta (BBA) - Bioenergetics* **2018**, *1859* (10), 1075–1085. <https://doi.org/10.1016/j.bbabi.2018.06.011>.
- (192) Gruszecki, W. I.; Kulik, A. J.; Janik, E.; Bednarska, J.; Luchowski, R.; Grudzinski, W.; Dietler, G. Nanoscale Resolution in Infrared Imaging of Protein-Containing Lipid Membranes. *Nanoscale* **2015**, *7* (35), 14659–14662. <https://doi.org/10.1039/C5NR03090K>.
- (193) Tamm, L. K.; Tatulian, S. A. Infrared Spectroscopy of Proteins and Peptides in Lipid Bilayers. *Quarterly Reviews of Biophysics* **1997**, *30* (4), 365–429. <https://doi.org/10.1017/S0033583597003375>.
- (194) Pozzi, E. A.; Goubert, G.; Chiang, N.; Jiang, N.; Chapman, C. T.; McAnally, M. O.; Henry, A.-I.; Seideman, T.; Schatz, G. C.; Hersam, M. C.; Duyne, R. P. V. Ultrahigh-Vacuum Tip-Enhanced Raman Spectroscopy. *Chem. Rev.* **2017**, *117* (7), 4961–4982. <https://doi.org/10.1021/acs.chemrev.6b00343>.
- (195) Pollard, B.; Maia, F. C. B.; Raschke, M. B.; Freitas, R. O. Infrared Vibrational Nanospectroscopy by Self-Referenced Interferometry. *Nano Lett.* **2016**, *16* (1), 55–61. <https://doi.org/10.1021/acs.nanolett.5b02730>.
- (196) D. Sonntag, M.; M. Klingsporn, J.; B. Zrimsek, A.; Sharma, B.; K. Ruvuna, L.; Duyne, R. P. V. Molecular Plasmonics for Nanoscale Spectroscopy. *Chemical Society Reviews* **2014**, *43* (4), 1230–1247. <https://doi.org/10.1039/C3CS60187K>.

Reference

- (197) Seo, J.; Hoffmann, W.; Warnke, S.; Huang, X.; Gewinner, S.; Schöllkopf, W.; Bowers, M. T.; von Helden, G.; Pagel, K. An Infrared Spectroscopy Approach to Follow β -Sheet Formation in Peptide Amyloid Assemblies. *Nature Chemistry* **2016**. <https://doi.org/10.1038/nchem.2615>.
- (198) Guttman, P.; Bittencourt, C.; Rehbein, S.; Umek, P.; Ke, X.; Van Tendeloo, G.; Ewels, C. P.; Schneider, G. Nanoscale Spectroscopy with Polarized X-Rays by NEXAFS-TXM. *Nature Photonics* **2012**, *6* (1), 25–29. <https://doi.org/10.1038/nphoton.2011.268>.
- (199) Lu, F.; Jin, M.; Belkin, M. A. Tip-Enhanced Infrared Nanospectroscopy via Molecular Expansion Force Detection. *Nature Photonics* **2014**, *8* (4), 307–312. <https://doi.org/10.1038/nphoton.2013.373>.
- (200) Katzenmeyer, A. M.; Holland, G.; Kjoller, K.; Centrone, A. Absorption Spectroscopy and Imaging from the Visible through Mid-Infrared with 20 Nm Resolution. *Analytical Chemistry* **2015**, *87* (6), 3154–3159. <https://doi.org/10.1021/ac504672t>.
- (201) Tittl, A.; Leitis, A.; Liu, M.; Yesilkoy, F.; Choi, D.-Y.; Neshev, D. N.; Kivshar, Y. S.; Altug, H. Imaging-Based Molecular Barcoding with Pixelated Dielectric Metasurfaces. *Science* **2018**, *360* (6393), 1105–1109. <https://doi.org/10.1126/science.aas9768>.
- (202) Costa, J. C. S.; Taveira, R. J. S.; Lima, C. F. R. A. C.; Mendes, A.; Santos, L. M. N. B. F. Optical Band Gaps of Organic Semiconductor Materials. *Optical Materials* **2016**, *58*, 51–60. <https://doi.org/10.1016/j.optmat.2016.03.041>.
- (203) Watkins, D. W.; Jenkins, J. M. X.; Grayson, K. J.; Wood, N.; Steventon, J. W.; Vay, K. K. L.; Goodwin, M. I.; Mullen, A. S.; Bailey, H. J.; Crump, M. P.; MacMillan, F.; Mulholland, A. J.; Cameron, G.; Sessions, R. B.; Mann, S.; Anderson, J. L. R. Construction and in Vivo Assembly of a Catalytically Proficient and Hyperthermostable de Novo Enzyme. *Nature Communications* **2017**, *8* (1), 358. <https://doi.org/10.1038/s41467-017-00541-4>.
- (204) Hoppmann, C.; Maslennikov, I.; Choe, S.; Wang, L. In Situ Formation of an Azo Bridge on Proteins Controllable by Visible Light. *J. Am. Chem. Soc.* **2015**, *137* (35), 11218–11221. <https://doi.org/10.1021/jacs.5b06234>.
- (205) Lee, S.; Kwon, O.; Jeon, M.; Song, J.; Shin, S.; Kim, H.; Jo, M.; Rim, T.; Doh, J.; Kim, S.; Son, J.; Kim, Y.; Kim, C. Super-Resolution Visible Photoactivated Atomic Force Microscopy. *Light: Science & Applications* **2017**, *6* (11), e17080. <https://doi.org/10.1038/lssa.2017.80>.
- (206) Xiang, W.; Wang, Z.; Kubicki, D. J.; Tress, W.; Luo, J.; Prochowicz, D.; Akin, S.; Emsley, L.; Zhou, J.; Dietler, G.; Grätzel, M.; Hagfeldt, A. Europium-Doped CsPbI₂Br for Stable and Highly Efficient Inorganic Perovskite Solar Cells. *Joule* **2019**, *3* (1), 205–214. <https://doi.org/10.1016/j.joule.2018.10.008>.
- (207) Li, J.; Huang, B.; Esfahani, E. N.; Wei, L.; Yao, J.; Zhao, J.; Chen, W. Touching Is Believing: Interrogating Halide Perovskite Solar Cells at the Nanoscale via Scanning Probe Microscopy. *npj Quant Mater* **2017**, *2* (1), 1–7. <https://doi.org/10.1038/s41535-017-0061-4>.
- (208) Strelcov, E.; Dong, Q.; Li, T.; Chae, J.; Shao, Y.; Deng, Y.; Gruverman, A.; Huang, J.; Centrone, A. CH₃NH₃PbI₃ Perovskites: Ferroelasticity Revealed. *Science Advances* **2017**, *3* (4), e1602165. <https://doi.org/10.1126/sciadv.1602165>.
- (209) Rendell, R. W.; Scalapino, D. J. Surface Plasmons Confined by Microstructures on Tunnel Junctions. *Phys. Rev. B* **1981**, *24* (6), 3276–3294. <https://doi.org/10.1103/PhysRevB.24.3276>.
- (210) Mal'shukov, A. G. Surface-Enhanced Raman Scattering. The Present Status. *Physics Reports* **1990**, *194* (5), 343–349. [https://doi.org/10.1016/0370-1573\(90\)90033-X](https://doi.org/10.1016/0370-1573(90)90033-X).
- (211) Konopsky, V. N. Operation of Scanning Plasmon Near-Field Microscope with Gold and Silver Tips in Tapping Mode: Demonstration of Subtip Resolution. *Optics Communications* **2000**, *185* (1), 83–93. [https://doi.org/10.1016/S0030-4018\(00\)00994-9](https://doi.org/10.1016/S0030-4018(00)00994-9).
- (212) Johnson, P. B.; Christy, R. W. Optical Constants of the Noble Metals. *Phys. Rev. B* **1972**, *6* (12), 4370–4379. <https://doi.org/10.1103/PhysRevB.6.4370>.
- (213) Shubeita, G. T.; Sekatskii, S. K.; Dietler, G.; Letokhov, V. S. Local Fluorescent Probes for the Fluorescence Resonance Energy Transfer Scanning Near-Field Optical Microscopy. *Appl. Phys. Lett.* **2002**, *80* (15), 2625–2627. <https://doi.org/10.1063/1.1467695>.
- (214) Magrab, E. B. *Vibrations of Elastic Systems: With Applications to MEMS and NEMS*; Solid Mechanics and Its Applications; Springer Netherlands, 2012.
- (215) Hinrichs, K.; Shaykhtudinov, T. Polarization-Dependent Atomic Force Microscopy–Infrared Spectroscopy (AFM-IR): Infrared Nanopolarimetric Analysis of Structure and Anisotropy of Thin Films and Surfaces. *Appl Spectrosc* **2018**, *72* (6), 817–832. <https://doi.org/10.1177/0003702818763604>.
- (216) U., U. B. *Lambdachrome Laser Dyes*; Lambda Physik AG: Goettingen, 2000.

- (217) Qiu, S.; Chu, H.; Zou, Y.; Xiang, C.; Zhang, H.; Sun, L.; Xu, F. Thermochemical Studies of Rhodamine B and Rhodamine 6G by Modulated Differential Scanning Calorimetry and Thermogravimetric Analysis. *J Therm Anal Calorim* **2016**, *123* (2), 1611–1618. <https://doi.org/10.1007/s10973-015-5055-5>.
- (218) Dazzi, A.; Glotin, F.; Carminati, R. Theory of Infrared Nanospectroscopy by Photothermal Induced Resonance. *Journal of Applied Physics* **2010**, *107* (12), 124519. <https://doi.org/10.1063/1.3429214>.
- (219) Katzenmeyer, A. M.; Holland, G.; Chae, J.; Band, A.; Kjoller, K.; Centrone, A. Mid-Infrared Spectroscopy beyond the Diffraction Limit via Direct Measurement of the Photothermal Effect. *Nanoscale* **2015**, *7* (42), 17637–17641. <https://doi.org/10.1039/C5NR04854K>.
- (220) Chen, C.; Hayazawa, N.; Kawata, S. A 1.7 Nm Resolution Chemical Analysis of Carbon Nanotubes by Tip-Enhanced Raman Imaging in the Ambient. *Nature Communications* **2014**, *5*, 3312. <https://doi.org/10.1038/ncomms4312>.
- (221) Arroyo, J. O.; Kukura, P. Non-Fluorescent Schemes for Single-Molecule Detection, Imaging and Spectroscopy. *Nature Photonics* **2016**, *10* (1), 11–17. <https://doi.org/10.1038/nphoton.2015.251>.
- (222) Miyasaka, T.; Watanabe, T.; Fujishima, A.; Honda, K. Light Energy Conversion with Chlorophyll Monolayer Electrodes. In Vitro Electrochemical Simulation of Photosynthetic Primary Processes. *J. Am. Chem. Soc.* **1978**, *100* (21), 6657–6665. <https://doi.org/10.1021/ja00489a017>.
- (223) Strebeyko, P. Size and Power of Chlorophyll a Molecule. *Photosynthetica* **2000**, *38* (1), 159–160. <https://doi.org/10.1023/A:1026720729911>.
- (224) Werner, W. S. M.; Glantschnig, K.; Ambrosch-Draxl, C. Optical Constants and Inelastic Electron-Scattering Data for 17 Elemental Metals. *Journal of Physical and Chemical Reference Data* **2009**, *38* (4), 1013–1092. <https://doi.org/10.1063/1.3243762>.
- (225) Ciesielski, A.; Skowronski, L.; Trzcinski, M.; Górecka, E.; Trautman, P.; Szoplik, T. Evidence of Germanium Segregation in Gold Thin Films. *Surface Science* **2018**, *674*, 73–78. <https://doi.org/10.1016/j.susc.2018.03.020>.
- (226) Aas, E. Refractive Index of Phytoplankton Derived from Its Metabolite Composition. *J Plankton Res* **1996**, *18* (12), 2223–2249. <https://doi.org/10.1093/plankt/18.12.2223>.
- (227) Song, W.; Patel, A.; Qureshi, H. Y.; Han, D.; Schipper, H. M.; Paudel, H. K. The Parkinson Disease-Associated A30P Mutation Stabilizes α -Synuclein against Proteasomal Degradation Triggered by Heme Oxygenase-1 over-Expression in Human Neuroblastoma Cells. *Journal of Neurochemistry* **2009**, *110* (2), 719–733. <https://doi.org/10.1111/j.1471-4159.2009.06165.x>.
- (228) Schwab, K.; Frahm, S.; Horsley, D.; Rickard, J. E.; Melis, V.; Goatman, E. A.; Magbagbeolu, M.; Douglas, M.; Leith, M. G.; Baddeley, T. C.; Storey, J. M. D.; Riedel, G.; Wischik, C. M.; Harrington, C. R.; Theuring, F. A Protein Aggregation Inhibitor, Leuco-Methylthionium Bis(Hydromethanesulfonate), Decreases α -Synuclein Inclusions in a Transgenic Mouse Model of Synucleinopathy. *Front Mol Neurosci* **2018**, *10*. <https://doi.org/10.3389/fnmol.2017.00447>.
- (229) Wen, Y.; Li, W.; Poteet, E. C.; Xie, L.; Tan, C.; Yan, L.-J.; Ju, X.; Liu, R.; Qian, H.; Marvin, M. A.; Goldberg, M. S.; She, H.; Mao, Z.; Simpkins, J. W.; Yang, S.-H. Alternative Mitochondrial Electron Transfer as a Novel Strategy for Neuroprotection. *J Biol Chem* **2011**, *286* (18), 16504–16515. <https://doi.org/10.1074/jbc.M110.208447>.
- (230) Congdon, E. E.; Wu, J. W.; Myeku, N.; Figueroa, Y. H.; Herman, M.; Marinac, P. S.; Gestwicki, J. E.; Dickey, C. A.; Yu, W. H.; Duff, K. E. Methylthionium Chloride (Methylene Blue) Induces Autophagy and Attenuates Tauopathy in Vitro and in Vivo. *Autophagy* **2012**, *8* (4), 609–622. <https://doi.org/10.4161/auto.19048>.
- (231) Lee, B. I.; Suh, Y. S.; Chung, Y. J.; Yu, K.; Park, C. B. Shedding Light on Alzheimer's β -Amyloidosis: Photosensitized Methylene Blue Inhibits Self-Assembly of β -Amyloid Peptides and Disintegrates Their Aggregates. *Scientific Reports* **2017**, *7* (1), 7523. <https://doi.org/10.1038/s41598-017-07581-2>.
- (232) Maschke, A.; Calí, N.; Appel, B.; Kiermaier, J.; Blunk, T.; Göpferich, A. Micronization of Insulin by High Pressure Homogenization. *Pharm Res* **2006**, *23* (9), 2220–2229. <https://doi.org/10.1007/s11095-006-9019-0>.
- (233) Fusco, G.; Chen, S. W.; Williamson, P. T. F.; Cascella, R.; Perni, M.; Jarvis, J. A.; Cecchi, C.; Vendruscolo, M.; Chiti, F.; Cremades, N.; Ying, L.; Dobson, C. M.; Simone, A. D. Structural Basis of Membrane Disruption and Cellular Toxicity by α -Synuclein Oligomers. *Science* **2017**, *358* (6369), 1440–1443. <https://doi.org/10.1126/science.aan6160>.
- (234) Lautenschläger, J.; Stephens, A. D.; Fusco, G.; Ströhl, F.; Curry, N.; Zacharopoulou, M.; Michel, C. H.; Laine, R.; Nespovitaya, N.; Fantham, M.; Pinotsi, D.; Zago, W.; Fraser, P.; Tandon, A.; George-Hyslop, P. S.; Rees, E.; Phillips, J. J.; Simone, A. D.; Kaminski, C. F.; Schierle, G. S. K. C-Terminal Calcium Binding of α -Synuclein Modulates Synaptic Vesicle Interaction. *Nature Communications* **2018**, *9* (1), 712. <https://doi.org/10.1038/s41467-018-03111-4>.

Reference

- (235) Nielsen, L.; Khurana, R.; Coats, A.; Frokjaer, S.; Brange, J.; Vyas, S.; Uversky, V. N.; Fink, A. L. Effect of Environmental Factors on the Kinetics of Insulin Fibril Formation: Elucidation of the Molecular Mechanism. *Biochemistry* **2001**, *40* (20), 6036–6046. <https://doi.org/10.1021/bi002555c>.
- (236) Bekard, I. B.; Asimakis, P.; Bertolini, J.; Dunstan, D. E. The Effects of Shear Flow on Protein Structure and Function. *Biopolymers* **2011**, *95* (11), 733–745. <https://doi.org/10.1002/bip.21646>.
- (237) Adamcik, J.; Mezzenga, R. Adjustable Twisting Periodic Pitch of Amyloid Fibrils. *Soft Matter* **2011**, *7* (11), 5437. <https://doi.org/10.1039/c1sm05382e>.
- (238) Fares, M.-B.; Maco, B.; Oueslati, A.; Rockenstein, E.; Ninkina, N.; Buchman, V. L.; Masliah, E.; Lashuel, H. A. Induction of de Novo α -Synuclein Fibrillization in a Neuronal Model for Parkinson's Disease. *PNAS* **2016**, *113* (7), E912–E921. <https://doi.org/10.1073/pnas.1512876113>.
- (239) Deguire, S. M.; Ruggeri, F. S.; Fares, M.-B.; Chiki, A.; Cendrowska, U.; Dietler, G.; Lashuel, H. A. N-Terminal Phosphorylation of Huntingtin: A Molecular Switch for Regulating Htt Aggregation, Helical Conformation, Internalization and Nuclear Targeting. *bioRxiv* **2018**, 358234. <https://doi.org/10.1101/358234>.
- (240) Grigolato, F.; Colombo, C.; Ferrari, R.; Rezabkova, L.; Arosio, P. Mechanistic Origin of the Combined Effect of Surfaces and Mechanical Agitation on Amyloid Formation. *ACS Nano* **2017**, *11* (11), 11358–11367. <https://doi.org/10.1021/acsnano.7b05895>.
- (241) Habchi, J.; Chia, S.; Galvagnion, C.; Michaels, T. C. T.; Bellaiche, M. M. J.; Ruggeri, F. S.; Sanguanini, M.; Idini, I.; Kumita, J. R.; Sparr, E.; Linse, S.; Dobson, C. M.; Knowles, T. P. J.; Vendruscolo, M. Cholesterol Catalyses A β 42 Aggregation through a Heterogeneous Nucleation Pathway in the Presence of Lipid Membranes. *Nature Chemistry* **2018**, *10* (6), 673–683. <https://doi.org/10.1038/s41557-018-0031-x>.
- (242) Tiiman, A.; Noormägi, A.; Friedemann, M.; Krishtal, J.; Palumaa, P.; Tõugu, V. Effect of Agitation on the Peptide Fibrillization: Alzheimer's Amyloid- β Peptide 1-42 but Not Amylin and Insulin Fibrils Can Grow under Quiescent Conditions. *Journal of Peptide Science* **2013**, *19* (6), 386–391. <https://doi.org/10.1002/psc.2513>.
- (243) Lee, C. F.; Bird, S.; Shaw, M.; Jean, L.; Vaux, D. J. Combined Effects of Agitation, Macromolecular Crowding, and Interfaces on Amyloidogenesis. *J Biol Chem* **2012**, *287* (45), 38006–38019. <https://doi.org/10.1074/jbc.M112.400580>.
- (244) Dobson, J.; Kumar, A.; Willis, L. F.; Tuma, R.; Higazi, D. R.; Turner, R.; Lowe, D. C.; Ashcroft, A. E.; Radford, S. E.; Kapur, N.; Brockwell, D. J. Inducing Protein Aggregation by Extensional Flow. *PNAS* **2017**, 201702724. <https://doi.org/10.1073/pnas.1702724114>.
- (245) Batzli, K. M.; Love, B. J. Agitation of Amyloid Proteins to Speed Aggregation Measured by ThT Fluorescence: A Call for Standardization. *Materials Science and Engineering: C* **2015**, *48*, 359–364. <https://doi.org/10.1016/j.msec.2014.09.015>.
- (246) Manno, M.; Giacomazza, D.; Newman, J.; Martorana, V.; San Biagio, P. L. Amyloid Gels: Precocious Appearance of Elastic Properties during the Formation of an Insulin Fibrillar Network. *Langmuir* **2010**, *26* (3), 1424–1426. <https://doi.org/10.1021/la903340v>.
- (247) Campioni, S.; Carret, G.; Jordens, S.; Nicoud, L.; Mezzenga, R.; Riek, R. The Presence of an Air–Water Interface Affects Formation and Elongation of α -Synuclein Fibrils. *J. Am. Chem. Soc.* **2014**, *136* (7), 2866–2875. <https://doi.org/10.1021/ja412105t>.
- (248) Bernhardt, N. A.; Berhanu, W. M.; Hansmann, U. H. E. Mutations and Seeding of Amylin Fibril-Like Oligomers. *J. Phys. Chem. B* **2013**, *117* (50), 16076–16085. <https://doi.org/10.1021/jp409777p>.
- (249) Liao, Z.; Lampe, J. W.; Ayyaswamy, P. S.; Eckmann, D. M.; Dmochowski, I. J. Protein Assembly at the Air–Water Interface Studied by Fluorescence Microscopy. *Langmuir* **2011**, *27* (21), 12775–12781. <https://doi.org/10.1021/la203053g>.
- (250) Song, Y.; Shimanovich, U.; Michaels, T. C. T.; Ma, Q.; Li, J.; Knowles, T. P. J.; Shum, H. C. Fabrication of Fibrillosomes from Droplets Stabilized by Protein Nanofibrils at All-Aqueous Interfaces. *Nature Communications* **2016**, *7*, 12934. <https://doi.org/10.1038/ncomms12934>.
- (251) Jordens, S.; Riley, E. E.; Usov, I.; Isa, L.; Olmsted, P. D.; Mezzenga, R. Adsorption at Liquid Interfaces Induces Amyloid Fibril Bending and Ring Formation. *ACS Nano* **2014**, *8* (11), 11071–11079. <https://doi.org/10.1021/nn504249x>.
- (252) Wuest, S. L.; Gantenbein, B.; Ille, F.; Egli, M. Electrophysiological Experiments in Microgravity: Lessons Learned and Future Challenges. *npj Microgravity* **2018**, *4* (1), 7. <https://doi.org/10.1038/s41526-018-0042-3>.
- (253) Sieber, M.; Hanke, W.; Kohn, F. P. M. Modification of Membrane Fluidity by Gravity. *Open Journal of Biophysics* **2014**, *04*, 105. <https://doi.org/10.4236/ojbiphy.2014.44012>.

- (254) Sieber, M.; Kaltenbach, S.; Hanke, W.; Kohn, F. P. M. Conductance and Capacity of Plain Lipid Membranes under Conditions of Variable Gravity. *Journal of Biomedical Science and Engineering* **2016**, *09*, 361. <https://doi.org/10.4236/jbise.2016.98031>.
- (255) Dinarelli, S.; Longo, G.; Dietler, G.; Francioso, A.; Mosca, L.; Pannitteri, G.; Boumis, G.; Bellelli, A.; Girasole, M. Erythrocyte's Aging in Microgravity Highlights How Environmental Stimuli Shape Metabolism and Morphology. *Sci Rep* **2018**, *8* (1), 1–12. <https://doi.org/10.1038/s41598-018-22870-0>.
- (256) Goldermann, M.; Hanke, W. Ion Channel Are Sensitive to Gravity Changes. *Microgravity sci. Technol.* **2001**, *13* (1), 35. <https://doi.org/10.1007/BF02873330>.
- (257) Takamatsu, Y.; Koike, W.; Takenouchi, T.; Sugama, S.; Wei, J.; Waragai, M.; Sekiyama, K.; Hashimoto, M. Protection against Neurodegenerative Disease on Earth and in Space. *npj Microgravity* **2016**, *2*, 16013. <https://doi.org/10.1038/npjmgrav.2016.13>.
- (258) Bell, D.; Durrance, S.; Kirk, D.; Gutierrez, H.; Woodard, D.; Avendano, J.; Sargent, J.; Leite, C.; Saldana, B.; Melles, T.; Jackson, S.; Xu, S. Self-Assembly of Protein Fibrils in Microgravity. *Gravitational and Space Research* **2018**, *6* (1), 10–26.
- (259) Ruggeri, F. S.; Habchi, J.; Cerreta, A.; Dietler, G. AFM-Based Single Molecule Techniques: Unraveling the Amyloid Pathogenic Species. *Curr Pharm Des.* **2016**, *22* (26), 3950–3970.
- (260) Perni, M.; Galvagnion, C.; Maltsev, A.; Meisl, G.; Müller, M. B. D.; Challa, P. K.; Kirkegaard, J. B.; Flagmeier, P.; Cohen, S. I. A.; Cascella, R.; Chen, S. W.; Limboker, R.; Sormanni, P.; Heller, G. T.; Aprile, F. A.; Cremades, N.; Cecchi, C.; Chiti, F.; Nollen, E. A. A.; Knowles, T. P. J.; Vendruscolo, M.; Bax, A.; Zaslhoff, M.; Dobson, C. M. A Natural Product Inhibits the Initiation of α -Synuclein Aggregation and Suppresses Its Toxicity. *Proc Natl Acad Sci USA* **2017**, *114* (6), E1009–E1017. <https://doi.org/10.1073/pnas.1610586114>.
- (261) Ruggeri, F. S.; Šneideris, T.; Vendruscolo, M.; Knowles, T. P. J. Atomic Force Microscopy for Single Molecule Characterisation of Protein Aggregation. *Archives of Biochemistry and Biophysics* **2019**, *664*, 134–148. <https://doi.org/10.1016/j.abb.2019.02.001>.
- (262) Hoyer, W.; Antony, T.; Cherny, D.; Heim, G.; Jovin, T. M.; Subramaniam, V. Dependence of α -Synuclein Aggregate Morphology on Solution Conditions. *Journal of Molecular Biology* **2002**, *322* (2), 383–393. [https://doi.org/10.1016/S0022-2836\(02\)00775-1](https://doi.org/10.1016/S0022-2836(02)00775-1).
- (263) Manzano, A.; Herranz, R.; Toom, L. A. den; Slaa, S. te; Borst, G.; Visser, M.; Medina, F. J.; Loon, J. J. W. A. van. Novel, Moon and Mars, Partial Gravity Simulation Paradigms and Their Effects on the Balance between Cell Growth and Cell Proliferation during Early Plant Development. *npj Microgravity* **2018**, *4* (1), 1–11. <https://doi.org/10.1038/s41526-018-0041-4>.
- (264) Herranz, R.; Anken, R.; Boonstra, J.; Braun, M.; Christianen, P. C. M.; de Geest, M.; Hauslage, J.; Hilbig, R.; Hill, R. J. A.; Lebert, M.; Medina, F. J.; Vagt, N.; Ullrich, O.; van Loon, J. J. W. A.; Hemmersbach, R. Ground-Based Facilities for Simulation of Microgravity: Organism-Specific Recommendations for Their Use, and Recommended Terminology. *Astrobiology* **2012**, *13* (1), 1–17. <https://doi.org/10.1089/ast.2012.0876>.
- (265) Pietsch, J.; Sickmann, A.; Weber, G.; Bauer, J.; Egli, M.; Wildgruber, R.; Infanger, M.; Grimm, D. A Proteomic Approach to Analysing Spheroid Formation of Two Human Thyroid Cell Lines Cultured on a Random Positioning Machine. *PROTEOMICS* **2011**, *11* (10), 2095–2104. <https://doi.org/10.1002/pmic.201000817>.
- (266) van Loon, J. J. W. A. Some History and Use of the Random Positioning Machine, RPM, in Gravity Related Research. *Advances in Space Research* **2007**, *39* (7), 1161–1165. <https://doi.org/10.1016/j.asr.2007.02.016>.
- (267) Wuest, S. L.; Richard, S.; Kopp, S.; Grimm, D.; Egli, M. Simulated Microgravity: Critical Review on the Use of Random Positioning Machines for Mammalian Cell Culture. *BioMed Res Int* **2015**, *2015*, 971474.
- (268) Borst, A. G.; van Loon, J. J. W. A. Technology and Developments for the Random Positioning Machine, RPM. *Microgravity Science and Technology* **2009**, *21* (4), 287–292. <https://doi.org/10.1007/s12217-008-9043-2>.
- (269) Pronchik, J.; He, X.; Giurleo, J. T.; Talaga, D. S. In Vitro Formation of Amyloid from α -Synuclein Is Dominated by Reactions at Hydrophobic Interfaces. *J. Am. Chem. Soc.* **2010**, *132* (28), 9797–9803. <https://doi.org/10.1021/ja102896h>.
- (270) Zhu, H.-L.; Meng, S.-R.; Fan, J.-B.; Chen, J.; Liang, Y. Fibrillization of Human Tau Is Accelerated by Exposure to Lead via Interaction with His-330 and His-362. *PLOS ONE* **2011**, *6* (9), e25020. <https://doi.org/10.1371/journal.pone.0025020>.
- (271) Galvagnion, C.; Buell, A. K.; Meisl, G.; Michaels, T. C. T.; Vendruscolo, M.; Knowles, T. P. J.; Dobson, C. M. Lipid Vesicles Trigger α -Synuclein Aggregation by Stimulating Primary Nucleation. *Nature Chemical Biology* **2015**, *11* (3), 229–234. <https://doi.org/10.1038/nchembio.1750>.

Reference

- (272) Iljina, M.; Dear, A. J.; Garcia, G. A.; De, S.; Tosatto, L.; Flagmeier, P.; Whiten, D. R.; Michaels, T. C. T.; Frenkel, D.; Dobson, C. M.; Knowles, T. P. J.; Klenerman, D. Quantifying Co-Oligomer Formation by α -Synuclein. *ACS Nano* **2018**, *12* (11), 10855–10866. <https://doi.org/10.1021/acsnano.8b03575>.
- (273) Meisl, G.; Michaels, T. C. T.; Linse, S.; Knowles, T. P. J. Kinetic Analysis of Amyloid Formation. In *Amyloid Proteins; Methods in Molecular Biology*; Humana Press, New York, NY, 2018; pp 181–196. https://doi.org/10.1007/978-1-4939-7816-8_12.
- (274) Brown, J. W. P.; Buell, A. K.; Michaels, T. C. T.; Meisl, G.; Carozza, J.; Flagmeier, P.; Vendruscolo, M.; Knowles, T. P. J.; Dobson, C. M.; Galvagnion, C. β -Synuclein Suppresses Both the Initiation and Amplification Steps of α -Synuclein Aggregation via Competitive Binding to Surfaces. *Scientific Reports* **2016**, *6*, 36010. <https://doi.org/10.1038/srep36010>.
- (275) Rudiuk, S.; Cohen-Tannoudji, L.; Huille, S.; Tribet, C. Importance of the Dynamics of Adsorption and of a Transient Interfacial Stress on the Formation of Aggregates of IgG Antibodies. *Soft Matter* **2012**, *8* (9), 2651–2661. <https://doi.org/10.1039/C2SM07017K>.
- (276) Monica Castellanos, M.; A. Pathak, J.; H. Colby, R. Both Protein Adsorption and Aggregation Contribute to Shear Yielding and Viscosity Increase in Protein Solutions. *Soft Matter* **2014**, *10* (1), 122–131. <https://doi.org/10.1039/C3SM51994E>.
- (277) Cai, H.; Wei-na, C.; Sunggoan, J.; Sarah, R.; Stuart, M.; Bronwen, M. Metabolic Dysfunction in Alzheimers Disease and Related Neurodegenerative Disorders. *Curr. Alzheimer Res* **2012**, *9*, 5–17.
- (278) Mayeux, R.; Stern, Y. Epidemiology of Alzheimer Disease. *Cold Spring Harb Perspect Med.* **2012**, *2* (8).
- (279) Cohen, S. I. A.; Linse, S.; Luheshi, L. M.; Hellstrand, E.; White, D. A.; Rajah, L.; Otzen, D. E.; Vendruscolo, M.; Dobson, C. M.; Knowles, T. P. J. Proliferation of Amyloid-B42 Aggregates Occurs through a Secondary Nucleation Mechanism. *PNAS* **2013**, *110* (24), 9758–9763. <https://doi.org/10.1073/pnas.1218402110>.
- (280) Wei, G.; Su, Z.; P. Reynolds, N.; Arosio, P.; W. Hamley, I.; Gazit, E.; Mezzenga, R. Self-Assembling Peptide and Protein Amyloids: From Structure to Tailored Function in Nanotechnology. *Chemical Society Reviews* **2017**, *46* (15), 4661–4708. <https://doi.org/10.1039/C6CS00542J>.
- (281) Ling, S.; Kaplan, D. L.; Buehler, M. J. Nanofibrils in Nature and Materials Engineering. *Nature Reviews Materials* **2018**, *3* (4), 18016. <https://doi.org/10.1038/natrevmats.2018.16>.
- (282) Seuring, C.; Verasdonck, J.; Ringler, P.; Cadalbert, R.; Stahlberg, H.; Böckmann, A.; Meier, B. H.; Riek, R. Amyloid Fibril Polymorphism: Almost Identical on the Atomic Level, Mesoscopically Very Different. *J. Phys. Chem. B* **2017**, *121* (8), 1783–1792. <https://doi.org/10.1021/acs.jpcc.6b10624>.
- (283) Paravastu, A. K.; Leapman, R. D.; Yau, W.-M.; Tycko, R. Molecular Structural Basis for Polymorphism in Alzheimer's β -Amyloid Fibrils. *Proceedings of the National Academy of Sciences* **2008**, *105* (47), 18349–18354.
- (284) Lewandowski, J. R.; van der Wel, P. C. A.; Rigney, M.; Grigorieff, N.; Griffin, R. G. Structural Complexity of a Composite Amyloid Fibril. *J. Am. Chem. Soc.* **2011**, *133* (37), 14686–14698. <https://doi.org/10.1021/ja203736z>.
- (285) Wheeler, M. A.; Jaronen, M.; Covacu, R.; Zandee, S. E. J.; Scalisi, G.; Rothhammer, V.; Tjon, E. C.; Chao, C.-C.; Kenison, J. E.; Blain, M.; Rao, V. T. S.; Hewson, P.; Barroso, A.; Gutiérrez-Vázquez, C.; Prat, A.; Antel, J. P.; Hauser, R.; Quintana, F. J. Environmental Control of Astrocyte Pathogenic Activities in CNS Inflammation. *Cell* **2019**, *176* (3), 581-596.e18. <https://doi.org/10.1016/j.cell.2018.12.012>.
- (286) Rellán-Álvarez, R.; Lobet, G.; Dinneny, J. R. Environmental Control of Root System Biology. *Annual Review of Plant Biology* **2016**, *67* (1), 619–642. <https://doi.org/10.1146/annurev-arplant-043015-111848>.
- (287) Morris, R. J.; Eden, K.; Yarwood, R.; Jourdain, L.; Allen, R. J.; MacPhee, C. E. Mechanistic and Environmental Control of the Prevalence and Lifetime of Amyloid Oligomers. *Nat Commun* **2013**, *4* (1), 1–8. <https://doi.org/10.1038/ncomms2909>.
- (288) Kurouski, D.; Lu, X.; Popova, L.; Wan, W.; Shanmugasundaram, M.; Stubbs, G.; Dukor, R. K.; Lednev, I. K.; Nafie, L. A. Is Supramolecular Filament Chirality the Underlying Cause of Major Morphology Differences in Amyloid Fibrils? *J. Am. Chem. Soc.* **2014**, *136* (6), 2302–2312. <https://doi.org/10.1021/ja407583r>.
- (289) Morel, B.; Varela, L.; Azuaga, A. I.; Conejero-Lara, F. Environmental Conditions Affect the Kinetics of Nucleation of Amyloid Fibrils and Determine Their Morphology. *Biophys J* **2010**, *99* (11), 3801–3810. <https://doi.org/10.1016/j.bpj.2010.10.039>.
- (290) Teoh, C. L.; Griffin, M. D. W.; Howlett, G. J. Apolipoproteins and Amyloid Fibril Formation in Atherosclerosis. *Protein Cell* **2011**, *2* (2), 116–127. <https://doi.org/10.1007/s13238-011-1013-6>.
- (291) Pellarin, R.; Schuetz, P.; Guarnera, E.; Cafilisch, A. Amyloid Fibril Polymorphism Is under Kinetic Control. *J. Am. Chem. Soc.* **2010**, *132* (42), 14960–14970. <https://doi.org/10.1021/ja106044u>.

- (292) Verel, R.; Tomka, I. T.; Bertozzi, C.; Cadalbert, R.; Kammerer, R. A.; Steinmetz, M. O.; Meier, B. H. Polymorphism in an Amyloid-Like Fibril-Forming Model Peptide. *Angewandte Chemie International Edition* **2008**, *47* (31), 5842–5845. <https://doi.org/10.1002/anie.200800021>.
- (293) Jean, L.; Lee, C. F.; Vaux, D. J. Enrichment of Amyloidogenesis at an Air-Water Interface. *Biophysical Journal* **2012**, *102* (5), 1154–1162. <https://doi.org/10.1016/j.bpj.2012.01.041>.
- (294) Leiske, D. L.; Shieh, I. C.; Tse, M. L. A Method To Measure Protein Unfolding at an Air-Liquid Interface. *Langmuir* **2016**, *32* (39), 9930–9937. <https://doi.org/10.1021/acs.langmuir.6b02267>.
- (295) C. Lee, S. J.; Nam, E.; Jin Lee, H.; G. Savelieff, M.; Hee Lim, M. Towards an Understanding of Amyloid- β Oligomers: Characterization, Toxicity Mechanisms, and Inhibitors. *Chemical Society Reviews* **2017**, *46* (2), 310–323. <https://doi.org/10.1039/C6CS00731G>.
- (296) Schladitz, C.; Vieira, E. P.; Hermel, H.; Mohwald, H. Amyloid- β -Sheet Formation at the Air-Water Interface. *Biophysical Journal* **1999**, *77* (6), 3305–3310. [https://doi.org/10.1016/S0006-3495\(99\)77161-4](https://doi.org/10.1016/S0006-3495(99)77161-4).
- (297) Zhou, J.; Ruggeri, F. S.; Zimmermann, M. R.; Meisl, G.; Longo, G.; Sekatskii, S. K.; Knowles, T. P. J.; Dietler, G. Effects of Sedimentation, Microgravity, Hydrodynamic Mixing and Air-Water Interface on α -Synuclein Amyloid Formation. *Chem. Sci.* **2020**. <https://doi.org/10.1039/D0SC00281J>.
- (298) Thomas, C. R.; Geer, D. Effects of Shear on Proteins in Solution. *Biotechnol Lett* **2011**, *33* (3), 443–456. <https://doi.org/10.1007/s10529-010-0469-4>.
- (299) Liu, L.; Qi, W.; Schwartz, D. K.; Randolph, T. W.; Carpenter, J. F. The Effects of Excipients on Protein Aggregation during Agitation: An Interfacial Shear Rheology Study. *Journal of Pharmaceutical Sciences* **2013**, *102* (8), 2460–2470. <https://doi.org/10.1002/jps.23622>.
- (300) Vogel, V.; Sheetz, M. Local Force and Geometry Sensing Regulate Cell Functions. *Nature Reviews Molecular Cell Biology* **2006**, *7* (4), 265–275. <https://doi.org/10.1038/nrm1890>.
- (301) Hardy, J.; Cullen, K. Amyloid at the Blood Vessel Wall. *Nature Medicine* **2006**, *12* (7), 756–757. <https://doi.org/10.1038/nm0706-756>.
- (302) Smith, E. E.; Greenberg, S. M. Beta-Amyloid, Blood Vessels and Brain Function. *Stroke* **2009**, *40* (7), 2601–2606. <https://doi.org/10.1161/STROKEAHA.108.536839>.
- (303) Mikhaylov, A.; Sekatskii, S. K.; Dietler, G. DNA Trace: A Comprehensive Software for Polymer Image Processing. *Journal of Advanced Microscopy Research* **2013**, *8* (4), 241–245. <https://doi.org/info:doi/10.1166/jamr.2013.1164>.
- (304) Xu, Z.; Paparcone, R.; Buehler, M. J. Alzheimer’s A β (1-40) Amyloid Fibrils Feature Size-Dependent Mechanical Properties. *Biophys J* **2010**, *98* (10), 2053–2062. <https://doi.org/10.1016/j.bpj.2009.12.4317>.
- (305) del Mercato, L. L.; Maruccio, G.; Pompa, P. P.; Bochicchio, B.; Tamburro, A. M.; Cingolani, R.; Rinaldi, R. Amyloid-like Fibrils in Elastin-Related Polypeptides: Structural Characterization and Elastic Properties. *Biomacromolecules* **2008**, *9* (3), 796–803. <https://doi.org/10.1021/bm7010104>.
- (306) Becker, J. L.; Souza, G. R. Using Space-Based Investigations to Inform Cancer Research on Earth. *Nature Reviews Cancer* **2013**, *13* (5), 315–327. <https://doi.org/10.1038/nrc3507>.
- (307) Wuest, S. L.; Stern, P.; Casartelli, E.; Egli, M. Fluid Dynamics Appearing during Simulated Microgravity Using Random Positioning Machines. *PLOS ONE* **2017**, *12* (1), e0170826. <https://doi.org/10.1371/journal.pone.0170826>.
- (308) Kapur, S.; Mohan, S.; Baylink, D. J.; Lau, K.-H. W. Fluid Shear Stress Synergizes with Insulin-like Growth Factor-I (IGF-I) on Osteoblast Proliferation through Integrin-Dependent Activation of IGF-I Mitogenic Signaling Pathway. *J. Biol. Chem.* **2005**, *280* (20), 20163–20170. <https://doi.org/10.1074/jbc.M501460200>.
- (309) Ruschak, A. M.; Miranker, A. D. Fiber-Dependent Amyloid Formation as Catalysis of an Existing Reaction Pathway. *PNAS* **2007**, *104* (30), 12341–12346. <https://doi.org/10.1073/pnas.0703306104>.
- (310) Bishop, M. F.; Ferrone, F. A. Kinetics of Nucleation-Controlled Polymerization. A Perturbation Treatment for Use with a Secondary Pathway. *Biophysical Journal* **1984**, *46* (5), 631–644. [https://doi.org/10.1016/S0006-3495\(84\)84062-X](https://doi.org/10.1016/S0006-3495(84)84062-X).
- (311) Usov, I.; Mezzenga, R. Correlation between Nanomechanics and Polymorphic Conformations in Amyloid Fibrils. *ACS Nano* **2014**, *8* (11), 11035–11041. <https://doi.org/10.1021/nn503530a>.
- (312) vandenAkker, C. C.; Engel, M. F. M.; Velikov, K. P.; Bonn, M.; Koenderink, G. H. Morphology and Persistence Length of Amyloid Fibrils Are Correlated to Peptide Molecular Structure. *J. Am. Chem. Soc.* **2011**, *133* (45), 18030–18033. <https://doi.org/10.1021/ja206513r>.

Reference

- (313) Witz, G.; Rechendorff, K.; Adamcik, J.; Dietler, G. Conformation of Circular DNA in Two Dimensions. *Phys. Rev. Lett.* **2008**, *101* (14), 148103. <https://doi.org/10.1103/PhysRevLett.101.148103>.
- (314) Guerrero-Ferreira, R.; Taylor, N. M.; Mona, D.; Ringler, P.; Lauer, M. E.; Riek, R.; Britschgi, M.; Stahlberg, H. Cryo-EM Structure of Alpha-Synuclein Fibrils. *eLife* **7**. <https://doi.org/10.7554/eLife.36402>.
- (315) Bortolini, C.; Jones, N. C.; Hoffmann, S. V.; Wang, C.; Besenbacher, F.; Dong, M. Mechanical Properties of Amyloid-like Fibrils Defined by Secondary Structures. *Nanoscale* **2015**, *7* (17), 7745–7752. <https://doi.org/10.1039/C4NR05109B>.
- (316) Adamcik, J.; Lara, C.; Usov, I.; Sun Jeong, J.; S. Ruggeri, F.; Dietler, G.; A. Lashuel, H.; W. Hamley, I.; Mezzenga, R. Measurement of Intrinsic Properties of Amyloid Fibrils by the Peak Force QNM Method. *Nanoscale* **2012**, *4* (15), 4426–4429. <https://doi.org/10.1039/C2NR30768E>.
- (317) Foderà, V.; Pagliara, S.; Otto, O.; Keyser, U. F.; Donald, A. M. Microfluidics Reveals a Flow-Induced Large-Scale Polymorphism of Protein Aggregates. *J. Phys. Chem. Lett.* **2012**, *3* (19), 2803–2807. <https://doi.org/10.1021/jz301375d>.
- (318) Knowles, T. P. J.; De Simone, A.; Fitzpatrick, A. W.; Baldwin, A.; Meehan, S.; Rajah, L.; Vendruscolo, M.; Welland, M. E.; Dobson, C. M.; Terentjev, E. M. Twisting Transition between Crystalline and Fibrillar Phases of Aggregated Peptides. *Phys. Rev. Lett.* **2012**, *109* (15), 158101. <https://doi.org/10.1103/PhysRevLett.109.158101>.
- (319) Gruziel, M.; Szymczak, P. From Ribbons to Tubules: A Computational Study of the Polymorphism in Aggregation of Helical Filaments. *Soft Matter* **2015**, *11* (31), 6294–6304. <https://doi.org/10.1039/C5SM00652J>.
- (320) Soto, C. Unfolding the Role of Protein Misfolding in Neurodegenerative Diseases. *Nat Rev Neurosci* **2003**, *4* (1), 49–60. <https://doi.org/10.1038/nrn1007>.
- (321) Knowles, T. P. J.; Buehler, M. J. Nanomechanics of Functional and Pathological Amyloid Materials. *Nature Nanotechnology* **2011**, *6* (8), 469–479. <https://doi.org/10.1038/nnano.2011.102>.
- (322) Jiménez, J. L.; Nettleton, E. J.; Bouchard, M.; Robinson, C. V.; Dobson, C. M.; Saibil, H. R. The Protofilament Structure of Insulin Amyloid Fibrils. *Proceedings of the National Academy of Sciences* **2002**, *99* (14), 9196–9201.
- (323) Vilar, M.; Chou, H.-T.; Lührs, T.; Maji, S. K.; Riek-Loher, D.; Verel, R.; Manning, G.; Stahlberg, H.; Riek, R. The Fold of α -Synuclein Fibrils. *PNAS* **2008**, *105* (25), 8637–8642. <https://doi.org/10.1073/pnas.0712179105>.
- (324) Khurana, R.; Ionescu-Zanetti, C.; Pope, M.; Li, J.; Nielson, L.; Ramírez-Alvarado, M.; Regan, L.; Fink, A. L.; Carter, S. A. A General Model for Amyloid Fibril Assembly Based on Morphological Studies Using Atomic Force Microscopy. *Biophysical Journal* **2003**, *85* (2), 1135–1144.
- (325) Dufrêne, Y. F.; Ando, T.; Garcia, R.; Alsteens, D.; Martinez-Martin, D.; Engel, A.; Gerber, C.; Müller, D. J. Imaging Modes of Atomic Force Microscopy for Application in Molecular and Cell Biology. *Nature Nanotechnology* **2017**, *12* (4), 295–307. <https://doi.org/10.1038/nnano.2017.45>.
- (326) Lin, Y.-C.; Komatsu, H.; Ma, J.; Axelsen, P. H.; Fakhraai, Z. Quantitative Analysis of Amyloid Polymorphism Using Height Histograms to Correct for Tip Convolution Effects in Atomic Force Microscopy Imaging. *RSC Adv.* **2016**, *6* (115), 114286–114295. <https://doi.org/10.1039/C6RA24031C>.
- (327) Assenza, S.; Adamcik, J.; Mezzenga, R.; De Los Rios, P. Universal Behavior in the Mesoscale Properties of Amyloid Fibrils. *Phys. Rev. Lett.* **2014**, *113* (26), 268103. <https://doi.org/10.1103/PhysRevLett.113.268103>.
- (328) Marko, J. F.; Siggia, E. D. Stretching DNA. *Macromolecules* **1995**, *28* (26), 8759–8770. <https://doi.org/10.1021/ma00130a008>.
- (329) Smith, J. F.; Knowles, T. P. J.; Dobson, C. M.; MacPhee, C. E.; Welland, M. E. Characterization of the Nanoscale Properties of Individual Amyloid Fibrils. *PNAS* **2006**, *103* (43), 15806–15811. <https://doi.org/10.1073/pnas.0604035103>.
- (330) Manning, G. S. Limiting Laws and Counterion Condensation in Polyelectrolyte Solutions II. Self-Diffusion of the Small Ions. *J. Chem. Phys.* **1969**, *51* (3), 934–938. <https://doi.org/10.1063/1.1672158>.
- (331) Manning, G. S. Electrostatic Free Energies of Spheres, Cylinders, and Planes in Counterion Condensation Theory with Some Applications. *Macromolecules* **2007**, *40* (22), 8071–8081. <https://doi.org/10.1021/ma071457x>.
- (332) Søndergaard, C. R.; Olsson, M. H. M.; Rostkowski, M.; Jensen, J. H. Improved Treatment of Ligands and Coupling Effects in Empirical Calculation and Rationalization of pK_a Values. *J. Chem. Theory Comput.* **2011**, *7* (7), 2284–2295. <https://doi.org/10.1021/ct200133y>.
- (333) Olsson, M. H. M.; Søndergaard, C. R.; Rostkowski, M.; Jensen, J. H. PROPKA3: Consistent Treatment of Internal and Surface Residues in Empirical pK_a Predictions. *J. Chem. Theory Comput.* **2011**, *7* (2), 525–537. <https://doi.org/10.1021/ct100578z>.

- (334) Batys, P.; Luukkonen, S.; Sammalkorpi, M. Ability of the Poisson–Boltzmann Equation to Capture Molecular Dynamics Predicted Ion Distribution around Polyelectrolytes. *Phys. Chem. Chem. Phys.* **2017**, *19* (36), 24583–24593. <https://doi.org/10.1039/C7CP02547E>.
- (335) Bouchard, M.; Zurdo, J.; Nettleton, E. J.; Dobson, C. M.; Robinson, C. V. Formation of Insulin Amyloid Fibrils Followed by FTIR Simultaneously with CD and Electron Microscopy. *Protein Science* **2000**, *9* (10), 1960–1967.
- (336) Paparcone, R.; W. Cranford, S.; J. Buehler, M. Self-Folding and Aggregation of Amyloid Nanofibrils. *Nanoscale* **2011**, *3* (4), 1748–1755. <https://doi.org/10.1039/C0NR00840K>.
- (337) Py, C.; Reverdy, P.; Doppler, L.; Bico, J.; Roman, B.; Baroud, C. N. Capillary Origami: Spontaneous Wrapping of a Droplet with an Elastic Sheet. *Phys. Rev. Lett.* **2007**, *98* (15), 156103. <https://doi.org/10.1103/PhysRevLett.98.156103>.
- (338) Lamour, G.; Yip, C. K.; Li, H.; Gsponer, J. High Intrinsic Mechanical Flexibility of Mouse Prion Nanofibrils Revealed by Measurements of Axial and Radial Young's Moduli. *ACS Nano* **2014**, *8* (4), 3851–3861. <https://doi.org/10.1021/nn5007013>.
- (339) Lee, G.; Lee, W.; Lee, H.; Lee, C. Y.; Eom, K.; Kwon, T. Self-Assembled Amyloid Fibrils with Controllable Conformational Heterogeneity. *Scientific Reports* **2015**, *5*, 16220. <https://doi.org/10.1038/srep16220>.
- (340) Zhou, X.; Liu, J.; Li, B.; Pillai, S.; Lin, D.; Liu, J.; Zhang, Y. Assembly of Glucagon (Proto)Fibrils by Longitudinal Addition of Oligomers. *Nanoscale* **2011**, *3* (8), 3049–3051. <https://doi.org/10.1039/C1NR10332F>.
- (341) Vestergaard, B.; Groenning, M.; Roessle, M.; Kastrop, J. S.; van de Weert, M.; Flink, J. M.; Frokjaer, S.; Gajhede, M.; Svergun, D. I. A Helical Structural Nucleus Is the Primary Elongating Unit of Insulin Amyloid Fibrils. *PLoS Biol* **2007**, *5* (5). <https://doi.org/10.1371/journal.pbio.0050134>.
- (342) Sweers, K. K. M.; Segers-Nolten, I. M. J.; Bennink, M. L.; Subramaniam, V. Structural Model for α -Synuclein Fibrils Derived from High Resolution Imaging and Nanomechanical Studies Using Atomic Force Microscopy. *Soft Matter* **2012**, *8* (27), 7215–7222. <https://doi.org/10.1039/C2SM25426C>.
- (343) De Jong, K. L.; Incedon, B.; Yip, C. M.; DeFelippis, M. R. Amyloid Fibrils of Glucagon Characterized by High-Resolution Atomic Force Microscopy. *Biophysical Journal* **2006**, *91* (5), 1905–1914. <https://doi.org/10.1529/biophysj.105.077438>.
- (344) Arimon, M.; Díez-Pérez, I.; Kogan, M. J.; Durany, N.; Giralt, E.; Sanz, F.; Fernández-Busquets, X. Fine Structure Study of A β 1-42 Fibrillogenesis with Atomic Force Microscopy. *The FASEB Journal* **2005**, *19* (10), 1344–1346. <https://doi.org/10.1096/fj.04-3137fje>.
- (345) Sidhu, A.; Segers-Nolten, I.; Raussens, V.; Claessens, M. M. A. E.; Subramaniam, V. Distinct Mechanisms Determine α -Synuclein Fibril Morphology during Growth and Maturation. *ACS Chem. Neurosci.* **2017**, *8* (3), 538–547. <https://doi.org/10.1021/acscchemneuro.6b00287>.
- (346) Meisl, G.; Yang, X.; Dobson, C. M.; Linse, S.; Knowles, T. P. J. Modulation of Electrostatic Interactions to Reveal a Reaction Network Unifying the Aggregation Behaviour of the A β 42 Peptide and Its Variants. *Chem. Sci.* **2017**, *8* (6), 4352–4362. <https://doi.org/10.1039/C7SC00215G>.
- (347) Knowles, T. P. J.; Smith, J. F.; Craig, A.; Dobson, C. M.; Welland, M. E. Spatial Persistence of Angular Correlations in Amyloid Fibrils. *Phys. Rev. Lett.* **2006**, *96* (23), 238301. <https://doi.org/10.1103/PhysRevLett.96.238301>.

Jiangtao Zhou

Doctoral assistant

Institute of Physics, Swiss Federal Institute of Technology, Lausanne (EPFL)

Address: BSP 408, Rte de la Sorge, CH-1015 Lausanne, Switzerland

E-mail: jiangtao.zhou@epfl.ch; jiangtaozhou1511@gmail.com

Telephone: +41 21 693 04 45



Education

Sep. 2016 - Now **Swiss Federal Institute of Technology, Lausanne (EPFL), Switzerland**

PhD in Laboratory of Physics of Living Matter (LPMV), with Prof. Giovanni Dietler
Department of Biophysics, Institute of Physics

Feb. 2015 - Jun. 2015 **Nanyang Technological University (NTU), Singapore**

Exchanging student in optical biosensing, with Prof. Shum Ping and Prof. Lingbo Liu
School of Electrical and Electronics Engineering

Sep. 2012 - Jun. 2015 **Shenzhen University (SZU), Shenzhen, China**

Master student of Optical sensing
School of Optical Engineering

Sep. 2012 - Jun. 2015 **Anhui Jianzhu University (AJU), Hefei, China**

Bachelor student in Electronics Engineering
School of Electronics and Electric Engineering

Research Experience

Sep. 2016 - Now **Research Assistant** (LPMV, EPFL, Switzerland)

Atomic force microscopy (AFM) and AFM-infrared nanospectroscopy
Amyloid fibrils and neurodegenerative diseases

Jul. 2015 - Jun. 2016 **Research Associate** (CINTRA, NTU Singapore)

Optical fiber biosensor
DNA and blood applications

Sep. 2012 - Jun. 2015 **Postgraduate researcher** (NTU Singapore, SZU China)

Optical fiber sensors based on M-Z and F-P interferometer
Fiber sensor based on femtosecond laser micromachining

Academic highlights

- **Selected Journal Publication List** (Total number see [Google Scholar](#)):
 1. **J. Zhou**, G. Dietler and et al. Interprotofilament interaction and the configurational identification of hierarchically twisted amyloid fibrils. (In preparation)
 2. **J. Zhou**, R. S. Rugguri, L. Venturelli, L. Keiser, S. K. Sekatskii, F. Gallaire, S. Kasas, G. Longo, T. P. J. Knowles, and G. Dietler*. Environmental control of amyloid polymorphism and order-order transition among fibril polymorphs. (In Submission)
 3. **J. Zhou**, R. S. Rugguri, M. R. Zimmermann, G. Meisl, G. Longo, S. K. Sekatskii, T. P. J. Knowles* and G.

- Dietler*. Effects of sedimentation, microgravity hydrodynamic mixing and air-water interface on α -synuclein amyloid formation. *Chemical Science* 11, 3687-3693, 2020.
4. **J. Zhou**, A. Smirnov, G. Dietler*, S. K. Sekatskii*. Gap plasmon-enhanced high spatial resolution imaging by Photothermal Induced Resonance in visible range. *Nano Letters* 19 (11), 8278-8286, 2019.
 5. **J. Zhou**, S. Sekatskii, R. Welc, G. Dietler*, W.I. Gruszecki*. The role of xanthophylls in the supramolecular organization of the photosynthetic complex LHCII in lipid membranes studied by high-resolution imaging and nanospectroscopy. *Biochimica et Biophysica Acta (BBA)-Bioenergetics*, 148117, 2019.
 6. S. Sekatskii, **J. Zhou**, G. Dietler. Identification and study of polymorphic structures of hierarchically twisted amyloid fibrils by atomic force microscopy. *Biophysical Journal* 116 (3), 50a.
 7. H. Jia, E. Mailand, **J. Zhou**, Z. Huang, G. Dietler, J. M. Kolinski, X. Wang and M. S. Sakar*. Universal Soft Robotic Microgripper. *Small* 15 (4), 1803870, 2019. (Inside Front Cover)
 8. W. Xiang, Z. Wang, D. J. Kubicki, W. Tress, J. Luo, D. Prochowicz, S. Akin, L. Emsley, **J. Zhou**, G. Dietler, M. Grätzel and A. Hagfeldt*. Europium-Doped CsPbI₂Br for Stable and Highly Efficient Inorganic Perovskite Solar Cells, *Joule*, 3 (1), 205-214, 2018.
 9. **J. Zhou**, K. Guo, J. He, M. Hou, Z. Zhang, C. Liao, Y. Wang, G. Xu, Y. Wang*. Novel fabrication technique for phase-shifted fiber Bragg gratings using a variable-velocity scanning beam and a shielded phase mask. *Opt. Express* 26(10): 13311-13321, 2018.
 10. K. Guo†, **J. Zhou**†, J. He, C. Liao, Y. Wang, Z. Li, K. Yang, S. Liu and Y. Wang*. An all-fiber Fan-Out device for varying twin-core fiber types. *J. Lightwave Technol.* 35(23): 5121-5126, 2017. († equal contribution)
 11. **J. Zhou**, Y. Wang*, C. Liao, B. Sun, J. He, G. Yin, S. Liu, Z. Li, G. Wang, X. Zhong and J. Zhao. Intensity modulated refractive index sensor based on Michelson interferometer with Fresnel reflection at the fiber tip. *Sensors and Actuators B* 208(2015), 315-319.
 12. **J. Zhou**, C. Liao, Y. Wang*, G. Yin, X. Zhong, K. Yang, B. Sun, G. Wang and Z. Li. Simultaneous measurement of strain and temperature by employing fiber Mach-Zehnder interferometer. *Opt. Express* 22(2): 1680-1686, 2014.
 13. **J. Zhou**, Y. Wang*, C. Liao, G. Yin, X. Xu, K. Yang, X. Zhong, Q. Wang and Z. Li. Intensity-Modulated Strain Sensor Based on Fiber In-Line Mach-Zehnder Interferometer. *IEEE Photon. Technol. Lett.* 26(5): 508-511, 2014.

• Patent list:

1. Yiping Wang, **Jiangtao Zhou**, Changrui Liao, Intensity-modulated fiber Michelson strain sensor and fabricating method, Chinese Patent, Patent Code: ZL 201420082778.7.
2. Yiping Wang, **Jiangtao Zhou**, Changrui Liao, The universal twin core fiber splitter, Chinese Patent (in process)

• Awards and Grants:

1. Excellent post-graduate student award (2016)
2. National Graduates Scholarship of China (2014)
3. Best Post-graduate Scholarship in Shenzhen University (2014)
4. Outstanding award of summer school of optical fiber technology (2013)

• Skills:

AFM, AFM nanoindentation, AFM infrared/visible spectroscopy, AFM force spectroscopy, SEM, TEM, CryoEM, Femtosecond-laser micromachining, optical fiber sensor

• Interests:

Basketball, travelling and photography.